UNIVERSITY OF NAPLES FEDERICO II

PH. D. PROGRAM IN

STRUCTURAL AND GEOTECHNICAL ENGINEERING AND SEISMIC RISK (XXXIV CYCLE)

Thesis for the Degree of Doctor of Philosophy

The effects of seismic sequences on seismic hazard and structural vulnerability

by

MABEL ORLACCHIO

ADVISOR: PROFESSOR IUNIO IERVOLINO

CO-ADVISOR: DR. GEORGIOS BALTZOPOULOS

2022

DIST

Scuola Politecnica e delle Scienze di Base
Department of Structures for Engineering and Architecture

La borsa di dottorato è stata cofinanziata con risorse del
Programma Operativo Nazionale Ricerca e Innovazione 2014-2020 (CCI 2014IT16M2OP005),
Fondo Sociale Europeo, Azione I.1 "Dottorati Innovativi con caratterizzazione Industriale"

UNIONE EUROPEA
Fondo Sociale Europeo

Ministero dell'Università
e della Ricerca

PON
RICERCA
E INNOVAZIONE
2014 - 2020

Exister c'est oser se jeter dans le monde.

(Simone de Beauvoir)

The effects of seismic sequences on seismic hazard and structural vulnerability

Ph.D. Thesis presented

for the fulfillment of the Degree of Doctor of Philosophy

in Structural and Geotechnical Engineering and Seismic Risk

by

MABEL ORLACCHIO

2022

Approved as to style and content by

Prof. Iunio Iervolino, Advisor

Dr. Georgios Baltzopoulos, Co-advisor

University of Naples Federico II
Ph.D. Program in Structural and Geotechnical Engineering and Seismic Risk

XXXIV cycle - Chairman: Prof. Iunio Iervolino

www.dist.unina.it/dottorati-di-ricerca/dottorati

Candidate's declaration

I hereby declare that this thesis submitted to obtain the academic degree of Philosophiæ Doctor (Ph.D.) in Structural and Geotechnical Engineering and Seismic Risk is my own unaided work, that I have not used other than the sources indicated, and that all direct and indirect sources are acknowledged as references.
Parts of this dissertation have been published in international journals and/or conference articles (see list of the author's publications at the end of the thesis).

Naples, March 10, 2022

Mabel Orlacchio

Abstract

Current practice for seismic risk assessment typically considers that structural damage can only occur in a single seismic event. However, neglecting that earthquakes occur in clusters, both in space and in time, can lead to an underestimation of both seismic hazard and structural vulnerability. Indeed, past research has shown that neglecting aftershocks (seismic events following the mainshock in a sequence), can lead to non-negligible differences in the assessment of seismic hazard. From the point of view of structural vulnerability, the necessity of considering the effects of seismic sequences has also been highlighted by recent seismic events, such as the seismic sequences in Christchurch (2010-2011), in Emilia-Romagna (2012) and in central Italy (2016-2017), to name a few. These events showed that at least part of the seismic damage documented on the building heritage was due to the cumulative effect of multiple shocks clustered closely in time. Therefore, this thesis focuses on two components of seismic risk, i.e., the seismic hazard and structural vulnerability, and on how to treat them in order to account for sequence effects.

In the context of seismic hazard, the thesis applies the *Sequence-Based Probabilistic Seismic Hazard Analysis* procedure to the United Kingdom. This part has been developed in collaboration with the firm *Ove Arup and Partners London* with the objectives of developing national hazard maps taking into account the effects of seismic sequences and investigating the effects of aftershocks in the assessment of seismic hazard.

At the same time, regarding seismic vulnerability, the thesis addresses various issues in the estimation of state-dependent fragility curves, which are fragility models that allow for the possibility that a structure may have already been damaged by previous shocks. Initially, the assessment of state-dependent fragilities is addressed using back-to-back incremental dynamic analysis applied to individual structures belonging to classes of reinforced concrete and masonry buildings. In one case, state-dependent fragilities have been evaluated for a masonry building as part of the collaboration with the firm *Arup Italy*. On the other hand, the evaluation for building classes has been carried out within the European research project *RISE* (*Real-time earthquake rIsk reduction for a reSilient Europe*). These evaluations have allowed touching some critical points that characterize the estimation of state-dependent fragilities such as: the limitation of computational costs, the choice of the intensity measure, the definition of engineering demand parameters, and limit states.

Finally, in order to reduce the computational cost of the methodology for state-dependent fragility assessment, a simplified method applicable to first-mode dominated reinforced concrete structures is presented, based on nonlinear static analysis and on a new proposed predictive model, which allows predicting the distribution of capacity curve parameters for already damaged structures.

Keywords: seismic sequences, aftershocks, state-dependent fragilities, sequence-based seismic reliability; damage accumulation.

Sintesi in lingua italiana

Nella pratica corrente di valutazione del rischio sismico si assume generalmente che il danno strutturale sia causato da singoli eventi sismici. Tuttavia, trascurare che in realtà i terremoti si verifichino raggruppati nello spazio e nel tempo può portare ad una sostanziale sottostima sia della pericolosità sismica che della vulnerabilità strutturale. La ricerca in tale ambito ha, infatti, dimostrato che non considerare le repliche sismiche (eventi sismici che seguono la scossa principale) può portare anche a differenze significative nella valutazione della pericolosità sismica. Per quanto riguarda la vulnerabilità strutturale, la necessità di considerare gli effetti delle sequenze è stata evidenziata anche da recenti eventi sismici, quali le sequenze di Christchurch (2010-2011), dell'Emilia-Romagna (2012) e dell'Italia Centrale (2016-2017), per citarne alcune. Questi eventi hanno mostrato che almeno parte dei danni sismici osservati sul patrimonio edilizio era dovuto all'effetto cumulato di scosse che si sono susseguite in breve tempo.

La presente tesi si focalizza pertanto su due delle componenti del rischio, cioè la pericolosità sismica e la vulnerabilità strutturale, e su come trattarle per tener conto del verificarsi di sequenze sismiche.

Nell'ambito della pericolosità sismica, la presente tesi applica la procedura di *Sequence-Based Probabilistic Seismic Hazard Analysis* al Regno Unito. Tale parte, è stata sviluppata in collaborazione con *Ove Arup and Partners London* con l'obiettivo di sviluppare mappe di pericolosità della nazione che tengano conto degli effetti delle sequenze sismiche, nonché di indagare gli effetti dell'inclusione delle scosse secondarie nella valutazione della pericolosità simica.

Parallelamente nell'ambito della vulnerabilità sismica, la tesi affronta da diversi punti di vista la stima delle fragilità stato-dipendenti, modelli di fragilità che consentono di tener conto del fatto che l'evento sismico possa colpire una struttura che si trova in condizioni non intatte, già danneggiata da eventi precedenti. Inizialmente, è stato affrontato il calcolo delle fragilità stato-dipendenti mediante il metodo rigoroso dell'analisi dinamica incrementale back-to-back applicato a singole strutture appartenenti a classi di edifici in cemento armato e muratura. Nel dettaglio, le fragilità stato-dipendenti sono state valutate per un edificio in muratura nell'ambito della collaborazione con *Arup Italia*. La valutazione per classi di edifici è stata, invece, condotta nell'ambito del progetto di ricerca Europeo *RISE* (*Real-time earthquake rIsk reduction for a reSilient Europe*). Tali valutazioni hanno consentito di affrontare alcuni punti critici della stima delle fragilità stato-dipendenti quali: la limitazione dell'onere computazionale, la scelta della misura di intensità, la definizione di un adeguato parametro ingegneristico di domanda e degli stati limite.

Nell'ottica di ridurre l'onere computazionale della metodologia rigorosa di valutazione delle fragilità stato-dipendenti, viene infine presentato un metodo

semplificato applicabile alle strutture in cemento armato il cui comportamento è dominato dal primo modo di vibrare. Tale metodo è basato sull'analisi statica non lineare e su un modello predittivo appositamente sviluppato che consente di prevedere la distribuzione dei parametri che definiscono la curva di capacità di strutture già danneggiate.

Parole chiave*:* Sequenze sismiche, fragilità stato-dipendenti, affidabilità sismica basata sulle sequenze; cumulo del danno.

Acknowledgments

I would like to sincerely appreciate my advisor, Professor Iunio Iervolino, for supervising and advising me during these years; for giving me the opportunity to work on interesting and innovative topics. His compliance and devotion to research have always spurred me to give my best and overcome my limitations.

I would like to thank my co-advisor Dr. Georgios Baltzopoulos for his guidance and support to my work and for always providing me with new insights and alternative points of view during these years.

I would like to acknowledge Dr. Eugenio Chioccarelli and Dr. Pasquale Cito for their technical support and collaboration, and the whole research group with whom I shared these years.

The research presented in this dissertation has been supported by the Italian Ministry of University and Research (MUR) under program PON 2014-2020 (CCI 2014IT16M2OP005), Fondo Sociale Europeo, Azione I.1 "Dottorati innovative con caratterizzazione Industriale". The program had as corporate partners the firms Arup Italy and Arup London. Therefore, I would like to thank my tutors, Dr. Barbara Polidoro, Dr. Daniele Dozio, and Dr. Manuela Villani, who guided me during the collaborations, thank you for your suggestions and support of my work. An affectionate thank you goes to the entire office of Arup Italy that welcomed me during the months I spent in Milan, despite the pandemic I will always keep a good memory of this first work experience.

Finally, I would like to express my gratitude to the reviewers of this thesis, Prof. Anastasios Sextos (University of Bristol) and Dr. Helen Crowley (EUCENTRE; Pavia, Italy) for their valuable comments that helped me to improve the quality of my thesis.

Contents

CHAPTER 1

CHAPTER 2

CHAPTER 3

CHAPTER 4

CHAPTER 5

CHAPTER 6

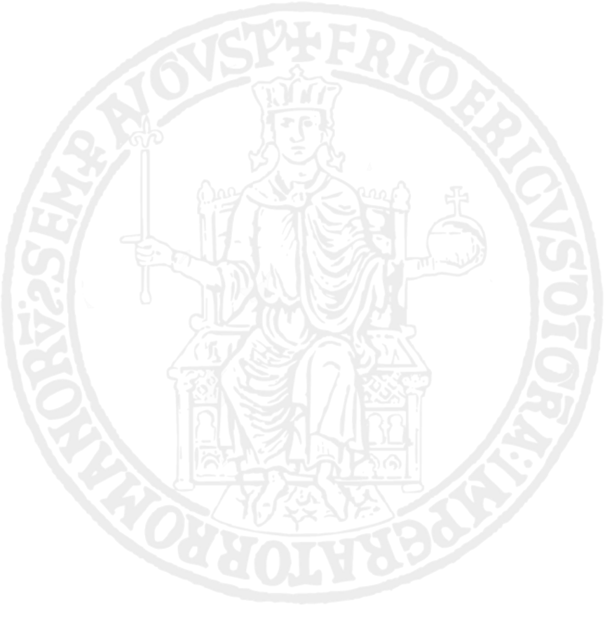

List of Acronyms

The following acronyms are used throughout the thesis.

APSHA	Aftershock Probabilistic Seismic Hazard Analysis
BGS	British Geological Survey
CA	Cloud Analysis
CDF	Cumulative distribution function
CNR	Council for National Research
DM	Damage measure
DS	Damage state
DV	Decision variable
EDP	Engineering Demand Parameter
ESDOF	Equivalent single-degree-of-freedom system
ETAS	Epidemic-type aftershock sequences
GM	Ground motion
GMPE	Ground motion prediction equation
GR	Gutenberg-Richter
HPP	Homogenous Poisson process
IDA	Incremental dynamic analysis
IM	Intensity measure
IMK	Ibarra-Medina-Krawinkler
MAF	Mean annual frequency
MSA	Multiple Stripe Analysis
NAM	Nederlandse Aardolie Maatschappij
NHPP	Non-homogenous Poisson process
NLDA	Non-linear dynamic analysis

PBEE	Performance-Based Earthquake Engineering
PDF	Probability density function
PEER	Pacific Earthquake Engineering Research
PSDA	Probabilistic Seismic Demand Analysis
PSHA	Probabilistic Seismic Hazard Analysis
RC	Reinforced concrete
RISE	Real-time earthquake risk reduction for a resilient Europe
RV	Random variable
SDOF	Single-degree-of-freedom system
SERA	Seismology and Earthquake Engineering Research Infrastructure Alliance for Europe
SLC	Limit state of near collapse
SLD	Limit state of damage
SLS	Limit state of serviceability
SPSHA	Sequence-Based Probabilistic Seismic Hazard Analysis
3D	Three-dimensional
UHS	Uniform hazard spectrum
URM	Unreinforced masonry

List of Figures

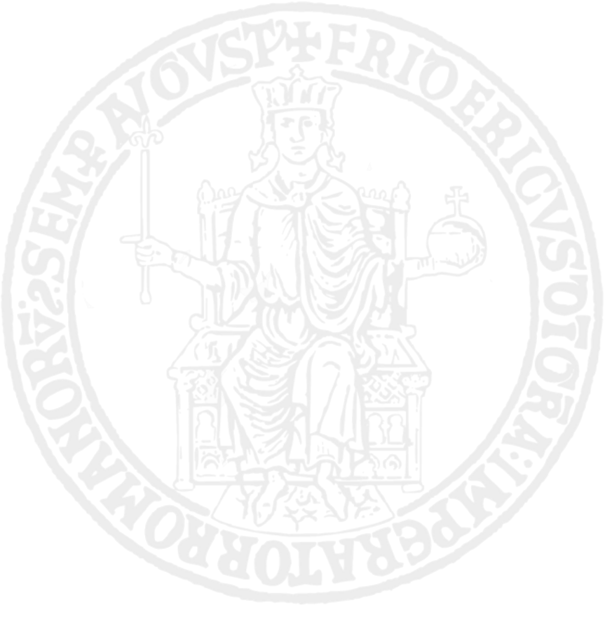

List of Tables

1

Introduction

1.1. Background and motivation

Current practice of seismic-risk assessment only considers the occurrence of single seismic events, both from the point of view of seismic hazard, i.e., through the application of Probabilistic Seismic Hazard Analysis (PSHA; Cornel, 1968); and from the point of view of structural vulnerability assessment, which does not take the issue of damage accumulation into account; i.e., each seismic event finds the structure in its intact condition, with no consideration of any possible damage caused by earlier earthquakes. However, the assumption that the risk to the built environment arises exclusively from single earthquakes is refused by the very nature of seismic events, which actually occur in time-space clusters (mainshock-aftershocks sequences). Moreover, past disasters have clearly demonstrated that aftershocks often cause additional damage to buildings and infrastructure, exacerbating the harm caused by the main earthquake. Recent seismic events, including the sequences in Christchurch in 2010-2011 and Emilia-Romagna in 2012, as well as the earthquakes in central Italy in 2016-2017, have highlighted the potential pitfalls of the current approach and indicate a clear need to revisit how seismic-risk assessment is carried out.

This thesis concentrates on two of the components of risk referred to above: seismic hazard and structural vulnerability, with the focus on elements that enable the classical risk-assessment framework to be extended to cover the issue of seismic sequences.

1.1.1. Sequence-Based Seismic Risk Analysis (Probabilistic Seismic Risk Analysis that accounts for earthquake sequences)

Seismic risk can be defined as the probability that a pre-defined level of losses (expressed in terms of human lives, economic assets or cultural value) is exceeded due to the occurrence of earthquakes within a reference time-period. The risk can be estimated at different territorial levels. i.e., global, regional or site-specific. Loss can therefore encompass a single structure, a city, or an entire area.

Seismic risk is a function of three components: *seismic hazard; seismic vulnerability and exposure*. The first of these is represented by the frequency and the intensity of the seismic events occurring in a particular territory and calculates the probability that a fixed seismic-intensity threshold at the site of interest is exceeded over a certain period of time. The second element, seismic vulnerability, is the physical environment's susceptibility to sustaining damage due to seismic events of a given magnitude. It is represented by the probability that a certain level of damage occurs during an event with a set intensity, defined by an intensity measure (IM). Finally, *exposure* takes into account the location, quality and quantity of assets and activities that may be affected, both directly and indirectly, by seismic events and refers to the probability that a set amount of economic loss is exceeded at a set damage level.

The best current practice for seismic-loss assessment relies on the Performance-Based Earthquake Engineering framework (PBEE; Cornell and Krawinkler, 2000; Krawinkler and Miranda, 2004), which was developed by the Pacific Earthquake Engineering Research (PEER) Center. The framework was designed to improve the decision-making in relation to the seismic performances of facilities. Consequently, the assumed *decision variable* (DV) can cover costs, number of casualties, or the duration of any industry downtime. Any other DVs of primary interest to decision-makers can be also taken into account. The risk-assessment procedure has four stages, as seen in Figure 1.1: 1) hazard analysis (i.e., quantifying the frequency and intensity of earthquakes and ground motions); 2) structural analysis (which aims to determine the structural-response parameters); 3) damage analysis (i.e., the quantification of damage states and their relationship to response parameters); and 4) loss analysis (the evaluation of financial losses, downtime and casualties, as well as the consequences for owners and society).

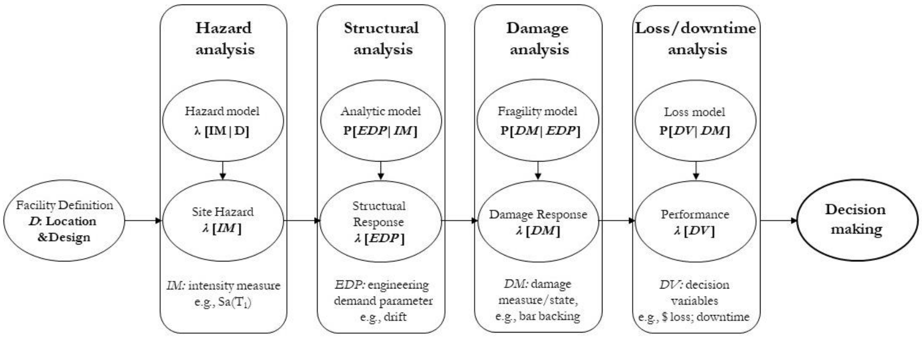

Figure 1.1 Overview of the PEER seismic-loss assessment methodology (adapted from Krawinkler, 2005).

The main advantage of this approach is the opportunity it provides to compartmentalize the different phases of assessing seismic risk by separating them into discipline-specific contributions (engineering seismology, structural engineering, cost analyses, decision making). Despite this division, the four independent stages are linked through interfacing output variables: Intensity Measures (IMs), Engineering Demand Parameters ($EDPs$) and Damage Measures (DMs). The first step is the hazard analysis, which determines the annual rate of exceedance of a ground motion intensity measure at a site of interest. This is achieved with the PSHA (Cornell, 1968), the fundamentals of which are described in what follows.

The structural analysis aims to compute a vector of $EDPs$, i.e., the structural-response parameters that can be related to the damage caused to structural and non-structural components, as well as to the contents of the structure. An example of an appropriate EDP is the interstorey drift, although it is possible to use any other structural parameter that enables investigators to control for the evolutionary state of the structural damage up to the point of collapse. The relationship between $EDPs$ and IMs is typically identified via non-linear dynamic analyses (NLDAs) and their outputs. This is often referred to as Probabilistic Seismic Demand Analysis (PSDA; Shome and Cornell, 2006), and is the conditional probability that the EDP will exceed a specified threshold value, edp_{DS}, assuming that the IM is equal to a particular value im; $P\left[EDP > edp_{DS} \middle| IM = im\right]$. The integration of this probability over the hazard curve provides the mean annual frequency of exceedance of the EDP.

The DM interfacing variable can be introduced to relate $EDPs$ to the relevant DVs. This facilitates the computation of DVs from $EDPs$. In the damage analysis phase, $EDPs$ are related to DMs of the building's components (structural, non-structural or contents). A DM is defined for each constituent of interest and describes the extent of the damage caused during an earthquake. The output of the damage analysis is the relationship between $EDPs$ and DMs, and expresses the probability of being in a certain damage state dm, given that the EDP is equal to a given value, edp_{DS} $P\left[DM = dm \middle| EDP = edp_{DS}\right]$. Such relationships are generally computed using analytical/numerical modeling, laboratory testing or field experience.

The aim of the fourth stage, the loss analysis, is to estimate the exceedance frequency of various performance levels. Performance can be parameterized via one or more DVs, which are defined at the system or building level. If the relationships $P\left[DM = dm \middle| EDP = edp_{DS}\right]$ for all the relevant damage states of all the relevant components are known, the DVs of interest can be evaluated either directly or using cost functions that relate the damage states to costs.

The entire procedure, which forms the basis of the performance assessment, can be summarized in the following triple integral, which computes the mean annual frequency (MAF, λ) of exceeding of a DV threshold (Yeo and Cornell, 2005):

$$\lambda(DV) = \iiint G(DV \mid DM) \cdot dG(DM \mid EDP) \cdot dG(EDP \mid IM) \cdot \left| d\lambda(IM) \right|. \quad (1.1)$$

In Eq.(1.1) $\lambda(IM)$ is the mean annual rate of exceeding a given IM level; $G(X \mid Y) = P\left(X \geq x \mid Y = y\right)$ is the complementary cumulative distribution function (CCDF) of X given Y; and $dG(X|Y)$ and $d\lambda(IM)$ are the differentials of $G(X|Y)$ and $\lambda(IM)$. The key assumption of the entire procedure is the conditional independence of DV and DM from IM and of DV from EDP. This implies that intermediate variables, i.e., EDP and DM, used to relate IM to DV, have been chosen to ensure that the conditioning information is not "carried forward". As an example, $EDPs$ should be selected so that DMs (and DVs) do not vary with intensity, once EDP has been specified. Similarly, IMs should be chosen to ensure that, once it is given, the dynamic response is not also influenced by other ground motion characteristics, e.g., magnitude or source-to-site distance.

In its classical formulation, seismic-risk analysis does not take into account the fact that earthquakes occur in spatio-temporal clusters (mainshock-aftershocks sequences) and that a structure can be hit by multiple subsequent events. The formulation of the PEER Center's PBEE framework employs PSHA in the hazard-analysis phase. Meanwhile, a convenient time-invariant representation of the failure probability is assumed for the vulnerability assessment. In effect, therefore, only intact structures are considered in risk evaluation, it being assumed that enough time will elapse until the next event for stakeholders to restore a damaged structure to its initial state.

Consequently, changes are required to this classical seismic-risk assessment to ensure that its evaluations of seismic hazard and structural vulnerability take the occurrence of earthquake sequences into account. One way of doing this would be to employ the so-called Sequence-Based Probabilistic Seismic Hazard Analysis (SPSHA, Iervolino et al., 2014) to account the effects of aftershocks in long-term hazard. SPSHA is a well-established procedure that, in analytical terms, combines the classical PSHA and the aftershock probabilistic seismic-hazard analysis (APSHA, Yeo and Cornell, 2009a), producing a seismic-hazard integral that accounts for mainshock-aftershocks seismic sequences. More details on the SPSHA are set out in the following paragraphs.

The occurrence of mainshock-aftershock sequences should also be considered in the assessment of seismic vulnerability. This would take into account the fact that structural failure may be caused not only by a single shock but also due to damage accumulated over multiple seismic events. Indeed, earthquakes are known to be clustered in both space and time, meaning that repairs may not be possible between shocks. This can be made by computing the state-dependent fragility curves, assuming the simplest form of dependency between damage increments for which structural vulnerability, given the features of a particular earthquake, depends on (only) the state of the structure at the time of the shock (Iervolino et al., 2016).

The main concepts at the hearth of both classical probabilistic seismic hazard analysis and SPSHA, as well as the methods employed to assess vulnerability, are set out in the following sections.

1.1.2. Objectives of the thesis

The main objective of this thesis is to comprehensively deal with the issue of including the effects of seismic sequences in seismic risk analysis. This is approached having regard to two complementary elements: 1) seismic hazard and 2) structural vulnerability.

The inclusion of seismic sequences in any assessment of the first element can be achieved with the SPSHA, which is a well-established procedure first presented by Iervolino et al. (2014) and widely used in the case of Italy (Iervolino et al., 2018; Chioccarelli et al., 2021). Consequently, this part of the thesis examines its application to another country, i.e. the United Kingdom (UK), in order to: 1) develop the national seismic-hazard maps of the country that take into account the effects of seismic sequences, and 2) quantify the increments in the UK's seismic hazard as a result of the aftershocks. This part of the thesis was carried out in collaboration with the firm *Ove Arup and Partners London.*

The inclusion of seismic sequences in the context of the second complementary element - structural vulnerability - is possible through the use of state-dependent fragility curves that allow taking into account the damage-accumulation process that occurs due to multiple seismic events after the mainshock. This part of the thesis has several objectives. First of all, the assessment of state-dependent fragility curves of individual structures belonging to classes of reinforced concrete (RC) and masonry buildings which is conducted via the rigorous procedure of back-to-back incremental dynamic analysis (IDA). In one case, thanks to the collaboration with the firm *Arup Italy,* the state-dependent fragility functions were evaluated for a case-study building representative of the masonry terraced houses common in an area near Groningen in the north of the Netherlands. This type of structure (in this location) was chosen because commercial gas production in the region means that such buildings experience earthquakes and have been studied widely in recent years as a result. On the other hand, the state-dependent fragilities were assessed for existing Italian building classes. The structures under consideration, i.e., existing residential RC and masonry buildings in Italy, are taken from the outcomes of the SERA project (Seismology and Earthquake Engineering Research Infrastructure Alliance for Europe). The current assessment has also been conducted within the ongoing European research project RISE (Real-time earthquake rIsk reduction for a reSilient Europe). These assessments have allowed dealing with the main issues concerning the assessment of state-dependent fragilities such as: the limitation of computational costs, the choice of the intensity measure, the definition of engineering demand parameters and limit states.

Finally, a simplified method for the assessment of state-dependent fragilities based on non-linear static (also known as *pushover)* analysis is presented. This was developed to lower the computational costs compared to the classic, more rigorous approach, enabling the evaluation of state-dependent fragilities in first-mode dominated reinforced concrete (RC) structures. This simplified method also required the development of a predictive model for evaluating the central tendency and record-to-record variability of constant-ductility residual displacements of bilinear single-degree-of-freedom systems (SDOFs) that degrade in strength and stiffness under cyclic loading.

1.1.3. Organization of the thesis

This thesis is structured such that the remainder of **Chapter 1** provides an overview of the main concepts behind the extension of the classical seismic-risk assessment to also cover the issue of seismic sequences. More specifically, the essential elements of the PSHA and SPSHA are briefly described in relation to seismic hazard. Then, with respect to structural vulnerability, are introduced the analytical methods for the assessment of the fragility curves for both intact structures (i.e., structure-specific fragility curves) and already-damaged structures (i.e., state-dependent fragility curves).

The rest of the thesis is organized as follows. **Chapter 2** presents a national-scale application of PSHA and SPSHA to the UK, with hazard maps of the country produced for three IMs and four return periods. A comparison of the results of the two methodologies informs an assessment of the seismic-hazard damage increments caused by aftershocks. The work in this part of the thesis was developed in collaboration with the firm *Ove Arup and Partners London.*

Chapter 3 deals with the evaluation of the structure-specific and state-dependent seismic fragility functions of the Dutch unreinforced masonry (URM) building representative of the masonry terraced houses located in the northern region of the Netherlands, near Groningen. The fragilities of the intact structure are first assessed via Cloud Analysis, analyzing the three-dimensional model developed with LS-DYNA finite element software. Subsequently, the assessment of state-dependent fragilities is conducted using two equivalent, inelastic, SDoF systems, each of which represents a direction of the structure and whose definition is based on the pushover curves obtained from the analysis of the original model. The work in this part of the thesis has been developed in collaboration with *Arup Italy.*

Chapter 4 presents the analytical assessment via back-to-back IDA of the structural vulnerability models for Italian building classes, which are one of the outcomes of the RISE project. The structures under consideration are taken from the SERA project and relate to existing residential RC and masonry Italian buildings. Two issues affecting the assessment of fragility functions are also addressed, i.e., the choice of the IM and the identification of the number of ground motion records to execute the NLDAs.

Chapter 5 introduces the predictive model used for evaluating the central tendency and record-to-record variability of constant-ductility residual displacements of bilinear SDoF systems that exhibit strength and stiffness degradation under cyclic loading. This is typically observed in RC structures with predominantly flexural behavior. Some of the model's applications are also presented with particular attention paid to its use in the probabilistic prediction of the post-earthquake pushover curve of a damaged structure. This is the heart of the simplified methodology developed in the thesis for estimating state-dependent seismic fragility functions (introduced in the following chapter). Meanwhile, **Chapter 6** outlines this simplified approach, which is based on nonlinear static analyses and the predictive model described in Chapter 5. After introducing the stages of the methodology, the simplified method is compared to the rigorous one, i.e., the back-to-back Incremental Dynamic Analysis (IDA), through the application to a case study.

Finally, the important contributions and findings of the study are summarized and discussed in the last part of the thesis.

1.2. Classical and Sequence-Based Probabilistic Seismic Hazard Analysis

The classical PSHA was first formulated in the milestone work by Cornell, (1968). Its goal is to estimate the average number of mainshocks per unit-time (often one year) that cause an IM threshold im at a site of interest to be exceeded (i.e., the exceedance rate). This rate, indicated herein as $\lambda_{im,E}$, is time-invariant and defines the homogenous Poisson process (HPP) regulating the occurrence of earthquakes that cause the im to be exceeded over time. So, for a single seismic source zone affecting the site, $\lambda_{im,E}$ is computed as per Eq. (1.2) (Kramer, 1996):

$$\lambda_{im,E} = \nu_{\mathrm{E}} \cdot \int_{r_{\mathrm{E},min}}^{r_{\mathrm{E},max}} \int_{m_{\mathrm{E},min}}^{m_{\mathrm{E},max}} \mathrm{P}[IM_E > im \mid M_E = m, \mathrm{R}_E = r, \underline{\theta}] \cdot f_{M_E,\mathrm{R}_E}(m,r) \cdot dm \cdot dr. \quad (1.2).$$

In this equation, ν_E is the rate of mainshocks with a magnitude equal to or greater than the minimum ($m_{\mathrm{E},min}$) deemed possible for the seismic source and it is calibrated based on a de-clustered catalog. The term $\mathrm{P}\left[IM_E > im \mid M_E = m, \mathrm{R}_E = r, \underline{\theta}\right]$, which is obtained with a ground motion prediction equation (GMPE), represents the conditional probability that the im is exceeded due to a mainshock with a magnitude equal to m and a source-to-site distance equal to r. This probability also depends on $\underline{\theta}$, which allows additional parameters such as local soil site conditions and the rupture mechanism of the source to be taken into account.

The joint probability density function (PDF) of the mainshock magnitude $\left(M_E\right)$ and distance $\left(R_E\right)$ is $f_{M_E,R_E}\left(m,r\right)$. Assuming that M_E and R_E are stochastically independent random variables (RVs), this is calculated as $f_{M_E,R_E}\left(m,r\right)=f_{M_E}\left(m\right)\cdot f_{R_E}\left(r\right)$, where $f_{M_E}\left(m\right)$ and $f_{R_E}\left(r\right)$ are the marginal distributions of the magnitude and distance of the mainshocks, respectively. The former is defined between $m_{E,min}$ and the maximum considered for the source, $m_{E,max}$. It is generally described using a truncated exponential distribution derived from the Gutenberg-Richter (GR) relationship (Gutenberg and Richter, 1944). The distribution of the latter, which is defined as being between $r_{E,min}$ and $r_{E,max}$, generally only depends on the geometry of the source and the position of the site with respect to the source itself.

In the case of multiple seismic sources, say s in number, the calculation is conducted one source at a time and the results are added up: $\lambda_{im,E}=\sum_{i=1}^{s}\lambda_{im,E,i}$.

The SPSHA enables account to be taken of the effect of aftershocks (i.e., ignoring foreshocks). It uses the same input as the PSHA, that is, the rate of mainshocks from a de-clustered catalog. A non-homogenous Poisson process (NHPP) is used to model the occurrence of aftershocks, conditional to mainshock's magnitude and location. In these hypotheses, the main outcome of the SPSHA is the average number of seismic sequences that, in the unit of time, cause at least one exceedance of im at the site. This rate, referred to here as λ_{im}, defines the HPP process regulating the occurrence of both mainshocks, and subsequent aftershocks, that lead to the exceedance of im over time. This is calculated with Eq. (1.3):

$$\lambda_{im}=\nu_E\cdot\left\{1-\int_{r_{E,min}}^{r_{E,max}}\int_{m_{E,min}}^{m_{E,max}}\mathrm{P}\left[IM_E\leq im\,|\,M_E=m,\mathrm{R}_E=r,\underline{\theta}\right]\times\right.$$
$$\left.\times e^{-E\left[N_{A|m}\left(0,\Delta T_A\right)\right]\cdot\int_{r_{A,min}}^{r_{A,max}}\int_{m_{A,min}}^{m}\mathrm{P}\left[IM_A>im|M_A=m_A,\mathrm{R}_A=r_A,\underline{\theta}\right]\cdot f_{M_A,\mathrm{R}_A|M_E,\mathrm{R}_E}\left(m_A,r_A|m,r\right)\cdot dm_A\cdot dr_A}\cdot f_{M_E,\mathrm{R}_E}\left(m,r\right)\cdot dm\cdot dr\right\}.\tag{1.3}$$

The (A) subscript in this equation denotes terms pertaining to aftershocks. $\mathrm{P}\left[IM_E \leq im \mid M_E = m, \mathrm{R}_E = r, \underline{\theta}\right]$ is equal to $1-\mathrm{P}\left[IM_E > im \mid M_E = m, \mathrm{R}_E = r, \underline{\theta}\right]$. The exponential term represents the probability that none of the aftershocks, triggered by a mainshock with magnitude $M_E = m$ and a distance $R_E = r$ (strictly speaking, it should be location, not distance), causes the exceedance of im between $t = 0$ (i.e., the occurrence time of the mainshock) and the duration of the sequence, ΔT_A. $P\left[IM_A > im_A \mid M_A = m_A, \mathrm{R}_A = r_A, \underline{\theta}\right]$ is obtained with the GMPE and is the probability that im is exceeded given an aftershock with a magnitude $M_A = m_A$ and a source-to-site distance $R_A = r_A$. The term $f_{M_A,\mathrm{R}_A|M_E,\mathrm{R}_E}$ is the joint PDF of the magnitude and distance of aftershocks and it is conditional on the features of the mainshock (i.e., magnitude and location) occurring at the source. Assuming that M_A and R_A are conditionally independent RVs, this function is $f_{M_A,\mathrm{R}_A|M_E,\mathrm{R}_E} = f_{M_A|M_E} \cdot f_{\mathrm{R}_A|M_E,\mathrm{R}_E}$, where $f_{M_A|M_E}$ is the conditional distribution of the aftershocks' magnitude (i.e., following the GR) and $f_{\mathrm{R}_A|M_E,\mathrm{R}_E}$ is the conditional distribution of the site's distance to the aftershocks. The magnitude distribution of the aftershocks is bounded by a minimum magnitude $m_{A,min}$ and m (i.e., the mainshock's magnitude). The location of aftershocks with respect to the site depends on the location and magnitude of the mainshock. The distribution of the aftershocks' distance is bounded within $r_{A,min}$ and $r_{A,max}$, which are the minimum and maximum values possible for R_A, respectively. $E\left[N_{A|m}\left(0,\Delta T_A\right)\right]$ is the expected number of aftershocks with a magnitude between $m_{A,min}$ and m, generated by a mainshock with a magnitude $M_E = m$, in ΔT_A. This is computed according to Yeo and Cornell (2009):

$$E\left[N_{A|m}\left(0,\Delta T_A\right)\right] = \frac{10^{a+b\cdot\left(m-m_{A,min}\right)} - 10^{a}}{p-1} \cdot \left[c^{1-p} - \left(\Delta T_A + c\right)^{1-p}\right], \tag{1.4}$$

where c and p are the parameters of the modified Omori law, which models the temporal decay of the rate of aftershocks, and a and b define the GR relationship for the aftershocks.

The hazard curve for PSHA and SPSHA, respectively, are obtained by calculating Eq. (1.2) and Eq. (1.3) for different im values within a range of interest.

1.3. Fragility curves of intact structures and state-dependent fragility curves

A structure-specific, seismic fragility function defines the conditional probability that a structure will fail to meet some performance objective if the ground-shaking intensity measure (IM) is at a specific level im. This failure is often referred to as the exceedance of a *limit-* or *damage*-state (DS) and traditionally relates to an intact structure that experiences a single seismic event. In the simplest of cases, fragility can be defined using an appropriate measure of the structural response (EDP), and a threshold value thereof, edp_{DS}. The exceedance of this threshold is taken to signify the structure's transition from its initial state (intact conditions) to the generic DS, as expressed by Eq. (1.5):

$$P\left[f\,|\,IM=im\right]=P\left[DS\,|\,IM=im\right]=P\left[EDP>edp_{DS}\,|\,IM=im\right]. \tag{1.5}$$

If seismic reliability calculations are expected to account for seismic sequences, it is necessary to evaluate the probability that an already-damaged structure transits in a single seismic event from one DS, say DS_A, to another more severe one, DS_B. A state-dependent fragility function will provide that probability, conditional upon the occurrence of a shaking intensity im during one of the shocks in the cluster. This can be expressed as $P\left[EDP>edp_{DS_B|DS_A}\,|DS_A\cap IM=im\right]$. In this case, $edp_{DS_B|DS_A}$ denotes the EDP threshold for DS_B when the structure is in the damage condition identified in DS_A Meanwhile, the state-dependent fragility can simply be denoted as $P\left[DS_B\,|DS_A\cap IM=im\right]$.

The following paragraphs describe the analytical methods for the estimation of the fragility functions of the intact structures and the state-dependent fragility curves.

1.3.1. Analysis methodologies

This section describes the state-of-the-art of the analytical methods used to estimate fragility functions. Such methodologies in PBEE typically consist of subjecting the numerical model of the structure to NLDAs, collecting the structural response to a suite of accelerograms. The analytical methodologies used in these fragility calculations can be classified according to the type of fragility functions they are able to estimate, i.e., structure-specific fragility curves for intact structures or state-dependent fragility curves. There are alternative procedures available in the literature for characterizing the relationship between an EDP and an IM and for assessing the fragility curves of intact structures. More specifically, common NLDAs methods in earthquake-engineering research are: *Incremental Dynamic Analysis* (IDA; Vamvatsikos and Cornell 2001, 2004); *Multiple Stripe Analysis* (MSA, Jalayer and Cornell, 2008), and *Cloud Analysis* (CA, Jalayer et al., 2015, 2017).

In relation to the assessment of state-dependent fragility curves, the extended version of IDA, referred to as *back-to-back IDA* (Luco et al., 2004; Ryu et al., 2011; Goda, 2012; Ruiz-García, 2012; Raghunandan et al., 2015; Goda, 2015) is described in what follows. Also introduced are the simplified pushover analysis-based procedures for the simplified estimation of state-dependent fragilities.

1.3.2. Methodologies for assessing structure-specific seismic fragility

1.3.2.1. Incremental dynamic analysis

IDA is a type of NLDA developed to investigate the dynamic behavior of structures at different levels of seismic intensity, covering the entire range of structural behavior, from elastic to non-linear, and ultimately, to collapse (Vamvatsikos and Cornell, 2001, 2004). The procedure involves performing multiple NLDAs using a suite of accelerograms. Each record of the set is progressively scaled in amplitude to increasing levels of shaking intensity in order to cover a broad range of IM levels. The structural response, expressed in terms of an EDP, is registered at each IM level for each acceleration record. This produces a continuous $EDP-IM$ relationship, termed as IDA curve or dynamic pushover.

Some assumptions form the basis of this procedure:

- The sufficiency of the IM chosen to represent the seismic intensity. This leads to the assumption that the EDP random variable conditioned on the IM is independent of other ground motion features, i.e., the magnitude and source-to-site distance (e.g., Luco and Cornell, 2007).
- The scaling robustness of the IM. The assumption here is that the use of scaled records does not introduce bias into the distribution of the structural response obtained from the analyses (Iervolino and Cornell, 2005).

An example of an IDA is reported in Figure 1.2a.

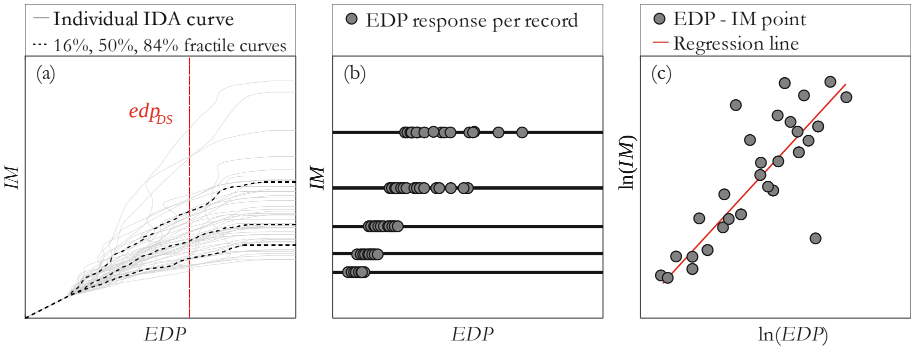

Figure 1.2 Dynamic analysis methods for the assessment of fragility curves: 50 IDA curves of an SDoF oscillator with 16, 50 and 84% fractile curves and EDP threshold (a); example of an MSA obtained for five IM levels (b); logarithmic-scale scatter plot of the EDP-IM responses obtained via CA and the corresponding least-squares regression line (c).

Ensuring parallelism with the non-linear static analysis reveals that each IDA curve has a distinct linear elastic region, which terminates at the occurrence of the first non-linearity. Subsequently, the curves develop in a non-monotonic manner, i.e., swinging back and forth, representing increases and decreases in the rate of damage accumulation. The final horizontal branch of each IDA curves denotes the onset of dynamic instability, which is a phenomenon that consists of unrestricted deformations growth for small IM increments. Consequently, IDA flat-lines correspond to a structure's side-sway collapse of the structure.

As shown in Figure 1.2a, a common way of summarizing IDA results for an entire set of records is to calculate and plot the 16, 50, and 84% fractile IDA curves of the EDP given IM, or vice-versa (Vamvatsikos and Cornell, 2004). This corresponds to the mean plus/minus one standard deviation of a Gaussian distribution.

The analytical derivation of the fragility curves typically involves fitting a parametric-probability model to the results of an IDA. The model generally chosen is lognormal, although other types can also be used (i.e., the gamma distribution). Two alternative approaches can be employed to assess fragility from the IDA results: the *IM-based* and the *EDP-based*. In both cases, an EDP threshold, edp_{DS}, can be defined, so that its exceedance will be tantamount to failure (see Eq. (1.5)). The IM-based method entails finding the intersections of the IDA curves, im_{DS}, with the vertical line passing through the threshold edp_{DS} value (Figure 1.2a). These im_{DS} values can be regarded as realizations of a RV, IM_{DS}, which is the seismic intensity to which the ground motion must be scaled for the structure to achieve the DS. The fragility function can then be considered as the probability of IM_{DS} being equal or lower than the level of seismic intensity that may occur at the site, i.e., $P[DS \mid IM = im] = P[IM_{DS} \leq im]$. Assuming that IM_{DS} follows a lognormal distribution, the fragility function can be estimated according to Eq. (1.6):

$$\begin{cases} P[DS \mid IM = im] = P[IM_{DS} \leq im] = \Phi\left[\left(\ln(im) - \eta\right)/\beta\right] \\ \eta = \dfrac{1}{n} \cdot \sum_{i=1}^{n} \ln\left(im_{DS,i}\right) \\ \beta = \sqrt{\dfrac{1}{n-1} \cdot \sum_{i=1}^{n} \left[\ln\left(im_{DS,i}\right) - \eta\right]^2} \end{cases} \tag{1.6}$$

where η and β are the parameter estimates (median and logarithmic standard deviation) of the assumed lognormal distribution of IM_{DS}, $im_{DS,i}$ is the realization of the RV coming from to the *i*-th record; and $\Phi(\cdot)$ is the standard Gaussian (cumulative) function.

Of course, it is not necessary to adopt a parametric model for IM-based fragility; in fact, a non-parametric representation can be obtained directly from the sample of IM_{DS} values, according to Eq. (1.7):

$$P[f \mid IM = im] = n^{-1} \sum_{i=1}^{n} I_{\left(im_{f,i} \leq im\right)} \tag{1.7}$$

where $I_{\left(im_{f,i} \leq im\right)}$ is an indicator function that returns 1 if $im_{f,i} \leq im$ or 0 if $im_{f,i} > im$.

Structural fragility can also be calculated using the EDP-based approach which is suitable for both the IDA and the MSA. The next paragraph describes employing this approach to assess structural fragilities.

1.3.2.2. Multiple-stripe analysis

Multiple Stripe Analysis is a NLDA methodology suitable for performance-based assessments considering a wide range of ground motion intensities and multiple performance objectives, ranging from the onset of damage through to global collapse (Jalayer and Cornell, 2008).

Similar to IDA, MSA calculates the EDP-response of a structure at various, increasing levels of the seismic intensity. The main difference between the two procedures is that MSA provides the opportunity to use different suites of records for each IM level. Consequently, MSA can only produce the same results as IDA only if the same set of records is employed at different intensity levels.

The record selection for MSA is carried out by selecting suites of records that reflect the site-specific seismic hazard at each IM level in order to render the seismic structural demand hazard consistent (Lin et al., 2013a, 2013b; Jayaram et al., 2011). This ensures that the spectral shapes of the selected records are compatible with the expected spectral shapes for a given intensity measure. An example of MSA's results is contained in Figure 1.2(b), in which the EDP responses have been obtained for five IM levels.

Structural fragility can be computed in MSA by adopting the EDP-based approach, which can be used when the EDP responses are obtained at discrete (fixed) IM levels. When these EDP responses are plotted against the corresponding IM values, they are disposed in horizontal stripes (e.g., Figure 1.2b), one for each of the levels of shaking intensity under consideration.

Counting the fraction of records in each stripe that cause the limit state threshold, edp_{DS}, to be exceeded enables the fragility parameters η and β to be obtained via the maximum-likelihood method described in Baker (2015) and reported in Eq.(1.8):

$$\begin{aligned}\{\eta,\beta\} = \underset{\eta,\beta}{argmax}\Bigg[\sum_{j=1}^{u}\Bigg(&\ln\binom{n}{q_j} + q_j\cdot\ln\left\{\Phi\left[\frac{\ln(im_j)-\eta}{\beta}\right]\right\} + \\ &+(n-q_j)\cdot\ln\left\{1-\Phi\left[\frac{\ln(im_j)-\eta}{\beta}\right]\right\}\Bigg)\Bigg]\end{aligned} \tag{1.8}$$

where u is the number of IM levels considered (i.e., the number of stripes, with each stripe containing responses from n records), and q_j is the number of failures observed at the stripe corresponding to $IM = im_j$ (Figure 1.2b). In this formulation, cases of non-convergent analysis (or collapse cases), say c_j in number, are also counted in q_j. This means that they are accounted for, despite the potential absence of a meaningful EDP value. It should be noted that, in cases where the observed numbers of failures q_j remain excessively low when the stripes overall are considered, the maximum-likelihood estimates implied in Eq. (1.8) can experience numerical problems. A viable alternative for considering fragility, consistent with the EDP-based approach, is the three-parameter-per-intensity model adopted by Shome and Cornell (2000).

1.3.2.3. Cloud analysis

Cloud analysis gets its name from its use of a set of unscaled records chosen to cover a vast range of intensity values. In this way, typically only a single record corresponds to each IM level resulting in a "cloud" of points in the $EDP-IM$ plane. An example is the scatter plot in Figure 1.2(c).

To estimate the statistical properties of the cloud data, a conventional linear regression, where homoscedastic Gaussian residuals are assumed, is applied to the data in the logarithmic scale. This equates to fitting a power-law curve to the cloud data in the arithmetic scale.

Consequently, the cloud method enables the obtention of a probabilistic relationship between an EDP and IM that predicts the conditional median of EDP for a given level of IM, denoted as $\eta_{EDP|IM}$:

$$\ln \eta_{EDP|IM}\left(IM\right) = \ln a + b \cdot \ln\left(IM\right) \tag{1.9}$$

where $\ln a$ and b are constant coefficients that are estimated from linear regression. The conditional logarithmic standard deviation of EDP given IM, $\beta_{EDP|IM}$ can be estimated as:

$$\beta_{EDP|IM} = \sqrt{\sum_{i=1}^{N}\left(\ln EDP_i - \ln\left(a \cdot IM_i^b\right)\right)^2 \Big/ \left(N-2\right)} \tag{1.10}$$

where EDP_i and IM_i represent the corresponding cloud data for the i-th record in the set and N is the number of records.

Generally, in relation to ultimate limit states, some of the records selected may induce structural collapse, resulting in very large EDP values. In these cases, the displacement demand values obtained from NLDAs are unreliable but known to exceed a certain limiting value. Including these records and their corresponding $EDPs$ in simple CA would thus be of questionable validity. Consequently, to correctly treat the results of the nonlinear dynamic analyses, a different procedure can be undertaken when estimating the probability of failure. This involves explicitly considering the collapse cases, partitioning the cloud data into two parts: NoC, which refers to the records for the structure does not collapse and; C, corresponding to the records inducing the collapse (Jalayer and Cornell, 2008). In this case, the structural fragility for a prescribed limit state, i.e., DS, can be set out using the Total Probability Theorem:

$$\begin{aligned} P\left[EDP > edp_{DS} \middle| IM = im\right] = {} & P\left[EDP > edp_{DS} \middle| IM = im, NoC\right] \cdot \left(1 - P\left[C \mid IM = im\right]\right) + \\ & + P\left[EDP > edp_{DS} \middle| IM = im, C\right] \cdot P\left[C \mid IM = im\right] \end{aligned} \tag{1.11}$$

where $P\left[EDP > edp_{DS} \middle| IM = im, NoC\right]$ is the conditional probability that the EDP is greater than the threshold edp_{DS} given that the collapse has not taken place. This probability can be described using a lognormal distribution (Jalayer and Cornell, 2008; Jalayer et al., 2017) as reported in Eq. (1.12):

$$P\left[EDP > edp_{DS} \middle| IM = im, NoC\right] = \Phi\left(\frac{\ln \eta_{EDP|IM,NoC}}{\beta_{EDP|IM,NoC}}\right) = \Phi\left(\frac{\ln\left(a \cdot IM_a^{\ b}\right)}{\beta_{EDP|IM,NoC}}\right) \tag{1.12}$$

where $\eta_{EDP|IM,NoC}$ and $\beta_{EDP|IM,NoC}$ are the conditional median and standard deviation of the logarithm of the EDP, evaluated based on the portion of NoC data.

$P\left[EDP > edp_{DS} \middle| IM = im, C\right]$ is the conditional probability that the EDP is greater than the threshold edp_{DS} given that the collapse has taken place. This term is therefore equal to unity. Meanwhile, $P\left[C \mid IM = im\right]$ is the probability of collapse and can be evaluated using logistic regression (a.k.a., logit) as a function of IM as reported in the following, where α_0 and α_1 are the parameters of the logistic regression.

$$P\left[C \mid IM\right] = \frac{1}{1 + e^{-(\alpha_0 + \alpha_1 \cdot ln\, IM)}}. \tag{1.13}$$

1.3.3. Methodologies for assessing state-dependent seismic fragility

1.3.3.1. Back-to-back Incremental Dynamic Analysis (back-to-back IDA)

As already discussed, one way of estimating a state-dependent version of a fragility function analytically is to use an IDA variant known by some authors as back-to-back IDA (Luco et al., 2004; Ryu et al., 2011; Goda, 2012; Ruiz-García, 2012; Raghunandan et al., 2015; Goda, 2015*)*. This extension of IDA is intended to produce a probabilistic description of the seismic response for structures already damaged by an initial seismic event, meaning that, before repairs are possible, they are susceptible to the effects of subsequent events, including mainshock-aftershock sequences.

In back-to-back IDA, the structural model is first subjected to a set of records hitting the structure in its intact (or initial) state, each scaled in amplitude to the lowest im value that results in $EDP = edp_{DS_A}$. At the end of each run, a different realization of the structure is produced, which can be viewed as having made the transition to DS_A. Then, each damaged incarnation of the structure is subjected to a second set of accelerograms that represents a subsequent event of the same cluster. Similar to the traditional IDA, the second set of records is scaled to progressively increasing im levels until $EDP = edp_{DS_B|DS_A}$ is verified for the damaged structure, at an intensity of the shock which can be noted as $im_{DS_B,i}$ for the i-th succession of base accelerations. As the results for the traditional fragility case obtained with an IDA, these intensity values can be used in the manner shown in Eq. (1.6) to estimate the parameters of a lognormal model of the state-dependent fragility.

Figure 1.3 contains an example of back-to-back IDA curves wherein, at an intensity of zero, the curves start from a residual EDP value that the damaged structure has inherited from the initial event. Therefore, like a traditional IDA, the end result of the back-to-back version is a set of continuous $EDP - IM$ curves. The difference is that these curves no longer describe the seismic behavior of the original structure, but that of the structure that has been subjected to a specific damaged state.

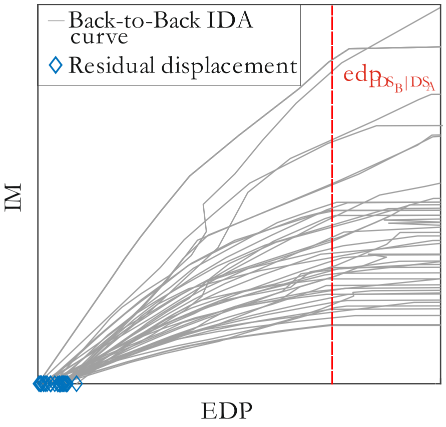

Figure 1.3 Example of back-to-back IDA curves for the assessment of state-dependent fragilities.

1.3.3.2. Pushover-Based Fragility

The classical rigorous methods for assessing state-dependent fragility functions usually require significant computational effort, and certainly more than that needed to investigate fragility curves for intact structures. Consequently, it was crucial to develop simplified, less time-consuming approaches, which are often based on the non-linear static, or pushover, analysis. An example of these methods is the static approach introduced by Luco et al., (2004), which enables the quantification of the residual capacity of mainshock-damaged structures. Unlike the dynamic method based on back-to-back IDA; the static methodology is based on the application of the SPO2IDA tool to the pushover curve of the damaged structure. SPO2IDA was first introduced by Vamvatsikos and Cornell, (2006) and represents a simple and effective link between IDA curves and Nonlinear Static Analysis. This spreadsheet tool comprises a set of analytical equations for predicting the median value and variability of the maximum seismic response of SDoF systems with various quadrilinear backbone curves. These equations use the parameters defining the pushover curve and the natural vibration period to estimate the 16, 50, and 84% fractile IDA curves. Although the method was developed for intact structures, attempts have been made to extend it to the case of damaged structures, as in the work by Luco et al., (2004), or Bazzurro et al., (2004). In the latter study, the SPO2IDA algorithm was used to evaluate the residual capacity of a damaged structure at a certain damage state The authors demonstrated that the calculation of the median value of the residual capacity of the structure in each damage state and the capacity of the intact structure can be exploited to identify a tagging criterion of the damage state reached by the structure following the main seismic event.

References

Baker, J.W. (2015), Efficient analytical fragility function fitting using dynamic structural analysis, *Earthq. Spectra*, 31(1).

Bazzurro, P., C.A. Cornell, C. Menun, and M. Motahari (2004), Guidelines for seismic assessment of damaged buildings, *Proc. 13th World Conf. Earthq. Eng.*, (1708).

Chioccarelli, E., P. Cito, F. Visini, and I. Iervolino (2021), Sequence-based hazard analysis for Italy considering a grid seismic source model, *Ann. Geophys.*, In press.

Cornell, C.A. (1968), Engineering seismic risk analysis, *Bull. Seismol. Soc. Am.*, 58, 1583–1606.

Cornell, C.A., and H. Krawinkler (2000), Progress and Challenges in Seismic Performance Assessment., *PEER Cent. News*, 3, 1–3.

Goda, K. (2012), Nonlinear response potential of Mainshock-Aftershock sequences from Japanese earthquakes, *Bull. Seismol. Soc. Am.*, 102(5), 2139–2156.

—— (2015), Record selection for aftershock incremental dynamic analysis, *Earthq. Eng. Struct. Dyn.*, 44, 1157–1162.

Gutenberg, B., and C.F. Richter (1944), Frequency of earthquakes in California, *Bull. Seismol. Soc. Am.*, 64(5), 185–188.

Iervolino, I., E. Chioccarelli, and M. Giorgio (2018), Aftershocks' effect on structural design actions in Italy, *Bull. Seismol. Soc. Am.*, 108(4), 2209–2220.

Iervolino, I., and C.A. Cornell (2005), Record selection for nonlinear seismic analysis of structures, *Earthq. Spectra*, 21(3), 685–713.

Iervolino, I., M. Giorgio, and E. Chioccarelli (2016), Markovian modeling of seismic damage accumulation, *Earthq. Eng. Struct. Dyn.*, 45(3), 441–461.

Iervolino, I., M. Giorgio, and B. Polidoro (2014), Sequence-based probabilistic seismic hazard analysis, *Bull. Seismol. Soc. Am.*, 104(2), 1006–1012.

Jalayer, F., and C.A. Cornell (2008), Alternative non-linear demand estimation methods for probability-based seismic assessments, *Earthq. Eng. Struct. Dyn.*, 13(6), 1834–1849.

Jalayer, F., R. De Risi, and G. Manfredi (2015), Bayesian Cloud Analysis: Efficient structural fragility assessment using linear regression, *Bull. Earthq. Eng.*, 13(4), 1183–1203.

Jalayer, F., H. Ebrahimian, A. Miano, G. Manfredi, and H. Sezen (2017), Analytical fragility assessment using unscaled ground motion records, *Earthq. Eng. Struct. Dyn.*

Jayaram, N., T. Lin, and J.W. Baker (2011), A Computationally efficient ground-motion selection algorithm for matching a target response spectrum mean and variance, *Earthq. Spectra*, 27(3), 797–815.

Kramer, S.L. (1996), *Geotechnical Earthquake Engineering*, Prentice-Hall, New Jersey.

Krawinkler, H. (2005), Van Nuys Hotel Building Testbed Report: Exercising Seismic Performance Assessment, *PEER Rep. 2005/11 Pacific Earthq. Eng. Res. Center. Dep. Civ. Environ. Eng. Stanford Univ.*

Krawinkler, H., and E. Miranda (2004), Performance-based earthquake engineering, Earthquake Engineering: From Engineering Seismology to Performance-Based Engineering. Chapter 9, pp. 9-1 to 9-59.

Lin, T., S.C. Harmsen, J.W. Baker, and N. Luco (2013a), Conditional spectrum computation incorporating multiple causal earthquakes and ground-motion prediction models, *Bull. Seismol. Soc. Am.*, 103(2 A), 1103–1116.

Lin, T., C.B. Haselton, and J.W. Baker (2013b), Conditional spectrum-based ground motion selection. Part I: Hazard consistency for risk-based assessments, *Earthq. Eng. Struct. Dyn.*, 42(12), 1847–1865.

Luco, N., P. Bazzurro, and C.A. Cornell (2004), "Dynamic versus static computation of the residual capacity of a mainshock-damaged building to withstand an aftershock," in: *13th World Conference on Earthquake Engineering, Vancouver, B.C., Canada August 1-6*.

Luco, N., and C.A. Cornell (2007), Structure-specific scalar intensity measures for near-source and ordinary earthquake ground motions, *Earthq. Spectra*, 23(2), 357–392.

Raghunandan, M., A.B. Liel, and N. Luco (2015), Aftershock collapse vulnerability assessment of reinforced concrete frame structures, *Earthq. Eng. Struct. Dyn.*, 44(3), 419–439.

Ruiz-García, J. (2012), Mainshock-aftershock ground motion features and their influence in building's seismic response, *J. Earthq. Eng.*, 16(5), 719–737.

Ryu, H., N. Luco, S.R. Uma, and A.B. Liel (2011), Developing fragilities for mainshock-damaged structures through incremental dynamic analysis, *Proc. Ninth Pacific Conf. Earthq. Eng.*, (225), 8.

Shome, N., and C.A. Cornell (2000), Structural seismic demand analysis: Consideration of collapse, *8th ACSE Spec. Conf. Probabilistic Mech. Struct. Reliab.*, (3), PMC2000--119.

—— (2006), "Probabilistic seismic demand analysis for a vector of parameters.," in: *8th US National Conference on Earthquake Engineering, San Francisco, CA*.

Vamvatsikos, D., and C.A. Cornell (2001), Incremental Dynamic Analysis, *Earthq. Eng. Struct. Dyn.*, 31(3), 491–514.

—— (2004), Applied incremental dynamic analysis, *Earthq. Spectra*, 20(2), 523–553.

Vamvatsikos, D., and C.A. Cornell (2006), Direct estimation of the seismic demand and capacity of oscillators with multi-linear static pushovers through IDA, *Earthq. Eng. Struct. Dyn.*, 35(9), 1097–1117.

Yeo, G.L., and C.A. Cornell (2005), "Stochastic characterization and decision bases under time-dependent aftershock risk in performance-based earthquake engineering, PEER Report 2005/13."

Yeo, G.L., and C.A. Cornell (2009), A probabilistic framework for quantification of aftershock ground-motion hazard in California: Methodology and parametric study, *Earthq. Eng. Struct. Dyn.*, 38(1), 45–60.

2

Sequence Based Hazard Maps for the United Kingdom

Abstract

This study was carried out in collaboration with the firm Ove Arup and Partners.
From this chapter is derived the following paper:

- *Orlacchio M., Cito P., Polidoro B., Villani M., Iervolino I. (2021), "Sequence based hazard maps for the United Kingdom" (Under review).*

The current practice of probabilistic seismic hazard analysis (PSHA) does not take into account that earthquakes actually occur in time-space clusters. The input for PSHA is based on de-clustered seismic catalogs, used to characterize only the mainshocks, that is, the largest magnitude events within each cluster. However, the so-called sequence-based PSHA (SPSHA; Iervolino et al., 2014), allows us including the effect of aftershocks in hazard analysis, that is, the events following the mainshock, still conveniently resourcing from de-clustered catalogs. In the United Kingdom (UK), the seismic source model developed for the national seismic hazard assessment has been recently updated by the British Geological Survey (BGS; British Geological Survey, 2020). In this study, the source model developed by the BGS (one directly derived from it, in fact) is used to implement SPSHA in the UK. The calibration of the model for the occurrence of aftershocks, that is, the modified Omori's law, is fitted on a few sequences and under some simplifying assumptions. The results, represented by hazard maps for selected spectral ordinates and exceedance return periods of interest for structural engineering, are compared to the PSHA counterparts to discuss the increase in the design seismic actions when the effects of aftershocks are considered. The maps show that, based on the modeling of aftershock sequences considered in the study, in the UK this increase can be up to 14%, at least for the spectral ordinates and exceedance return periods herein investigated. The discussed maps are provided as supplemental material to this paper.

Keywords: seismic hazard, seismic sequences, aftershocks, hazard increments.

2.1. Introduction

In the United Kingdom (UK), design seismic actions for structural design are based on probabilistic seismic hazard analysis (PSHA; McGuire, 2004). For a given ground motion intensity measure (IM), PSHA allows to computing the rate of seismic events causing exceedance of a selected threshold at the site of interest. In the classical PSHA, the rate of exceedance is time-invariant and defines the homogenous Poisson process (HPP) describing the occurrence of earthquakes causing exceedance of the ground motion threshold over time (Cornell, 1968).

Although earthquakes typically occur in spatio-temporal clusters, classical PSHA complies with the HPP assumption of earthquakes occurrence considering only the largest magnitude event within each cluster, conventionally recognized as the mainshock, while (the effects of) the other events in the cluster are neglected. To achieve this, seismicity parameters for the definition of the input models used for PSHA are derived from a catalog in which foreshocks and aftershocks, that is, the earthquakes preceding and following the mainshock, respectively, are preliminarily removed using de-clustering techniques (e.g., Gardner and Knopoff, 1974).

For short-term risk management purposes, Yeo and Cornell (2009) develop aftershock PSHA (APSHA), which provides the probability that aftershocks, in a given time interval, cause exceedance of a ground motion IM value at the site of interest. In the framework of APSHA, occurrence of aftershocks in time is characterized by means of a nonhomogeneous Poisson process (NHPP), conditional to the occurrence of a mainshock of given magnitude and location, and whose rate is modeled according to the modified Omori law (Utsu, 1961). (Although, in principle, other models describing aftershock occurrence can be embedded in SPHSA in lieu of the modified Omori law.)

Iervolino et al. (2014) show that it is possible to include the effects of aftershocks in long-term hazard assessment avoiding the violation of the HPP hypothesis and possible catalog incompleteness with respect to aftershocks, using the so-called sequence-based PSHA (i.e., SPSHA). Acknowledging that mainshock-aftershocks sequences occur at the same rate as the mainshocks, SPSHA combines PSHA and APSHA resulting in a relatively easy-to-implement hazard integral, which allows computing the rate of mainshock-aftershock sequences causing exceedance of a given IM threshold at the site. Because SPSHA models the occurrence of aftershocks by means of the modified Omori law, it neglects foreshocks that, although can also possibly contribute to hazard, are generally considered of minor relevance to structural engineering with respect to aftershocks (Yeo and Cornell, 2009).

Before proceeding any further, it is to note that there are other approaches that allow accounting for earthquake clusters in seismic hazard analysis (e.g., Zhang et al., 2018, 2021; Papadopoulos et al., 2021; Marzocchi and Taroni, 2014). One of these approaches, which is often assumed as a benchmark by seismologists, is the one referred to as epidemic-type aftershock sequences (ETAS; Ogata, 1988). However, Wang et al. (2021), considering a point source model, recently discussed that the differences in hazard results between SPSHA and ETAS-based seismic hazard analysis are of limited relevance, if any, for earthquake engineering purposes.

Recently, the British Geological Survey (BGS, British Geological Survey, 2020) has developed new PSHA-based hazard maps for the UK. The study presented herein, similar to what was done in Iervolino et al. (2018) and Chioccarelli et al. (2021) for Italy, aims to investigate the implications, on the definition of design seismic actions in the UK, stemming from including seismic sequences in hazard analysis. To do so, the SPSHA procedure is developed at the national scale, using a simplified, yet validated, version of the BGS source model where the validation consists of comparing the PSHA results against the official BGS counterpart. The parameters of the modified Omori law, required by SPSHA, are calibrated based on a few sequences (because of a general paucity of aftershock data in the UK) from a catalog developed for the UK (Villani et al., 2020).

The SPSHA results for the entire country are presented by hazard maps in terms of (5% damped) spectral (pseudo) accelerations at three vibration periods, as the IMs, and for four exceedance return periods $\left(T_r\right)$ of structural design interest. Subsequently, SPSHA results are compared to those from PSHA, implemented using the simplified hazard model, to discuss the effects of aftershocks on design seismic actions in the UK.

The paper is structured such that the essentials of SPSHA are recalled, first. Then, the source model is introduced followed by the calibration of the modified Omori law for the UK. After presenting the hazard maps, the hazard increases due to aftershocks countrywide are discussed by comparing SPSHA results to the PSHA counterpart. Moreover, considering three sites in the UK exposed to comparatively low, mid and high seismic hazard, the aftershock effects are explored with reference to a wide range of spectral periods and return periods, using uniform hazard spectra (UHS). A simple sensitivity analysis of the parameters of the modified Omori law precedes some final remarks that close the study.

2.2. Classical and Sequence-Based Probabilistic Seismic Hazard Analysis

Classical PSHA provides the average number of mainshocks per unit-time (often in one year) causing exceedance of a IM threshold $\left(im\right)$ at the site of interest; i.e., the exceedance rate, $\lambda_{im,E}$. This is time-invariant and defines the HPP regulating the occurrence of earthquakes causing exceedance of im over time. Classically, $\lambda_{im,E}$ is computed using Eq.(2.1); i.e., the hazard integral, which is herein written considering a single seismic source zone affecting the site (e.g., Kramer, 1996):

$$\lambda_{im,E} = \nu_E \cdot \int_{r_{E,min}}^{r_{E,max}} \int_{m_{E,min}}^{m_{E,max}} \mathrm{P}[IM_E > im \mid M_E = m, R_E = r, \underline{\theta}] \cdot f_{M_E,R_E}(m,r) \cdot dm \cdot dr. \quad (2.1)$$

The subscript, E, is added in order to distinguish the rate $\lambda_{im,E}$ from the rate evaluated using SPSHA, to follow. In the equation, ν_E is the rate of mainshocks with magnitude equal to or larger than the minimum ($m_{E,min}$) deemed possible for the source and it is calibrated based on a de-clustered catalog. The $f_{M_E,R_E}(m,r)$ term is the joint probability density function (PDF) of the mainshock magnitude (M_E) and source-to-site distance (R_E). Assuming that M_E and R_E are stochastically independent random variables, it is $f_{M_E,R_E}(m,r) = f_{M_E}(m) \cdot f_{R_E}(r)$, where $f_{M_E}(m)$ and $f_{R_E}(r)$ are the marginal distributions of magnitude and distance of mainshocks, respectively. The distribution of magnitude is defined between $m_{E,min}$ and the maximum magnitude considered for the source, $m_{E,max}$, and is generally described by a truncated exponential distribution derived by the Gutenberg-Richter (GR) relationship (Gutenberg and Richter, 1944). The distribution of the distance, which is defined between $r_{E,min}$ and $r_{E,max}$, generally only depends on the geometry of the source and the position of the site with respect to the source itself. The term $\mathrm{P}\left[IM_E > im \mid M_E = m, R_E = r, \underline{\theta}\right]$, provided by a ground motion prediction equation (GMPE), represents the conditional probability that im is exceeded due to a mainshock with magnitude equal to m and source-to-site distance equal to r. This probability also depends on $\underline{\theta}$, which allows us to account for additional parameters such as local soil site conditions, rupture mechanism of the source and/or others. Considering multiple sources only entails the summation of $\lambda_{im,E}$ referring to each source.

SPSHA allows us to account for the effect of aftershocks (i.e., neglecting foreshocks) in the hazard assessment, using the same input as in the case of PSHA, that is, the rate of mainshocks from a de-clustered catalog, and modelling the occurrence of aftershocks using a NHPP, conditional to the mainshock magnitude and location. In these hypotheses, the main result of SPSHA is the average number of seismic sequences that causes at least one exceedance of im at the site in the unit time. This rate, herein referred to as λ_{im}, defines the HPP process regulating the occurrence of mainshocks, and following aftershocks, that cause exceedance of im over time, and it is computed via Eq. (2.2):

$$\lambda_{im} = \nu_E \cdot \left\{ 1 - \int_{r_{E,min}}^{r_{E,max}} \int_{m_{E,min}}^{m_{E,max}} \mathrm{P}\left[IM_E \le im \mid M_E = m, \mathrm{R}_E = r, \underline{\theta} \right] \times e^{-E\left[N_{A|m}(0,\Delta T_A)\right] \cdot \int_{r_{A,min}}^{r_{A,max}} \int_{m_{A,min}}^{m} \mathrm{P}\left[IM_A > im \mid M_A = m_A, \mathrm{R}_A = r_A, \underline{\theta}\right] \cdot f_{M_A,\mathrm{R}_A|M_E,\mathrm{R}_E}(m_A, r_A | m, r) \cdot dm_A \cdot dr_A} \cdot f_{M_E,\mathrm{R}_E}(m,r) \cdot dm \cdot dr \right\} \tag{2.2}$$

In the equation, the (A) subscript denotes terms pertaining to aftershocks. $\mathrm{P}\left[IM_E \le im \mid M_E = m, \mathrm{R}_E = r, \underline{\theta}\right]$ is equal to $1 - \mathrm{P}\left[IM_E > im \mid M_E = m, \mathrm{R}_E = r, \underline{\theta}\right]$, whereas the exponential term represents the probability that none of the aftershocks, triggered by the mainshock with magnitude $M_E = m$ and distance $R_E = r$ (strictly speaking, it should be location rather than distance), causes exceedance of im between $t = 0$ (i.e., the occurrence time of the mainshock) and the duration of the sequence, ΔT_A. $P\left[IM_A > im_A \mid M_A = m_A, \mathrm{R}_A = r_A, \underline{\theta}\right]$, which is provided by the GMPE, is the probability that im is exceeded given an aftershock of magnitude $M_A = m_A$ and source to site distance $R_A = r_A$. The term $f_{M_A,\mathrm{R}_A|M_E,\mathrm{R}_E}$ is the joint PDF of magnitude and distance of aftershocks, which is conditional on the features of the mainshock (i.e., magnitude and location) occurring on the source. Assuming that M_A and R_A are conditionally independent random variables, it is $f_{M_A,\mathrm{R}_A|M_E,\mathrm{R}_E} = f_{M_A|M_E} \cdot f_{\mathrm{R}_A|M_E,\mathrm{R}_E}$, where $f_{M_A|M_E}$ is the conditional distribution of aftershocks magnitude (i.e., following the GR) and $f_{\mathrm{R}_A|M_E,\mathrm{R}_E}$ is the conditional distribution of the distance of the site to aftershocks. The magnitude distribution of the aftershocks is bounded by a minimum magnitude $m_{A,min}$ and m (i.e., the mainshock magnitude). The location of aftershocks with respect to the site depends on the location and magnitude of the mainshock. The distribution of the aftershocks distance is bounded within $r_{A,min}$ and $r_{A,max}$, which are the minimum and maximum values possible for R_A, respectively. $E\left[N_{A|m}\left(0,\Delta T_A\right)\right]$ is the expected number of aftershocks, with magnitude between $m_{A,min}$ and m, generated by a mainshock with magnitude $M_E = m$, in ΔT_A, and it is computed according to Yeo and Cornell (2009):

$$E\left[N_{A|m}\left(0,\Delta T_A\right)\right] = \frac{10^{a+b\cdot\left(m-m_{A,min}\right)} - 10^{a}}{p-1} \cdot \left[c^{1-p} - \left(\Delta T_A + c\right)^{1-p}\right], \tag{2.3}$$

where c and p are the parameters of the modified Omori law, which in fact models the temporal decay of the aftershocks rate, whereas a and b define the GR relationship for aftershocks.

Computing Eq. (2.1) and Eq. (2.2) for different im values in a range of interest provides the hazard curve for PSHA and SPSHA, respectively. Hazard curves for different spectral ordinates, in turn, allow retrieving the UHS, i.e., the spectra whose ordinates (when considered individually) have the same exceedance return period, for the site of interest. Hereafter, the spectral ordinates of PSHA and SPHA-based UHS ordinates will be indicated as sa_{PSHA} and sa_{SPSHA}, respectively. Obviously, it is $\lambda_{im} \geq \lambda_{im,E}$ for any im value; thus $sa_{SPSHA} \geq sa_{PSHA}$.

2.3. Source Model and GMPE

2.3.1. BGS logic tree

Both PSHA and SPSHA presented in this work were implemented by using the source model recently updated by the BGS. The PSHA study of the BGS features a complex logic tree, consisting of several branches. In each branch, the source model is based on 22 seismic source zones, whose geometry and ID are shown in Figure 2.1 (together with five sites of interest that will be considered later). The source model is defined on the basis of the current understanding of seismicity in the UK, taking also into account the surrounding areas which are considered to have some impact on the seismic hazard of the country; i.e., the Viking Graben (VIKI), the Normandy (NORM) and the Belgium-Pas de Calais region (PASC). For each zone, the expected magnitude frequency distribution of the earthquakes follows a GR relationship, with minimum magnitude equal to 3.0. The uncertainties affecting the seismicity parameters of the zones are taken into account using of 100 branches of the logic tree, varying in terms of maximum magnitude, $b-$ value and annual rate of mainshocks with (moment) magnitude equal to or larger than 3.0, $\nu_E\left(M \geq 3.0\right)$. More specifically, according to the logic tree, four maximum magnitude (i.e., 6.5, 6.7, 6.9 and 7.1) and 25 couples of the $b-$ values and $\nu_E\left(M \geq 3.0\right)$ are identified for each source zone.

Considering the mean of the 25 $\nu_E\left(M \geq 3.0\right)$ values, which is also provided by the BGS for each source zone, one can observe that the lowest $\nu_E\left(M \geq 3.0\right)$ is 0.0037 events per year for the zone named BALA, whereas the largest rate 1.12 events per year, is for the MMCW zone. It is worth noting that seismicity for two zones; i.e., MMCW and MENA, is defined using a bi-partite GR magnitude distribution (British Geological Survey, 2020). The first GR distribution models the occurrence of mainshocks in the range of magnitude between 3.0 and 4.5, while the other applies between 4.5 and $m_{E,max}$. Both BALA and MMCW zones are located at the westward side of the UK; in the remaining part of the country, the rate of earthquakes with magnitude equal to or larger than 3.0 is within 0.1 and 0.47 events per year.

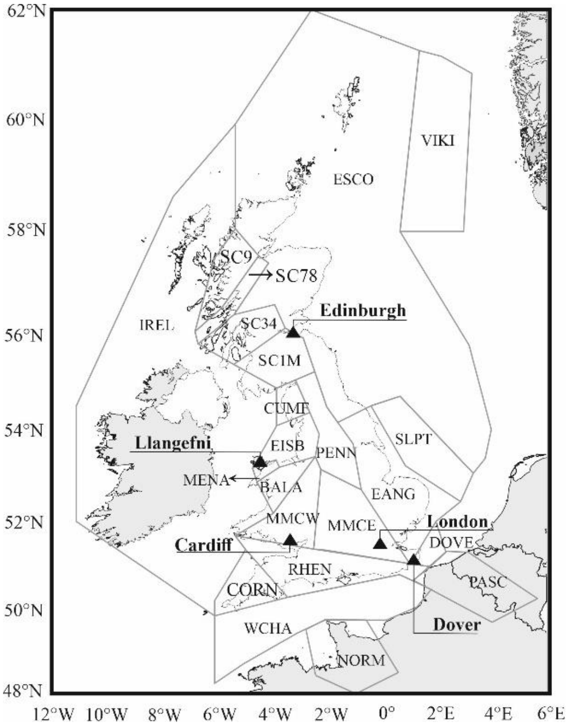

Figure 2.1 The seismic source model used in this study with zone names and location of five sites.

The logic tree implemented by the BGS also accounts for the uncertainty affecting the hypocentral depth considering four possible values; i.e., 5 km, 10 km, 15 km and 20 km. Strike-slip is the dominant rupture mechanism for all the seismic sources.

The BGS study follows the same multi-GMPE approach used in Tromans et al. (2019), which considers five GMPEs: Atkinson and Boore (2006, 2011), Rietbrock et al. (2013), Bindi et al. (2014), Boore et al. (2014) and Cauzzi et al. (2015). These populate the logic tree with different weights. Bindi et al. (2014) and Boore et al. (2014) are given the largest weight, 0.3; Cauzzi et al. (2015) is given 0.2, whereas 0.1 is assumed for Atkinson and Boore (2006, 2011) and Rietbrock et al. (2013). To account for both the effects of elastic amplification due to shear wave velocity structure and near-surface attenuation specific for the UK, the host-to-target adjustments (Cotton et al., 2006; Atik et al., 2014) are applied to each of the five GMPEs. The adjustment factors were developed considering rock site conditions and three values of the target spectral decay parameter: 0.016 s, 0.027 s, and 0.047 s.

2.3.2. Simplified source model

In this study, the BGS seismic hazard model was adopted for developing both PSHA and SPSHA, yet with some simplifications aimed at avoiding the implementation of the full logic tree. More specifically, for each seismic zone, the GR relationship was defined by considering the weighted mean values (over the 25 values in the BGS study) of $\nu_E\left(M \geq 3.0\right)$ and b. The maximum magnitude was set equal to 6.5 for all the sources, which corresponds to the value of the branch with the largest weight.

Among the two GMPEs with the highest weight in the BGS work, the one of Bindi et al. (2014) was selected and used to compute both $\mathrm{P}\left[IM_E \leq im \mid M_E = m, R_E = r, \underline{\theta}\right]$ and $\mathrm{P}\left[IM_A > im \mid M_A = m_A, R_A = r_A, \underline{\theta}\right]$ in Eq. (2.1) and Eq. (2.2). This GMPE adopts the Joyner-Boore distance or R_{JB} (Joyner and Boore, 1981) up to 300 km. In the analyses, assuming a uniform distribution for earthquakes epicenters (both mainshocks and aftershocks), the epicentral distance $\left(R_{EPI}\right)$ was converted to R_{JB} according to Eq. (2.4), which is given by (Montaldo et al., 2005).

$$R_{JB} = 3.5525 + 0.8845 \cdot R_{EPI}. \tag{2.4}$$

The selected GMPE has a magnitude range of applicability between 4.0 and 7.6; therefore, to avoid extrapolation, earthquakes with magnitude lower than 4.0 were not considered in the hazard assessment (also considering that earthquakes with magnitude lower than 4.0 are typically not of interest to earthquake engineering). Consequently, for each source, $\nu_E\left(M \geq 3.0\right)$, (i.e., that provided by the BGS) was reduced, according to the GR, to exclude earthquakes with magnitude less than 4.0, which is, therefore, the minimum magnitude considered herein for both PSHA and SPSHA (this is also in agreement with the PSHA analyses carried out by the BGS). Similarly, portions of sources at distances larger than 300 km were not considered in the analyses. The predominant strike-slip style was attributed via terms provided by Bindi et al. (2014) for that rupture mechanism. summarizes all the source characteristics finally considered.

Table 2.1 Mainshocks seismicity parameters of seismic zones considered (MENA and MMCW zones are reported twice because of their bi-partite GR).

Zone	$m_{E,min}$	$m_{E,max}$	b -value	$\nu_E\left(M \geq 4.0\right)$ [events per year]
CORN	4.0	6.5	1.03	5.60E-03
RHEN	4.0	6.5	1.00	5.00E-03
WCHA	4.0	6.5	0.99	1.33E-02
DOVE	4.0	6.5	1.00	6.00E-03
SLPT	4.0	6.5	0.97	1.82E-02
EANG	4.0	6.5	0.99	1.13E-02
MMCE	4.0	6.5	0.96	7.68E-03
PENN	4.0	6.5	0.94	2.64E-02
MMCW1	4.0	4.5	1.01	1.17E-02
MMCW2	4.5	6.5	1.02	9.71E-02
MENA1	4.0	4.5	1.01	6.84E-03
MENA2	4.5	6.5	1.00	3.16E-02
EISB	4.0	6.5	0.99	8.19E-03
CUMF	4.0	6.5	1.02	5.73E-03
BALA	4.0	6.5	1.00	3.70E-04
SC1M	4.0	6.5	1.01	1.95E-03
SC34	4.0	6.5	1.00	1.20E-02
SC78	4.0	6.5	0.99	1.84E-02
SC9	4.0	6.5	1.04	1.55E-02
ESCO	4.0	6.5	1.00	1.50E-02
IREL	4.0	6.5	1.01	2.93E-03
VIKI	4.0	6.5	1.01	4.59E-02
NORM	4.0	6.5	0.86	5.11E-02
PASC	4.0	6.5	1.00	1.90E-02

The PSHA and SPSHA discussed in the following were developed assuming the average shear-wave velocity of the upper 30 m equal to 800 m/s (i.e., rock site conditions) at all sites. Moreover, the GMPE was corrected to account for the host-to-target adjustment, considering the median value of spectral decay parameter equal to 0.027 s, which is the value corresponding to the branch with the largest weight in the logic tree defined by the BGS. The adjustment factors developed by the BGS for the GMPE of Bindi et al. (2014) and used in this study are equal to 1.24, 1.19 and 1.06 for peak ground acceleration $\left(PGA\right)$, $Sa\left(T = 0.2\text{s}\right)$ and $Sa\left(T = 1.0\text{s}\right)$, respectively; i.e., the IMs considered for the hazard maps discussed in the following. The adjustments do not depend on magnitude and source-to-site distance and apply to the mean of the GMPE; i.e., they correspond to a so-called linear effect. Therefore, herein the adjustment factors are applied directly modifying a-posteriori the ordinates of the unadjusted

UHS of interest as discussed in Iervolino (2016), which has been shown to be a rigorous procedure in case of GMPEs with linear effects.

2.3.3. Validation

The simplifications to the BGS source model do not affect the results concerning the aftershocks effect on the hazard assessment (to follow), as PSHA and SPSHA are performed using the same input data. However, the results of PSHA conducted via the simplified source model for the sites of Cardiff, Dover, Edinburgh and London (see Figure 2.1 for the location of the sites), are compared to those obtained within the BGS study (Mosca et al., 2022). Figure 2.2 shows the comparisons in terms of UHS and hazard curves for the four sites. Panels (a) and (b) describe the UHS computed by the BGS and those developed in this study, for the return periods of 475 years (yr) and 2475 yr, respectively. The second row of Figure 2.2 shows the hazard curves in terms of PGA (Figure 2.2c) and spectral (pseudo) accelerations (Sa) corresponding to the vibration period (T) equal to 0.2 s (Figure 2.2d) and 1.0 s (Figure 2.2e) evaluated for the four sites.

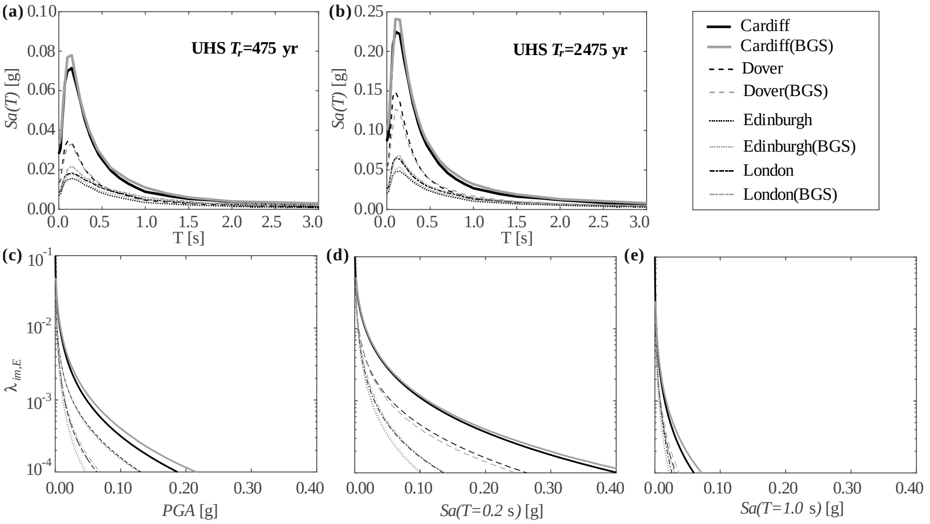

Figure 2.2 Comparison of the results obtained in the study by means of PSHA to the BGS counterparts in terms of UHS with $T_r = 475\,\text{yr}$ (a) and $T_r = 2475\,\text{yr}$ (b), and hazard curves for PGA (c), $Sa(T = 0.2\text{s})$ (d) and $Sa(T = 1.0\text{s})$ (e) for the sites of Cardiff, Dover, Edinburgh and London.

The figure shows that the results obtained using the simplified input model are in good agreement with those obtained considering the full logic tree, even if some differences can be found. To measure them, the absolute differences between the spectral ordinates obtained in this study and those from the BGS work were quantified for 17 spectral ordinates, in a range of vibration periods between 0 s and 3.0 s. For example, considering $T_r = 475\,\text{yr}$, which is a typical return period in structural design, those differences, on average, are equal to 0.0027 g, 2.23e-04 g, 0.0012 g and 0.0011 g for Cardiff, Dover, Edinburgh and London, respectively.

2.3.4. Aftershock occurrence model

The parameters $\{a, b, c, p\}$ in Eq. (2.3), required for SPSHA, are typically calibrated empirically via data from multiple aftershocks sequences for the region of interest; e.g., Reasenberg and Jones (1989) for California and Lolli and Gasperini (2003), for Italy. For the UK, there are no specific studies available. To overcome this issue, two earthquake catalogs were preliminarily investigated. One is that provided by the BGS, which includes 73 mainshock-aftershocks sequences occurring in the whole UK and the surrounding areas. The second one is that of Villani et al. (2020), containing 213 earthquakes attributed to 48 mainshock-aftershocks sequences occurring within 300 km from Anglesey, North Wales; see Villani et al. (2020) for a map of the events.

The $\{a, c, p\}$ parameters were estimated, for each sequence, using the maximum likelihood method (e.g., Ogata, 1983; Utsu and Ogata, 1995). However, convergence issues have arisen for the short sequences; i.e., those with less than five aftershocks, which are 71 and 44 in the BGS catalog and the Villani et al. (2020) catalog, respectively. Moreover, there is no sufficient information about the events occurring in the two remaining in the BGS catalogue, and therefore they were neglected. Thus, only the four sequences from the catalog of Villani et al. (2020) were considered for calibrating the parameters of the modified Omori law. For the selected sequences, Table 2.2 shows the ID according to the considered catalog, the event name, the date and time of the mainshock, latitude and longitude of the epicenter of the mainshock, the mainshock magnitude, the minimum magnitude of aftershocks and the number of aftershocks in each sequence N_{aft}.

For each sequence, the $\{a, c, p\}$ parameters were calibrated by setting the $b-$value equal to one (Helmstetter, 2003). The mean values, which are used for the SPSHA, are $a = -1.71$, $c = 0.002$ and $p = 0.68$. To qualitatively assess the goodness-of-fit of these parameters, Figure 2.3 represents the ratio of the cumulative number of aftershocks within each sequence, $N_A(t)$, as a function of the time t elapsed since the mainshock (expressed in days), to the term $10^{a+b(m-m_{A,min})}$; i.e., the aftershock productivity of each sequence.

Table 2.2 List of sequences detected in the earthquake catalog having a number of aftershocks greater than five.

Seq. ID	Event name	Date	Time	Lat	Long	$M_E = m$	$m_{A,min}$	N_{aft}
155	Caernarvon	19-06-1903	10:40	53.03°	-4.28°	4.60	2	14
200	Caernarvon	12-12-1940	21:20	53.03°	-4.18°	4.40	2	7
313	Lleyn Peninsula	19-07-1984	6:56	52.96°	-4.28°	5.00	2	22
515	Manchester	21-10-2002	11:42	53.48°	-2.20°	2.90	2	51

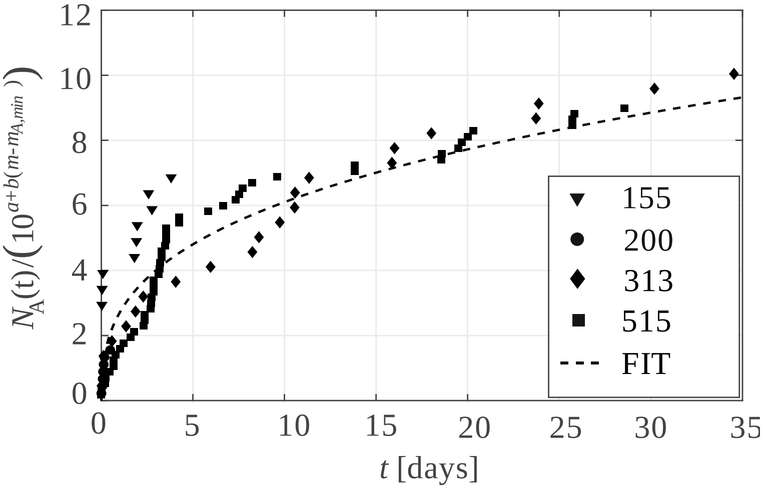

Figure 2.3 Representation of the four sequences detected for the UK. The smooth curve represents the modified Omori formula obtained using the mean values of the parameters $\{a,c,p\}$.

It is worth noting that, generally, the uncertainty of $\{a,c,p\}$ may also be quantified (e.g., Ogata, 1978; Kutoyantis, 1982); but the discussed paucity of data would require to adopt other approaches, such as multi-model inference methods (e.g., Zhang and Shields, 2018), yet this is considered of secondary importance and it is left out of the scopes of the study. Moreover, the small dataset of sequences has led to a relatively simple calibration. In other words, the considered aftershock sequences are those assumed to be complete above the minimum aftershock magnitude assumed in SPSHA, which is $m_{A,min} = 4.0$; i.e., the minimum magnitude of the considered GMPE.

To complete the characterization of the aftershocks in the framework of SPSHA, a model for aftershocks location is needed, which in turn serves to compute $f_{R_A|M_E,R_E}$ in Eq. (2.2). Similar to previous studies (Iervolino et al., 2014, 2018; Chioccarelli et al., 2021), it was assumed that aftershocks may occur, with the same probability, within a circular area, centered on the mainshock location, whose size, S_A, expressed in squared kilometers, depends on the magnitude of the mainshock according to the model of Utsu (1970):

$$S_A = 10^{m-4.1}. \tag{2.5}$$

Alternative models for the shape of the area enclosing aftershocks can be found in literature (e.g., Kanamori and Anderson, 1975) and could be equivalently used in SPSHA. An interesting approach is that of Zhuang et al. (2002), who model the probability distribution of aftershocks location with a bell-shape decay from the mainshock location, yet they discuss that such a model relies on the same understanding at the basis of that given by Utsu (1970).

Thus, it is expected that selecting an alternative model for the shape of the area enclosing aftershocks does not significantly affect the results. Finally, for the hazard analyses the duration of the aftershock sequence, ΔT_A, was assumed arbitrarily equal to 90 days from the occurrence of the mainshock, although, in principle, this duration could be mainshock-magnitude-dependent. This assumption is consistent with the other studies applying SPSHA (Iervolino et al., 2018; Chioccarelli et al., 2021); nevertheless, it has been observed that the Omori law's parameters calibrated for the UK renders the results of hazard analysis slightly more dependent on ΔT_A than the previous studies. (See Sensitivity analysis section).

2.4. Analysis and Results

The analyses were carried out through the REASSESS software (Chioccarelli et al., 2019), in which the simplified source model for the UK was implemented (and made available for eventual further studies). PSHA and SPSHA hazard curves, in terms of PGA, $Sa(T=0.2\text{s})$ and $Sa(T=1.0\text{s})$, were computed for more than four thousand sites across all the country, which are the nodes of a regular grid spacing 0.250° and 0.125° longitude and latitude, respectively.

2.4.1. Hazard maps

PSHA and SPSHA results for any site in the UK are represented in Figure 2.4 for PGA, and in Figure 2.5 and Figure 2.6 for $Sa(T=0.2\text{s})$ and $Sa(T=1.0\text{s})$, respectively. In each figure, the top panels, from (a) to (d), show the ground motion intensity measure that the figure refers with exceedance return period from 95yrs to 2475yrs according to PSHA; those at the bottom, from (e) to (h), represent the results when mainshock-aftershock sequences are taken into account in SPSHA.

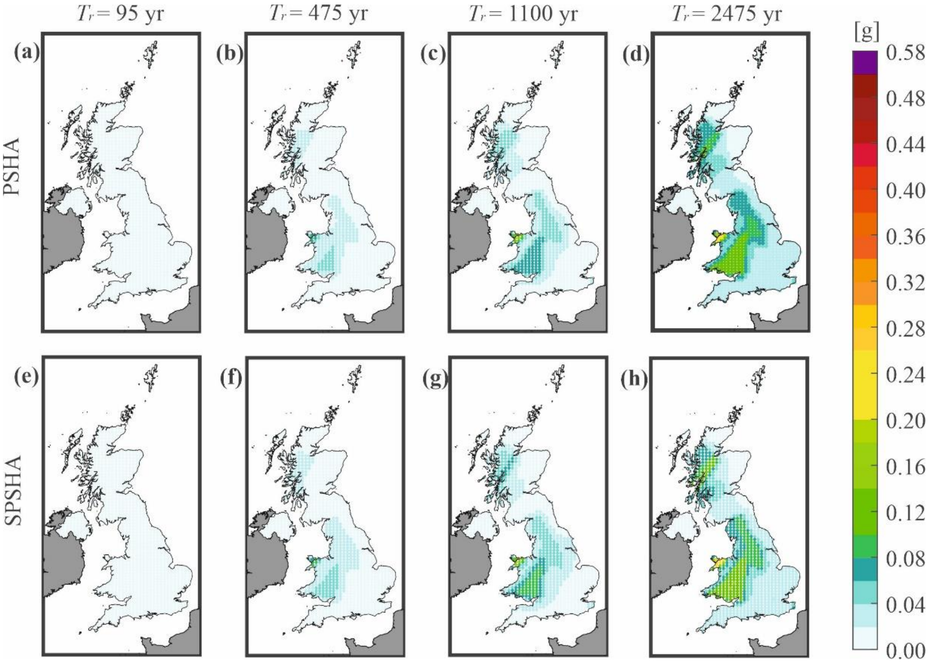

Figure 2.4 Maps of PGA on rock with $T_r = 95\,\text{yr}$, $T_r = 475\,\text{yr}$, $T_r = 1100\,\text{yr}$ and $T_r = 2475\,\text{yr}$, from left to right, obtained using PSHA (panels a-d) and SPSHA (panels e-h).

Looking at the figures, it can be observed that, for each spectral and exceedance return period, sites with the highest hazard are located in the western UK; i.e., in the area enclosing the seismic zones EISB, MENA, BALA and MMCW. This area also includes the sites exposed to the largest sequence-based seismic hazard, according to the bottom panels. This is somehow expected, as the more frequent and stronger (in terms of magnitude) the mainshocks the larger the number of expected aftershocks. The largest PGA which is exceeded once every 2475 yr (on average) due to mainshocks-aftershocks sequences is equal to 0.272 g; for the same return period, the largest values for $Sa(T = 0.2\text{s})$ and $Sa(T = 1.0\text{s})$ across the country are 0.564 g and 0.061 g, respectively. The sites with the lowest hazard are enclosed by the ESCO zone in the north-eastern area of the UK. For example, in the proximity of Aberdeen (2.1° W, 57.16° N), a PGA value of 0.012 g is exceeded, on average, once every 2475 yr, even considering the aftershock effects; for the same return period, the lowest ground motion intensity at the same site is equal to 0.022 g for $Sa(T = 0.2\,\text{s})$ and 0.008 g for $Sa(T = 1.0\,\text{s})$. The south-east area of the UK is exposed to relatively moderate seismic hazard. For example, at the site of Norwich (1.30° E, 52.63° N), the largest PGA, $Sa(T = 0.2\text{s})$ and

$Sa(T=1.0\text{s})$ for $T_r = 2475\,\text{yr}$ using SPSHA, are equal to 0.031 g, 0.0606 g and 0.013 g, respectively.

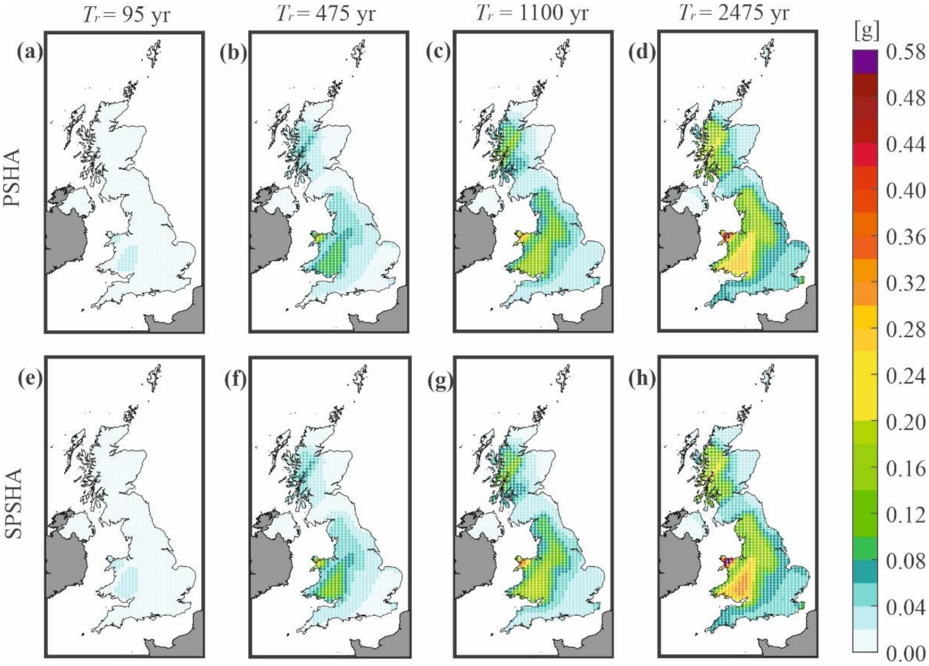

Figure 2.5 Maps of $Sa(T=0.2\text{s})$ on rock with $T_r = 95\,\text{yr}$, $T_r = 475\,\text{yr}$, $T_r = 1100\,\text{yr}$ and $T_r = 2475\,\text{yr}$, from left to right, obtained using PSHA (panels a-d) and SPSHA (panels e-h).

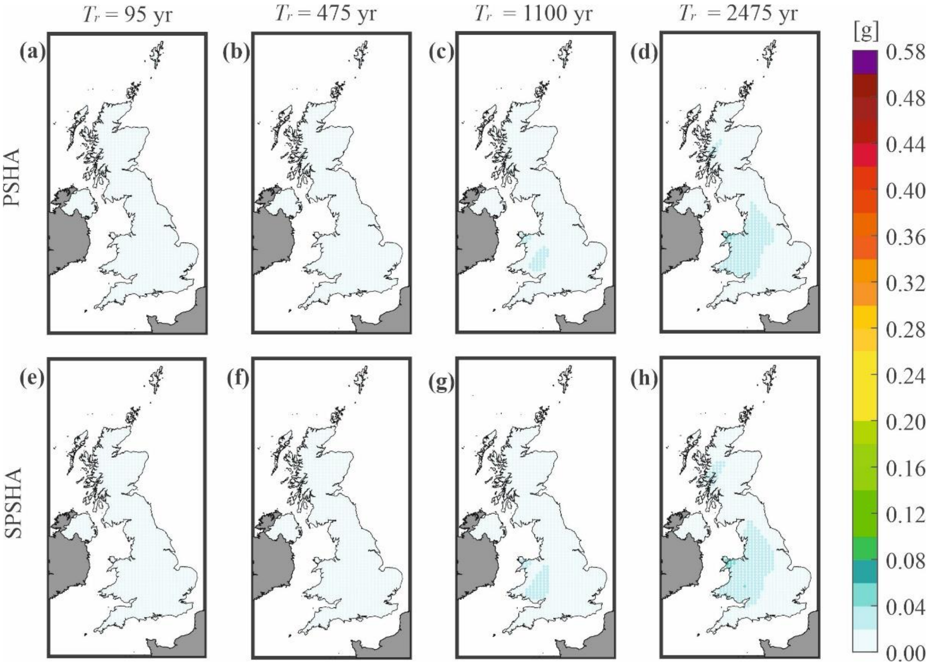

Figure 2.6 Maps of $Sa(T=1.0\text{s})$ on rock with $T_r = 95\,\text{yr}$, $T_r = 475\,\text{yr}$, $T_r = 1100\,\text{yr}$ and $T_r = 2475\,\text{yr}$, from left to right, obtained using PSHA (panels a-d) and SPSHA (panels e-h).

It appears that the hazard increase due to aftershocks is not the same across the country. This is not unexpected, as the magnitude and number of aftershocks increase with seismic hazard due to mainshocks (see also Iervolino et al., 2018; Chioccarelli et al., 2021). Moreover, results reveal that aftershock effect varies with the exceedance return period and spectral ordinate, as discussed in the following. To analyze quantitatively the results, Figure 2.7 shows the distributions of the differences between SPSHA and PSHA results across the country, computed at each site as $sa_{SPSHA} - sa_{PSHA}$; dividing this difference by sa_{PSHA} gives the relative hazard increases due to aftershocks, relatively to PSHA results; i.e., $(sa_{SPSHA} - sa_{PSHA})/sa_{PSHA}$. In both the figures, the top, middle and bottom rows refer to PGA, $Sa(T=0.2\,\text{s})$ and $Sa(T=1.0\,\text{s})$, respectively; in each row, panels from left to right show the difference for exceedance return periods from 95 yr to 2475 yr.

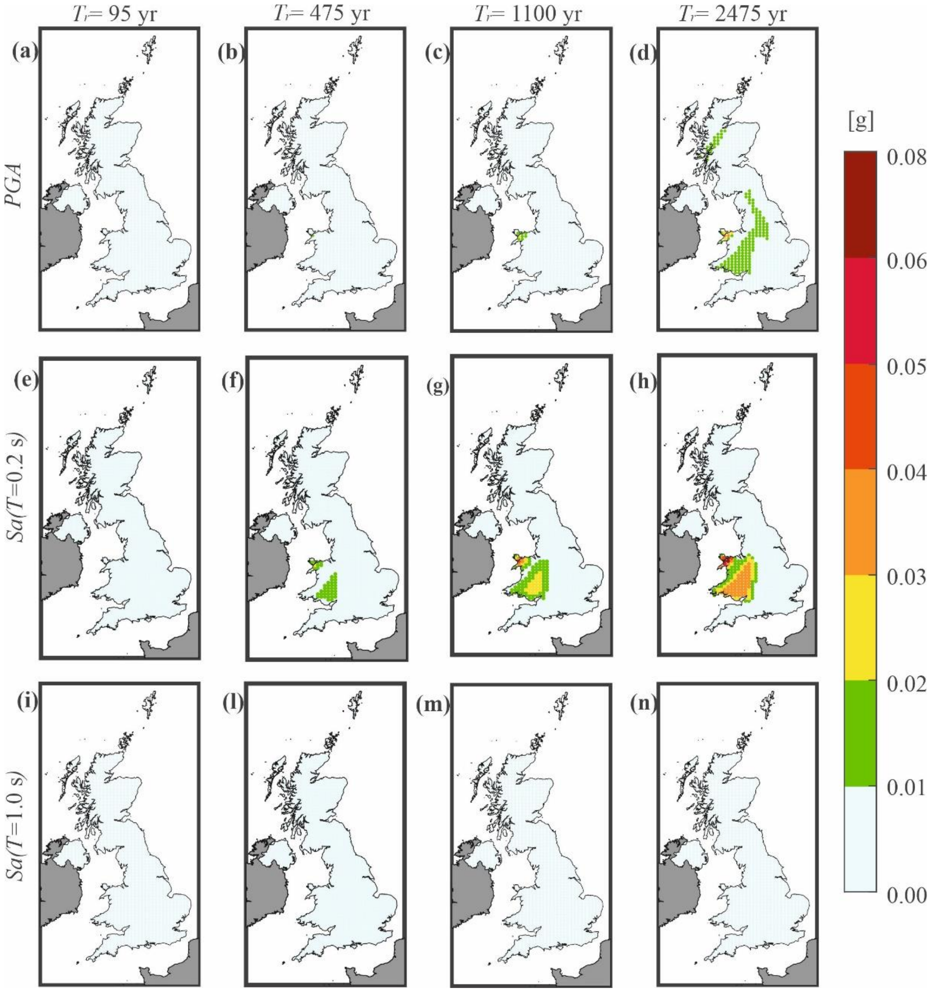

Figure 2.7 Absolute differences between SPSHA and PSHA results in terms of *PGA* (top), $Sa(T = 0.2\text{s})$ (middle) and $Sa(T = 1.0\text{s})$ (bottom), with $T_r = 95\,\text{yr}$, $T_r = 475\,\text{yr}$, $T_r = 1100\,\text{yr}$ and $T_r = 2475\,\text{yr}$, from left to right.

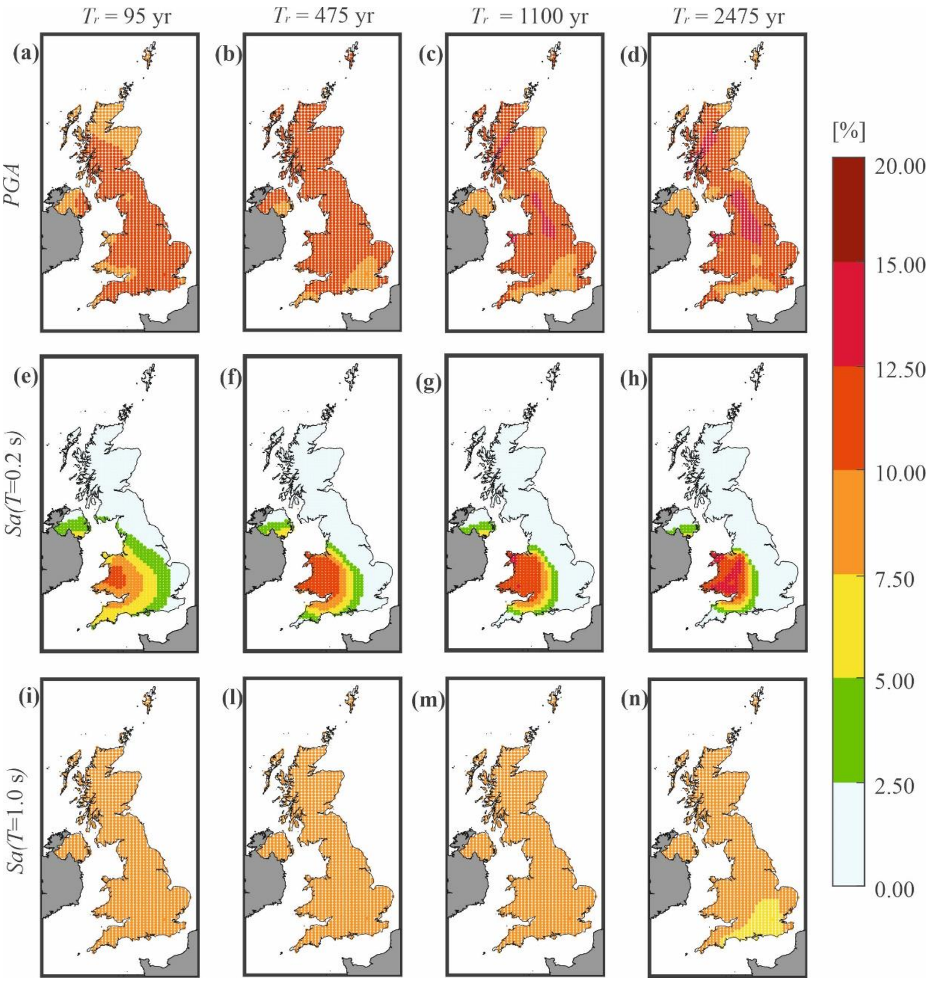

Figure 2.8 Relative differences between SPSHA and PSHA results in terms of PGA (top), $Sa(T=0.2\text{s})$ (middle) and $Sa(T=1.0\text{s})$ (bottom), with $T_r=95\,\text{yr}$, $T_r=475\,\text{yr}$, $T_r=1100\,\text{yr}$ and $T_r=2475\,\text{yr}$, from left to right.

As already mentioned, for each spectral ordinate and exceedance return period, it can be observed that aftershocks effect tends to increase (decrease) the seismic hazard increase (decrease) according to classical PSHA, in both absolute and relative terms. Looking at the figures vertically, it is found that, for each return period, the trend of the differences is the same as that of hazard results with the vibration period, which depends on the GMPE; i.e., it is comparatively larger at the low vibration periods. In fact, according to the maps, the maximum differences over the whole country are observed for $Sa(T=0.2\,\text{s})$, whereas the lowest are recorded for $Sa(T=1.0\,\text{s})$; differences in terms of PGA are in an intermediate situation. On average over the country, the absolute difference ranges from 3.88E-04 g, for $T_r = 95\,\text{yr}$, to 0.005 g, for $T_r = 2475\,\text{yr}$, for PGA, whereas they are 3.77E-04 g and 0.004 g for $T_r = 95\,\text{yr}$ and $T_r = 2475\,\text{yr}$, respectively, for $Sa(T = 0.2\text{s})$; for $Sa(T = 1.0\text{s})$, increments are very low, being about 0.001 g, on average, for the largest return period (see Table 2.3, Table 2.4 and Table 2.5).

Table 2.3 Average and maximum difference, in absolute and relative terms, of SPSHA results with respect to PSHA counterparts for PGA .

$T_r\,[\text{yr}]$	PGA			
	95	475	1100	2475
Average percentage difference [%]	10.2	10.7	10.8	10.9
Average absolute difference [g]	3.88E-04	0.0016	0.0030	0.0051
Maximum percentage difference [%]	10.9	12.2	13.2	13.8
Maximum absolute difference [g]	0.001	0.010	0.020	0.033

Table 2.4 Average and maximum difference, in absolute and relative terms, of SPSHA results with respect to PSHA counterparts for $Sa(T = 0.2\text{s})$.

$T_r\,[\text{yr}]$	$Sa(T = 0.2\text{s})$			
	95	475	1100	2475
Average percentage difference [%]	3.2	2.9	2.7	2.4
Average absolute difference [g]	3.77E-04	0.0015	0.0026	0.0041
Maximum percentage difference [%]	10.8	12.2	13.5	13.8
Maximum absolute difference [g]	0.003	0.022	0.043	0.069

Table 2.5 Average and maximum difference, in absolute and relative terms, of SPSHA results with respect to PSHA counterparts for $Sa(T = 1.0\text{s})$.

$T_r\,[\text{yr}]$	$Sa(T = 1.0\text{s})$			
	95	475	1100	2475
Average percentage difference [%]	9.2	9.6	9.1	8.3
Average absolute difference [g]	1.18E-04	4.99E-04	8.52E-04	0.0013
Maximum percentage difference [%]	9.8	9.9	10.0	9.9
Maximum absolute difference [g]	2.72E-04	0.002	0.003	0.006

Considering the ensemble of the return periods discussed so far, the average relative increments over the country are within 10.2% and 10.9% for PGA, 2.4% and 3.2% for $Sa(T = 0.2\text{s})$, and 8.3% and 9.6% for $Sa(T = 1.0\text{s})$. For each spectral ordinate, one can observe that absolute differences tend to increase with the increasing return period. However, the largest increment over the country, in absolute terms, is well below 0.1 g. Looking at the map in Figure 2.7, it is found that, in the proximity of the high hazardous MENA zone, the difference between SPSHA and PSHA results, in terms of $Sa(T = 0.2\text{s})$ with $T_r = 2475\,\text{yr}$, is equal to 0.069 g. Given the spectral ordinate, the trend of the relative increments as a function of the return period is non-monotonic. The largest percentage difference is found for $T_r = 2475\text{yr}$ in the case of PGA (North England) and $Sa\left(T = 0.2\text{s}\right)$ (northwest Wales), being about 13.8% in both the cases, whereas, for $Sa\left(T = 1.0\text{s}\right)$, it is about 10% (western Scotland) for $T_r = 1100\,\text{yr}$. In order to summarize the results represented in Figure 2.7 and Figure 2.8, the average and maximum differences, in both absolute and relative terms, are given in Table 2.3, Table 2.4 and Table 2.5 for each spectral and exceedance return period.

To close this section, the aftershock effects on design seismic actions discussed so far are briefly compared to those estimated for Italy by Iervolino et al. (2018). Due to the larger seismic hazard, it is expected that aftershock effects in Italy (see Figure 2 and Figure 3 in Iervolino et al., 2018) are more significant, both in relative and absolute terms, than those for the UK. For example, considering PGA and the largest return period $\left(T_r = 2475\,\text{yr}\right)$, for the most hazardous sites, the relative increment in Italy (about 28%) can be even twice that found for the UK (about 14%). Still with reference to PGA and $T_r = 2475\,\text{yr}$, the largest absolute difference between SPSHA and PSHA results are equal to 0.116g and 0.033g for Italy and the UK, respectively. Such a difference is also related to the fact that, for the same return period, spectral accelerations according to PSHA for the UK are lower than the Italian counterpart, yet by a larger ratio. More precisely, in the most hazardous areas of Italy PGA for $T_r = 2475\,\text{yr}$ (about 0.6 g) is almost three time the largest PGA (for the same return period) for the UK (about 0.25 g).

2.4.2. Site-specific hazard Analysis

In the previous section, it has been shown that aftershock effects on design seismic actions depend on the seismic hazard of the site, the spectral and exceedance return period. Now, SPSHA and PSHA results are discussed in more detail for the sites of Edinburgh (3.19° W, 55.95° N), Cardiff (3.18° W, 51.49° N) and Llangefni (4.31° W, 53.25° N). They were selected because representative of comparatively low, medium and high hazard level across the country according to PSHA, respectively. The location of the considered sites is shown in Figure 2.1. The aim is to (i) investigate the increase in seismic hazard due to aftershocks with respect to an interval of spectral and return periods larger than those considered in the previous section, and (ii) to give insights on the differences between PSHA- and SPSHA-based hazard results.

PSHA and SPSHA results for the sites are compared in Figure 2.9.

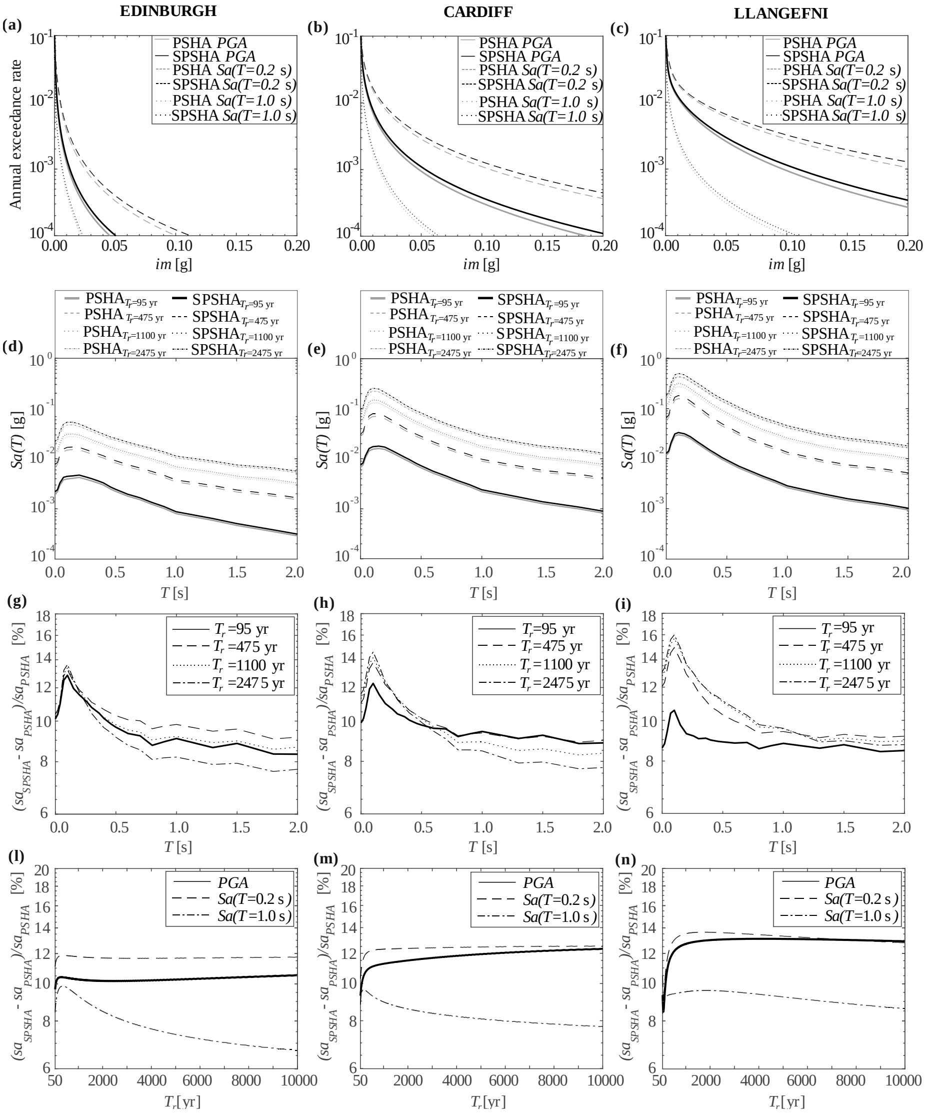

Figure 2.9 Results of hazard analysis for the three sites of interest: hazard curves in terms of PGA, $Sa(T=0.2\text{s})$ and $Sa(T=1.0\text{s})$ for the site of Edinburgh (a), Cardiff (b) and Llangefni (c), UHS with $T_r = 95\,\text{yr}$, $T_r = 475\,\text{yr}$, $T_r = 1100\,\text{yr}$ and $T_r = 2475\,\text{yr}$ for the site of Edinburgh (d), Cardiff (e) and Llangefni (f); relative hazard increase as function of the spectral period, for four T_r values, for the site of Edinburgh (g), Cardiff (h) and Llangefni (i); relative hazard increase as function of T_r in terms of PGA, $Sa(T=0.2\text{s})$ and $Sa(T=1.0\text{s})$ for the site of Edinburgh (l), Cardiff (m) and Llangefni(n).

The columns of Figure 2.9, each referring to a site, are ordered following the increasing seismic hazard, from left to right. Panels from (a) to (c) represent the hazard curves in terms of PGA, $Sa(T = 0.2\,\mathrm{s})$ and $Sa(T = 1.0\,\mathrm{s})$ according to PSHA (grey lines) and SPSHA (black lines). Panels from (d) to (f) show the UHS obtained from PSHA (grey lines) and SPSHA (black lines) for the return periods considered before. The spectral ordinates were computed considering 24 natural vibration periods, which are those used in the GMPE of Bindi et al. (2014). Based on these UHS, the relative hazard increments, as defined in the previous section, are represented in panels from (g) to (i), for each $Sa(T)$ and exceedance return period. In addition, the effect of aftershocks on the hazard, in terms of PGA, $Sa(T = 0.2\,\mathrm{s})$ and $Sa(T = 1.0\,\mathrm{s})$, as a function of return period from 50 yr to 10000 yr is shown in panels from (l) to (n).

Looking at the figure, it can be observed that the largest hazard increases are for the low-to-mid vibration periods (i.e., lower than 0.3 s), independently on the seismic hazard of the site and the considered exceedance return period. At each site, the largest relative differences are for the vibration period equal to 0.1 s, and all return periods: more specifically, they are 13.6%, 14.6% and 16% for Edinburgh, Cardiff and Llangefni, respectively. Panels from (g) to (i) also show that, considering the long vibration periods (i.e., larger than 1.0 s), the hazard increments at each site are lower than those found at the short periods and is almost constant: in fact, considering the return periods from 95 yr to 2475yr, they range from about 7.5% to 10% for both Edinburgh and Cardiff, whereas they are around 9% for any return period in the case of Llangefni. This reveals that the contribution of aftershocks to seismic hazard tends to decrease with the increasing of the spectral period, independently of the seismic hazard of the site and the exceedance return period; see as Iervolino et al. (2018) and Chioccarelli et al., (2021) for a discussion on this issue.

Panels from (g) to (i) confirm that the relative increment in the design seismic actions due to aftershocks, with respect to PSHA results, does not monotonically increase with the return period. For example, back to $Sa(T = 1.0\,\mathrm{s})$, it can be observed that the largest difference is found for $T_r = 475\,\mathrm{yr}$ in the case of Edinburgh, whereas it is $T_r = 2475\,\mathrm{yr}$ for the other two sites. Thus, one may be interested in exploring the trend of the hazard increment in a range of return periods wider than that considered so far. To do this, one should look at panels from (l) to (n). They reveal that, at each site, the increments increase in a very limited range of return periods, and tend to flatten out at T_r values larger than 4000 yr (and up to the largest herein considered) in the case of PGA and $Sa(T = 0.2\,\mathrm{s})$, whereas, for $Sa(T = 1.0\,\mathrm{s})$, they monotonically decrease for return periods from 2000 yr onwards. This is expected from the disaggregation of sequence-based seismic hazard (i.e., Chioccarelli et al., 2018), according to which the contribution of aftershocks to hazard as a function of T_r is not the same at the different vibration periods. For Edinburgh, the maximum increments for PGA, $Sa(T=0.2\,\mathrm{s})$ and $Sa(T=1.0\,\mathrm{s})$ are about 10.5%, 11.9% and 9.9%, respectively. They occur at different return periods, being $T_r=9980\,\mathrm{yr}$ for PGA, $T_r=470\,\mathrm{yr}$ $Sa(T=0.2\,\mathrm{s})$ and $T_r=360\,\mathrm{yr}$ for $Sa(T=1.0\,\mathrm{s})$. Considering the site of Cardiff, the maximum increases in terms of PGA, $Sa(T=0.2\,\mathrm{s})$ and $Sa(T=1.0\,\mathrm{s})$ are equal to 12.3%, 12.5% and 9.6% and they occur at return periods of 9990 yr, 9690 yr and 170 yr, respectively. Finally, for Llangefni, the maximum percentage difference between SPSHA and PSHA results in terms of PGA is equal to 13.1% and it is observed for $T_r=4060\,\mathrm{yr}$; in the case of $Sa(T=0.2\,\mathrm{s})$, the largest difference is similar to that for PGA, being equal to 13.6%, but it is found for $T_r=1720\,\mathrm{yr}$; looking at the trend for $Sa(T=1.0\,\mathrm{s})$, the peak, which is equal to 9.6%, occurs at $T_r=1830\,\mathrm{yr}$.

2.5. Sensitivity analysis

Because the paucity of seismic sequences leads to a simplified calibration of the modified Omori law parameters, this section deals with some sensitivity analysis of the results to such parameters, that is, $\{a,c,p\}$ and ΔT_A.

First, the 2475 yr UHS derived via the SPSHA based on the mean parameters, $\{a=-1.71, c=0.0023, p=0.68\}$, (i.e., those pictured in panels from (d) to (f) of Figure 2.9) are compared to those obtained by using $\{a=-1.66, c=0.0295, p=0.93\}$, that is, the parameters for Italy by Lolli and Gasperini (2003), a country of a generally larger seismic hazard than the UK. The comparison is given in Figure 2.10 where it appears that the differences are limited.

Moreover, even if not given here for the sake of brevity, the four sets of parameters obtained from each of the four seismic sequences considered, were also used to derive the UHS for the same sites and same return period just discussed. The found differences are in the order of 10%-15% with respect to the spectra obtained with the parameters obtained pooling all the sequences together.

Finally, still considering the 2475 yr UHS for the sites of Edinburgh, Cardiff and Llangefni, Figure 2.11 shows the sensitivity of the relative hazard increase, with respect to PSHA results, to the ΔT_A interval assumed in the analysis. It is shown that to vary ΔT_A from 90 to 365 days does not significantly affect the results.

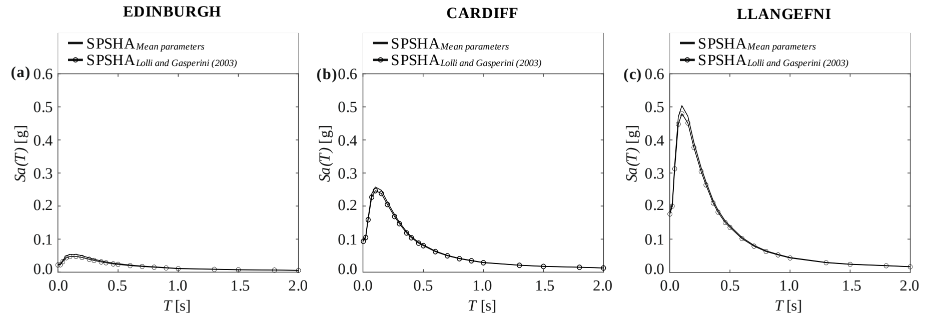

Figure 2.10 Comparison of UHS with $T_r = 2475\,\text{yr}$ obtained from hazard analysis conducted using the mean parameters calibrated for the UK and those for Italy by Lolli and Gasperini (2003) for the site of Edinburgh (a), Cardiff (b) and Llangefni (c).

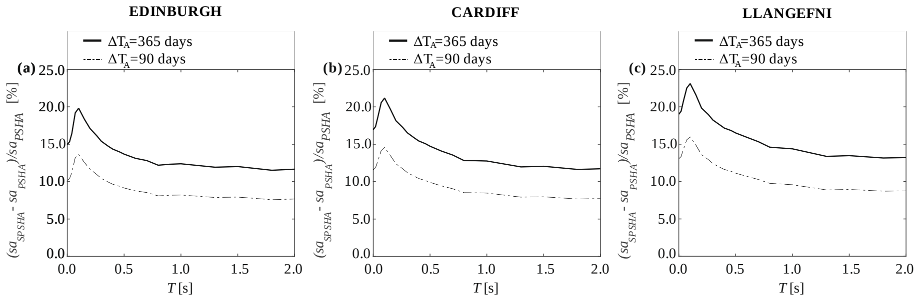

Figure 2.11 Comparison of UHS with $T_r = 2475\,\text{yr}$ obtained from hazard analysis conducted using the mean parameters calibrated for the UK with $\Delta T_A = 90$ days and $\Delta T_A = 365$ days for the site of Edinburgh (a), Cardiff (b) and Llangefni (c).

2.6. Conclusions

For reasons mainly related to the ease of calibration and use, implied by the homogeneous Poisson process assumption for earthquake occurrence and the limited completeness of information about foreshocks and aftershocks in seismic catalogs, classical PSHA only considers mainshocks in determining the rate of seismic events that exceed a ground motion intensity at a site of interest. However, sequence-based probabilistic seismic hazard analysis allows us to account for the effect of aftershock in the hazard assessment keeping the same advantages of PSHA. In fact, SPSHA still resources from a de-clustered catalog and assumes the homogeneous Poisson process assumption for the occurrence of mainshock-aftershocks sequences. Finally, SPSHA relies on an analytical formulation that is relatively easy to implement. Moreover, literature recently discussed that it is in good agreement with other seismic sequences modeling approaches, generally more cumbersome in calibration and simulation.

In the presented study, SPSHA was applied to investigate the hazard increase due to aftershocks in the UK, using the recent source model from the BGS. The parameters of the modified Omori law, which is used to model aftershock occurrence, were calibrated in a simplified manner based on four seismic sequences occurred in the UK (no more than that due to paucity of quality data), assumed to be complete in the magnitude range of interest. A very simple sensitivity analysis was carried out to assess the effect of the modified Omori law parameters on the results. It was verified that using parameters for a high-seismicity country such as Italy, does not lead to relevant differences in the hazard results.

Considering four exceedance return periods of interest to structural engineering within 95 yr and 2475 yr, hazard maps, in terms of PGA, $Sa(T=0.2\,\mathrm{s})$ and $Sa(T=1.0\,\mathrm{s})$, resulting from SPSHA were computed for rock site conditions, and compared to the PSHA counterparts based on the same source model and GMPE. Moreover, with reference to three sites, the PSHA and SPSHA results, for exceedance return periods up to 10000 yr and 24 spectral ordinates, were compared and discussed in greater detail to give further insights about the aftershock implications. Finally, the aftershock effects estimated for the UK were briefly compared to a previous SPSHA study for Italy, a relatively larger seismic hazard country. Some remarks that can be drawn from the results are listed in the following.

- For each spectral and return period, the hazard increase tends to be more relevant in the areas covering most of Wales, North Central England and western Scotland.
- For a given spectral ordinate, the largest percentage increase due to aftershocks over the country has a non-monotonic trend with the return period; the largest value across the country, equal to 10%, was found at $T_r = 1100\,\mathrm{yr}$ for $Sa(T=1.0\,\mathrm{s})$, while, for PGA and $Sa(T=0.2\,\mathrm{s})$, it is 14% at $T_r = 2475\,\mathrm{yr}$.
- For a given spectral ordinate, the maximum absolute differences between SPSHA and PSHA results over the country monotonically increase with return period (in the range considered). Nationwide, for $T_r = 2475\,\mathrm{yr}$, the largest difference between SPSHA and PSHA are equal to 0.033 g, 0.069 g and 0.006 g in the case of PGA, $Sa(T=0.2\,\mathrm{s})$ and $Sa(T=1.0\,\mathrm{s})$, respectively.

- On average across the country, the absolute differences, in the case of $T_r = 2475\,\text{yr}$, are equal to 0.0051 g, 0.0041 g and 0.0013 g for PGA, $Sa(T = 0.2\,\text{s})$ and $Sa(T = 1.0\,\text{s})$, respectively.
- Considering the range of return periods between 95 yr and 2475 yr, the largest average percentage differences are equal to 11% in the case of PGA, 3% for $Sa(T = 0.2\,\text{s})$, and 10% for $Sa(T = 1.0\,\text{s})$; they were found at $T_r = 2475\,\text{yr}$, $T_r = 95\,\text{yr}$ and $T_r = 475\,\text{yr}$, respectively.
- The analysis for specific sites revealed that the aftershock effects are more significant at vibration periods lower than 0.3 s, and tend to decrease for those larger, becoming almost constant from 1.0 s onwards. The largest relative difference between SPSHA and PSHA results was found at 0.1 s for all sites. With reference to Llangefni, which is the site characterized by the highest seismic hazard countrywide, the return period for which the largest hazard increase is found significantly varies among the different spectral ordinates, being equal to 4060 yr, 1720 yr and 1830 yr for PGA, $Sa(T = 0.2\,\text{s})$ and $Sa(T = 1.0\,\text{s})$, respectively.
- In the most hazardous sites of the UK, the hazard percentage increments of SPSHA results with respect to PSHA are about a half than those found in the most hazardous areas of Italy, although in Italy the larger spectral acceleration associated to a given return period can be three times larger than the analogous one in the UK.

References

Atik, L. Al, A. Kottke, N. Abrahamson, and J. Hollenback (2014).Kappa (ϰ) scaling of ground-motion prediction equations using an inverse random vibration theory approach.*Bulletin of the Seismological Society of America*.104(1).336–346.

Atkinson, G.M., and D.M. Boore (2006).Earthquake ground-motion prediction equations for eastern North America.*Bulletin of the Seismological Society of America*.96(6).2181–2205.

—— (2011).Modifications to existing ground-motion prediction equations in light of new data.*Bulletin of the Seismological Society of America*.101(3).1121–1135.

Bindi, D., M. Massa, L. Luzi, G. Ameri, F. Pacor, R. Puglia, and P. Augliera (2014).Pan-European ground-motion prediction equations for the average horizontal component of PGA, PGV, and 5%-damped PSA at spectral periods up to 3.0 s using the RESORCE dataset.*Bulletin of Earthquake Engineering*.12(1).391–430.

Boore, D.M., J. Stewart, E. Seyhan, and G.M. Atkinson (2014).NGA-West2 Equations for Predicting PGA, PGV, and 5% Damped PSA for Shallow Crustal Earthquakes.*Earthquake Spectra*.30.1057–1085.

British Geological Survey (2020).“National seismic hazard maps for the UK: 2020 update (Open Report OR/20/053).”

Cauzzi, C., E. Faccioli, M. Vanini, and A. Bianchini (2015).Updated predictive equations for broadband (0.01–10 s) horizontal response spectra and peak ground motions, based on a global dataset of digital acceleration records.*Bulletin of Earthquake Engineering*.13(6).1587–1612.

Chioccarelli, E., P. Cito, and I. Iervolino (2018).“Disaggregation of Sequence-based seismic hazard.”in: *Proceedings of 16th European Conference on Earthquake Engineering*.

Chioccarelli, E., P. Cito, I. Iervolino, and M. Giorgio (2019).REASSESS V2.0: software for single- and multi-site probabilistic seismic hazard analysis.*Bulletin of Earthquake Engineering*.17(4).1769–1793.

Chioccarelli, E., P. Cito, F. Visini, and I. Iervolino (2021).Sequence-based hazard analysis for Italy considering a grid seismic source model.*Annals of Geophysics*.

Cornell, C.A. (1968).Engineering seismic risk analysis.*Bulletin of the Seismological Society of America*.58.1583–1606.

Cotton, F., F. Scherbaum, J.J. Bommer, and H. Bungum (2006).Criteria for selecting and adjusting ground-motion models for specific target regions: Application to central Europe and rock sites.*Journal of Seismology*.10(2).137–156.

Gardner, J.K., and L. Knopoff (1974).Bulletin of the Seismological Society of America .*Bulletin of the Seismological Society of America*.64(5).1363–1367.

Gutenberg, B., and C.F. Richter (1944).Frequency of earthquakes in California.*Bulletin of the Seismological Society of America*.64(5).185–188.

Helmstetter, A. (2003), Is Earthquake Triggering Driven by Small Earthquakes?, *Phys. Rev. Lett.*, 91(5), 3–6.

Iervolino, I. (2016).Soil-invariant seismic hazard and disaggregation.*Bulletin of the Seismological Society of America*.106(4).1900–1907.

Iervolino, I., E. Chioccarelli, and M. Giorgio (2018).Aftershocks’ effect on structural design actions in Italy.*Bulletin of the Seismological Society of*

America.108(4).2209–2220.

Iervolino, I., M. Giorgio, and B. Polidoro (2014). Sequence-based probabilistic seismic hazard analysis.*Bulletin of the Seismological Society of America*.104(2).1006–1012.

Joyner, W.B., and D.M. Boore (1981).Peak horizontal acceleration and velocity from strong-motion records including records from the 1979 Imperial Valley, California, earthquake.*Bulletin of the Seismological Society of America*.71(6).2011–2038.

Kanamori, H., and D.L. Anderson (1975).Theoretical basis of some empirical relations in seismology.*Bulletin of the seismological society of America*.65(5).1073–1095.

Kramer, S.L. (1996).*Geotechnical Earthquake Engineering*.Prentice-Hall, New Jersey.

Kutoyantis, Y.A. (1982).Multidimensional parameter estimation of the intensity function of inhomogeneous Poisson processes.*Probl. Control Inf. Theory*.11(4).325–334.

Lolli, B., and P. Gasperini (2003).Aftershocks hazard in Italy part I: Estimation of time-magnitude distribution model parameters and computation of probabilities of occurrence.*Journal of Seismology*.7(2).235–257.

Marzocchi, W., and M. Taroni (2014).Some thoughts on declustering in probabilistic seismic-hazard analysis.*Bulletin of the Seismological Society of America*.104(4).1838–1845.

McGuire, R.K. (2004).Seismic Hazard and Risk Analysis.*Earthquake Engineering Research Institute Publication*.(Report MNO-10. Oakland, CA, USA).

Montaldo, V., E. Faccioli, G. Zonno, A. Akinci, and L. Malagnini (2005).Treatment of ground-motion predictive relationships for the reference seismic hazard map of Italy.*Journal of Seismology*.9(3).295–316.

Mosca, I., S. Sargeant, B. Baptie, R.M.W. Musson, and T. Pharaoh (2022). The 2020 national seismic hazard model for the United Kingdom. *Bulletin of Earthquake Engineering* 20, 633-675.

Ogata, Y. (1978).The asymptotic behaviour of the maximum likelihood estimators for the stationary point processes.*Ann. Inst. Statist. Math.,*.30(A).243–261.

—— (1983).Estimation of the parameters in the modified omori formula for aftershock frequencies by the maximum likelihood procedure.*Journal of*

Physics of the Earth.31(2).115–124.

—— (1988).Statistical models for earthquake occurrences and residual analysis for point processes.*Journal of the American Statistical Association*.83(401).9–27.

Papadopoulos, A.N., P. Bazzurro, and W. Marzocchi (2021).Exploring probabilistic seismic risk assessment accounting for seismicity clustering and damage accumulation: Part I. Hazard analysis.*Earthquake Spectra*.37(2).803–826.

Reasenberg, P., and L. Jones (1989).Earthquake hazard after a mainshock in California.*Science*.243.1173–1175.

—— (1994).Earthquake aftershocks: update.*Science*.265.1251–1252.

Rietbrock, A., F. Strasser, and B. Edwards (2013).A stochastic earthquake ground-motion prediction model for the United Kingdom.*Bulletin of the Seismological Society of America*.103(1).57–77.

Tromans, I.J., G. Aldama-Bustos, J. Douglas, A. Lessi-Cheimariou, S. Hunt, M. Daví, R.M.W. Musson, G. Garrard, F.O. Strasser, and C. Robertson (2019).*Probabilistic seismic hazard assessment for a new-build nuclear power plant site in the UK*.vol. 17, Springer Netherlands.

Utsu, T. (1961).A statistical study on the occurence of afthershocks.*The Geophysical Magazine*.30.521–605.

—— (1970).Aftershocks and Earthquake Statistics (I): Some parameters which characterize an aftershock sequence and their interrelations.*Journal of the Faculty of Science, Hokkaido University*.3.129–195.

Utsu, T., and Y. Ogata (1995).The centenary of the omori formula for a decay law of aftershock activity.*Journal of Physics of the Earth*.43(1).1–33.

Villani, M., Z. Lubkowski, M. Free, R.M.W. Musson, B. Polidoro, R. McCully, A. Koskosidi, C. Oakman, T. Courtney, and M. Walsh (2020), A probabilistic seismic hazard assessment for Wylfa Newydd, a new nuclear site in the United Kingdom, *Bull. Earthq. Eng.*, 18(9), 4061–4089.

Wang, S., M.J. Werner, and R. Yu (2021).How Well Does Poissonian Probabilistic Seismic Hazard Assessment (PSHA) Approximate the Simulated Hazard of Epidemic-Type Earthquake Sequences ?.*Bulletin of the Seismological Society of America*.1–19.

Yeo, G.L., and C.A. Cornell (2009).A probabilistic framework for quantification of aftershock ground-motion hazard in California: Methodology and parametric study.*Earthquake Engineering and Structural Dynamics*.38.45–60.

Zhang, J., and M.D. Shields (2018).On the quantification and efficient propagation of imprecise probabilities resulting from small datasets.*Mechanical Systems and Signal Processing*.98.465–483.

Zhang, L., K. Goda, M.J. Werner, and S. Tesfamariam (2021).Spatiotemporal seismic hazard and risk assessment of M9.0 megathrust earthquake sequences of wood-frame houses in Victoria, British Columbia, Canada.*Earthquake Engineering and Structural Dynamics*.50(1).6–25.

Zhang, L., M.J. Werner, and K. Goda (2018).Spatiotemporal seismic Hazard and risk assessment of aftershocks of M 9 megathrust earthquakes.*Bulletin of the Seismological Society of America*.108(6).3313–3335.

Zhuang, J., Y. Ogata, and D. Vere-Jones (2002).Stochastic declustering of space-time earthquake occurrences.*Journal of the American Statistical Association*.97(458).369–380.

3

Evaluation of state-dependent seismic fragilities for specific buildings: Dutch unreinforced masonry.

Abstract

This study was carried out in collaboration with Arup Italy.
This chapter deals with the assessment of state-dependent fragility curves of a case-study structure representative of the unreinforced masonry (URM) buildings (specifically terraced houses) in the Groningen region of the Netherlands. This is an area where the seismicity induced by gas-extraction practices makes it essential to develop an understanding of the risks that are the result.

A three-dimensional model of the structure was developed in collaboration with Arup Italy using the LS-DYNA finite element software. This was employed to analyze the building via the Cloud Analysis procedure to assess the fragilities of the intact structure at different damage states. Subsequently, to limit the typical computational effort involved in assessing state-dependent fragilities, two single-degree-of-freedom (SDoF) systems representing the structural behavior in the building's two main directions were developed and analyzed using back-to-back Incremental Dynamic Analysis (IDA).

Keywords: sequence-based seismic reliability, back-to-back IDA, SDoF systems, unreinforced masonry.

3.1. Introduction

The evaluation of the seismic performance of unreinforced masonry (URM) structures is a popular topic of discussion globally. In the Netherlands in recent years, some regions began to experience seismic events because of the reservoir depletion caused by commercial gas-extraction processes (Vlek, 2019). These began in 1963 and have triggered shallow earthquakes since the early 1990s, with the highest moment magnitude equal to 3.6 experienced near Huizinge on 16 August 2012. The induced seismicity had a wide impact on the built environment which was mainly composed of URM buildings that were not designed to sustain seismic loading. These structures presented in fact specific characteristics such as very slender walls, limited cooperation between the walls and floors, and the use of cavity walls that are often connected by weak and corroded ties.

This phenomenon triggered a global research program involving many Dutch and international universities, knowledge institutions, and recognized experts. The primary goals of the program were to assess the hazard and risk resulting from gas extraction-induced seismicity and then develop risk-mitigation strategies. In this context, the exploration and production company Nederlandse Aardolie Maatschappij (NAM) contracted Arup to: 1) conduct a study to define a preventive structural-upgrade strategy for existing buildings in the Groningen region of the Netherlands, with the goal of reducing the damage caused by the induced seismicity, and 2) verify whether the structures conform with the requirements set out in the standard National Practice Guidelines 9998 (NAM, 2018).

This chapter considers the assessment of state-dependent fragility functions of a structure representing the terraced house typology built widely in the Groningen area from 1960-1980 and which was affected the most by the gas extraction-induced seismicity referred to above.

A three-dimensional (3D) finite element model of the structure was constructed in a collaboration with Arup Italy. This was then analyzed using the LS-DYNA finite element software via Cloud Analysis methodology (Jalayer et al., 2015, 2017). Subsequently, the assessment of state-dependent fragility curves was conducted using the single-degree-of-freedom (SDoF) approximation of the structure. Two equivalent SDoF (ESDoF) systems were defined based on the static and dynamic pushover curves obtained for the two principal directions of the original 3D structural model. These SDoFs were subjected to back-to-back Incremental Dynamic Analysis (IDA) procedure (Luco et al., 2004; Ryu et al., 2011; Goda, 2012; Ruiz-García, 2012; Raghunandan et al., 2015; Goda, 2015) to obtain the state-dependent fragilities. Some concluding remarks can be found at the end of this chapter.

3.2. Prototype building

The prototype building was based on the real terraced houses built in large numbers in the Groningen region (north-east Netherlands) from 1960-1980.

In more detail, the case-study structure represents a two-unit terraced house with two stories, large window openings to the front and rear, and all the other construction features that are typical of the buildings in the Groningen area. The structure is composed of: 1) external masonry cavity walls formed by calcium silicate (CaSi) inner leaf with a load-bearing function and a clay brick outer leaf connected by masonry metal wall ties; 2) load-bearing internal walls and party walls formed of CaSi; 3) reinforced concrete slabs; 4) a timber roof; and 5) shallow foundations. Some of the construction details typical of these terraced houses are set out in Figure 3.1 (for further information on this structural typology, see Graziotti et al., 2017).

The building is 12.5 m long, 7.80 m wide and 8.80 m high. The height includes a 1.0 m underground section (distance from the laying surface to the ground floor). Each unit of the structure has an extension, as is common for this type of building. This has approximate dimensions of 3.70 m x 2.20 m x 3.50 m. Figure 3.2 portrays different views of this model house.

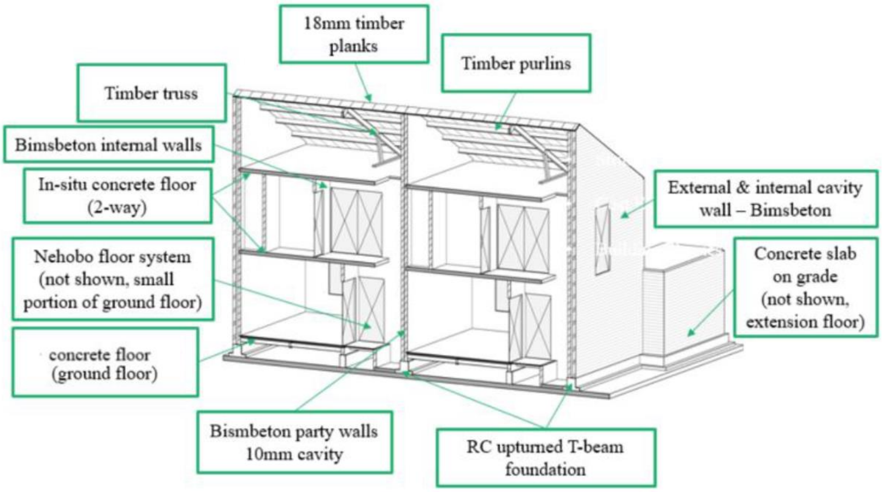

Figure 3.1 Characteristics of the case-study building.

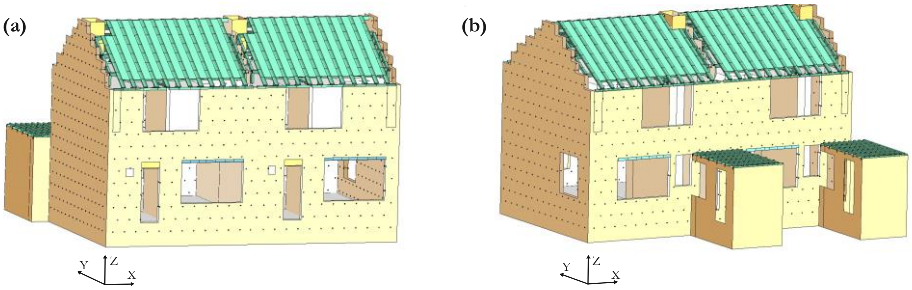

Figure 3.2 Views of the terraced house case-study.

The structure is composed of four walls in the X-direction and five walls in the Y-direction. Their geometric features are shown in Figure 3.3 and Figure 3.4, respectively. Figure 3.3 shows the X-direction's four walls. Panels (a) and (b) correspond to the two external walls and panels (c) and (d) to the two internal ones. Figure 3.4 shows the five walls in the Y-direction. Panels (a) and (b) correspond to the two external walls, panel (c) shows the wall separating the two units of the structure, and panel (d) represents the internal wall of each unit. The openings of each wall are also reported in Figure 3.3 and Figure 3.4.

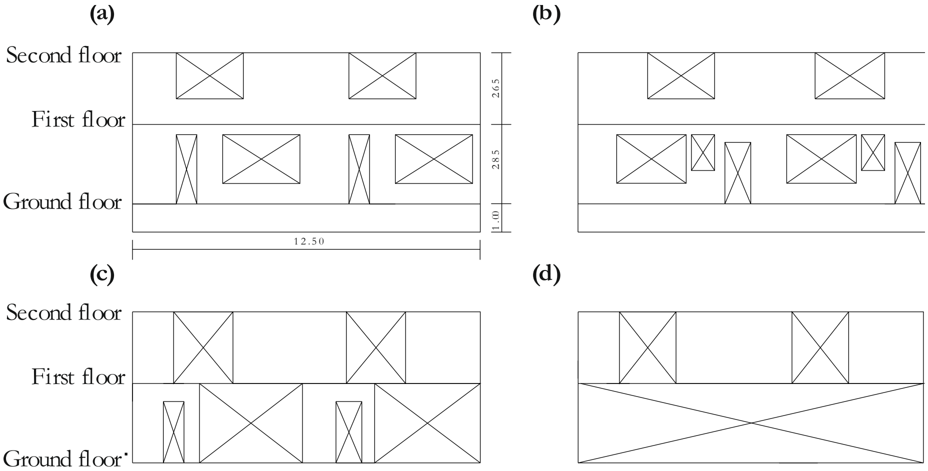

Figure 3.3 Geometry of the walls disposed along the X-direction: frontal wall (a), back wall (b) and internal walls (c-d).

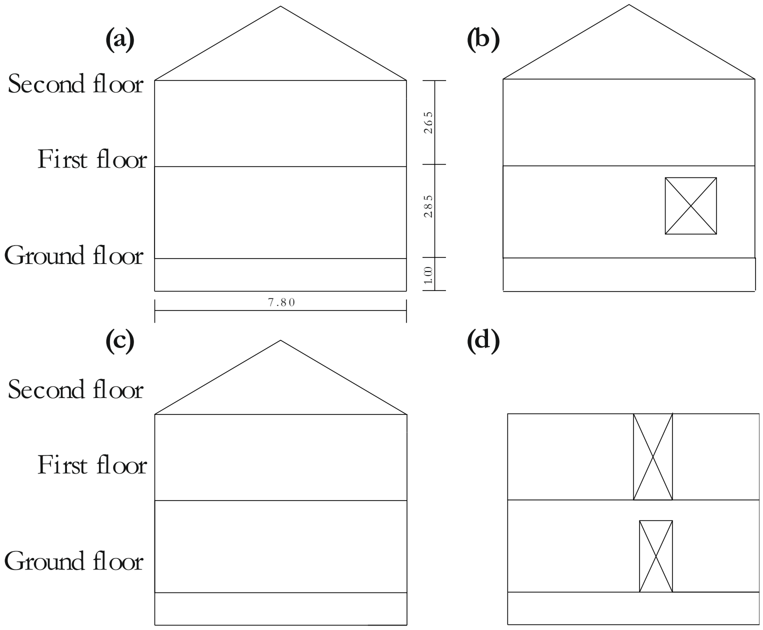

Figure 3.4 Geometry of the walls disposed along the Y-direction: external walls (a-b); unit partition wall (c), and internal wall of each unit(d).

It should be noted that, after the study commissioned by NAM (Arup, 2013), the structure was modeled taking into account reinforcement measures designed by Arup to ensure compliance with the standard National Practice Guidelines (NPR) 9998.

3.3. Finite Element Modelling approach

A 3D finite element model of the structure was produced in collaboration with Arup Italy using LS-DYNA, which is a versatile finite element analysis program adopted for seismic analyses, among many other applications. The program is used widely by Arup due to its capacities to both model components of buildings, soils and soil-structure interaction and due to quick solutions for large, complex models on multi-processor distributed-memory computer platforms.

To model the URM walls, a user material model for the shell elements (*MAT_SHELL_MASONRY) was developed and implemented by Arup in LS-DYNA. This is not part of the standard LS-DYNA release. The material model is used with a relatively coarse mesh and adopts a homogenized representation of the brick-mortar conglomerate. It takes into account the orientation of horizontal and vertical mortar joints and the difference in their stress-strain behavior based on the interlocking of units. The response and failure modes taken into account are: 1) the non-linear compressive response and toe-crushing; 2) cyclic bed-joint crack opening/closing and sliding; 3) the head-joint opening combined with bed-joint sliding; and 4) the interlocking pattern of bricks, which causes an anisotropic response to shear loading. The material model is described in detail in the study by Sturt et al. (2018), which also reports the procedure for validating the material. A testing campaign was carried out in 2015 to characterize the CaSi masonry typically that is typical of the load-bearing inner leaf of modern Dutch cavity wall systems. These experiments were performed at TU Delf in the Netherlands (Messali et al., 2017) and at EUCENTRE in Italy (Graziotti et al., 2017). The testing included in-plane and out-plane tests on wall specimens and full-scale shaking table tests of URM houses.

Figure 3.5 shows different views of the 3D finite element model developed in LS_DYNA. It also shows the coordinate system considered, which was set by placing the X-axis along the larger structure's dimension and Y-axis along the transverse direction.

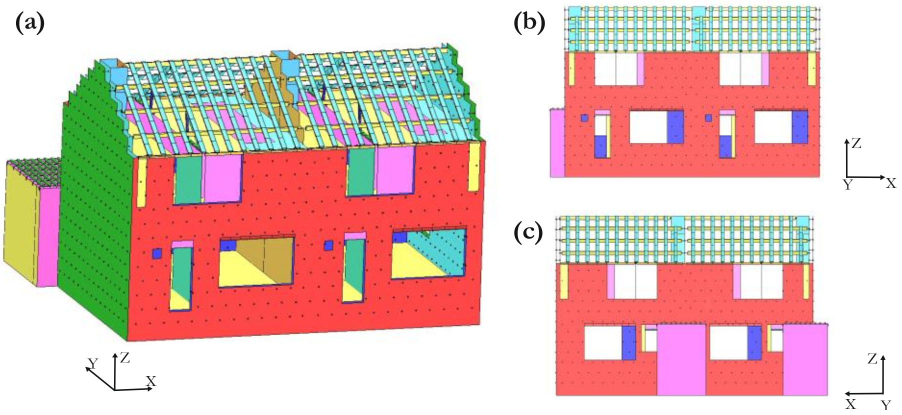

Figure 3.5 Views of the three-dimensional finite element model of the case-study's terraced house.

3.4. Modal (Eigenvalue) Analysis

In the first step, modal analysis was performed by calculating the first 20 modes of the building. Structures built with the configuration described in the previous paragraphs generally exhibit two very different seismic behaviors in the two principal directions. These structures are more flexible and vulnerable in the longitudinal direction, i.e., the X-direction (Graziotti et al., 2017). This was confirmed by the modal analysis, with the first mode showing in-plane deformations in the weak direction and the activation of the larger part of the mass of the structure in the X-direction (participating mass equal to 57.67 %). Hereafter, this is therefore referred to as the first mode, with a period of natural vibration, T_1, equal to 0.20 s.

In the Y-direction, the first major mode was mode 17, with participating mass of 22.90%. The other modes were generally local and concentrated in the roof of the structure. Table 3.1 shows the period of natural vibration and the effective mass and participating mass in the X- and Y-directions.

Table 3.1 Modes of the case-study building.

		X-direction		Y-direction	
Mode	Period [s]	Eff. Mass [kg]	Partic. [%]	Eff. Mass [kg]	Partic. [%]
1	0.199	1.45E+05	57.65%	2.80E+02	0.11%
2	0.175	1.55E+01	0.01%	2.51E+03	1.00%
3	0.175	7.34E+01	0.02%	3.29E+03	1.31%
4	0.174	4.97E+01	0.02%	4.82E+00	0.00%
5	0.174	3.05E+01	0.02%	1.32E+03	0.53%
6	0.165	2.82E+02	0.11%	7.67E+03	3.05%
7	0.161	1.45E+01	0.00%	1.86E+03	0.74%

Table 3.1 (*Continued*) Modes of the case-study building.

		X-direction		Y-direction	
Mode	Period [s]	Eff. Mass [kg]	Partic. [%]	Eff. Mass [kg]	Partic. [%]
8	0.161	3.04E+03	1.22%	1.80E+02	0.07%
9	0.159	4.46E+02	0.17%	5.62E+02	0.23%
10	0.114	5.59E+03	2.23%	6.48E+03	2.58%
11	0.113	1.93E+03	0.77%	2.93E+04	11.66%
12	0.113	1.45E+03	0.58%	2.74E+02	0.11%
13	0.111	2.23E+02	0.09%	1.98E+03	0.79%
14	0.111	9.70E+02	0.38%	2.81E+02	0.11%
15	0.110	6.45E+02	0.26%	2.82E-01	0.00%
16	0.105	1.54E+04	6.13%	2.80E+04	11.14%
17	0.102	1.32E+04	5.25%	5.75E+04	22.90%
18	0.094	7.40E+02	0.30%	4.52E+02	0.18%
19	0.087	2.72E+01	0.01%	4.56E+00	0.00%
20	0.086	1.60E+01	0.00%	1.38E+01	0.00%

3.5. Non-linear static (pushover) analysis

A non-linear static analysis was carried out by applying in the perpendicular directions of the structure (X and Y) two load patterns in both positive and negative orientations of the seismic loads and recording the static nonlinear response. The inverse triangular and uniform (mass-proportional) force distributions were used for the analysis. The first type of distribution is typically similar and represents the forces produced by the dominant mode of vibration. Meanwhile, the uniform distribution represents a possible soft-storey mechanism where the response is controlled by the ground-level story. These distributions can be taken as the upper and lower boundaries of the actual response of the dynamic analyses. Generally, the real failure mode is predicted by one of these distributions. Table 3.2 shows the lateral-load proportions.

Table 3.2 Lateral-load proportions.

	Mass Floor [kg]	Uniform Distribution	Triangular Distribution
Second floor	73043	1.00	1.00
First floor	87827	1.20	0.52

Subsequently, in addition to the static pushover analyses performed applying the two force distributions in the X- and Y-directions; the cyclic pushover assessments were executed using the loading protocol relating to the displacement shown in Figure 3.6 and defined according to the Protocol ISO 16670. This protocol concerns displacement cycles grouped in phases at displacement levels that increase incrementally. The protocol has two displacement patterns. The first one consists of five single, fully reversed cycles at displacements of 1.25%, 2.50%, 5.0%, 7.5% and 10% of the ultimate displacement. The second pattern has three fully reversed cycles of equal amplitude, at displacements of 20%, 40 %, 60%, 80%, 100% and 120% of the ultimate displacement. The ultimate displacement is assumed equal to 0.04 m.

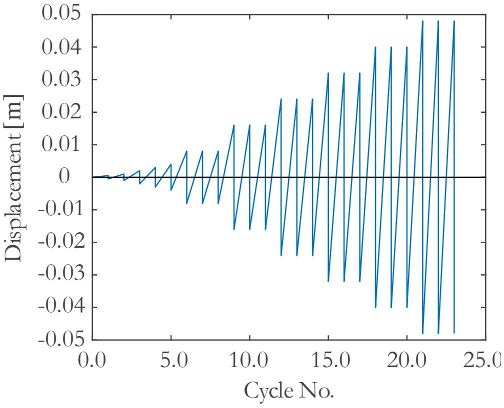

Figure 3.6 Loading protocol for the cyclic pushover analyses.

The results of the static and cyclic pushover analyses obtained for the two force-distribution types are reported in Figure 3.7 in terms of the base shear, V_b, and the displacement of the control point, i.e., the barycenter of the top floor. Panels (a) and (b) represent the results obtained applying the uniform distribution of forces whereas panels (c) and (d) refer to the application of the triangular force distribution. The figure also shows several characteristic points individuated on the static pushover curves: 1) the point of maximum base shear (point A in the positive direction of the load and A’ in the negative direction); 2) the point of a 20% reduction in the base shear (point B in the load’s positive direction and B’ in its negative direction); and 3) the point of a 50% reduction in the base shear (point C in the positive direction of the load and C’ in the negative direction). The values of the points’ coordinates in terms of base shear, V_b, and displacement of the top floor, δ, are set out in Table 3.3 and in Table 3.4 for the uniform and triangular force-distributions, respectively.

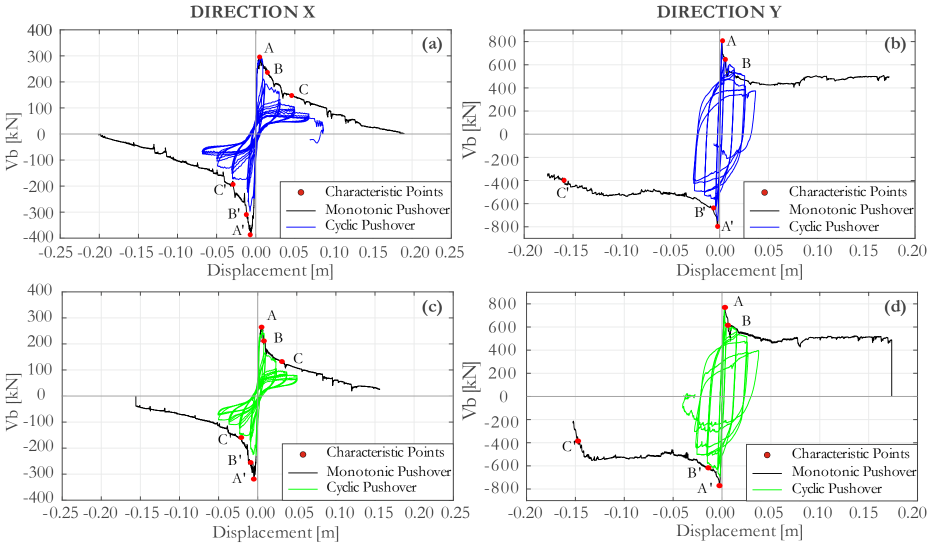

Figure 3.7 Results of the static and cyclic pushover analyses performed by applying the uniform distribution of forces in the X direction (a) and the Y direction (b). Results of the static and cyclic pushover analyses performed by applying the triangular distribution of forces in the X direction (c) and the Y direction (d).

Table 3.3 Coordinates of the characteristic points relating to the uniform distribution of forces.

	Direction X		Direction Y	
	$Disp\ [m]$	$V_b\ [kN]$	$Disp\ [m]$	$V_b\ [kN]$
A	0.005	295.6	0.003	807.6
B	0.015	236.5	0.006	646.09
C	0.046	147.8	-	403.8
A’	-0.007	-386.8	-0.002	-796.4
B’	-0.012	-309.4	-0.006	-637.1
C’	-0.029	-193.4	-0.159	-398.2

Table 3.4 Coordinates of the characteristic points relating to the triangular distribution of forces.

	Direction X		Direction Y	
	$Disp\ [m]$	$V_b\ [kN]$	$Disp\ [m]$	$V_b\ [kN]$
A	0.005	264.5	0.003	769.3
B	0.008	211.6	0.006	615.4
C	0.031	132.3	-	384.6
A’	-0.005	-318.9	-0.003	-770.6
B’	-0.009	-255.1	-0.014	-616.5
C’	-0.021	-159.5	-0.147	-385.3

3.6. Assessment of seismic fragilities using the 3D finite element model

There are several procedures to conduct a nonlinear dynamic analysis (NLDA) for the purpose of collecting the data required to estimate the fragility functions. One of these methods is Cloud Analysis, which was used in this study to assess of the fragility curves of the case-study's system. The cloud data encompass pairs of ground motion intensity measure (IM) and its corresponding structural response, generally expressed using an engineering demand parameter (EDP). The statistical properties of the cloud data can be estimated by applying a conventional linear regression (using least squares) to the data on the natural logarithmic scale, which is the standard basis for the underlying log-normal distribution model (Jalayer et al., 2015, 2017).

Consequently, the cloud method enables the identification of a probabilistic relationship between an EDP and IM. This predicts the conditional median of EDP for a given level of IM denoted as $\eta_{EDP|IM}$:

$$\ln \eta_{EDP|IM}\left(IM\right) = \ln a + b \cdot \ln\left(IM\right) \tag{3.1}$$

where $\ln a$ and b are constant coefficients that are estimated from the linear regression. The conditional logarithmic standard deviation of the EDP given IM, $\beta_{EDP|IM}$, can be estimated as:

$$\beta_{EDP|IM} = \sqrt{\sum_{i=1}^{N}\left(ln\, EDP_i - ln\left(a \cdot IM_i^b\right)\right)^2 \Big/ \left(N-2\right)} \tag{3.2}$$

where EDP_i and IM_i are the corresponding cloud data for the i-th record in the set and N is the number of records.

A structure-specific seismic fragility function defines the conditional probability that the structure, given a certain IM level, im, fails to meet some performance objective. This failure is often termed the exceedance of a limit or damage state, DS, that can be defined using a threshold value of engineering demand parameter, edp_{DS}. The fragility function can therefore be written as $P\left[EDP > edp_{DS} \middle| IM = im\right]$, or sometimes simply written as $P\left[DS \mid IM = im\right]$. This probability in the case of a Cloud Analysis can be described using a lognormal distribution (Jalayer and Cornell, 2008; Jalayer et al., 2017) , as reported in Eq. (3.3) :

$$P\left[EDP > edp_{DS} \middle| IM = im\right] = \Phi\left(\frac{ln\,\eta_{EDP|IM}}{\beta_{EDP|IM}}\right) = \Phi\left(\frac{ln\left(a \cdot IM_a^{\ b}\right)}{\beta_{EDP|IM}}\right). \tag{3.3}$$

For ultimate limit states in general, structural collapse can be induced by some of the selected records, resulting in very large EDP values. In these cases, the displacement demands from NLDAs are unreliable, being known to exceed a particular limiting value. A different procedure can, however, be utilized to estimate the probability of failure. This involves the explicit consideration of collapse cases, dividing the cloud data into two parts: NoC, referring to the records where the structure does not collapse; and C, where it does (Jalayer and Cornell, 2008). The structural fragility for a prescribed limit state can be written using the Total Probability Theorem:

$$\begin{aligned} P\left[EDP > edp_{DS}\middle|IM = im\right] = {} & P\left[EDP > edp_{DS}\middle|IM = im, NoC\right] \cdot \left(1 - P\left[C \mid IM = im\right]\right) + \\ & + P\left[EDP > edp_{DS}\middle|IM = im, C\right] \cdot P\left[C \mid IM = im\right] \end{aligned} \tag{3.4}$$

where $P\left[EDP > edp_{DS}\middle|IM = im, NoC\right]$ is the conditional probability that EDP is greater than the threshold edp_{DS} given that the collapse has not taken place. This probability can be described using a lognormal distribution (Jalayer and Cornell, 2008; Jalayer et al., 2017) as reported in Eq. (3.3), but the conditional median and standard deviation of the logarithm of EDP are evaluated considering the portion of NoC data, i.e. $\eta_{EDP|IM,NoC}$ and $\beta_{EDP|IM,NoC}$.

$P\left[EDP > edp_{DS}\middle|IM = im, C\right]$ is the conditional probability that the EDP is greater than the threshold edp_{DS}, given that the collapse has occurred. This term is thus equal to unity. As reported in the following, $P\left[C \mid IM = im\right]$ is the probability of collapse, which can be evaluated using logistic regression (a.k.a., logit) as a function of IM:

$$P\left[C \mid IM\right] = \frac{1}{1 + e^{-(\alpha_0 + \alpha_1 \cdot ln\, IM)}} \tag{3.5}$$

where α_0 and α_1 are the parameters of the logistic regression.

3.6.1. Choosing the Engineering Demand Parameter (EDP) and defining the limit states

State-of-the-art analytical methods for estimating fragility functions rely on subjecting the structure to NLSAs to collect the building's responses to a suite of accelerograms. The choice of EDP is therefore crucial. The EDP is synthetic measure of the structural response and can be used to determine if a structure has failed to meet a particular performance objective. Commonly used $EDPs$ for structures include drift/deformation quantities, which are generally among the better indicators of damage.

For masonry structures, both the choice of an EDP that represents the global building performance and the relative definitions given to suitable limit states are still open issues (Mouyiannou et al., 2014; Lagomarsino and Cattari, 2015; Kappos and Papanikolaou, 2016). This is because achieving a local limit condition would not be an adequate representation of the overall damage sustained by the building. Indeed, the lack of proper connections between orthogonal walls, and between walls and floors, is quite common in existing masonry buildings and can facilitate the activation of local failure modes. Early local damage modes may prevent the development of a global building response governed by the in-plane behavior of masonry walls and the floor in-plane stiffness. In this case, only the global behavior of the structure is investigated assuming that the upgrade measures, designed by Arup (Arup, 2013) ensured compliance with the standard NPR guidelines. This enables the development of global building response to prevent local failures.

The choice of the EDP and the quantification of the limit states for the fragility curves assessment were based on the Italian Guidelines and Technical Instructions of the Council for National Research, (CNR), specially, CNR-DT 212/2013 (CNR, 2013). These guidelines provide suggestions for the 3D modelling of a structure and the use of non-linear dynamic analyses as the analysis methodology. In this case-study, the limit states were defined using a multiscale approach that considers 1) the exceedance of a predetermined level of drift in a certain number of elements (piers and spandrels); 2) the inter-storey drift in the individual walls or the achievement of predefined levels of deformation in the slabs (if flexible); and 3) the global response evaluated on the capacity curve of the structure. The definitions of *damage* (SLD), *serviceability* (SLS) and *near collapse* (SLC) limit states in the multiscale approach are described in brief below.

As non-linear continuous modeling was adopted to assess the level of drift achieved by each element during the dynamic analyses, the piers and spandrels of each masonry wall are defined a-posteriori according to Parisi and Augenti, (2015).

3.6.1.1. Limit state of damage (SLD)

In the multiscale approach, the variable of the limit state of damage, Y_{SLD}, for masonry buildings is defined as per Eq. (3.6):

$$Y_{SLD} = max\left(Y_{SLD,S}, Y_{SLD,M}, Y_{SLD,G}\right) \tag{3.6}$$

where: $Y_{SLD,S}$ is the limit state variable defined at the level of the structural element, based on the cumulative damage to the piers and spandrels (see Eq. (3.8)); $Y_{SLD,M}$ is the maximum value of the D/C (demand over capacity) ratio in terms of the interstorey drift, meaning that, at the macro-element level, this control can be significant in relation to the damage to non-structural elements; and $Y_{SLD,G}$ is the ratio between the maximum displacement of a control point during the time-history analysis and the displacement corresponding to the attainment of the maximum base shear evaluated on the pushover curve, which is obtained using the same control point.

The limit state variable defined at the level of the structural element, $Y_{SLD,S}$, is defined as:

$$Y_{SLD,S} = \frac{1}{\tau_{SLD}} max\left(\sum\nolimits_{SLD,S}, \sum\nolimits_{SLD,M}.\right). \tag{3.7}$$

τ_{SLD} is a threshold, representing the maximum cumulative damage allowed for the SLD, assumed in this case to be 3.0%. This threshold prevents the SLD from being reached when only one element (pier or spandrel) achieves the maximum drift; and $\sum_{SLD,S}$ and $\sum_{SLD,P}$ represent the cumulative damage caused to the spandrels and piers, respectively. This cumulative damage is evaluated as the percentage of spandrels/piers of the buildings that achieved a certain level of damage, as defined by element drift limits (level 4 for spandrels and level 3 for piers). These are contained in CNR-DT 212/2013 (CNR, 2013), and are also set out in Table 3.5 and Table 3.6 for the piers and spandrels, respectively. For the purposes of the current assessment, consideration was given to the minimum drift-range values and the shear-failure mode for the piers, i.e., corresponding to drift limits of 0.25% and 0.8% for the piers and spandrels, respectively.

Table 3.5 Range of drift for piers at different damage levels and different failure modes CNR-DT 212/2013.

		Drift [%]	
Damage level	3	4	5
Flexural	0.4÷0.8	0.8÷1.2	1.2÷1.8
Shear	0.25÷0.4	0.4÷0.6	0.6÷0.9

Table 3.6 Ranges of drift for spandrels at different damage levels according to CNR-DT 212/2013.

		Drift [%]	
Damage level	3	4	5
	0.4÷0.6	0.8÷1.2	1.8÷2.2

Therefore, $\sum_{SLD,S}$ and $\sum_{SLD,P}$ in Eq.(3.7) are evaluated in Eq. (3.8)as:

$$\begin{aligned}\sum\nolimits_{SLD,S} &= \frac{1}{N_S}\sum\nolimits_S H\left(\frac{D_j}{C_j}-1\right)\\ \sum\nolimits_{SLD,P} &= \frac{\sum\nolimits_P A_j \cdot H\left(\frac{D_j}{C_j}-1\right)}{\sum\limits_P A_j}\end{aligned} \tag{3.8}$$

where: N_S is the number of spandrels in the building; A_j represents the resistant areas of the piers; and H is a dummy variable that returns 0 for $D_j < C_j$ and 1 for $D_j \geq C_j$. Meanwhile, $Y_{SLD,M}$ is defined as in Eq. (3.9):

$$Y_{SLD,M} = \frac{\vartheta_p}{\vartheta_{SLD,M}} = \frac{\vartheta_p}{0.2\%} \tag{3.9}$$

in which ϑ_p is the maximum interstory drift and the threshold, $\vartheta_{SLD,M}$, is assumed to be 0.2 % according to CNR-DT 212/2013.

3.6.1.2. Limit state of serviceability (SLS)

In the serviceability limit state, a variable measuring the spread of damage in a construction is defined, i.e., Y_{SLS}. This is directly related to the possibility that the damage can be repairable. In the case of masonry buildings (unlike for RC constructions), it is not necessary to represent the damage and related repair costs of non-structural elements, as their prevalence is marginal (essentially being almost all structural walls). However, it seems to be appropriate to assign different weights to the damage caused to the vertical piers and horizontal spandrels, since the latter are decidedly less significant and more easily repairable (as they are not fundamental for carrying vertical loads). Furthermore, in relation to the piers, it is also necessary to attribute weights commensurate with the corresponding resistant areas. Therefore, Y_{SLS} is evaluated as follows:

$$Y_{SLS} = \frac{1}{\tau_{SLS}}\begin{cases}\alpha_P \sum_{i=1}^{n_P} w_i c\left(\dfrac{D_i}{C_{i,SLS}}\right) + (1-\alpha_P)\cdot\sum_{j=1}^{n_S} w_j c\left(\dfrac{D_j}{C_{j,SLS}}\right)\\ 1 \quad when\ Y_{SLC} \geq 1\end{cases} \tag{3.10}$$

where τ_{SLS} is a threshold of the conventional global cost of repair operations, assumed in this case to be 0.6. The coefficient α_P expresses the weight of the masonry piers on the total economic value of the structural elements of the building and was assumed equal 0.8. These sums are extended to all the piers n_P

and the spandrels n_S of the structure. The conventional repair-cost function, $c\left(D_i/C_{i,SLS}\right)$, is shown in Figure 3.8.

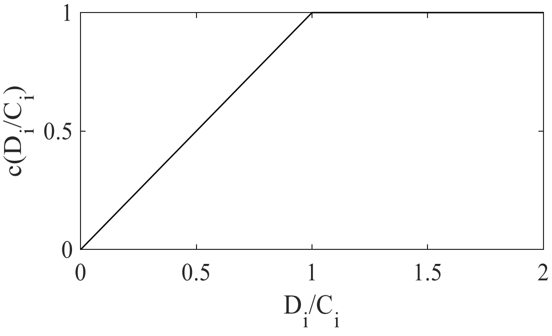

Figure 3.8 Plot of the conventional repair cost function in Eq. (3.10).

Moreover, the weights associated with the repair costs of the piers are evaluated in Eq. (3.10) as $A_i\Big/\sum_k A_k$, where A_i is the resistant area of the i-th pier. The weights, w_j, of the repair costs for the spandrels are equal to $1/n_S$. Finally, the variable Y_{SLC} controls the attainment of the collapse-prevention limit state, which is defined in the next paragraph. This control assumes that SLS can never succeed the SLC, and is required because certain collapse mechanisms, e.g., weak-storey, do not lead to a significant spread of damage in a building and the cost function does not increase beyond a particular value.

The weighted sum appearing in Eq. (3.10), i.e., the numerator of Y_{SLS}, is also known as the conventional global cost of repair.

3.6.1.3. Limit state of near collapse (SLC)

Similar to the SLD, in the near-collapse limit state, the variable Y_{SLC} is defined as:

$$Y_{SLC} = max\left(Y_{SLC,S}, Y_{SLC,M}, Y_{SLC,G}\right) \tag{3.11}$$

in which $Y_{SLC,S} = \dfrac{1}{\tau_{SLC}} \sum_{SLC,P} = \dfrac{1}{3.0\%} \sum_{SLC,P}$. In this case, $\sum_{SLC,P}$ is evaluated as per Eq. (3.8). It is assumed that the maximum capacity of the piers is reached at the damage level 5, corresponding to a drift of 0.6%, as reported in Table 3.5 for the shear-failure mode. The threshold, τ_{SLC}, represents the maximum cumulative damage allowed in the SLC and is assumed to be 3.0%. The limit state variable associated with the macro elements, $Y_{SLC,M}$, is defined as in the SLD, with an assumption made that the limit threshold of the inter-story drift is 0.6%.

Finally, the limit state variable associated with the global response of the building, $Y_{SLC,G}$, is the ratio between the maximum displacement of a control point during the time-history analysis and the displacement corresponding to a percentage degradation equal to 40% of the structure's global base shear (60% of the maximum base shear).

3.6.2. Record selection for the Cloud Analysis

A set of 40 records was selected from the NGA-West2 database to execute the NDLAs. As the real-life structures upon which ours was modeled are subjected to earthquakes due to gas extraction, the record selection was conducted without any special regard being paid to the fault style, but instead only to the avoidance of the effects of impulsive earthquakes and in consideration of soil category B. This is based on the Eurocode 8 classification (CEN, 2004), and is characterized by a shear-waves velocity ranging from 360 m/s and 800 m/s in the top 30 m ($V_{s,30}$).

Other selection criteria related to the execution of the Cloud Analysis procedure were also taken into account (Jalayer et al., 2015, 2017). Reducing errors in any estimation of the regression slope in this type of investigation requires a set of records covering a vast range of intensity values. This was achieved using as reference intensity measure the pseudo-acceleration at the natural vibration period of the first mode of the structure in the X-direction: $T_1 = 0.20s$, i.e., $Sa(T_1)$. The records were selected giving due consideration to increasing values of $Sa(T_1)$, evaluated considering the component H_1 and covering a range of accelerations between 0.008g and 1.33g.

It is also important to ensure that a significant portion of the records, generally more than the 30%, has an EDP close to the value of the adopted limit state. This guarantees that there are enough data points in the region under consideration. Since different limit states were of interest, the final selection criterion was met by choosing records with increasing $Sa(T_1)$ values; with account taken of constant increments of pseudo-acceleration.

Finally, selecting too many records (commonly more than 10%) from the same seismic event should be avoided in order to reduce the potential correlation between the EDP values assessed for different records.

The main characteristics of the records used to execute the NLDAs are set out in Table 3.7. In particular, the following are reported: the RSN identification number; the name and year of the seismic event; the name of the recording station;

the moment magnitude of the event, M_w; the Joyner & Boore distance or R_{JB} (Joyner and Boore, 1981); and the shear-waves velocity in the top 30 m ($V_{s,30}$).

Table 3.7 Characteristics of the selected records.

RSN	Event Name	Year	Station Name	M_w	R_{JB} [km]	$V_{s,30}$ [m/s]
32	"Parkfield"	1966	"San Luis Obispo"	6.19	63.34	493.5
40	"Borrego Mtn"	1968	"San Onofre - So Cal Edison"	6.63	129.11	442.88
41	"Lytle Creek"	1970	"Castaic - Old Ridge Route"	5.33	103.23	450.28
55	"San Fernando"	1971	"Buena Vista - Taft"	6.61	111.37	385.69
76	"San Fernando"	1971	"Maricopa Array #3"	6.61	109.01	441.25
81	"San Fernando"	1971	"Pearblossom Pump"	6.61	35.54	529.09
132	"Friuli_ Italy-02"	1976	"Forgaria Cornino"	5.91	14.65	412.37
230	"Mammoth Lakes-01"	1980	"Convict Creek"	6.06	1.1	382.12
236	"Mammoth Lakes-03"	1980	"Convict Creek"	5.91	2.67	382.12
288	"Irpinia_ Italy-01"	1980	"Brienza"	6.9	22.54	561.04
290	"Irpinia_ Italy-01"	1980	"Mercato San Severino"	6.9	29.79	428.57
304	"Irpinia_ Italy-02"	1980	"Tricarico"	6.2	64.36	496.46
413	"Coalinga-05"	1983	"Skunk Hollow"	5.77	7.27	480.32
434	"Borah Peak_ ID-01"	1983	"ANL-767 Reactor Plant (Bsmt)"	6.88	100.22	445.66
435	"Borah Peak_ ID-01"	1983	"ANL-768 Power Plant (Bsmt)"	6.88	100.22	445.66
481	"Lazio-Abruzzo_ Italy"	1984	"Roccamonfina"	5.8	45.47	475.1
513	"N. Palm Springs"	1986	"Anza Fire Station"	6.06	42.17	360.45
546	"Chalfant Valley-01"	1986	"Lake Crowley - Shehorn Res."	5.77	24.37	456.83
548	"Chalfant Valley-02"	1986	"Benton"	6.19	21.55	370.94
572	"Taiwan SMART1(45)"	1986	"SMART1 E02"	7.3	51.35	671.52
587	"New Zealand-02"	1987	"Matahina Dam"	6.6	16.09	551.3
590	"Whittier Narrows-01"	1987	"Altadena - Eaton Canyon"	5.99	8.72	375.16
592	"Whittier Narrows-01"	1987	"Arcadia - Campus Dr"	5.99	4.53	367.53
753	"Loma Prieta"	1989	"Corralitos"	6.93	0.16	462.24
763	"Loma Prieta"	1989	"Gilroy - Gavilan Coll."	6.93	9.19	729.65
815	"Griva_ Greece"	1990	"Kilkis"	6.1	26.75	454.56
816	"Georgia_ USSR"	1991	"Ambralauri"	6.2	63.53	399.61
819	"Georgia_ USSR"	1991	"Oni"	6.2	42.19	392.67
823	"Roermond_ Netherlands"	1992	"OLF"	5.3	80.67	483.02
824	"Roermond_ Netherlands"	1992	"WBS"	5.3	100.81	525.95
897	"Landers"	1992	"Twentynine Palms"	7.28	41.43	635.01
954	"Northridge-01"	1994	"Big Tujunga_ Angeles Nat F"	6.69	19.1	550.11
1041	"Northridge-01"	1994	"Mt Wilson - CIT Seis Sta"	6.69	35.53	680.37
1125	"Kozani_ Greece-01"	1995	"Kastoria"	6.4	47.79	579.4
1126	"Kozani_ Greece-01"	1995	"Kozani"	6.4	14.13	649.67
1137	"Dinar_ Turkey"	1995	"Burdur"	6.4	35.59	468.44
1612	"Duzce_ Turkey"	1999	"Lamont 1059"	7.14	4.17	551.3
2619	"Chi-Chi_ Taiwan-03"	1999	"TCU067"	6.2	27.66	433.63
4491	"L'Aquila_ Italy"	2009	"Ortucchio"	6.3	35.07	388.01
4893	"Chuetsu-oki_ Japan"	2007	"Toyotsu Nakano"	6.8	61.16	561.59

Figure 3.9; Figure 3.10 and Figure 3.11 show the spectra for each component of the records used to conduct the NLDAs in the LS-DYNA program. The H_1 component of each record was applied in the X-direction of the structure and the components H_2 and V in the Y- and Z-directions, respectively (see Figure 3.5).

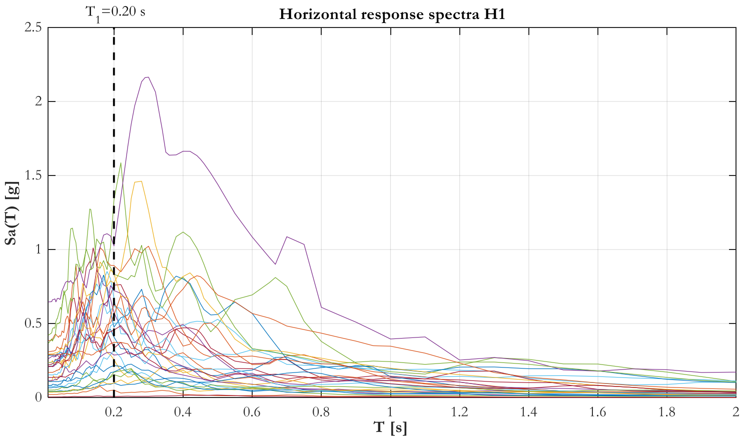

Figure 3.9 Spectra of the ground motions components H_1 applied in the X-direction of the structure.

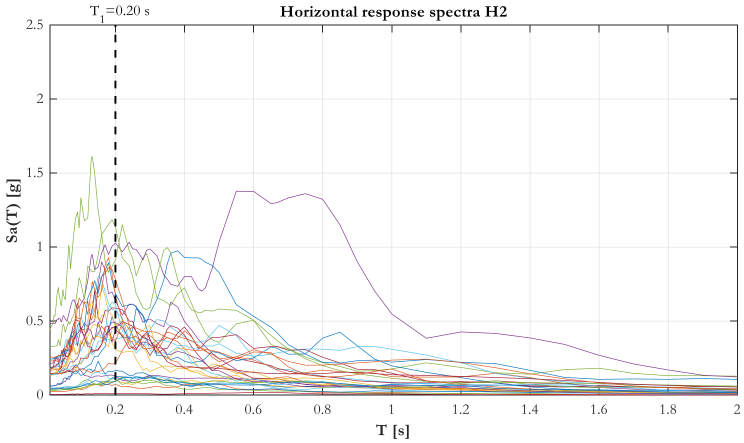

Figure 3.10 Spectra of the ground motions components H_2 applied in the Y-direction of the structure.

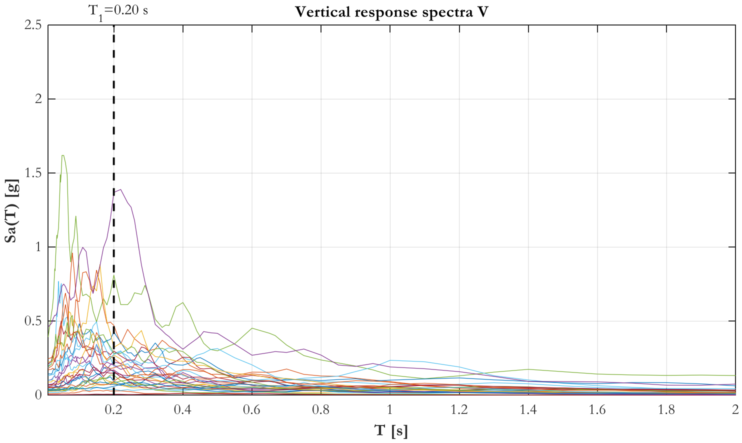

Figure 3.11 Spectra of the ground motions components V applied in the Z-direction of the structure.

3.6.3. Intensity Measure

Intensity measure had to be chosen before conducting the analytical estimation of the fragility curves of the intact structure. Three *IMs* were investigated: 1) the first-mode spectral acceleration, $Sa(T_1)$, evaluated on the component H_1 applied in the X-direction of the structure during the execution of the NLDAs; 2) $Sa(T_1)_{GM}$, which is the geometric mean of the spectral accelerations $Sa(T_1)$ evaluated using the components H_1 and H_2 applied in the X- and Y-directions of the structure, respectively , when performing the NLDAs; 3) the average spectral acceleration, $Sa_{avg}(T_1, T_2, \ldots, T_{20})$ (Baker and Cornell, 2006), evaluated using H_1 and with consideration given to 20 equally spaced periods in a range between 0.01s and 0.20 s.

The process of selecting the intensity measure for the execution of Cloud Analysis and the assessment of fragility curves of the structures was based on the concepts of sufficiency and efficiency, which have strict ties to the accuracy of structural-performance assessment (Luco 2002; Luco and Cornell 2007; Padgett et al. 2007). In fact, a *sufficient* IM renders the structural response conditionally independent, given the selected intensity measure, of the other earthquake characteristics involved in the seismic-hazard assessment at the construction site (i.e., magnitude and source-to-site distance). Meanwhile, an *efficient* IM leads to relatively little variability in the structural response given the IM. In the context of the Cloud Analysis, the efficiency of an IM can be measured by the standard error of the regression analysis, $\beta_{EDP|IM}$. Consequently, the most efficient IM produces the lowest $\beta_{EDP|IM}$ value.

On the other hand, establishing the IM's sufficiency requires an investigation of the effectiveness of the ground motion (GM) characteristics as further regression variables (in addition to IM). In other words, as regression variables, the GM features result in very little improvement to the regression prediction if the IM is sufficient. Any enhancement can be judged by the reduction in the dispersion of the regression residuals and/or the statistical significance of the regression coefficients corresponding to the GM characteristics (Jalayer, 2003).

In this study, the sufficiency was evaluated using a simplified statistical approach based on linear regression to measure the effectiveness of the GM characteristics as additional regression variables. This method requires a regression of the dependent variable, EDP, versus the independent variable, IM. Subsequently, plotting the residuals of the regression versus the GM characteristics enables a second linear regression to be performed. By highlighting any significant data trends, this approach facilitates the investigation of the potential dependence of EDP on the other GM characteristics. The significance of the trend can be measured by testing the hypothesis that the slope of the second linear regression is zero. This can be evaluated using the p-value, with a hypothesis rejected if this is lower than a set value (e.g., 0.05; 0.01) and IM is insufficient.

Next, the dependence of the structural response conditional on the three IMs was tested with respect to the moment magnitude (M_w), Joyner & Boore distance (R_{JB}), and the 5–95% significant duration ($D_{5-95\%}$). The standard residuals from the first linear regression were plotted against the moment magnitudes, the logarithm of distances and the logarithm of the 5–95% significant durations. A standard linear regression was then carried out. The statistical significance of the regression estimate was quantified using a p-value, and a value lower than 0.05 for any of the three parameters is considered to be a demonstration of the statistical significance between the residuals and that parameter.

It is common to check the dependence of an IM with respect to magnitude and distance (Luco and Cornell, 2007). In this study, however, the dependence on a measure of the ground shaking duration was also considered. The decision to do so was based on the evidence from previous research that the response of URM buildings (and other strength- and stiffness-degrading structures) is dependent on the length of any strong ground-shaking (Bommer et al., 2004). The interval related to 5–95% of the total Arias Intensity (Arias, 1970) of the record (the so-called 5–95% significant duration $D_{5-95\%}$) was selected as the preferred duration parameter.

3.6.4. Results of the Cloud Analysis

This section describes the assessment of the fragility curves, performed using the Cloud Analysis approach. The NLDAs were conducted by applying the three components of each record (H_1, H_2 and V) in the three directions of the structure, X, Y and Z (shown in Figure 3.2), respectively and recording the structural response.

The fragility curves were evaluated for the three damage states SLD, SLS and SLC, with single fragilities defined for the entire structure. It was assumed that the structural response was the maximum value of the damage state variables in the X- and the Y-directions for each record. It is worth recalling that the definition of the limit states (described in the previous paragraphs) exclusively considers the in-plane structural response and assumes the shear-failure mode for the piers. Each damage state is considered to have been achieved when the variables Y_{SLD}, Y_{SLS} and Y_{SLC} have a value equal to 1.0.

Table 3.8 reports the data for each record used to evaluate the fragility curves, i.e., the values for each record of the damage state variables Y_{SLD}, Y_{SLS} and Y_{SLC} as well as three IMs, $Sa(T_1)$; $Sa(T_1)_{GM}$ and Sa_{avg}. Moreover, , as described above, the magnitude, M_w, the Joyner & Boore distance, R_{JB} and the significant duration of the ground motions, $D_{5-95\%}$, were used to check the sufficiency of the IM.

Table 3.8 Data for assessing the fragility function and checking the sufficiency of the intensity measure.

RSN	$Sa(T_1)$ [g]	$Sa(T_1)_{GM}$ [g]	Sa_{avg} [g]	Y_{SLD} [−]	Y_{SLS} [−]	Y_{SLC} [−]	M_w [−]	R_{JB} [km]	$D_{5-95\%}$ [s]
32	0.035	0.036	0.021	0.339	0.058	0.075	6.19	63.34	17.84
40	0.097	0.111	0.059	5.898	0.120	0.547	6.63	129.11	28.00
41	0.050	0.061	0.036	0.809	0.104	0.034	5.33	103.23	9.18
55	0.028	0.034	0.018	3.549	0.062	0.586	6.61	111.37	20.435
76	0.022	0.021	0.014	7.366	0.057	0.571	6.61	109.01	22.85
81	0.256	0.281	0.248	3.514	1.667	1.190	6.61	35.54	13.73
132	0.574	0.605	0.486	5.864	0.832	0.601	5.91	14.65	4.495
230	1.334	1.102	0.832	23.403	1.094	15.476	6.06	1.10	9.185
236	0.616	0.593	0.408	12.468	1.667	2.381	5.91	2.67	6.30
288	0.760	0.668	0.518	8.507	0.711	0.970	6.9	22.54	10.3124
290	0.409	0.442	0.170	4.839	0.419	0.527	6.9	29.79	26.7061

Table 3.8 (*Continued*) Data for assessing the fragility function and checking the sufficiency of the intensity measure.

RSN	$Sa(T_1)$ $[g]$	$Sa(T_1)_{GM}$ $[g]$	Sa_{avg} $[g]$	Y_{SLD} $[-]$	Y_{SLS} $[-]$	Y_{SLC} $[-]$	M_w $[-]$	R_{JB} $[km]$	$D_{5-95\%}$ $[s]$
304	0.038	0.045	0.034	8.904	0.067	0.298	6.2	64.36	18.9341
413	0.892	0.837	0.604	14.558	1.667	2.381	5.77	7.27	5.265
434	0.091	0.082	0.049	0.566	0.087	0.088	6.88	100.22	15.88
435	0.081	0.098	0.069	0.853	0.101	0.184	6.88	100.22	15.56
481	0.098	0.098	0.058	2.211	0.123	0.230	5.8	45.47	12.5562
513	0.287	0.192	0.200	2.224	0.265	0.146	6.06	42.17	5.845
546	0.172	0.136	0.096	2.807	0.139	0.278	5.77	24.37	14.595
548	0.672	0.505	0.461	9.094	1.667	1.272	6.19	21.55	16.645
572	0.334	0.384	0.238	20.987	1.667	2.493	7.3	51.35	12.42
587	0.476	0.572	0.454	27.768	1.667	7.143	6.6	16.09	6.4
590	0.635	0.481	0.485	6.068	1.667	2.381	5.99	8.72	4.49
592	0.774	0.599	0.535	17.246	1.667	5.952	5.99	4.53	3.08
753	1.024	1.026	0.953	27.768	1.667	15.476	6.93	0.16	6.86
763	0.832	0.973	0.738	23.080	1.667	8.333	6.93	9.19	5
815	0.090	0.115	0.082	1.294	0.095	0.190	6.1	26.75	11.03
816	0.034	0.034	0.023	1.190	0.059	0.209	6.2	63.53	16.263
819	0.322	0.193	0.132	1.419	0.348	0.210	6.2	42.19	11.4036
823	0.008	0.009	0.007	0.310	0.0426	0.1034	5.3	80.67	9.8532
824	0.011	0.012	0.009	0.123	0.053	0.022	5.3	100.81	13.9216
897	0.217	0.190	0.149	14.433	0.181	0.898	7.28	41.43	30.7
954	0.557	0.611	0.342	5.537	0.691	0.513	6.69	19.1	10.72
1041	0.839	0.628	0.391	2.605	0.685	0.511	6.69	35.53	8.84
1125	0.043	0.037	0.028	0.836	0.067	0.104	6.4	47.79	15.765
1126	0.723	0.595	0.389	3.178	0.607	0.650	6.4	14.13	6.45
1137	0.155	0.120	0.068	4.182	0.214	0.468	6.4	35.59	16.37
1612	0.502	0.554	0.280	26.579	1.667	3.570	7.14	4.17	14.09
2619	0.456	0.454	0.325	16.321	1.667	2.735	6.2	27.66	6.585
4491	0.173	0.127	0.086	3.296	0.185	0.658	6.3	35.07	9.775
4893	0.373	0.282	0.308	17.246	1.667	8.333	6.8	61.16	8.91

Table 3.9 and Table 3.10 show the results of the Cloud Analysis and the sufficiency check for the SLD and SLC, respectively. In detail, the following are reported: the coefficients a and b, estimated from the linear regression in Eq. (3.1); the

conditional logarithmic standard deviation of EDP given IM, βEDP|IM (see Eq.(3.2)); the $p-value$; and the slopes, α, of the linear regressions obtained for the sufficiency check of the three alternative IMs against the magnitude, M_w, the distance, R_{JB}, and the significant duration of ground motions, $D_{5-95\%}$.

Table 3.9 Results of the Cloud Analysis and the sufficiency check performed for the damage limit state (SLD).

IM	a	b	$\beta_{EDP\|IM}$	$p-value$ (M_w)	$p-value$ (R_{JB})	$p-value$ $(D_{5-95\%})$	α_{M_w}	$\alpha_{R_{JB}}$	$\alpha_{D_{5-95\%}}$
$Sa(T_1)$	2.60	0.73	0.94	0.04	0.59	0.32	0.65	-0.08	0.30
$Sa(T_1)_{GM}$	2.74	0.79	0.91	0.06	0.71	0.27	0.59	-0.06	0.34
Sa_{avg}	3.09	0.84	0.88	0.05	0.81	0.14	0.62	-0.04	0.45

Table 3.10 Results of the Cloud Analysis and the sufficiency check performed for the near collapse limit state (SLC).

IM	a	b	$\beta_{EDP\|IM}$	$p-value$ (M_w)	$p-value$ (R_{JB})	$p-value$ $(D_{5-95\%})$	α_{M_w}	$\alpha_{R_{JB}}$	$\alpha_{D_{5-95\%}}$
$Sa(T_1)$	1.05	0.90	1.06	0.12	0.08	0.87	0.50	-0.21	-0.05
$Sa(T_1)_{GM}$	1.20	0.96	1.03	0.17	0.11	0.91	0.44	-0.19	-0.04
Sa_{avg}	1.66	1.04	0.96	0.16	0.20	0.70	0.45	-0.15	0.12

In relation to the assessment of the fragility curve for the SLS, the definition of the damage state variable Y_{SLS} in Eq. (3.10) required verification that the SLS would never succeed the SLC. Therefore, if the first term in Eq. (3.10) is greater than 1.0; Y_{SLS} assumes a limit value $Y_{SLS} = 1/0.6 = 1.67$. To account for these extreme cases, the approach in Jalayer and Cornell (2008) and governed by the Eq. (3.4), was adopted. Table 3.11 sets out the results of Cloud Analysis for the SLS for the NoC data (the cases where the structure does not experience the collapse, i.e., $Y_{SLS} < 1.67$). In detail, the following are reported: the coefficients a and b, estimated from the linear regression in Eq. (3.1); the conditional logarithmic standard deviation of EDP given IM, βEDP|IM (see Eq.(3.2)); the $p-value$; and the slopes, α, of the linear regressions performed for the IM sufficiency checks against the magnitude, M_w, the distance, R_{JB}, and the significant duration of the ground motions, $D_{5-95\%}$.

Table 3.11 Results of the Cloud Analysis and the sufficiency check performed for the serviceability limit state (SLS).

IM	a	b	$\beta_{EDP\|IM}$	$p-value$ (M_w)	$p-value$ (R_{JB})	$p-value$ $(D_{5-95\%})$	α_{M_w}	$\alpha_{R_{JB}}$	$\alpha_{D_{5-95\%}}$
$Sa(T_1)$	-0.32	0.70	0.27	0.60	0.35	0.49	-0.23	-0.16	-0.24
$Sa(T_1)_{GM}$	-0.18	0.75	0.28	0.99	0.47	0.58	0.00	-0.12	-0.19
Sa_{avg}	0.21	0.81	0.30	0.44	0.44	0.62	-0.34	-0.13	-0.17

The results summarized in Table 3.9, Table 3.10 and Table 3.11 reveal that the most efficient of the sufficient intensity measures for SLD and SLC is the average spectral acceleration, Sa_{avg}; for the SLS, it is the first-mode spectral-acceleration, $Sa(T_1)$. However, the Sa_{avg} IM was chosen to represent all three damage states, because it was also found to be sufficient for the SLS.

Figure 3.12 shows the linear regressions that take into account the IM selected for the three damage states.

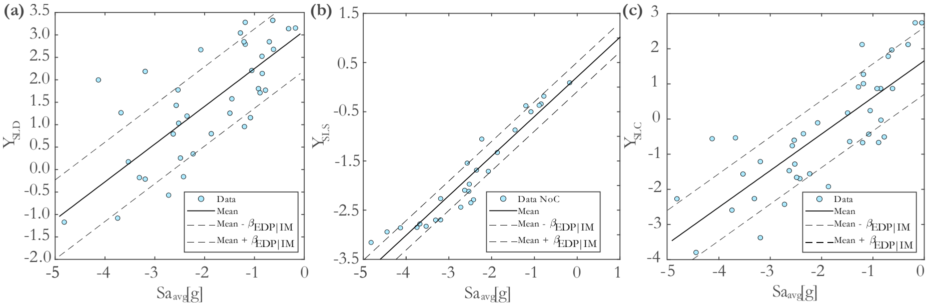

Figure 3.12 Linear regressions of the cloud data for SLD (a); SLS (b) and SLC (c).

Figure 3.13 contains an example of the sufficiency check conducted for the intensity measure, Sa_{avg}, and the SLC. The figure shows the scatter plots of the regressions residuals versus the moment magnitude, (M_w), the Joyner & Boore distance, (R_{JB}), and the 5–95% significant duration, ($D_{5-95\%}$). The p-values are also reported.

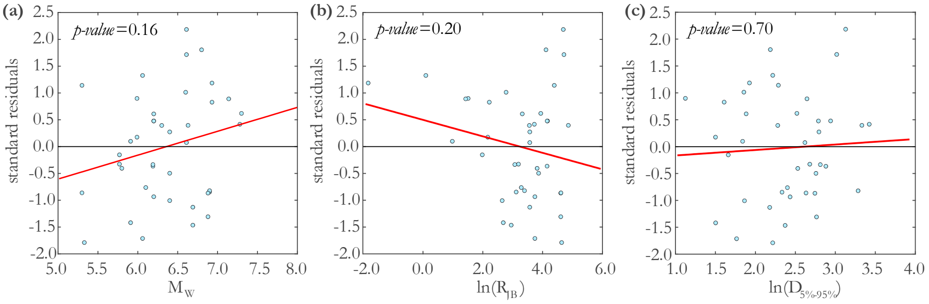

Figure 3.13 Sufficiency check for the case of SLC and the intensity measure Sa_{avg} in relation to the moment magnitude, M_w (a), the Joyner & Boore distance, R_{JB} (b), and of the 5–95% significant duration, $D_{5-95\%}$ (c).

Finally, the fragility curves of the structure were evaluated according to Eq. (3.3) for the SLD and SLC, with the results shown in Figure 3.14a. The medians, $\eta_{EDP|IM}$, and the standard deviations, $\beta_{EDP|IM}$, which define the fragility curve for the SLD and SLC, are reported in Table 3.12.

Table 3.12 Medians and standard deviations defining the fragility curve for the damage states SLD and SLC.

Damage state	Median $\eta_{EDP\|IM}$ [g]	Standard deviation $\beta_{EDP\|IM}$ [g]
SLD	0.025	1.051
SLC	0.204	0.920

The fragility curve for the SLS was evaluated according to Eq. (3.4). Figure 3.14b shows this curve, $P\left[Y_{SLS} \geq 1 \middle| IM = im\right]$, and all the components contributing to its assessment, namely: the probability of collapse, $P[C \mid IM = im]$, evaluated using the logistic regression; and the conditional probability that Y_{SLS} is greater than 1.0 given that the collapse has not taken place, $P\left[Y_{SLS} \geq 1 \middle| IM = im, Noc\right]$, assessed via a linear regression of the Noc cloud data.

It should be noted that the probability of collapse, $P[C \mid IM = im]$, in Figure 3.14b does not coincide with the fragility curves, $P\left[Y_{SLC} \geq 1 \middle| IM = im\right]$, in Figure 3.14a. This is because they were evaluated by taking into account different $EDPs$ and using different distribution models, i.e., the logit in the first case and the lognormal in the second one.

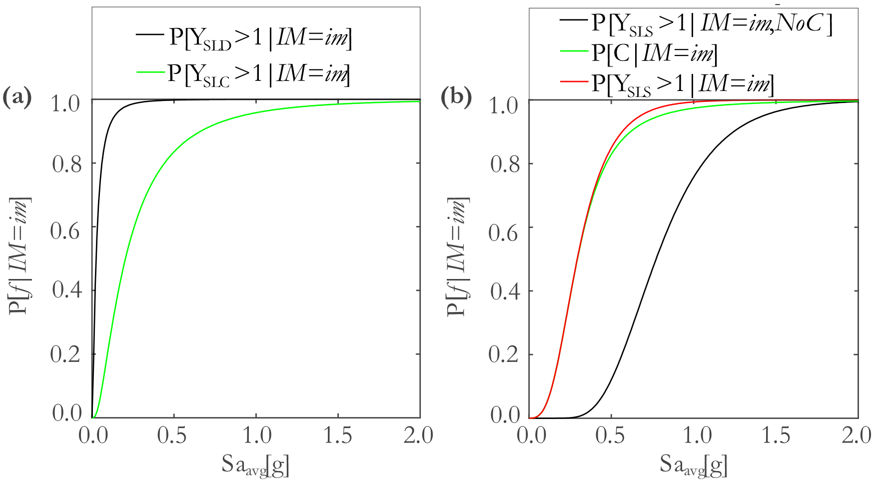

Figure 3.14 Fragility curves of the case-study structure for the SLD and SLC (a), and the fragility curve evaluated for the SLS and its components, according to Eq. (3.4) (b).

3.7. Assessment of state-dependent seismic fragility curves

If seismic-reliability calculations are expected to account for multiple earthquakes and damage accumulation, it becomes important to evaluate the probability that an already-damaged structure will make the transition from one damage state, DS_i, to another that is more severe, DS_j. This probability is defined by the state-dependent fragility function $P\left[EDP > edp_{DS_j} \middle| DS_i \cap IM = im\right]$ and represents the probability that the structure will achieve DS_j conditional on the occurrence of a shaking intensity im, and that the structure has already been found in DS_i. Here, the state-dependent fragility functions are simply written as $P\left[DS_j \middle| DS_i \cap IM = im\right]$.

The evaluation of the state-dependent fragility curves was conducted using the procedure referred to as back-to-back IDA (Luco et al., 2004; Ryu et al., 2011; Goda, 2012; Ruiz-García, 2012; Raghunandan et al., 2015; Goda, 2015). This requires a structure to be subjected to numerous NLDAs. The main disadvantage of the procedure is its high computational cost, particularly for the 3D structures. Therefore, in order to reduce the analysis time, a simplified procedure for analytical fragility estimation is used, that is based on non-linear static analysis. This requires the definition of a surrogate structure in the form of an inelastic equivalent single-degree-of-freedom (ESDoF) system, whose definition is based on the pushover curve of the original model. Two systems were defined and calibrated to reproduce the static and cyclic behavior of the 3D model in the two main directions (see Figure 3.7). The systems were analyzed using back-to-back IDA to assess the state-dependent fragility curves. Meanwhile, the fragility curves of the intact structure were evaluated via IDA to ensure a consistent comparison was possible (IDA, Vamvatsikos and Cornell, 2001, 2004).

The structure-specific and state-dependent fragility curves were obtained by applying the IM-based approach (Vamvatsikos and Cornell, 2001) to the IDA curves and the back-to-back IDA curves, respectively. So, for the former, the IM-based method entailed identifying the intersections of the IDA curves, im_{DSi}, with the vertical line passing through the EDP threshold that defines the attainment of the damage state. These im_{DSi} values can be viewed as realizations of a random variable (RV), IM_{DS_i}, which is the seismic intensity to which the ground motion needs to be scaled for the structure to achieve DS_i. The fragility function can then be defined as the probability that IM_{DS_i} is equal or lower than the level of seismic intensity possibly occurring at the site, i.e., $P\left[DS_i \mid IM = im\right] = P\left[IM_{DS_i} \le im\right]$. Assuming that IM_{DS_i} follows a lognormal distribution, the fragility function can be estimated according to Eq. (3.12):

$$\begin{cases} P\left[DS_i \mid IM = im\right] = P\left[IM_{DS_i} \le im\right] = \Phi\left[\left(\ln(im) - \eta\right)/\beta\right] \\ \eta = \dfrac{1}{n} \cdot \sum_{j=1}^{n} \ln\left(im_{DSi,j}\right) \\ \beta = \sqrt{\dfrac{1}{n-1} \cdot \sum_{j=1}^{n} \left[\ln\left(im_{DSi,j}\right) - \eta\right]^2} \end{cases} \tag{3.12}$$

where η and β are the parameter estimates (median and logarithmic standard deviation) of the assumed lognormal distribution of IM_{DS_i}; im_{DSi} is the realization of the RV coming from to the *j*-th record; and $\Phi(\cdot)$ is the standard Gaussian (cumulative) function.

3.7.1. Calibration of the equivalent SDoF oscillators

The conversion to the ESDoF models involved defining the characteristics of the SDoF oscillators (e.g., the equivalent mass, m^*, and the vibration period, T^*) and backbones parameters. Also characterized was the hysteretic behavior in the structure's two horizontal directions.

Two SDoFs, each representative of a direction of the structure, were calibrated based on the structural response shown in Figure 3.7. The backbone curves of the two ESDoF oscillators were obtained from the pushover curves of the original 3D structure scaled down by the corresponding modal participation factors Γ (Fajfar, 2000; $\Gamma = 1.00$ for the pushover curves obtained using a uniform force distribution and $\Gamma = 1.23$ in case of the triangular force distribution) and defining a multi-linear approximation of the resulting curves, as reported in Figure 3.15 for the latter distribution type. As the application of the triangular force distribution produced the lowest force and displacement values in both the X and Y-directions (F^*, δ^* coordinates), its resulting pushover curves were used to define the capacity curves of the two SDoF systems.

The mass, m^*, the period, T^*, and the force and displacement values at the points defining the linearized backbone curves of the ESDoFs are reported in Table 3.13 and Table 3.14 for the X and Y-directions, respectively. It can be seen that the structure had an asymmetric static response in both directions; therefore, the positive and negative directions of the load are specified using signs plus and minus in the subscript, respectively (e.g., $F_{i,X^+}{}^*$ and $F_{i,X-}{}^*$).

Table 3.13 Characteristics of the equivalent SDOF system representing the X direction of the structure.

	Direction X					
	$F_{X^+}{}^*$ [kN]	$\delta_{X^+}{}^*$ [m]	$F_{X^-}{}^*$ [kN]	$\delta_{X^-}{}^*$ [m]	m^* [kg]	T^* [s]
1	206.76	0.0029	-240.06	-0.0026	118713	0.239
2	142.05	0.0088	-133.570	-0.017		
3	96.09	0.0293	-81.681	-0.047		
4	26.84	0.1200	-31.341	-0.127		

Table 3.14 Characteristics of the equivalent SDOF system representing the Y direction of the structure.

	Direction Y					
	$F_{Y^+}{}^*$ [kN]	$\delta_{Y^+}{}^*$ [m]	$F_{Y^-}{}^*$ [kN]	$\delta_{Y^-}{}^*$ [m]	m^* [kg]	T^* [s]
1	603.39	0.0021	-626.49	-0.0021	118713	0.126
2	492.04	0.0051	-517.21	-0.007		
3	404.27	0.0321	-418.31	-0.033		
4	405.75	0.1410	-423.42	-0.114		

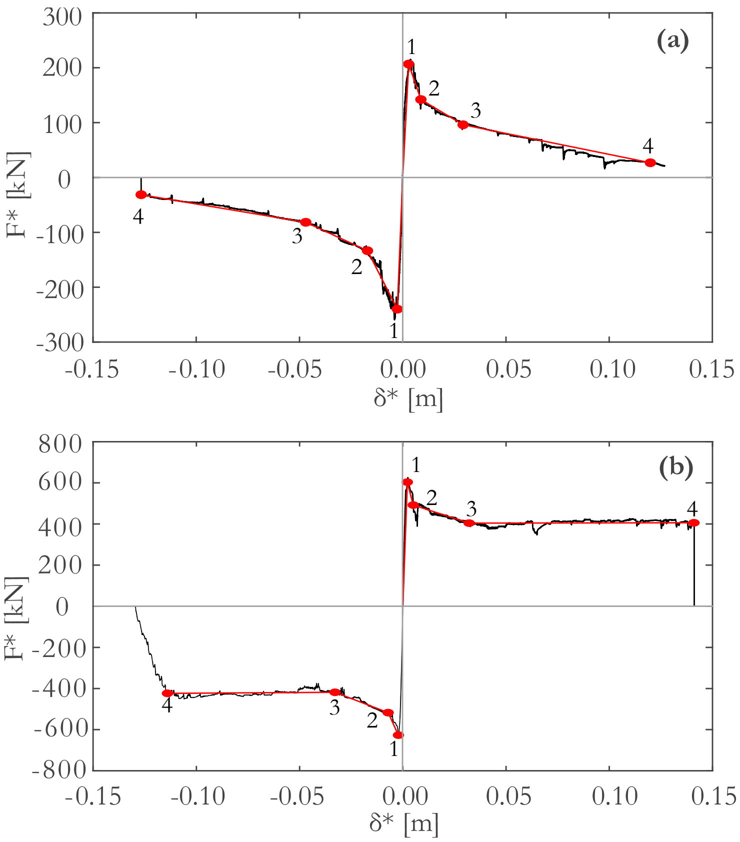

Figure 3.15 Definition of the backbone curves of the two SDoF systems representing the behavior of the entire structure in the X (a) and Y (b) direction.

In addition to the backbone curves, the hysteretic behavior assigned to each ESDoF system to execute the NLDAs was also calibrated based on the results of the cyclic pushovers shown in Figure 3.7. The two ESDoF systems were analyzed using the OpenSees platform (*Open System for Earthquake Engineering Simulation,* McKenna, 2011), meaning that each hysteresis was defined using a selection of the hysteresis rules available in the OpenSees material library. To reproduce the hysteretic behavior shown in the X-direction (Figure 3.7c), a hysteresis was defined as a combination of the flag-shaped hysteretic rule (Christopoulos et al., 2008) and a pinched load-deformation response with strength and stiffness degradation under cyclic loading (i.e., pinching4 Material in the OpenSees library). On the other hand, only the pinching4 Material was used for the Y-direction and calibrated to reproduce the behavior shown in Figure 3.7d.

Figure 3.16 reports the comparison between the hysteretic behavior of the 3D model (panels (a) and (c)) and the responses of the two ESDoF systems to the loading protocol shown in Figure 3.6 (panels (b) and (d)).

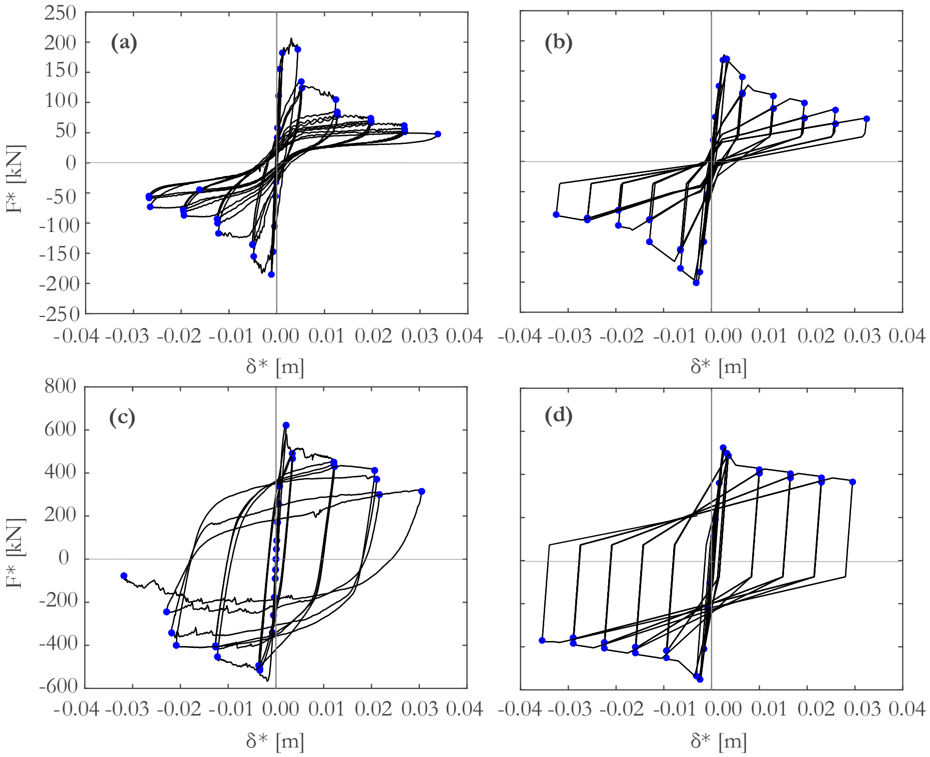

Figure 3.16 Comparison of the hysteretic behavior obtained by analyzing the three-dimensional structure (a) and the hysteretic law defined using the OpenSees platform (b) for the X- direction. Comparison of the hysteretic behavior obtained by analyzing the three-dimensional structure (c) and the hysteretic law defined using the OpenSees platform (d) for the Y- direction.

3.7.2. Fragility assessment

The assessment of the fragility curves of the intact structure and of the state-dependent fragility curves were conducted via IDA and back-to-back IDA, respectively. The same set of 30 records selected from the NESS dataset (Pacor et al., 2018) was used for both the IDA and the first and the second phases of the back-to-back IDA. All these analyses (IDA and back-to-back IDA) were performed using the OpenSees platform (Open System for Earthquake Engineering Simulation; McKenna, 2011) via a recent version of the DYANAS software (Baltzopoulos et al. 2018).

The fragility curves were assessed taking into account four damage states, from DS_1 to DS_4, defined in accordance with the study of Graziotti et al. (2017). In generally very good agreement with the literature (Lagomarsino and Cattari, 2015), this detects the global drifts corresponding to the different performance levels identified on the basis of a shaking-table test of a full-scale, representative specimen of a Dutch two-story terraced house in the Netherlands. Damage state

DS_1 was defined as the maximum level of displacement that can be achieved without causing any visible damage; DS_2 refers to the maximum displacement level achieved that causes only minor/slight structural damage, i.e., it could be easily repaired for a possible immediate occupancy; DS_3 relates to moderate structural damage (observed in all the piers of the structure) that could be viewed as a life-safety limit state; and DS_4 references a collapse prevention damage state. The values of maximum displacement, δ^*_i, that represent the attainment of the *i*-th damage state in the case-study structure and for all the performance levels considered are reported in Table 3.15.

Table 3.15 Values of maximum displacement representing the attainment of the four damage states.

δ^*_1 $[m]$	δ^*_2 $[m]$	δ^*_3 $[m]$	δ^*_4 $[m]$
0.0031	0.0047	0.015	0.047

The assessment of the fragility curves and the state-dependent fragility curves were conducted for the entire structure considering, for each record and the *i*-th damage state, the minimum value of im_{DSi} producing the achievement of the considered damage state in one of the two directions of the structure. The resulting medians, η, and standard deviations, β, defining the parametric fragility curves (see Eq.(3.12)) for the four damage states are reported in Table 3.16. The *IM* used for the assessments was the average spectral acceleration $Sa_{avg}(T_1, T_2, \ldots, T_{20})$, which was evaluated taking into account 20 equally spaced periods in a range between 0.01s and 0.2s.

The fragility curves of the intact structure are shown in panel (a) of Figure 3.17.

Table 3.16 Median, η, and logarithmic standard deviation, β, defining the structure's fragility curves (IM in g).

MEDIAN η				SIGMA β			
DS_1	DS_2	DS_3	DS_4	DS_1	DS_2	DS_3	DS_4
0.14	0.18	0.29	0.51	0.38	0.34	0.46	0.69

The state-dependent fragility curves were estimated by means of the back-to-back IDA, using a set of 30 records to represent the first damaging shock of the cluster, scaled to produce maximum displacements of 0.0031 m, 0.0047 m and 0.015 m corresponding to the attainment of DS_1, DS_2 and DS_3, respectively.

Thereafter, the same 30 subsequent-shock accelerograms per the initial shock were applied for a total of nine-hundred curves.

Table 3.17 contains the values for the median, η, and logarithmic standard deviation, β, defining the lognormal distribution obtained with Eq. (3.12), i.e., the structure's parametric state-dependent fragility curves. The first column in the table sets out the initial damage state, while the the rest of the rows represent the final damage states.

Panels (b), (c) and (d) in Figure 3.17 show the structure's state-dependent fragility curves, evaluated with the results of the Back-to-Back IDA and assuming a lognormal distribution. Each of the three panels in Figure 3.17 shows the curves obtained when considering all the possible transitions between damage states (from a damage state i to a damage state j) assuming the i-th initial damage state. Panel (b) shows curves obtained when DS_1 is taken to be the initial damage state, while panel (c) and (d) do so for the cases where DS_2 and DS_3, respectively, represent the initial damage. The fragility functions in each panel, which were assessed by assuming that the structure was initially in an intact condition, are also reported as reference to show the increases in fragility caused by the first shock.

Table 3.17 Median, η, and logarithmic standard deviation, β, defining the state-dependent fragility curves of the two SDoF systems (IM in g).

	MEDIAN η			SIGMA β		
	$DS2$	$DS3$	$DS4$	$DS2$	$DS3$	$DS4$
$DS1$	0.06	0.21	0.46	1.20	1.23	0.80
$DS2$	-	0.20	0.45	-	1.23	0.78
$DS3$	-	-	0.44	-	-	0.79

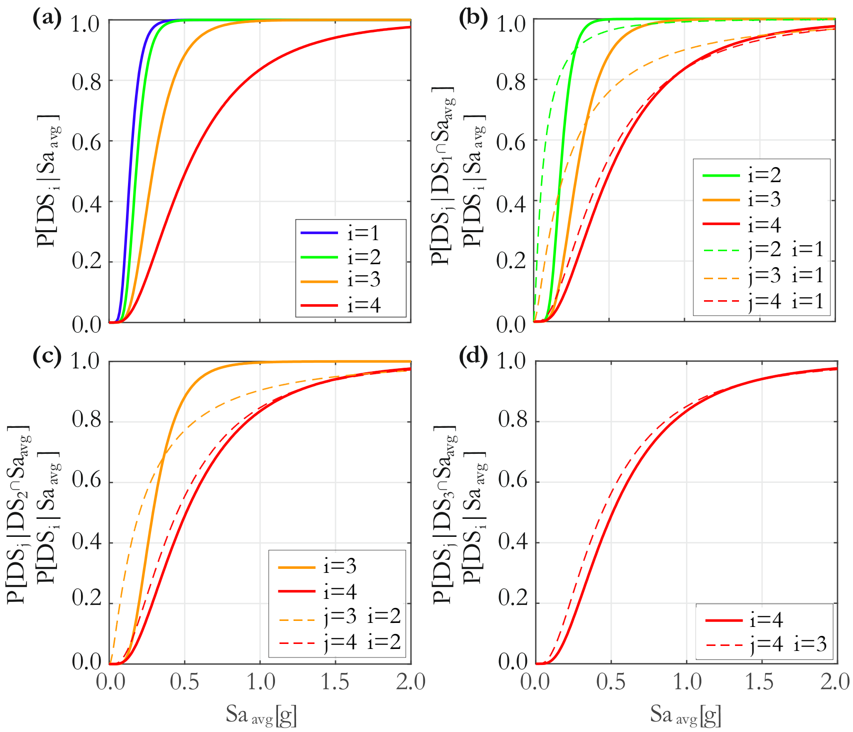

Figure 3.17 Structure-specific and state-dependent fragility curves of the case-study structure. Fragility curves of the intact structure (a); state-dependent fragility curves evaluated by treating DS_1 as the initial damage state (b); state-dependent fragility curves evaluated by treating DS_2 as the initial damage state (c); state-dependent fragility curves evaluated by treating DS_3 as the initial damage state (d).

3.8. Conclusions

Central to the discussion in this chapter has been the assessment of the fragility and state-dependent fragility curves of the case-study's model 3D structure, which is representative of the URM terraced houses in the Groningen region of the Netherlands. This type of building has been the subject of extensive research because of the seismicity induced by commercial gas extraction in the area.

In a first step, the structure-specific fragilities were evaluated by analyzing a 3D finite element model developed in collaboration with Arup Italy using the LS-DYNA software. The assessment was conducted using the Cloud Analysis, taking into account three damage states defined according to the Italian Guidelines and Technical Instructions of the National Research Council (CNR-DT 212/2013).

Subsequently, to limit the computational costs of assessing the state-dependent fragility curves, two SDoF systems representing the structural behavior in the model's two main directions were calibrated and analyzed using the back-to-back Incremental Dynamic Analysis. This assessment took into account four damage states available in the previous literature, which are defined based on the outcomes of a shaking-table test of a full-scale specimen of the type of structure modeled in this case study.

References

Arias, A. (1970), A measure of earthquake intensity, *Seism. Des. Nucl. Power Plants. Cambridge, Mass. Massachusetts Inst. Tech. Press*, 438–483.

Arup (2013), "Structural upgrading study, Groningen 2013."

Baker, J.W., and C.A. Cornell (2006), Which spectral acceleration are you using?, *Earthq. Spectra*, 22(2), 293–312.

Baltzopoulos, G., R. Baraschino, I. Iervolino, and D. Vamvatsikos (2018), Dynamic analysis of single-degree-of-freedom systems (DYANAS): a graphical user interface for OpenSees, *Eng. Struct.*, 177, 395–408.

Bommer, J.J., G. Magenes, J. Hancock, and P. Penazzo (2004), The influence of strong-motion duration on the seismic response of masonry structures, *Bull. Earthq. Eng.*, 2(1), 1–26.

CEN (2004), *EN 1998-1: Eurocode 8 - Design of structures for earthquake resistance. Part 1: General rules, seismic actions and rules for buildings*, European Committee for Standardization.

Christopoulos, C., R. Tremblay, H.-J. Kim, and M. Lacerte (2008), Self-Centering Energy Dissipative Bracing System for the Seismic Resistance of Structures: Development and Validation, *J. Struct. Eng.*, 134(1), 96–107.

CNR (2013), *Istruzioni per la Valutazione Affidabilistica della Sicurezza Sismica di Edifici Esistenti.*

Fajfar, P. (2000), A nonlinear analysis method for performance based seismic design., *Earthq. Spectra*, 16(3), 573–592.

Goda, K. (2012), Nonlinear response potential of Mainshock-Aftershock sequences from Japanese earthquakes, *Bull. Seismol. Soc. Am.*, 102(5), 2139–2156.

—— (2015), Record selection for aftershock incremental dynamic analysis, *Earthq. Eng. Struct. Dyn.*, 44, 1157–1162.

Graziotti, F., U. Tomassetti, S. Kallioras, A. Penna, and G. Magenes (2017), Shaking table test on a full scale URM cavity wall building, *Bull. Earthq. Eng.*, 15(12), 5329–5364.

Jalayer, F. (2003), Direct Probabilistic Seismic Analysis : Implementing Non-Linear Dynamic Assessments, Stanford University.

Jalayer, F., and C.A. Cornell (2008), Alternative non-linear demand estimation methods for probability-based seismic assessments, *Earthq. Eng. Struct. Dyn.*, 13(6), 1834–1849.

Jalayer, F., R. De Risi, and G. Manfredi (2015), Bayesian Cloud Analysis: Efficient structural fragility assessment using linear regression, *Bull. Earthq. Eng.*, 13(4), 1183–1203.

Jalayer, F., H. Ebrahimian, A. Miano, G. Manfredi, and H. Sezen (2017), Analytical fragility assessment using unscaled ground motion records, *Earthq. Eng. Struct. Dyn.*

Joyner, W.B., and D.M. Boore (1981), Peak horizontal acceleration and velocity from strong-motion records including records from the 1979 Imperial Valley, California, earthquake, *Bull. Seismol. Soc. Am.*, 71(6), 2011–2038.

Kappos, A.J., and V.K. Papanikolaou (2016), Nonlinear Dynamic Analysis of Masonry Buildings and Definition of Seismic Damage States, *Open Constr. Build. Technol. J.*, 10(1), 192–209.

Lagomarsino, S., and S. Cattari (2015), PERPETUATE guidelines for seismic performance-based assessment of cultural heritage masonry structures, *Bull. Earthq. Eng.*, 13(1), 13–47.

Luco, N. (2002), Probabilistic seismic demand analysis, SMRF connection fractures, and near-source effects.

Luco, N., P. Bazzurro, and C.A. Cornell (2004), “Dynamic versus static computation of the residual capacity of a mainshock-damaged building to withstand an aftershock,” in: *13th World Conference on Earthquake Engineering, Vancouver, B.C., Canada August 1-6*.

Luco, N., and C.A. Cornell (2007), Structure-specific scalar intensity measures for near-source and ordinary earthquake ground motions, *Earthq. Spectra*, 23(2), 357–392.

McKenna, F. (2011), OpenSees: A framework for earthquake engineering simulation, *Comput. Sci. Eng.*, 13(4), 58–66.

Messali, F., G. Ravenshorst, R. Esposito, and J. Rots (2017), "Large-scale testing program for the seismic characterization of Dutch masonry walls," in: *16th World Conference on Earthquake, WCEE.*

Mouyiannou, A., M. Rota, A. Penna, and G. Magenes (2014), Identification of suitable limit states from nonlinear dynamic analyses of masonry structures, *J. Earthq. Eng.*, 18(2), 231–263.

NAM (2018), "Groningen Earthquakes Structural Upgrading."

Pacor, F., C. Felicetta, G. Lanzano, S. Sgobba, R. Puglia, M. D'Amico, E. Russo, G. Baltzopoulos, and I. Iervolino (2018a), NESS v1.0: A worldwide collection of strong-motion data to investigate near source effects., *Seismol. Res. Lett.*, 89(6), 2299–2313.

—— (2018b), NESS v1.0: A worldwide collection of strong-motion data to investigate near source effects., *Seismol. Res. Lett.*

Padgett, J.E., B.G. Nielson, and R. Desroches (2007), Selection of optimal intensity measures in probabilistic seismic demand models of highway bridge portfolios, *Earthq. Eng. Struct. Dyn.*, 37, 711–725.

Parisi, F., and N. Augenti (2015), Nonlinear seismic behaviour of irregular URM walls with openings, *Anidis 2011*, (September 2011).

Raghunandan, M., A.B. Liel, and N. Luco (2015), Aftershock collapse vulnerability assessment of reinforced concrete frame structures, *Earthq. Eng. Struct. Dyn.*, 44(3), 419–439.

Ruiz-García, J. (2012), Mainshock-aftershock ground motion features and their influence in building's seismic response, *J. Earthq. Eng.*, 16(5), 719–737.

Ryu, H., N. Luco, S.R. Uma, and A.B. Liel (2011), Developing fragilities for mainshock-damaged structures through incremental dynamic analysis, *Proc. Ninth Pacific Conf. Earthq. Eng.*, (225), 8.

Sturt, R., C. Avanes, B. Muriithi, M. Bernardi, and Y. Huang (2018), A masonry material model for seismic analysis in LS-DYNA: implementation and validation, (September 2019).

Vamvatsikos, D., and C.A. Cornell (2001), Incremental Dynamic Analysis, *Earthq. Eng. Struct. Dyn.*, 31(3), 491–514.

—— (2004), Applied incremental dynamic analysis, *Earthq. Spectra*, 20(2), 523–553.

Vlek, C. (2019), Rise and reduction of induced earthquakes in the Groningen gas field, 1991–2018: statistical trends, social impacts, and policy change, *Environ. Earth Sci.*, 78(3), 1–14.

4

Evaluation of state-dependent seismic fragility curves for Italian structural classes

Abstract

From this chapter was derived the paper:

- *Orlacchio M., Chioccarelli E., Baltzopoulos G., Iervolino I. (2021), "State-dependent seismic fragility functions for Italian reinforced concrete structures: preliminary results." Proceedings of the 31st European Safety and Reliability Conference (ESREL), 19-23 September 2021, Angers, France.*

The present chapter deals with the analytical assessment of structural vulnerability models for Italian building classes that constitutes one of the results of the ongoing research project RISE (Real-time earthquake rIsk reduction for a reSilient Europe). The structures under consideration are taken from the outcomes of the SERA project (Seismology and Earthquake Engineering Research Infrastructure Alliance for Europe) and refer to existing reinforced concrete and masonry residential Italian buildings.

State-dependent fragility curves are evaluated via back-to-back incremental dynamic analyses using equivalent-single-degree-of-freedom systems. The analyses consider four damage states, identified by transient maximum inelastic displacement thresholds defined on the system's backbone curve, and are performed with the DYANAS software. Such fragilities are required to calculate the seismic structural reliability when it is possible for structural failure to be reached progressively, i.e., due to the cumulative effect of multiple earthquakes.

Keywords: sequence-based seismic reliability, back-to-back IDA, damage accumulation, SDOF systems, reinforced concrete, masonry.

4.1. Introduction

One of the challenges facing the ongoing research project RISE (*Real-time earthquake rIsk reduction for a reSilient Europe*) is accounting for earthquake sequences in short-term seismic risk assessment. This requires allowing for the fact that structural failure can occur not only due to a single seismic event but can also be reached progressively, due to damage accumulation in multiple earthquakes.

Seismic fragility functions are surrogate structural models that provide a structure's conditional probability of failure, given a certain level of seismic intensity in a single event. In this context, failure refers to a structure failing to meet some performance objective. An extension is represented by *state-dependent* fragility functions, that provide the probability that an already-damaged structure makes a transition from a damage state to another (worse) one, given the value of ground motion intensity. The evaluation of state-dependent fragility is a necessary ingredient to account for damage accumulation in multiple events in risk assessment (e.g., Iervolino et al. 2016, Iervolino et al. 2020).

Evaluation of structure-specific fragility functions can be made via non-linear dynamic analysis of a numerical model of the structure. Past research has suggested that the assessment of fragility functions representing structural typologies (or classes) can also be performed applying the same method to a limited number of structures, deemed representative of the entire class (e.g., Iervolino et al. 2007; Kazantzi and Vamvatsikos 2015).

This chapter presents the computation of the state-dependent fragility functions for the Italian reinforced concrete (RC) and masonry residential structure classes as identified in the SERA (*Seismology and Earthquake Engineering Research Infrastructure Alliance for Europe*) research project. In fact, within the SERA project, the capacity curves of equivalent-single-degree-of-freedom (ESDoF) systems representative of different classes of the European buildings portfolio were developed together with the corresponding fragility functions (Romao et al. 2019).

Although, for each RC building typology, the SERA project provided a set of capacity curves (Romao et al. 2019), the average capacity curves of each set are herein assumed to be representative of the entire typology. On the other hand, for the Italian masonry classes, the SERA project provides single capacity curves representative of each class.

The state-dependent fragilities are evaluated via the so-called *back-to-back Incremental Dynamic Analysis* or back-to-back IDA (Goda 2012; Ryu et al. 2011).

The chapter is structured as follows: first, the characteristics of the set of analyzed structures representative of the Italian RC and masonry buildings are described. Then, the methodology is outlined along with the definition of damage states used for the fragility assessment. The chosen intensity measure and the identification of the number of ground motion records for the execution of the nonlinear-dynamic analysis are also discussed. Finally, the results are presented, discussing the lognormal assumption for the state-dependent fragilities.

4.2. RISE project structures

European existing structural typologies were identified in accordance with the building taxonomy developed within SERA (Romao et al. 2019) on the basis of an updated version of the international standard (i.e., the GEM building taxonomy; Brzev et al. 2013). This taxonomy catalogues buildings considering four main characteristics: primary construction material (e.g., reinforced concrete, unreinforced masonry, steel, etc.); typology of the lateral load resisting system (e.g., wall, moment frame, infilled frame, etc.); height expressed in terms of number of stories and seismic capacity-related properties (e.g., ductility and/or design later force), which depend on the evolution of seismic design in the country (e.g., Petruzzelli and Iervolino 2021); if available, information about the presence of structural irregularities is also provided.

4.2.1. Italian RC structures

The Italian RC existing structures analyzed in this study are represented by a set of eighteen infilled frame buildings, each representing a building class. The building classes are distinguished in terms of number of stories and level of seismic design. The buildings/classes considered have one to six stories and are also identified in terms of code level of seismic design, i.e., absent or low. Moreover, low-code structures are divided further, based on their design (lateral) base shear, which is either 5% or 10% of the building weight (i.e., the seismic coefficient).

4.2.2. Italian masonry structures

The Italian masonry structures portfolio is represented in this study by a set of fifteen wall masonry structures: in detail, ten unreinforced masonry (MUR) buildings and five confined masonry structures (MCF). The MUR structures are classified on the basis of the masonry material in rubble stone masonry (MUR-STRUB); dressed stone masonry (MUR-STDRE) and masonry with clay bricks (MUR-CL99). All the MUR structures are no-ductile systems having at most five stories. More specifically, the set of ten unreinforced masonry buildings is composed of five MUR-STRUB structures having from one to five stories, two MUR-STDRE structures with number of stories equal to four and five, and three MUR-CL99 buildings having from three to five stories.

Finally, the five confined masonry structures have low level of available ductility and from one to five stories.

4.3. Methodology

4.3.1. Capacity curves and damage states definition

The structures described in the previous section are analyzed using equivalent single-degree-of-freedom systems or ESDoF (e.g., Suzuki and Iervolino 2019) characterized by piece-wise linear backbone curves and a pinched hysteretic behavior exhibiting degradation of strength and of (unloading and reloading) stiffness under cyclic loading. An example of the cyclic response of the analyzed systems is shown in Figure 4.1.

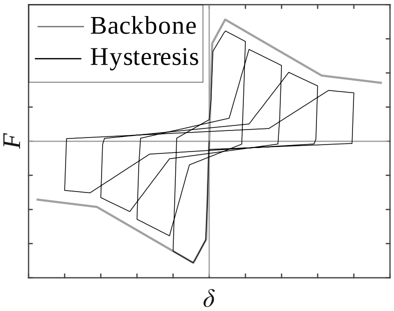

Figure 4.1 Example of backbone curve and cyclic response of an inelastic SDoF system with pinched hysteretic behavior and cyclic strength and stiffness degradation.

A generic backbone curve is presented in panel (a) of Figure 4.2 in terms of displacements, δ, and ratio of the reacting force over the mass of the structure, F/m, along with the points identifying the capacity curve. Figure 4.2a also shows the damage state thresholds considered in this study. Four damage states are considered ranging from *slight damage* (DS_1) to *collapse* (DS_4); all of them are defined according to the SERA project on the basis of Villar-Vega et al. (2017) and Lagomarsino and Giovinazzi (2006).

The engineering demand parameter, EDP, adopted for the identification of the damage states is the (absolute value of the) maximum transient inelastic response in terms of displacement. Thus, in order to account for damage initiation in non-structural elements, DS_1 is considered to have been reached when the maximum displacement equals or exceeds 75% of the displacement corresponding to the value of F_c/m, δ_c, whereas the collapse corresponds to the ultimate displacement capacity of the structure, δ_u. The definition of the intermediate damage states, that is, moderate damage DS_2 and extensive damage DS_3, follows closely the proposal originally presented by Lagomarsino and Giovinazzi, 2006). The thresholds of DS_2 and DS_3 are evenly spaced between the first and last damage state thresholds and are reached at the displacements equal to $0.50 \cdot \delta_c + 0.33 \cdot \delta_u$ and $0.25 \cdot \delta_c + 0.67 \cdot \delta_u$, respectively.

The backbone curves of the eighteen RC structures considered here are shown in Figure 4.2b whereas those of the fifteen masonry structures are reported in Figure 4.2c (numerical values defining each curve are available at the data repository Romao et al. 2020).

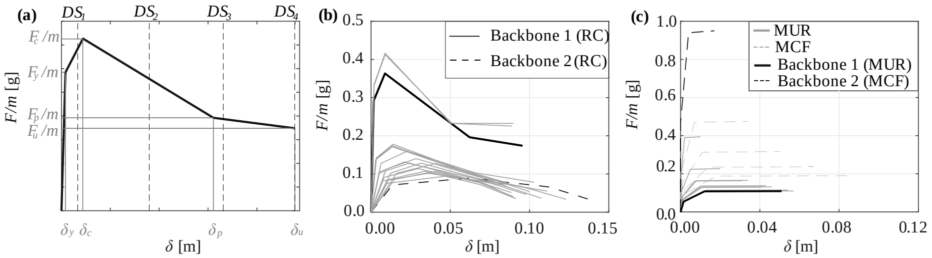

Figure 4.2 Example of capacity curve and definition of the four damage states used in the study (a); capacity curves of the analyzed reinforced concrete structures (b) capacity curves of the analyzed masonry structures.

Each backbone of the RC structures (Figure 4.2b), is determined as an average of the backbones of a multitude of structures comprising that class. More specifically, each piece-wise linear backbone is defined by four points $\left(\left\{\delta_y,F_y/m\right\},\left\{\delta_c,F_c/m\right\},\left\{\delta_p,F_p/m\right\},\left\{\delta_u,F_u/m\right\}\right)$– see Figure 4.2a – and the displacement-acceleration coordinates of each point on the representative curve is evaluated as the geometric mean of the corresponding points defining the capacity curves of the set. This geometric mean is obtained independently for the abscissa and the ordinate of each of the four points defining a representative average curve.

Two subsets of curves can be identified in Figure 4.2b; they are representative of one-story and more-than-one-story (from two to six) RC buildings, respectively. More specifically, the curves with the highest values of F/m correspond to one-story structures among which one has absent level of seismic design whereas the other two have low code level with design lateral force equal to 5.0% and 10.0% of the building weight, respectively. The one-story buildings have vibration periods of about 0.15s whereas the structures with more than one story have periods ranging from 0.29s to 0.88s.

In Figure 4.2c are reported the capacity curves representative of the unreinforced masonry structures classes (solid lines) and those of the confined masonry buildings (dashed lines). The capacity curves for masonry structures, differently from the case of the RC systems, are already representative of each masonry structures class and are directly provided within the SERA project in terms of coordinates of the four points $\left(\left\{\delta_y,F_y/m\right\},\left\{\delta_c,F_c/m\right\},\left\{\delta_p,F_p/m\right\},\left\{\delta_u,F_u/m\right\}\right)$ entirely defining the backbone curves. Both the unreinforced masonry buildings and the confined masonry structures have periods of vibration between 0.13s and 0.69s.

The state-dependent fragility curves were evaluated for the entire sets of eighteen RC structures and of fifteen masonry structures, whereas the choice of the intensity measure and the identification of the number of ground motion records for the execution of the nonlinear-dynamic analyses were conducted considering two benchmark systems among those reported in Figure 4.2b for the RC structures and two benchmark systems among those reported in Figure 4.2c for masonry structure. In Figure 4.2b the backbone 1 (solid line) was selected to be representative of a one-story RC building, which has a vibration period; i.e., T_{el} equal to 0.15s. On the other hand, backbone 2 (dashed line) is considered representative of taller RC structures and corresponds to a six-story building with T_{el} equal to 0.88s. In Figure 4.2c the backbone 1 (solid line) is representative of the unreinforced masonry buildings and has T_{el} equal to 0.69s. The backbone 2 (dashed line) is representative of the confined masonry structures which has a vibration period equal to 0.13s.

4.3.2. Fragility assessment

In this study, fragility functions (i.e., for the undamaged structure) and state-dependent fragility functions are evaluated using IDA (Vamvatsikos and Cornell 2002) and back-to-back IDA, respectively. For a selected set of records, IDA collects the response of a non-linear undamaged structure to the records that are progressively scaled in amplitude to represent increasing levels of seismic intensity. The results of the procedure can be expressed using the IDA curves that represent the structural response via the selected EDP as a function of the intensity measure, IM.

Back-to-back IDA is an extension of IDA, in which the structural model is first subjected to a set of records shaking the structure at its intact state, causing it to reach a damage state DS_i. This is numerically simulated by having each record scaled in amplitude to the lowest IM value that causes the structure to reach the EDP threshold for damage state DS_i; thus, each record produces a different realization of the now-damaged structural model, which can be considered to have made the transition to DS_i. Subsequently, each damaged incarnation of the structural model (i.e., the ESDoF) is subjected to a second set of accelerograms. The records of the second set are scaled until the damaged structure reaches a more severe damage, say DS_j, where $j > i$.

Applying the *IM*-based approach to the results of IDA (Vamvatsikos and Cornell 2001) and back-to-back IDA, fragility functions and state-dependent fragility functions are evaluated. This approach consists in finding the realizations of the random variable $\left(IM_{DS}\right)$ that is the seismic intensity leading the structure to equal or exceed a certain damage state threshold. Assuming that this random variable follows a lognormal distribution, the fragility functions can be estimated according to Eq. (4.1):

$$P\left[DS_i \mid IM = im\right] = P\left[IM_{DS} \leq im\right] = \Phi\left[\left(ln(im) - \eta\right)/\beta\right], \tag{4.1}$$

where $P\left[DS_i \mid IM = im\right]$ is the sought conditional probability that, given the intensity measure value, $IM = im$, the undamaged structure reaches or exceeds a certain damage state DS_i, whereas η and β are the parameters (median and logarithmic standard deviation) of the assumed lognormal distribution, and $\Phi(\cdot)$ is the standard Gaussian (cumulative) function.

Concerning the state-dependent fragility, two probability distribution models are investigated; i.e., the lognormal and the gamma distributions. The former is already defined in Eq. (1) whereas the cumulative density function of the latter is provided by Eq. (4.2):

$$P\left[DS_j \mid DS_i \cap IM = im\right] = \frac{1}{b^a \cdot \Gamma(a)} \cdot \int_0^{im} z^{a-1} \cdot e^{\frac{z}{b}} \cdot \mathrm{d}z, \tag{4.2}$$

where $P\left[DS_j \mid DS_i \cap IM = im\right]$ is the probability that an already damaged structure transitions from a damage state DS_i to a more severe damage state DS_j , a and b are parameters, and $\Gamma(\cdot)$ is the Gamma function.[1]

In this study, the same set of records selected within the NESS dataset (Pacor et al., 2018) is used for both the IDA and the first and the second phase of back-to-back IDA. (The definition of the records set size is discussed in the following sections.) All the analyses (IDA and back-to-back IDA) are performed using the OpenSEES platform (Open System for Earthquake Engineering Simulation; McKenna, 2011) via a recent version of the DYANAS software (Baltzopoulos et al. 2018).

4.3.3. Choice of the intensity measure

In the assessment of structural response by means of dynamic analysis, the choice of the ground motion intensity measure is of primary importance. Traditionally, the IM is selected on the basis of its characteristics of sufficiency and efficiency which are strictly tied to the accuracy of the structural performance assessment (Luco 2002; Luco and Cornell 2007; Padgett et al. 2007). In fact, a *sufficient* IM

---

[1] The parameters of both gaussian and gamma models depend on the initial damage state and the exceeded damage threshold. However, such a dependency is not explicitly reported in Eq. (4.1) and Eq. (4.22) for the sake of simplicity.

renders the structural response conditionally independent, given the selected intensity measure, of the other earthquake characteristics involved in the seismic hazard assessment for the construction site (i.e., magnitude and source-to-site distance), whereas an *efficient* IM produces a relatively small variability in the structural response given the IM. The concepts of sufficiency and efficiency are used in this study to select the intensity measure for the execution of the IDA and back-to-back IDA.

The IMs known to allow an efficient prediction of the response of reinforced-concrete structures, in terms of maximum roof- or interstory-displacement, generally include elastic response spectral values and somehow account for spectral shape (Eads et al. 2015; Bojórquez and Iervolino 2011). In this study, four IMs were preliminarily considered as candidates: the elastic spectral acceleration at the period 0.3s; $Sa(T=0.3s)$ (in accordance with Romao et al. 2019), the elastic spectral acceleration at the vibration period of the undamaged system, $Sa(T_{el})$, the geometric mean of spectral accelerations Sa_{avg} (Baker and Cornell 2006) and the I_{NP} intensity measure (Bojórquez and Iervolino, 2011). Hereafter, the geometric mean of spectral accelerations $Sa_{avg}(T_1,T_2,\ldots,T_{23})$ is evaluated considering the twenty-three periods of the ground motion prediction equation of Bindi et al. (2011), defined in a range between 0.0s and 2.75s, according to Eq.(4.3) :

$$Sa_{avg}(T_1,T_2,\ldots,T_{23})=\sqrt[23]{Sa(0.0\text{s})\cdot\ldots\cdot Sa(2.75\text{s})}. \tag{4.3}$$

The scalar intensity measure I_{NP} is also spectral-acceleration-based. In this case, it was defined using the same spectral ordinates considered for $Sa_{avg}(T_1,T_2,\ldots,T_{23})$, as shown in Eq.(4.4):

$$I_{NP}(T_1,T_2,\ldots,T_{23})=Sa(T_{el})\cdot\left[\frac{Sa_{avg}(T_1,T_2,\ldots,T_{23})}{Sa(T_{el})}\right]^{\alpha}, \tag{4.4}$$

where α is a parameter that, strictly speaking, requires structure-specific calibration, but is assumed equal to 0.4 in the following (Bojórquez and Iervolino, 2011). It can be noted that $Sa_{avg}(T_1,T_2,\ldots,T_{23})$ can be regarded as a special case of $Sa_{avg}(T_1,T_2,\ldots,T_{23})$, for $\alpha=1$.

Among the cited IMs, one had to be selected for computing fragility functions and state-dependent fragility function of all the analyzed buildings. To this aim, the four already mentioned benchmark systems are considered (see Figure 4.2b and Figure 4.2c).

As pertaining to sufficiency, past research has shown that intensity measures that account for spectral shape in a range of periods (i.e., Sa_{avg} and I_{NP} among those considered here) seem to perform better than single-spectral-ordinate IMs at higher damage states. This can be intuitively attributed to the fact that a damaged structure's stiffness is lower than what it was in intact conditions and, consequently, the range of vibration periods overall influencing the dynamic response increases.

On the other hand, to have an indication of the efficiency of the four investigated intensity measures, the coefficient of variation of the IM_{DS}, $COV_{IM_{DS}}$, is evaluated for increasing values of failure threshold, δ_{max}. Figure 4.3 shows the values of $COV_{IM_{DS}}$ assessed for the four different IMs and the four benchmark systems (two representative of the RC structures and two representative of the masonry structures).

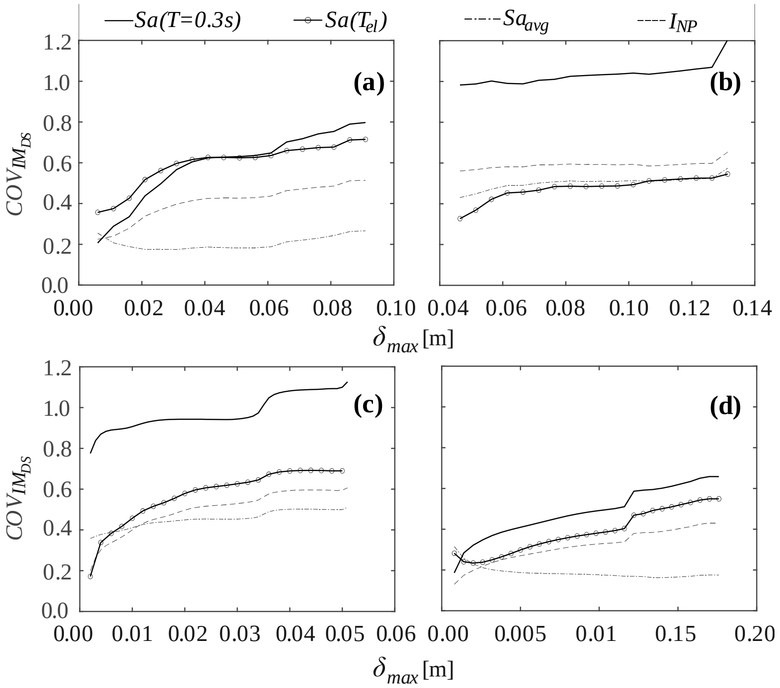

Figure 4.3 $COV_{IM_{DS}}$ as a function of δ_{max} evaluated for the four *IMs* for the first (a) and the second system (b) representative of the RC structures, the first (c) and the second (d) system representative of the masonry structures.

The figure shows that Sa_{avg} and I_{NP} are generally more efficient intensity measures than the single spectral ordinates (with the only exception for the backbone 2 of RC structures), as expected and confirms the findings of past research, that *IM* efficiency is damage-state-dependent (Kazantzi and Vamvatsikos 2015). For example, a previous work has indicated that the efficiency of I_{NP} with different α values (0.4 or 1) varies with damage state (Baltzopoulos et al., 2019). For the analyses, Sa_{avg} was used as the IM of choice, in other words I_{NP} with $\alpha = 1$.

4.3.4. Number of records

The issue addressed in this section concerns the identification of the number of ground motions used to perform dynamic analyses in other to balance the computational costs and the accuracy in fragility assessment. To this end, the statistical concept of estimation uncertainty (Iervolino, 2017; Baltzopoulos et al. 2019) is applied to the estimates of the parameters defining the parametric fragility Eq. (4.1).

The record sample size is selected trying to limit the estimation error of the two parameters η and β that define the fragility functions of the intact structures under the lognormal assumption. Although the gamma distribution is also contemplated as an alternative to the lognormal for the state-dependent fragilities, this consideration of estimation uncertainty is limited to the intact structures' fragility and the lognormal model. The quantitative measure of the uncertainty in the fragility assessment used in this study, is the coefficients of variation $COV_{\eta,}$ and COV_{β} evaluated for the estimators of the median η and of the standard deviation β, respectively. The coefficient of variation $COV_{\vartheta,}$ of a generic estimator ϑ is defined as the square root of $VAR\left[\vartheta\right]$ divided by $E\left[\vartheta\right]$, that is the ratio of the standard deviation and the expected value of ϑ. The terms $VAR\left[\vartheta\right]$ and $E\left[\vartheta\right]$ can be substituted by their estimates obtained using a parametric resampling scheme proposed in Baltzopoulos et al., 2019. This procedure entails randomly sampling l times (in this case 5000 times) from an assumed reference fragility model; i.e., the distribution of IM_{DS} defined by the results of IDA performed using the entire fifty-record set. This is repeated for a number of times, each time extracting different samples sizes N, varying from 20 to 50. In this context, sample size ostensibly corresponds to the number of records used in dynamic analysis, and $COV_{\vartheta,}$ is approximated as:

$$COV_{\vartheta} = \frac{\sqrt{VAR\left[\vartheta\right]}}{E\left[\vartheta\right]} \approx \frac{\sqrt{\frac{1}{l-1}\cdot\sum_{j=1}^{l}\left(\vartheta_j - \frac{1}{l}\cdot\sum_{k=1}^{l}\vartheta_k\right)^2}}{\frac{1}{l}\cdot\sum_{j=1}^{l}\vartheta_j}. \tag{4.5}$$

This procedure is implemented for the two benchmark systems shown in Figure 4.2b for RC structures and also for the two benchmark systems showed in Figure 4.2c for masonry structures considering their fragilities to collapse (i.e., DS_4). In Figure 4.4, the results obtained varying the size of the records set N from 20 to 50 are reported, in the panels (a) and (b) for the RC structures and in panels (c) and (d) for the masonry structures.

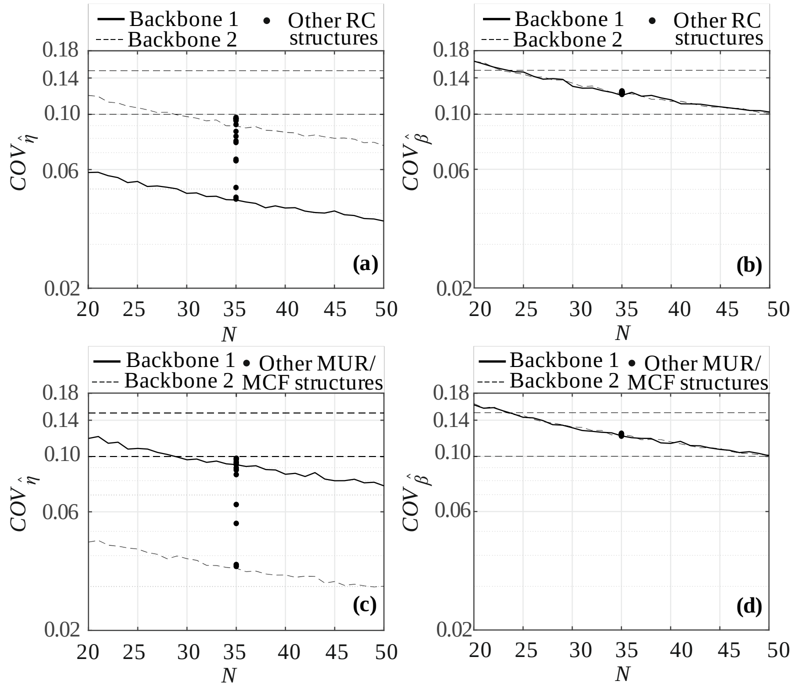

Figure 4.4 Coefficient of variation for the estimators of the median COV_{η} (a) and the standard deviation COV_{β} (b) of the DS_4 fragility curve of RC structures against the number of records N ; coefficient of variation for the estimators of the median COV_{η} (c) and the standard deviation COV_{β} (d) of the DS_4 fragility curve of masonry structures against the number of records N .

Through the described procedure, it is decided to use a number of records equal to 35 that allows maintaining COV_{β} between 10% and 15% for the four systems and COV_{η} below 10%. Moreover, Figure 4.4 also shows COV_{η} (Figure

4.4a-c) and COV_{β}, (Figure 4.4b-d) evaluated for all the other RC and masonry structures using 35 records in order to verify that the associated coefficients of variation of the two estimators also adhere to these limitations.

The defined set of 35 records is used for the execution of both IDA and back-to-back IDA.

4.4. Results

4.4.1. Reinforced concrete structures

4.4.1.1. Classical curves

Figure 4.5 and Figure 4.6 reports the fragility curves of the intact structures obtained analyzing via IDA the two benchmark systems shown in panel (b) of Figure 4.2. Each panel of Figure 4.5 and Figure 4.6 shows the comparison between the non-parametric fragility and the parametric fragility curve evaluated according to Eq.(4.1) for each arriving damage state; i.e. panel (a) refers to DS_1; panel (b) to DS_2; panel (c) to DS_3 and panel (d) to DS_4. Figure 4.5 and Figure 4.6 show the good agreement between the assumed lognormal distribution and the results obtained from the analyses.

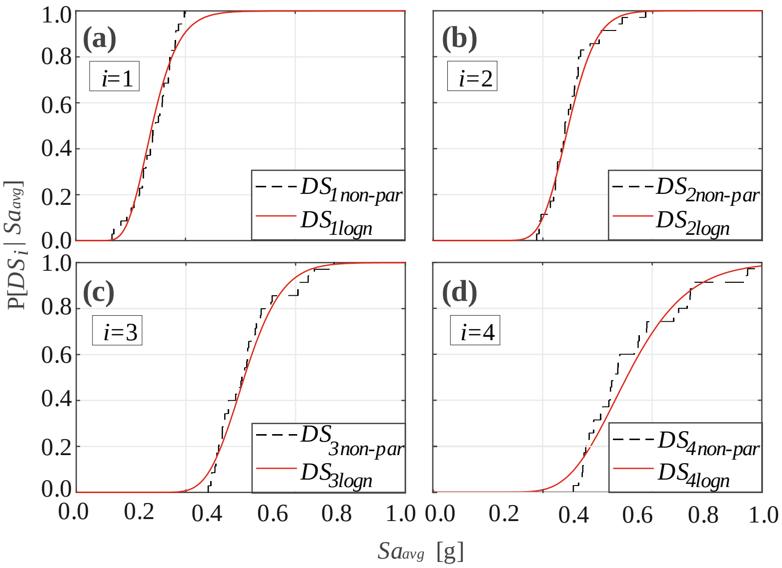

Figure 4.5 Fragility curves evaluated for the benchmark system 1 of RC structures for the four damage states DS_1 (a); DS_2 (b); DS_3 (c) and DS_4 (d).

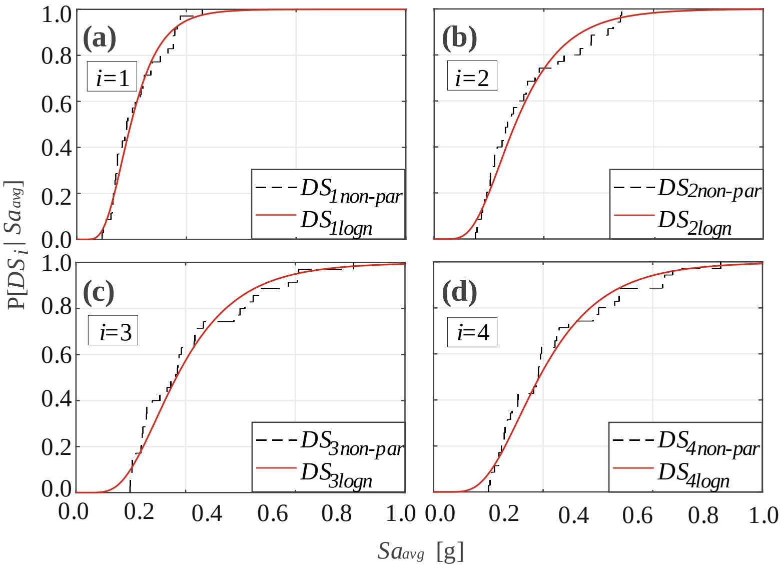

Figure 4.6 Fragility curves evaluated for the benchmark system 2 of RC structures for the four damage states DS_1 (a); DS_2 (b); DS_3 (c) and DS_4 (d).

Figure 4.7 shows the fragility curves obtained analyzing the entire set of eighteen RC structures. Similarly to Figure 4.5 and Figure 4.6, each panel of Figure 4.7 shows the fragility curves of the intact structures evaluated for each arriving damage state according to Eq.(4.1) (panel (a) for DS_1; panel (b) for DS_2; panel (c) for DS_3 and panel (d) for DS_4).

The values of median, η, and logarithmic standard deviation, β, defining the parametric fragilities of intact structures numbered from 1 to 18 are reported in Table 4.1. The table also shows for each structure the adopted code level of seismic design (absent or low); the height expressed in terms of number of stories (H) and the design lateral force (0%, 5% or 10% of the building weight). As previously mentioned, the one-story buildings are always less fragile than the other RC structures for all damage states considered.

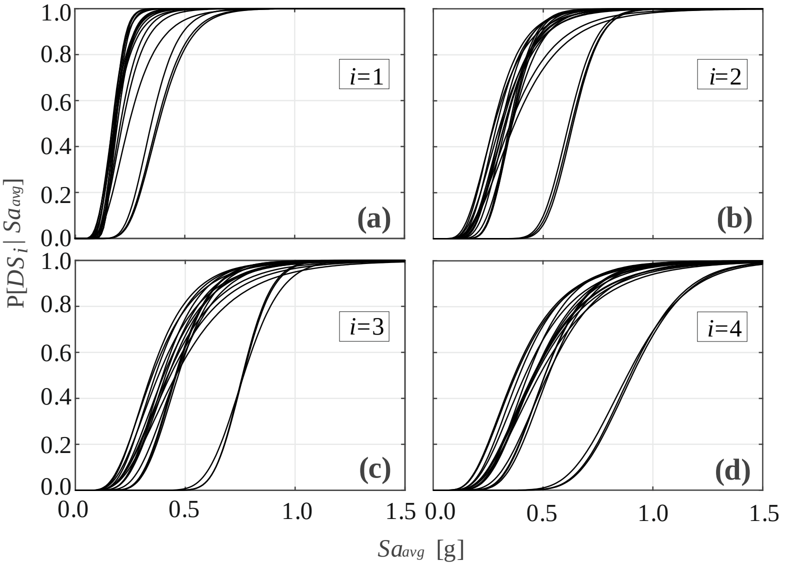

Figure 4.7 Fragility curves of RC structures evaluated for the four damage states DS_1 (a); DS_2 (b); DS_3 (c) and DS_4 (d).

Table 4.1 Median η and logarithmic standard deviation β defining the fragility curves of RC intact structures (IM in g).

#	Code Level	H	Lateral Force Coefficient (%)	MEDIAN η				SIGMA β			
				DS_1	DS_2	DS_3	DS_4	DS_1	DS_2	DS_3	DS_4
1	Absent	1	0.00	0.35	0.62	0.77	0.88	0.24	0.14	0.15	0.21
2	Absent	2	0.00	0.18	0.35	0.46	0.51	0.21	0.24	0.28	0.31
3	Absent	3	0.00	0.19	0.33	0.42	0.46	0.29	0.31	0.37	0.39
4	Absent	4	0.00	0.21	0.33	0.42	0.45	0.35	0.38	0.44	0.45
5	Absent	5	0.00	0.22	0.35	0.43	0.47	0.37	0.46	0.46	0.46
6	Absent	6	0.00	0.25	0.37	0.46	0.48	0.43	0.47	0.48	0.46
7	Low	1	5.00	0.38	0.64	0.76	0.90	0.23	0.12	0.11	0.17
8	Low	2	5.00	0.18	0.35	0.45	0.51	0.21	0.24	0.28	0.31
9	Low	3	5.00	0.17	0.31	0.40	0.43	0.28	0.31	0.35	0.37
10	Low	4	5.00	0.18	0.29	0.36	0.39	0.34	0.36	0.39	0.43
11	Low	5	5.00	0.17	0.27	0.34	0.37	0.27	0.29	0.32	0.36
12	Low	6	5.00	0.18	0.28	0.35	0.37	0.40	0.43	0.45	0.47
13	Low	1	10.00	0.37	0.63	0.76	0.91	0.24	0.13	0.11	0.18
14	Low	2	10.00	0.19	0.36	0.47	0.52	0.22	0.25	0.28	0.31
15	Low	3	10.00	0.19	0.36	0.46	0.52	0.28	0.30	0.34	0.37
16	Low	4	10.00	0.18	0.33	0.41	0.46	0.35	0.35	0.36	0.41
17	Low	5	10.00	0.17	0.31	0.40	0.46	0.35	0.37	0.42	0.45
18	Low	6	10.00	0.19	0.31	0.38	0.42	0.38	0.42	0.45	0.45

4.4.1.2. State-dependent fragility curves

For the state-dependent fragilities, the assumption of a lognormal distribution or, alternatively, of a gamma distribution is investigated. Figure 4.8 shows the comparison between the non-parametric state-dependent fragilities (identified by the *non-par* subscript in the legend) and the parametric ones evaluated using the lognormal distribution (*log* subscript) for the benchmark system 1 of RC structures. Each panel of the figure shows the state-dependent fragility curves referring to different starting damage state and having the same final damage state; i.e. panel (a) refers to final damage state DS_2 whereas panel (b) refers to DS_3 and panel (c) to DS_4. Figure 4.9 shows the same results reported in Figure 4.8 but compares the non-parametric state-dependent fragilities with the parametric ones evaluated using the gamma distribution (*gamma* subscript).

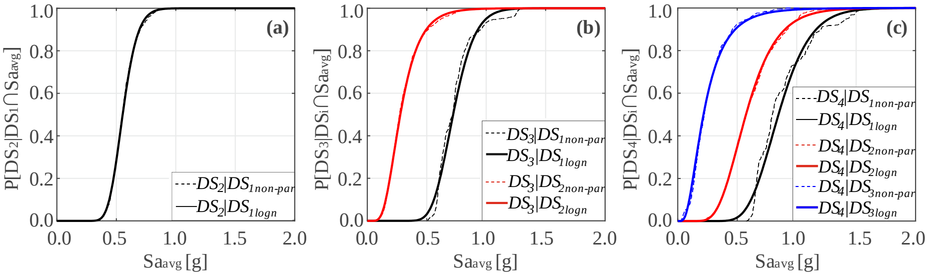

Figure 4.8 Comparison of the non-parametric and the parametric state-dependent fragility curves evaluated for the benchmark system 1 assuming the lognormal distribution and having different starting damage state and the same final state DS_2 (a), DS_3 (b) and DS_4 (c).

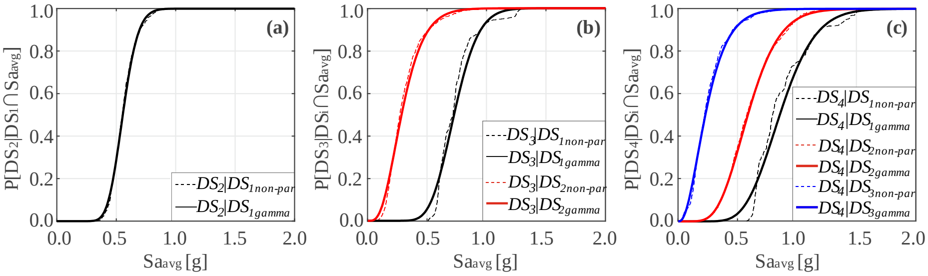

Figure 4.9 Comparison of the non-parametric and the parametric state-dependent fragility curves evaluated for the benchmark system 1 assuming the gamma distribution and having different starting damage state and the same final state DS_2 (a), DS_3 (b) and DS_4 (c).

The choice between the two possible distributions (*lognormal* and *gamma*) is conducted in terms of rates of failure, i.e., the rates of failure of the eighteen RC systems are calculated using the parametric state-dependent fragility curves evaluated using both the gamma and the lognormal distributions and are compared with the rates of failure obtained using the non-parametric state-dependent fragilities. The chosen distribution is the one best reproducing the rate results obtained using the non-parametric state-dependent fragilities.

Within the performance-based earthquake engineering (PBEE) framework, the failure rate λ_f is the rate of earthquakes causing some undesired performance for the structure and in case of an already damaged structure can be computed as follow:

$$\lambda_f = \int_{-\infty}^{+\infty} P\left[DS_j \mid DS_i \cap IM = im \right] \cdot \left| d\lambda_{im} \right| \tag{4.6}$$

where $P\left[DS_j \mid DS_i \cap IM = im \right]$ is the state-dependent fragility curve and $d\lambda_{im}$ is the differential of the hazard curve, that is, the function providing the rate of exceedance of im at the site of the construction, that is, λ_{im} from probabilistic seismic hazard analysis (PSHA; Cornell, 1968).

For the assessment of the failure rates are considered three Italian sites, i.e., L'Aquila, Naples and Milan; representative of high, intermediate and low seismic hazards, respectively. The hazard analysis for the three sites is performed via the REASSES software (Chioccarelli et al., 2018) considering the seismic source model of Meletti et al. (2008) with magnitude rates taken from Barani et al. (2009). The ground motion prediction equation considered is Bindi et al. (2011), consistently with the intensity measure used to develop the state-dependent fragility curves, and are assumed soil conditions B (CEN, 2004) .

Figure 4.10(a) shows the locations of the three sites considered and the seismogenic source zones of the model Meletti et al. (2008), whereas panel (b) provides the hazard curves computed via PSHA for the three sites in terms of Sa_{avg} .

The failure rates of the eighteen RC structures at the three Italian sites are shown in Table 4.2, Table 4.3 and Table 4.. The tables differ in the state-dependent fragility curves used for the assessment of the failure rates, i.e., non-parametric state-dependent fragility curves (Table 4.2); parametric state-dependent fragility curves evaluated assuming the lognormal distribution (Table 4.3) or using the gamma distribution (Table 4.).

Comparing the results obtained; it is found that modeling the state-dependent fragilities via a lognormal distribution provides failure rates closer to those obtained using the non-parametric results, for all the possible transitions between different damage states and considering the three levels of seismic hazard. Therefore, in this study the lognormal distribution was chosen to represent the state-dependent fragilities of RC structure classes.

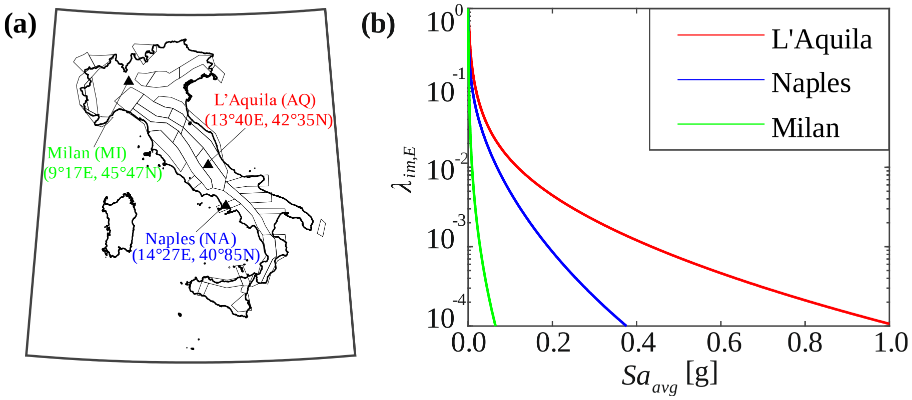

Figure 4.10 Seismic sources zones and sites' locations considered for the hazard analysis (a); annual exceedance rates of Sa_{avg} computed probabilistic seismic hazard analysis for the three sites (b).

Table 4.5 collects the values of the median, η, and logarithmic standard deviation, β, defining lognormal distribution, Eq. (4.1); i.e., the parametric state-dependent fragility curves for the eighteen RC structures. In the table, the fifth column gives the initial damage state wheres the damage state reported in the rest of the row represent the arrival damage states.

Figure 4.11 shows the state-dependent fragility curves obtained analyzing the entire set of eighteen RC structures via Back-to-Back IDA and assuming the lognormal distribution. Each panel of Figure 4.11 shows the state-dependent fragility curves obtained considering a possible transition between damage states, i.e. from DS_1 to DS_2 (panel a); from DS_1 to DS_3 (panel b); from DS_1 to DS_4 (panel c); from DS_2 to DS_3 (panel d);); from DS_2 to DS_4 (panel e) and from DS_3 to DS_4 (panel f).

Table 4.2 Failure rates for the RC structures computed using the non-parametric state-dependent fragility curves.

		L'AQUILA			NAPLES			MILAN		
#	λ_f	DS_2	DS_3	DS_4	DS_2	DS_3	DS_4	DS_2	DS_3	DS_4
1	DS_1	6.14E-04	3.15E-04	2.17E-04	2.56E-05	7.56E-06	4.16E-06	7.73E-09	1.36E-09	6.28E-10
	DS_2	\	3.21E-03	7.05E-04	\	6.57E-04	4.75E-05	\	1.54E-06	3.04E-08
	DS_3	\	\	6.23E-03	\	\	2.22E-03	\	\	2.80E-05
2	DS_1	2.45E-03	1.23E-03	9.45E-04	3.41E-04	1.03E-04	6.59E-05	3.78E-07	6.33E-08	3.39E-08
	DS_2	\	7.62E-03	2.33E-03	\	2.60E-03	3.82E-04	\	1.40E-05	6.97E-07
	DS_3	\	\	9.13E-03	\	\	3.42E-03	\	\	2.15E-05
3	DS_1	4.12E-03	1.77E-03	1.28E-03	9.25E-04	2.08E-04	1.20E-04	2.22E-06	1.92E-07	8.33E-08
	DS_2	\	9.06E-03	3.24E-03	\	3.43E-03	6.91E-04	\	2.40E-05	1.74E-06
	DS_3	\	\	2.13E-02	\	\	1.01E-02	\	\	9.24E-04

Table 4.2 (*Continued*) Failure rates for the RC structures computed using the non-parametric state-dependent fragility curves.

		L'AQUILA			NAPLES			MILAN		
#	λ_f	DS_2	DS_3	DS_4	DS_2	DS_3	DS_4	DS_2	DS_3	DS_4
4	DS_1	7.33E-03	2.38E-03	1.56E-03	2.52E-03	3.76E-04	1.80E-04	1.61E-05	5.33E-07	1.66E-07
	DS_2	\	1.11E-02	4.65E-03	\	4.64E-03	1.28E-03	\	4.54E-05	4.75E-06
	DS_3	\	\	1.85E-02	\	\	8.98E-03	\	\	3.10E-04
5	DS_1	7.50E-03	2.38E-03	1.53E-03	2.70E-03	3.99E-04	1.79E-04	1.98E-05	6.50E-07	1.69E-07
	DS_2	\	1.06E-02	4.48E-03	\	4.37E-03	1.23E-03	\	3.94E-05	4.59E-06
	DS_3	\	\	1.30E-02	\	\	5.86E-03	\	\	7.26E-05
6	DS_1	7.41E-03	2.49E-03	1.49E-03	2.64E-03	4.42E-04	1.72E-04	1.79E-05	7.96E-07	1.64E-07
	DS_2	\	1.01E-02	4.59E-03	\	4.15E-03	1.29E-03	\	3.87E-05	5.19E-06
	DS_3	\	\	1.57E-02	\	\	7.48E-03	\	\	1.89E-04
7	DS_1	5.89E-04	3.13E-04	2.03E-04	2.46E-05	7.27E-06	3.51E-06	7.94E-09	1.27E-09	4.81E-10
	DS_2	\	3.54E-03	8.36E-04	\	7.54E-04	6.63E-05	\	1.79E-06	5.13E-08
	DS_3	\	\	5.55E-03	\	\	1.66E-03	\	\	7.75E-06
8	DS_1	2.45E-03	1.26E-03	9.57E-04	3.41E-04	1.06E-04	6.67E-05	3.77E-07	6.62E-08	3.41E-08
	DS_2	\	8.93E-03	2.56E-03	\	3.40E-03	4.52E-04	\	2.94E-05	9.01E-07
	DS_3	\	\	1.39E-02	\	\	6.25E-03	\	\	1.20E-04
9	DS_1	4.07E-03	1.90E-03	1.43E-03	8.89E-04	2.33E-04	1.43E-04	1.95E-06	2.25E-07	1.07E-07
	DS_2	\	9.83E-03	3.43E-03	\	3.86E-03	7.50E-04	\	2.96E-05	1.94E-06
	DS_3	\	\	1.35E-02	\	\	6.04E-03	\	\	7.26E-05
10	DS_1	5.96E-03	2.52E-03	1.81E-03	1.75E-03	4.04E-04	2.29E-04	6.82E-06	5.65E-07	2.27E-07
	DS_2	\	1.29E-02	4.95E-03	\	5.73E-03	1.44E-03	\	9.32E-05	6.98E-06
	DS_3	\	\	1.77E-02	\	\	8.52E-03	\	\	1.90E-04
11	DS_1	5.83E-03	2.73E-03	2.05E-03	1.71E-03	4.82E-04	2.96E-04	6.66E-06	7.90E-07	3.56E-07
	DS_2	\	1.16E-02	5.06E-03	\	4.89E-03	1.45E-03	\	4.72E-05	5.92E-06
	DS_3	\	\	3.28E-02	\	\	1.65E-02	\	\	1.58E-03
12	DS_1	6.37E-03	3.02E-03	2.21E-03	2.06E-03	6.00E-04	3.44E-04	1.03E-05	1.25E-06	4.75E-07
	DS_2	\	1.10E-02	5.19E-03	\	4.60E-03	1.51E-03	\	4.03E-05	6.34E-06
	DS_3	\	\	1.86E-02	\	\	9.09E-03	\	\	1.56E-04
13	DS_1	6.03E-04	3.16E-04	2.01E-04	2.58E-05	7.38E-06	3.48E-06	8.56E-09	1.30E-09	4.79E-10
	DS_2	\	3.36E-03	7.88E-04	\	6.80E-04	5.84E-05	\	1.46E-06	4.05E-08
	DS_3	\	\	4.82E-03	\	\	1.25E-03	\	\	3.75E-06
14	DS_1	2.36E-03	1.20E-03	8.97E-04	3.19E-04	9.66E-05	5.94E-05	3.43E-07	5.78E-08	2.87E-08
	DS_2	\	8.51E-03	2.41E-03	\	3.27E-03	4.28E-04	\	3.20E-05	9.17E-07
	DS_3	\	\	1.08E-02	\	\	4.39E-03	\	\	4.62E-05
15	DS_1	2.88E-03	1.36E-03	9.78E-04	4.94E-04	1.29E-04	7.33E-05	8.14E-07	9.33E-08	4.06E-08
	DS_2	\	7.56E-03	2.41E-03	\	2.59E-03	4.09E-04	\	1.42E-05	7.12E-07
	DS_3	\	\	1.11E-02	\	\	4.65E-03	\	\	6.08E-05
16	DS_1	3.75E-03	1.83E-03	1.33E-03	7.91E-04	2.26E-04	1.30E-04	1.69E-06	2.22E-07	9.40E-08
	DS_2	\	8.43E-03	3.10E-03	\	3.10E-03	6.43E-04	\	2.06E-05	1.54E-06
	DS_3	\	\	1.18E-02	\	\	5.14E-03	\	\	6.00E-05
17	DS_1	3.29E-03	1.78E-03	1.32E-03	6.45E-04	2.26E-04	1.32E-04	1.27E-06	2.30E-07	1.01E-07
	DS_2	\	8.85E-03	3.17E-03	\	3.37E-03	6.97E-04	\	2.78E-05	2.37E-06
	DS_3	\	\	2.10E-02	\	\	9.90E-03	\	\	8.84E-04
18	DS_1	4.34E-03	2.20E-03	1.72E-03	1.08E-03	3.40E-04	2.22E-04	3.25E-06	4.73E-07	2.43E-07
	DS_2	\	9.54E-03	4.19E-03	\	3.80E-03	1.09E-03	\	3.08E-05	3.87E-06
	DS_3	\	\	1.66E-02	\	\	7.94E-03	\	\	1.84E-04

Table 4.3 Failure rates for the RC structures computed using the parametric state-dependent fragility curves obtained using the lognormal distribution.

		L'AQUILA			NAPLES			MILAN		
#	λ_f	DS_2	DS_3	DS_4	DS_2	DS_3	DS_4	DS_2	DS_3	DS_4
1	DS_1	6.15E-04	3.19E-04	2.22E-04	2.59E-05	8.28E-06	4.93E-06	7.99E-09	1.72E-09	9.76E-10
	DS_2	\	3.23E-03	6.98E-04	\	6.79E-04	4.53E-05	\	1.79E-06	2.76E-08
	DS_3	\	\	5.86E-03	\	\	1.94E-03	\	\	1.36E-05
2	DS_1	2.46E-03	1.24E-03	9.52E-04	3.54E-04	1.08E-04	7.20E-05	4.42E-07	7.97E-08	4.80E-08
	DS_2	\	7.65E-03	2.33E-03	\	2.63E-03	3.80E-04	\	1.57E-05	6.80E-07
	DS_3	\	\	9.29E-03	\	\	3.55E-03	\	\	2.80E-05
3	DS_1	4.13E-03	1.79E-03	1.31E-03	9.37E-04	2.29E-04	1.44E-04	2.44E-06	2.83E-07	1.61E-07
	DS_2	\	9.12E-03	3.25E-03	\	3.47E-03	7.06E-04	\	2.76E-05	2.04E-06
	DS_3	\	\	4.47E-02	\	\	2.37E-02	\	\	2.38E-03
4	DS_1	7.28E-03	2.41E-03	1.60E-03	2.48E-03	4.09E-04	2.13E-04	1.50E-05	7.86E-07	3.18E-07
	DS_2	\	1.11E-02	4.70E-03	\	4.68E-03	1.32E-03	\	5.23E-05	6.14E-06
	DS_3	\	\	1.75E-02	\	\	8.54E-03	\	\	1.83E-04
5	DS_1	7.44E-03	2.42E-03	1.57E-03	2.65E-03	4.38E-04	2.12E-04	1.94E-05	9.88E-07	3.29E-07
	DS_2	\	1.07E-02	4.54E-03	\	4.48E-03	1.29E-03	\	4.99E-05	6.35E-06
	DS_3	\	\	1.33E-02	\	\	6.02E-03	\	\	9.32E-05
6	DS_1	7.42E-03	2.53E-03	1.52E-03	2.65E-03	4.84E-04	2.04E-04	1.98E-05	1.22E-06	3.15E-07
	DS_2	\	1.03E-02	4.69E-03	\	4.29E-03	1.38E-03	\	4.96E-05	7.58E-06
	DS_3	\	\	1.53E-02	\	\	7.27E-03	\	\	1.48E-04
7	DS_1	5.86E-04	3.14E-04	2.08E-04	2.38E-05	7.44E-06	4.11E-06	7.18E-09	1.36E-09	7.06E-10
	DS_2	\	3.60E-03	8.26E-04	\	8.10E-04	6.28E-05	\	2.37E-06	4.62E-08
	DS_3	\	\	5.59E-03	\	\	1.71E-03	\	\	8.98E-06
8	DS_1	2.46E-03	1.27E-03	9.66E-04	3.49E-04	1.12E-04	7.33E-05	4.21E-07	8.20E-08	4.87E-08
	DS_2	\	8.85E-03	2.55E-03	\	3.35E-03	4.49E-04	\	2.67E-05	9.01E-07
	DS_3	\	\	1.34E-02	\	\	6.01E-03	\	\	8.20E-05
9	DS_1	4.08E-03	1.91E-03	1.47E-03	9.10E-04	2.51E-04	1.72E-04	2.26E-06	3.12E-07	2.03E-07
	DS_2	\	9.86E-03	3.43E-03	\	3.87E-03	7.57E-04	\	3.28E-05	2.17E-06
	DS_3	\	\	1.37E-02	\	\	6.18E-03	\	\	8.60E-05
10	DS_1	5.97E-03	2.55E-03	1.85E-03	1.77E-03	4.35E-04	2.68E-04	7.55E-06	8.05E-07	4.31E-07
	DS_2	\	1.25E-02	4.92E-03	\	5.51E-03	1.42E-03	\	7.14E-05	6.84E-06
	DS_3	\	\	1.73E-02	\	\	8.33E-03	\	\	1.51E-04
11	DS_1	5.86E-03	2.76E-03	2.10E-03	1.74E-03	5.14E-04	3.42E-04	7.83E-06	1.13E-06	6.61E-07
	DS_2	\	1.17E-02	5.08E-03	\	4.94E-03	1.47E-03	\	5.44E-05	6.96E-06
	DS_3	\	\	3.53E-02	\	\	1.88E-02	\	\	1.24E-03
12	DS_1	6.40E-03	3.03E-03	2.25E-03	2.07E-03	6.29E-04	3.85E-04	1.20E-05	1.68E-06	7.99E-07
	DS_2	\	1.12E-02	5.25E-03	\	4.70E-03	1.56E-03	\	5.05E-05	8.03E-06
	DS_3	\	\	1.87E-02	\	\	9.15E-03	\	\	1.69E-04
13	DS_1	6.00E-04	3.17E-04	2.06E-04	2.49E-05	7.56E-06	4.10E-06	7.63E-09	1.39E-09	7.12E-10
	DS_2	\	3.40E-03	7.80E-04	\	7.18E-04	5.61E-05	\	1.84E-06	3.86E-08
	DS_3	\	\	4.92E-03	\		1.35E-03	\	\	5.54E-06
14	DS_1	2.37E-03	1.20E-03	9.08E-04	3.28E-04	1.02E-04	6.61E-05	3.87E-07	7.14E-08	4.24E-08
	DS_2	\	\	2.39E-03	\	3.14E-03	4.11E-04	\	2.67E-05	8.20E-07
	DS_3	\	\	1.07E-02	\	\	4.36E-03	\	\	4.13E-05
15	DS_1	2.88E-03	1.37E-03	1.00E-03	5.03E-04	1.41E-04	8.98E-05	8.86E-07	1.35E-07	7.96E-08
	DS_2	\	7.59E-03	2.42E-03	\	2.62E-03	4.24E-04	\	1.61E-05	8.84E-07
	DS_3	\	\	1.09E-02	\	\	4.54E-03	\	0.00E+00	5.03E-05

Table 4.3 (*Continued*) Failure rates for the RC structures computed using the parametric state-dependent fragility curves obtained using the lognormal distribution.

		L'AQUILA			NAPLES			MILAN		
#	λ_f	DS_2	DS_3	DS_4	DS_2	DS_3	DS_4	DS_2	DS_3	DS_4
16	DS_1	3.77E-03	1.86E-03	1.38E-03	8.18E-04	2.52E-04	1.63E-04	2.03E-06	3.48E-07	2.07E-07
	DS_2	\	8.44E-03	3.10E-03	\	3.10E-03	6.55E-04	\	2.26E-05	1.81E-06
	DS_3	\	\	1.19E-02	\	\	5.21E-03	\	\	7.23E-05
17	DS_1	3.31E-03	1.83E-03	1.37E-03	6.72E-04	2.67E-04	1.68E-04	1.57E-06	4.43E-07	2.34E-07
	DS_2	\	8.84E-03	3.16E-03	\	3.36E-03	6.99E-04	\	2.80E-05	2.17E-06
	DS_3	\	\	2.19E-02	\	\	1.12E-02	\	\	4.75E-04
18	DS_1	4.35E-03	2.23E-03	1.76E-03	1.10E-03	3.74E-04	2.60E-04	3.78E-06	7.38E-07	4.57E-07
	DS_2	\	9.63E-03	4.23E-03	\	3.85E-03	1.13E-03	\	3.82E-05	4.90E-06
	DS_3	\	\	1.64E-02	\	\	7.85E-03	\	\	1.53E-04

Table 4.4 Failure rates for the RC structures computed using the parametric state-dependent fragility curves obtained using the gamma distribution.

		L'AQUILA			NAPLES			MILAN		
#	λ_f	DS_2	DS_3	DS_4	DS_2	DS_3	DS_4	DS_2	DS_3	DS_4
1	DS_1	6.20E-04	3.34E-04	2.39E-04	2.67E-05	9.69E-06	6.46E-06	8.65E-09	2.41E-09	1.76E-09
	DS_2	\	3.77E-03	7.17E-04	\	1.00E-03	5.28E-05	\	6.35E-06	4.55E-08
	DS_3	\	\	6.73E-03	\	\	2.52E-03	\	\	4.62E-05
2	DS_1	9.65E-03	3.06E-03	1.81E-03	4.08E-04	1.22E-04	8.57E-05	6.60E-07	1.12E-07	7.89E-08
	DS_2	\	1.78E-02	7.23E-03	\	3.39E-03	4.64E-04	\	4.29E-05	1.37E-06
	DS_3	\	\	2.44E-02	\	\	6.00E-03	\	\	1.84E-04
3	DS_1	2.58E-03	1.28E-03	9.94E-04	1.08E-03	3.00E-04	2.24E-04	4.02E-06	6.30E-07	5.61E-07
	DS_2	\	8.81E-03	2.47E-03	\	4.57E-03	9.26E-04	\	8.87E-05	5.57E-06
	DS_3	\	\	1.32E-02	\	\	1.04E-02	\	\	5.93E-04
4	DS_1	4.35E-03	1.95E-03	1.51E-03	2.95E-03	5.47E-04	3.30E-04	3.32E-05	2.04E-06	1.20E-06
	DS_2	\	1.08E-02	3.59E-03	\	7.12E-03	2.02E-03	\	2.66E-04	2.90E-05
	DS_3	\	\	2.10E-02	\	\	1.23E-02	\	\	7.21E-04
5	DS_1	7.98E-03	2.65E-03	1.84E-03	3.40E-03	6.48E-04	3.43E-04	6.01E-05	3.61E-06	1.42E-06
	DS_2	\	1.52E-02	5.79E-03	\	7.52E-03	2.23E-03	\	3.27E-04	4.39E-05
	DS_3	\	\	2.43E-02	\	\	1.06E-02	\	\	6.42E-04
6	DS_1	8.60E-03	2.78E-03	1.83E-03	4.04E-03	7.93E-04	3.45E-04	1.01E-04	6.09E-06	1.52E-06
	DS_2	\	1.58E-02	6.06E-03	\	8.68E-03	2.93E-03	\	4.90E-04	8.81E-05
	DS_3	\	\	2.14E-02	\	\	1.23E-02	\	\	8.46E-04
7	DS_1	5.84E-04	3.17E-04	2.26E-04	2.37E-05	7.71E-06	5.50E-06	7.22E-09	1.47E-09	1.30E-09
	DS_2	\	4.46E-03	8.53E-04	\	1.33E-03	7.44E-05	\	1.16E-05	8.12E-08
	DS_3	\	\	7.24E-03	\	\	2.75E-03	\	\	4.99E-05
8	DS_1	2.55E-03	1.30E-03	1.01E-03	3.90E-04	1.24E-04	8.79E-05	5.79E-07	1.12E-07	8.12E-08
	DS_2	\	1.02E-02	2.71E-03	\	4.23E-03	5.47E-04	\	7.64E-05	1.83E-06
	DS_3	\	\	1.57E-02	\	\	7.35E-03	\	\	2.26E-04
9	DS_1	4.33E-03	2.04E-03	1.71E-03	1.06E-03	3.08E-04	2.74E-04	3.84E-06	5.83E-07	7.50E-07
	DS_2	\	1.16E-02	3.75E-03	\	5.00E-03	9.61E-04	\	9.96E-05	5.26E-06
	DS_3	\	\	2.29E-02	\	\	1.15E-02	\	\	6.79E-04
10	DS_1	6.40E-03	2.77E-03	2.10E-03	2.06E-03	5.56E-04	3.95E-04	1.41E-05	1.79E-06	1.43E-06
	DS_2	\	1.49E-02	5.63E-03	\	6.91E-03	1.89E-03	\	2.15E-04	2.21E-05
	DS_3	\	\	2.22E-02	\	\	1.11E-02	\	\	5.17E-04

Table 4.4 (*Continued*) Failure rates for the RC structures computed using the parametric state-dependent fragility curves obtained using the gamma distribution.

		L'AQUILA			NAPLES			MILAN		
#	λ_f	DS_2	DS_3	DS_4	DS_2	DS_3	DS_4	DS_2	DS_3	DS_4
11	DS_1	6.42E-03	3.00E-03	2.41E-03	2.12E-03	6.60E-04	5.13E-04	1.72E-05	2.67E-06	2.42E-06
	DS_2	\	1.50E-02	5.89E-03	\	6.97E-03	2.00E-03	\	2.24E-04	2.36E-05
	DS_3	\	\	2.76E-02	\	\	1.41E-02	\	\	8.39E-04
12	DS_1	7.15E-03	3.35E-03	2.54E-03	2.58E-03	8.30E-04	5.52E-04	3.14E-05	4.60E-06	2.65E-06
	DS_2	\	1.57E-02	6.62E-03	\	7.41E-03	2.44E-03	\	2.81E-04	4.08E-05
	DS_3	\	\	2.60E-02	\	\	1.32E-02	\	\	7.06E-04
13	DS_1	5.98E-04	3.20E-04	2.25E-04	2.48E-05	7.88E-06	5.51E-06	7.71E-09	1.52E-09	1.32E-09
	DS_2	\	4.02E-03	8.06E-04	\	1.08E-03	6.64E-05	\	6.75E-06	6.67E-08
	DS_3	\	\	6.33E-03	\	\	2.24E-03	\	\	3.04E-05
14	DS_1	2.46E-03	1.23E-03	9.53E-04	3.69E-04	1.13E-04	8.02E-05	5.41E-07	9.71E-08	7.27E-08
	DS_2	\	9.63E-03	2.51E-03	\	3.96E-03	4.87E-04	\	8.04E-05	1.59E-06
	DS_3	\	\	1.30E-02	\	\	5.79E-03	\	\	1.39E-04
15	DS_1	3.04E-03	1.46E-03	1.17E-03	5.93E-04	1.76E-04	1.48E-04	1.51E-06	2.58E-07	3.06E-07
	DS_2	\	8.68E-03	2.66E-03	\	3.33E-03	5.64E-04	\	4.35E-05	2.34E-06
	DS_3	\	\	1.39E-02	\	\	6.36E-03	\	\	2.06E-04
16	DS_1	4.05E-03	2.05E-03	1.63E-03	9.91E-04	3.47E-04	2.74E-04	3.91E-06	9.09E-07	9.22E-07
	DS_2	\	9.62E-03	3.42E-03	\	3.87E-03	8.57E-04	\	6.04E-05	4.86E-06
	DS_3	\	\	1.94E-02	\	\	9.55E-03	\	\	5.54E-04
17	DS_1	3.58E-03	2.13E-03	1.67E-03	8.35E-04	4.21E-04	3.09E-04	3.28E-06	1.77E-06	1.35E-06
	DS_2	\	1.08E-02	3.63E-03	\	4.62E-03	9.94E-04	\	1.05E-04	7.75E-06
	DS_3	\	\	1.92E-02	\	\	9.41E-03	\	\	4.51E-04
18	DS_1	4.75E-03	2.48E-03	2.04E-03	1.36E-03	5.14E-04	4.05E-04	8.61E-06	2.14E-06	1.84E-06
	DS_2	\	1.32E-02	5.18E-03	\	6.05E-03	1.73E-03	\	2.14E-04	2.34E-05
	DS_3	\	\	2.34E-02	\	\	1.18E-02	\	\	6.86E-04

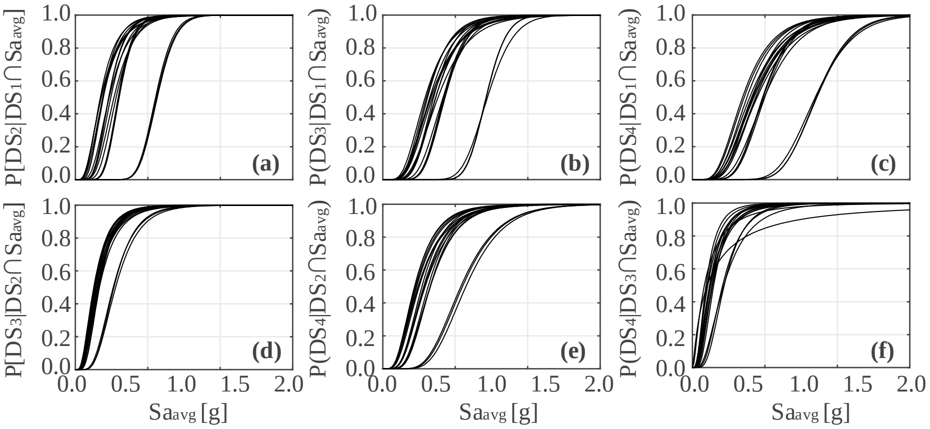

Figure 4.11 State-dependent fragility curves of RC structures.

Table 4.5 Median η and logarithmic standard deviation β defining the state-dependent fragility curves of RC structures (IM in g).

#	Code Level	H	Lateral Force Coefficient (%)	DS	DS_2		DS_3		DS_4	
					η	β	η	β	η	β
1	Absent	1	0.00	DS_1	0.55	0.18	0.72	0.20	0.85	0.25
				DS_2	\	\	0.28	0.45	0.57	0.35
				DS_3	\	\	\	\	0.22	0.63
2	Absent	2	0.00	DS_1	0.30	0.28	0.42	0.29	0.49	0.32
				DS_2	\	\	0.16	0.49	0.33	0.41
				DS_3	\	\	\	\	0.15	0.53
3	Absent	3	0.00	DS_1	0.23	0.38	0.37	0.36	0.44	0.40
				DS_2	\	\	0.15	0.54	0.28	0.48
				DS_3	\	\	\	\	0.10	1.55
4	Absent	4	0.00	DS_1	0.17	0.51	0.32	0.43	0.41	0.44
				DS_2	\	\	0.14	0.62	0.23	0.54
				DS_3	\	\	\	\	0.11	0.74
5	Absent	5	0.00	DS_1	0.18	0.58	0.33	0.47	0.42	0.45
				DS_2	\	\	0.14	0.63	0.24	0.57
				DS_3	\	\	\	\	0.13	0.69
6	Absent	6	0.00	DS_1	0.18	0.59	0.33	0.49	0.42	0.46
				DS_2	\	\	0.15	0.66	0.24	0.60
				DS_3	\	\	\	\	0.12	0.76
7	Low	1	5.00	DS_1	0.57	0.18	0.71	0.15	0.85	0.22
				DS_2	\	\	0.26	0.46	0.54	0.37
				DS_3	\	\	\	\	0.21	0.54
8	Low	2	5.00	DS_1	0.30	0.27	0.42	0.29	0.48	0.32
				DS_2	\	\	0.15	0.56	0.31	0.42
				DS_3	\	\	\	\	0.12	0.64
9	Low	3	5.00	DS_1	0.23	0.37	0.35	0.35	0.41	0.39
				DS_2	\	\	0.14	0.54	0.27	0.46
				DS_3	\	\	\	\	0.12	0.64
10	Low	4	5.00	DS_1	0.19	0.44	0.31	0.40	0.38	0.43
				DS_2	\	\	0.13	0.64	0.23	0.54
				DS_3	\	\	\	\	0.10	0.67
11	Low	5	5.00	DS_1	0.19	0.47	0.30	0.43	0.36	0.46
				DS_2	\	\	0.13	0.59	0.22	0.53
				DS_3	\	\	\	\	0.08	1.09
12	Low	6	5.00	DS_1	0.19	0.53	0.29	0.47	0.35	0.46
				DS_2	\	\	0.13	0.60	0.22	0.55
				DS_3	\	\	\	\	0.09	0.65
13	Low	1	10.00	DS_1	0.56	0.18	0.71	0.16	0.86	0.23
				DS_2	\	\	0.27	0.43	0.55	0.37
				DS_3	\	\	\	\	0.22	0.49
14	Low	2	10.00	DS_1	0.30	0.27	0.43	0.29	0.50	0.32
				DS_2	\	\	0.17	0.60	0.33	0.44
				DS_3	\	\	\	\	0.14	0.56
15	Low	3	10.00	DS_1	0.28	0.35	0.42	0.35	0.50	0.39
				DS_2	\	\	0.17	0.50	0.33	0.45
				DS_3	\	\	\	\	0.14	0.62

Table 4.5 (*Continued*) Median η and logarithmic standard deviation β defining the state-dependent fragility curves of RC structures (IM in g).

#	Code Level	H	Lateral Force Coefficient (%)	DS	DS_2		DS_3		DS_4	
					η	β	η	β	η	β
16	Low	4	10.00	DS_1	0.24	0.39	0.36	0.39	0.44	0.43
				DS_2	\	\	0.16	0.53	0.29	0.48
				DS_3	\	\	\	\	0.14	0.68
17	Low	5	10.00	DS_1	0.27	0.41	0.38	0.44	0.45	0.45
				DS_2	\	\	0.16	0.57	0.29	0.51
				DS_3	\	\	\	\	0.11	0.98
18	Low	6	10.00	DS_1	0.23	0.46	0.34	0.45	0.40	0.47
				DS_2	\	\	0.15	0.62	0.25	0.54
				DS_3	\	\	\	\	0.11	0.72

4.4.2. Masonry structures

4.4.2.1. Classical curves

Figure 4.12 and Figure 4.13 show the fragility curves of the intact structures obtained analyzing via IDA the two benchmark systems of masonry structures shown in panel (c) of Figure 4.2. Each panel of these figures represents the comparison between the non-parametric fragilities and the parametric fragility curves evaluated according to Eq.(4.1) for each arriving damage state; i.e. panel (a) refers to DS_1; panel (b) to DS_2; panel (c) to DS_3 and panel (d) to DS_4. Figure 4.12 and Figure 4.13 show the good agreement between the lognormal distribution with the results obtained analyzing the masonry structures.

In Figure 4.14 are reported the fragility curves obtained analyzing the entire set of fifteen masonry structures. Similarly to Figure 4.12 and Figure 4.13, each panel of Figure 4.14 shows the fragility curves of the intact structures evaluated for each arriving damage state using the lognormal distribution (Eq.(4.1)) i.e. panel (a) for DS_1; panel (b) for DS_2; panel (c) for DS_3 and panel (d) for DS_4.

The values of median, η, and logarithmic standard deviation, β, defining the parametric fragilities of intact structures numbered from 1 to 15 are reported in Table 4.6. The table also reports for each structure the masonry material, i.e., rubble stone unreinforced masonry (STRUB); dressed stone unreinforced masonry (STDRE), clay brick unreinforced masonry (CL99) and confined masonry structures (MCF). In addition, the masonry structures are characterized by the level of available ductility (non-ductile or low) and the height expressed in terms of number of stories (H).

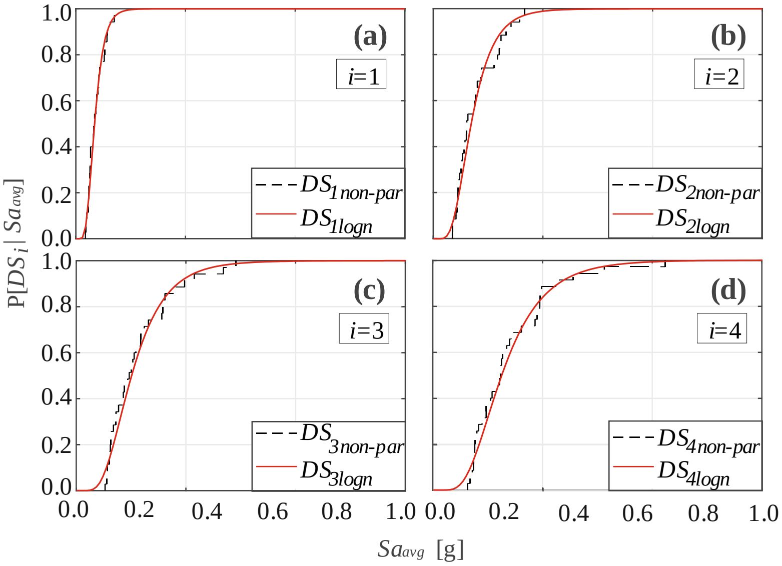

Figure 4.12 Fragility curves evaluated for the benchmark system 1 of masonry structures for the four damage states DS_1 (a); DS_2 (b); DS_3 (c) and DS_4 (d).

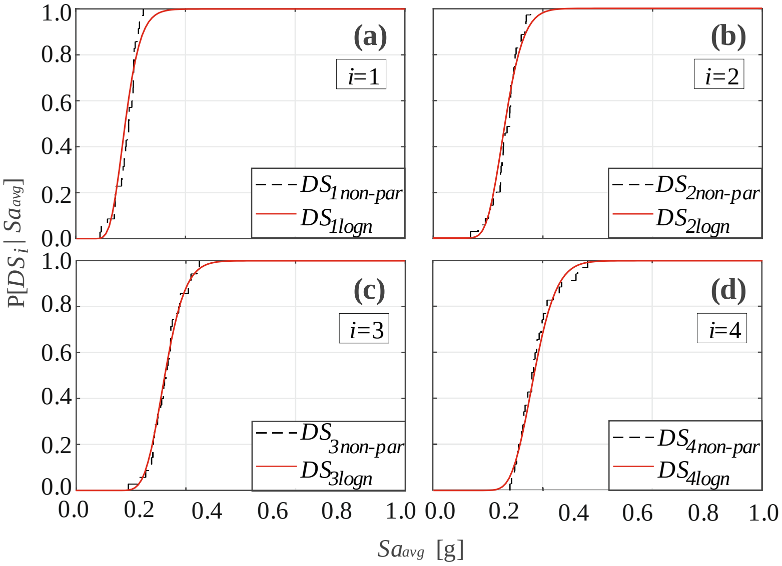

Figure 4.13 Fragility curves evaluated for the benchmark system 2 of masonry structures for the four damage states DS_1 (a); DS_2 (b); DS_3 (c) and DS_4 (d).

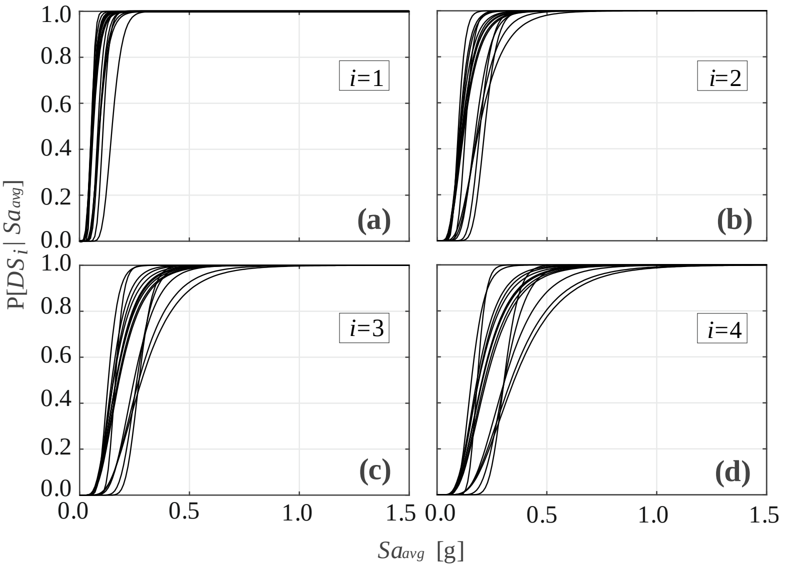

Figure 4.14 Fragility curves of masonry structures evaluated for the four damage states DS_1 (a); DS_2 (b); DS_3 (c) and DS_4 (d).

Table 4.6 Median η and logarithmic standard deviation β defining the state-dependent fragility curves of masonry structures (IM in g).

#	Material	Available Ductility	H	MEDIAN η				SIGMA β			
				DS_1	DS_2	DS_3	DS_4	DS_1	DS_2	DS_3	DS_4
1	STRUB	non-ductile	1	0.08	0.13	0.16	0.18	0.26	0.22	0.18	0.17
2	STRUB	non-ductile	2	0.06	0.10	0.13	0.16	0.21	0.25	0.28	0.30
3	STRUB	non-ductile	3	0.05	0.10	0.15	0.18	0.30	0.33	0.38	0.42
4	STRUB	non-ductile	4	0.05	0.11	0.15	0.19	0.37	0.42	0.45	0.47
5	STRUB	non-ductile	5	0.06	0.11	0.17	0.21	0.40	0.46	0.48	0.47
6	CL99	non-ductile	3	0.06	0.11	0.15	0.19	0.33	0.34	0.40	0.43
7	CL99	non-ductile	4	0.06	0.12	0.17	0.21	0.37	0.43	0.46	0.47
8	CL99	non-ductile	5	0.06	0.13	0.18	0.23	0.41	0.46	0.47	0.48
9	STDRE	non-ductile	4	0.06	0.12	0.17	0.21	0.36	0.40	0.44	0.47
10	STDRE	non-ductile	5	0.06	0.12	0.18	0.22	0.41	0.46	0.47	0.47
11	MCF	low	1	0.15	0.22	0.27	0.31	0.25	0.20	0.18	0.18
12	MCF	low	2	0.11	0.20	0.26	0.31	0.21	0.22	0.24	0.26
13	MCF	low	3	0.09	0.18	0.25	0.31	0.27	0.31	0.35	0.41
14	MCF	low	4	0.09	0.19	0.27	0.34	0.34	0.38	0.43	0.46
15	MCF	low	5	0.09	0.19	0.28	0.35	0.37	0.46	0.46	0.47

4.4.2.2. State-dependent fragility curves

For the state-dependent fragilities, the assumption of a lognormal distribution or, alternatively, of a gamma distribution is investigated also in the case of masonry structures. An example of comparison between the non-parametric state-dependent fragilities (identified by the *non-par* subscript in the legend) and the parametric ones evaluated using the lognormal distribution (*log* subscript) is shown in Figure 4.15 for the benchmark system 1 of masonry structures. Each panel of the figure shows the state-dependent fragility curves referring to different starting state and having the same final state; i.e. panel (a) refers to DS_2, panel (b) refers to DS_3 and refers to DS_4. Figure 4.16 shows the same results reported in Figure 4.15 but compares the non-parametric state-dependent fragilities with the parametric ones evaluated using the gamma distribution (*gamma* subscript).

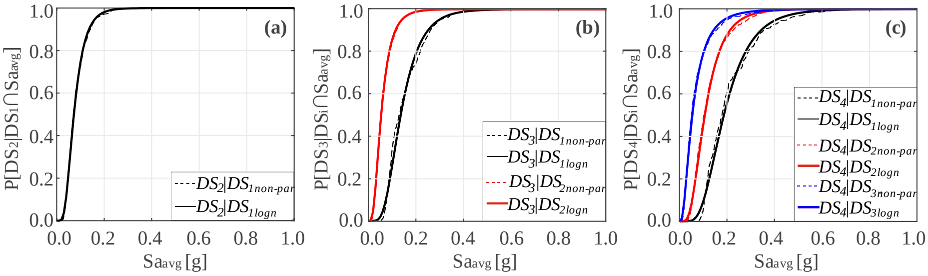

Figure 4.15 Comparison of the non-parametric and the parametric state-dependent fragility curves evaluated for the benchmark system 1 of masonry structures assuming the lognormal distribution and having different starting damage state and the same final state DS_2 (a), DS_3 (b) and DS_4 (c).

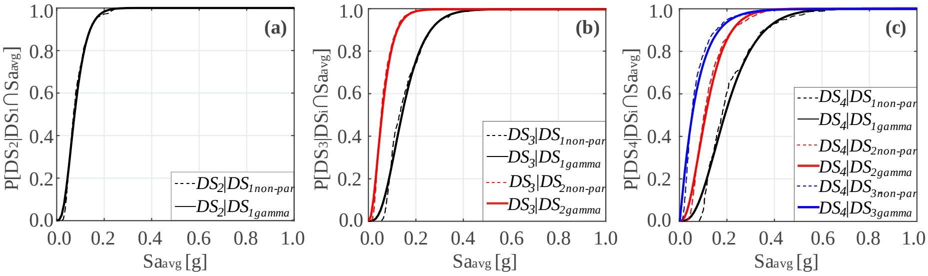

Figure 4.16 Comparison of the non-parametric and the parametric state-dependent fragility curves evaluated for the benchmark system 1 of masonry structures assuming the gamma distribution and having different starting damage state and the same final state DS_2 (a), DS_3 (b) and DS_4 (c).

The choice between the two possible distributions (*lognormal* and *gamma*) to define the state-dependent fragility curves is conducted also in case of the masonry structures in terms of failure rates (see Eq. (4.6)). The failure rates of the fifteen masonry structures at the three Italian sites (L'Aquila, Naples and Milan) are evaluated using the hazard curves shown in Figure 4.10b. The results for the three sites are shown in Table 4.7, Table 4.8 and in Table 4.9 in case failure rates evaluated using the non-parametric state-dependent fragilities, the parametric state-dependent fragilities obtained using the lognormal and the gamma distribution, respectively.

Comparing the results obtained; it is found that modeling the state-dependent fragilities via a lognormal distribution provides failure rates closer to those obtained using the non-parametric results, for all the possible transitions between different damage states and considering the three levels of seismic hazard. Therefore, the lognormal distribution was chosen to represent the state-dependent fragilities also for masonry structures classes.

Table 4.10 collects the values of the median, η, and logarithmic standard deviation, β, defining lognormal distribution, Eq. (4.1); i.e., the parametric state-dependent fragility curves for the fifteen masonry structures. In the table, the fifth column gives the initial damage state where the damage states reported in the rest of the row represent the arrival damage states.

Figure 4.17 shows the state-dependent fragility curves obtained analyzing the entire set of fifteen masonry structures via back-to-back IDA and assuming the lognormal distribution. Each panel of Figure 4.17 shows the state-dependent fragility curves obtained considering a possible transition between damage states, i.e. from DS_1 to DS_2 (panel a); from DS_1 to DS_3 (panel b); from DS_1 to DS_4 (panel c); from DS_2 to DS_3 (panel d);); from DS_2 to DS_4 (panel e) and from DS_3 to DS_4 (panel f).

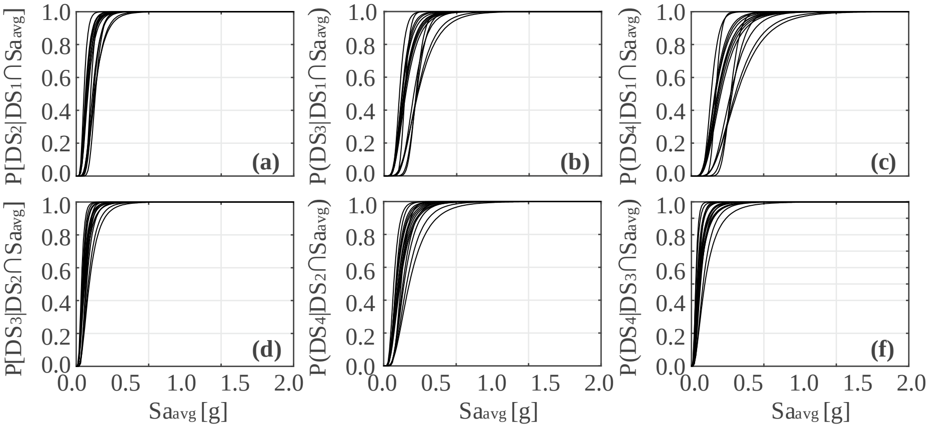

Figure 4.17 State-dependent fragility curves of masonry structures.

Table 4.7 Failure rates for the masonry structures computed using the non-parametric state-dependent fragility curves

		L'AQUILA			NAPLES			MILAN		
#	λ_f	DS_2	DS_3	DS_4	DS_2	DS_3	DS_4	DS_2	DS_3	DS_4
1	DS_1	1.35E-02	7.86E-03	6.00E-03	5.57E-03	2.40E-03	1.52E-03	3.75E-05	8.03E-06	3.52E-06
	DS_2	\	4.29E-02	1.81E-02	\	2.42E-02	8.53E-03	\	6.64E-04	9.42E-05
	DS_3	\	\	6.41E-02	\	\	3.70E-02	\	\	1.49E-03
2	DS_1	3.20E-02	1.26E-02	8.64E-03	1.74E-02	5.07E-03	2.88E-03	3.23E-04	3.06E-05	1.15E-05
	DS_2	\	5.09E-02	2.30E-02	\	2.91E-02	1.17E-02	\	9.35E-04	1.61E-04
	DS_3	\	\	6.30E-02	\	\	3.62E-02	\	\	1.52E-03
3	DS_1	2.38E-02	1.07E-02	7.18E-03	1.22E-02	4.06E-03	2.25E-03	1.76E-04	2.24E-05	8.39E-06
	DS_2	\	4.19E-02	1.82E-02	\	2.35E-02	8.71E-03	\	7.05E-04	1.04E-04
	DS_3	\	\	5.18E-02	\	\	2.94E-02	\	\	1.10E-03
4	DS_1	2.65E-02	1.09E-02	7.06E-03	1.39E-02	4.27E-03	2.24E-03	2.27E-04	2.68E-05	8.77E-06
	DS_2	\	3.96E-02	1.80E-02	\	2.20E-02	8.64E-03	\	6.29E-04	1.09E-04
	DS_3	\	\	4.23E-02	\	9.20E+01	2.36E-02	\	\	7.76E-04
5	DS_1	2.27E-02	9.69E-03	6.11E-03	1.15E-02	3.65E-03	1.81E-03	1.69E-04	2.10E-05	6.36E-06
	DS_2	\	3.45E-02	1.45E-02	\	1.89E-02	6.54E-03	\	4.86E-04	6.69E-05
	DS_3	\	\	4.02E-02	\	\	2.22E-02	\	\	8.47E-04
6	DS_1	2.47E-02	1.04E-02	6.96E-03	1.27E-02	3.92E-03	2.16E-03	1.95E-04	2.17E-05	8.00E-06
	DS_2	\	4.01E-02	1.74E-02	\	2.23E-02	8.22E-03	\	6.38E-04	9.41E-05
	DS_3	\	\	4.54E-02	\	\	2.56E-02	\	\	8.28E-04
7	DS_1	2.51E-02	9.88E-03	6.39E-03	1.30E-02	3.74E-03	1.93E-03	2.10E-04	2.19E-05	6.94E-06
	DS_2	\	3.59E-02	1.57E-02	\	1.97E-02	7.26E-03	\	5.37E-04	8.28E-05
	DS_3	\	\	4.05E-02	\	\	2.25E-02	\	\	7.41E-04
8	DS_1	2.00E-02	8.62E-03	5.33E-03	9.84E-03	3.08E-03	1.46E-03	1.27E-04	1.58E-05	4.51E-06
	DS_2	\	3.22E-02	1.34E-02	\	1.75E-02	5.91E-03	\	4.38E-04	5.99E-05
	DS_3	\	\	3.41E-02	\	\	1.87E-02	\	\	5.29E-04
9	DS_1	2.11E-02	9.29E-03	6.11E-03	1.05E-02	3.38E-03	1.79E-03	1.32E-04	1.77E-05	5.97E-06
	DS_2	\	3.58E-02	1.58E-02	\	1.97E-02	7.28E-03	\	4.99E-04	8.04E-05
	DS_3	\	\	3.92E-02	\	\	2.16E-02	\	9.20E+01	7.24E-04
10	DS_1	2.23E-02	9.25E-03	5.73E-03	1.13E-02	3.42E-03	1.64E-03	1.63E-04	1.89E-05	5.45E-06
	DS_2	\	3.29E-02	1.41E-02	\	1.79E-02	6.33E-03	\	4.56E-04	6.53E-05
	DS_3	\	\	3.67E-02	\	\	2.02E-02	\	\	6.81E-04
11	DS_1	1.08E-02	4.00E-03	2.72E-03	4.09E-03	7.77E-04	3.83E-04	2.51E-05	1.34E-06	4.05E-07
	DS_2	\	2.44E-02	1.07E-02	\	1.26E-02	4.03E-03	\	1.67E-04	2.18E-05
	DS_3	\	\	3.44E-02	\	9.20E+01	1.89E-02	\	\	3.86E-04
12	DS_1	9.05E-03	3.96E-03	2.67E-03	3.07E-03	7.70E-04	3.89E-04	1.30E-05	1.27E-06	4.42E-07
	DS_2	\	2.37E-02	9.94E-03	\	1.21E-02	3.75E-03	\	1.82E-04	2.51E-05
	DS_3	\	\	3.23E-02	\	\	1.76E-02	\	\	3.94E-04
13	DS_1	1.22E-02	4.85E-03	3.10E-03	4.99E-03	1.17E-03	5.60E-04	3.57E-05	2.80E-06	8.79E-07
	DS_2	\	2.34E-02	9.39E-03	\	1.20E-02	3.51E-03	\	1.90E-04	2.37E-05
	DS_3	\	\	2.89E-02	\	\	1.55E-02	\	\	3.30E-04
14	DS_1	1.02E-02	4.30E-03	2.69E-03	3.89E-03	1.00E-03	4.60E-04	2.30E-05	2.31E-06	6.79E-07
	DS_2	\	2.04E-02	8.18E-03	\	1.01E-02	2.92E-03	\	1.47E-04	1.69E-05
	DS_3	\	\	2.23E-02	\	\	1.14E-02	\	\	2.11E-04
15	DS_1	1.11E-02	4.32E-03	2.60E-03	4.45E-03	1.04E-03	4.46E-04	3.17E-05	2.60E-06	6.82E-07
	DS_2	\	1.89E-02	7.34E-03	\	9.24E-03	2.56E-03	\	1.41E-04	1.59E-05
	DS_3	\	\	2.02E-02	\	\	1.02E-02	\	\	1.88E-04

Table 4.8 Failure rates for the masonry structures computed using the parametric state-dependent fragility curves obtained using the lognormal distribution.

		L'AQUILA			NAPLES			MILAN		
#	λ_f	DS_2	DS_3	DS_4	DS_2	DS_3	DS_4	DS_2	DS_3	DS_4
1	DS_1	1.34E-02	7.83E-03	5.99E-03	5.52E-03	2.38E-03	1.52E-03	3.47E-05	7.63E-06	3.57E-06
	DS_2	\	4.27E-02	1.80E-02	\	2.41E-02	8.48E-03	\	6.57E-04	9.09E-05
	DS_3	\	\	6.40E-02	\	\	3.69E-02	\	\	1.56E-03
2	DS_1	3.20E-02	1.26E-02	8.67E-03	1.74E-02	5.09E-03	2.91E-03	3.27E-04	3.24E-05	1.25E-05
	DS_2	\	5.11E-02	2.31E-02	\	2.92E-02	1.17E-02	\	9.63E-04	1.69E-04
	DS_3	\	\	6.45E-02	\	\	3.67E-02	\	\	1.83E-03
3	DS_1	2.38E-02	1.07E-02	7.26E-03	1.22E-02	4.10E-03	2.33E-03	1.78E-04	2.52E-05	1.07E-05
	DS_2	\	4.17E-02	1.83E-02	\	2.34E-02	8.71E-03	\	6.65E-04	1.09E-04
	DS_3	\	\	5.26E-02	\	\	2.96E-02	\	\	1.28E-03
4	DS_1	2.65E-02	1.10E-02	7.19E-03	1.39E-02	4.33E-03	2.35E-03	2.42E-04	3.17E-05	1.22E-05
	DS_2	\	4.00E-02	1.82E-02	\	2.22E-02	8.72E-03	\	7.12E-04	1.22E-04
	DS_3	\	\	4.36E-02	\	\	2.42E-02	\	\	9.96E-04
5	DS_1	2.29E-02	9.80E-03	6.25E-03	1.16E-02	3.74E-03	1.93E-03	1.86E-04	2.68E-05	9.37E-06
	DS_2	\	3.48E-02	1.46E-02	\	1.90E-02	6.59E-03	\	5.37E-04	7.81E-05
	DS_3	\	\	4.13E-02	\	\	2.26E-02	\	\	1.06E-03
6	DS_1	2.47E-02	1.04E-02	7.00E-03	1.27E-02	3.94E-03	2.21E-03	2.02E-04	2.44E-05	1.02E-05
	DS_2	\	3.97E-02	1.75E-02	\	2.21E-02	8.25E-03	\	6.03E-04	1.02E-04
	DS_3	\	\	4.61E-02	\	\	2.58E-02	\	\	9.54E-04
7	DS_1	2.52E-02	9.99E-03	6.47E-03	1.30E-02	3.82E-03	2.02E-03	2.27E-04	2.69E-05	9.78E-06
	DS_2	\	3.63E-02	1.58E-02	\	1.99E-02	7.32E-03	\	6.04E-04	9.34E-05
	DS_3	\	\	4.21E-02	\	\	2.31E-02	\	\	1.00E-03
8	DS_1	2.01E-02	8.72E-03	5.45E-03	9.89E-03	3.17E-03	1.57E-03	1.40E-04	2.07E-05	6.88E-06
	DS_2	\	3.25E-02	1.35E-02	\	1.75E-02	5.99E-03	\	5.00E-04	7.01E-05
	DS_3	\	\	3.54E-02	\	\	1.92E-02	\	\	7.27E-04
9	DS_1	2.12E-02	9.37E-03	6.19E-03	1.05E-02	3.44E-03	1.87E-03	1.45E-04	2.15E-05	8.33E-06
	DS_2	\	3.63E-02	1.59E-02	\	1.99E-02	7.33E-03	\	5.60E-04	8.89E-05
	DS_3	\	\	3.96E-02	\	\	2.18E-02	\	\	7.98E-04
10	DS_1	2.25E-02	9.37E-03	5.85E-03	1.14E-02	3.51E-03	1.75E-03	1.81E-04	2.43E-05	8.05E-06
	DS_2	\	3.34E-02	1.43E-02	\	1.81E-02	6.45E-03	\	5.41E-04	7.92E-05
	DS_3	\	\	3.81E-02	\	\	2.07E-02	\	\	9.02E-04
11	DS_1	1.07E-02	3.99E-03	2.72E-03	4.05E-03	7.68E-04	3.85E-04	2.28E-05	1.25E-06	4.16E-07
	DS_2	\	2.44E-02	1.07E-02	\	1.26E-02	4.06E-03	\	1.75E-04	2.35E-05
	DS_3	\	\	3.46E-02	\	\	1.90E-02	\	\	4.09E-04
12	DS_1	9.05E-03	3.97E-03	2.68E-03	3.07E-03	7.88E-04	4.02E-04	1.31E-05	1.42E-06	5.16E-07
	DS_2	\	2.37E-02	9.93E-03	\	1.21E-02	3.75E-03	\	1.80E-04	2.47E-05
	DS_3	\	\	3.28E-02	\	\	1.78E-02	\	\	4.56E-04
13	DS_1	1.22E-02	4.87E-03	3.14E-03	4.97E-03	1.19E-03	6.00E-04	3.61E-05	3.28E-06	1.24E-06
	DS_2	\	2.34E-02	9.38E-03	\	1.20E-02	3.50E-03	\	2.02E-04	2.39E-05
	DS_3	\	\	2.93E-02	\	\	1.56E-02	\	\	3.78E-04
14	DS_1	1.03E-02	4.35E-03	2.74E-03	3.92E-03	1.06E-03	5.16E-04	2.58E-05	3.22E-06	1.16E-06
	DS_2	\	2.07E-02	8.25E-03	\	1.03E-02	2.98E-03	\	1.73E-04	2.07E-05
	DS_3	\	\	2.26E-02	\	\	1.15E-02	\	\	2.48E-04
15	DS_1	1.12E-02	4.39E-03	2.66E-03	4.49E-03	1.12E-03	5.12E-04	3.62E-05	3.92E-06	1.24E-06
	DS_2	\	1.90E-02	7.41E-03	\	9.26E-03	2.62E-03	\	1.56E-04	1.89E-05
	DS_3	\	\	2.09E-02	\	\	1.05E-02	\	\	2.64E-04

Table 4.9 Failure rates for the masonry structures computed using the parametric state-dependent fragility curves obtained using the gamma distribution.

		L'AQUILA			NAPLES			MILAN		
#	λ_f	DS_2	DS_3	DS_4	DS_2	DS_3	DS_4	DS_2	DS_3	DS_4
1	DS_1	1.33E-02	7.81E-03	6.02E-03	5.45E-03	2.37E-03	1.54E-03	3.38E-05	7.54E-06	3.73E-06
	DS_2	\	4.74E-02	1.83E-02	\	2.65E-02	8.69E-03	\	1.07E-03	1.06E-04
	DS_3	\	\	6.82E-02	\	\	3.88E-02	\	\	2.07E-03
2	DS_1	3.34E-02	1.29E-02	8.88E-03	1.82E-02	5.32E-03	3.05E-03	4.10E-04	3.88E-05	1.51E-05
	DS_2	\	5.79E-02	2.51E-02	\	3.27E-02	1.29E-02	\	1.65E-03	2.70E-04
	DS_3	\	\	8.47E-02	\	\	4.67E-02	\	\	4.16E-03
3	DS_1	2.49E-02	1.11E-02	7.80E-03	1.28E-02	4.38E-03	2.69E-03	2.34E-04	3.38E-05	1.89E-05
	DS_2	\	4.62E-02	2.01E-02	\	2.57E-02	9.84E-03	\	1.09E-03	1.97E-04
	DS_3	\	\	6.47E-02	\	\	3.57E-02	\	\	2.63E-03
4	DS_1	2.88E-02	1.19E-02	8.21E-03	1.52E-02	4.96E-03	3.03E-03	3.87E-04	5.74E-05	3.19E-05
	DS_2	\	5.11E-02	2.22E-02	\	2.79E-02	1.11E-02	\	1.79E-03	3.53E-04
	DS_3	\	\	5.92E-02	\	\	3.21E-02	\	\	2.63E-03
5	DS_1	2.58E-02	1.12E-02	7.55E-03	1.33E-02	4.64E-03	2.78E-03	3.63E-04	6.51E-05	3.47E-05
	DS_2	\	4.26E-02	1.79E-02	\	2.31E-02	8.59E-03	\	1.27E-03	2.46E-04
	DS_3	\	\	6.89E-02	\	\	3.68E-02	\	\	3.89E-03
6	DS_1	2.62E-02	1.09E-02	7.58E-03	1.36E-02	4.29E-03	2.60E-03	2.89E-04	3.50E-05	1.90E-05
	DS_2	\	4.32E-02	1.96E-02	\	2.39E-02	9.53E-03	\	9.33E-04	2.02E-04
	DS_3	\	\	5.69E-02	\	\	3.13E-02	\	\	2.09E-03
7	DS_1	2.80E-02	1.11E-02	7.54E-03	1.46E-02	4.56E-03	2.72E-03	4.09E-04	5.67E-05	2.92E-05
	DS_2	\	4.67E-02	1.93E-02	\	2.53E-02	9.40E-03	\	1.59E-03	2.79E-04
	DS_3	\	\	6.60E-02	\	\	3.54E-02	\	\	3.46E-03
8	DS_1	2.24E-02	1.01E-02	6.68E-03	1.12E-02	4.04E-03	2.36E-03	2.62E-04	5.51E-05	2.85E-05
	DS_2	\	4.29E-02	1.72E-02	\	2.31E-02	8.20E-03	\	1.46E-03	2.61E-04
	DS_3	\	\	5.92E-02	\	\	3.16E-02	\	\	3.06E-03
9	DS_1	2.27E-02	1.01E-02	6.99E-03	1.14E-02	3.95E-03	2.40E-03	2.22E-04	3.82E-05	2.10E-05
	DS_2	\	4.51E-02	1.91E-02	\	2.45E-02	9.26E-03	\	1.37E-03	2.47E-04
	DS_3	\	\	5.29E-02	\	\	2.86E-02	\	\	2.14E-03
10	DS_1	2.56E-02	1.07E-02	7.07E-03	1.32E-02	4.37E-03	2.54E-03	3.69E-04	6.01E-05	3.04E-05
	DS_2	\	4.69E-02	1.88E-02	\	2.52E-02	9.11E-03	\	1.80E-03	3.22E-04
	DS_3	\	\	6.69E-02	\	\	3.56E-02	\	\	3.79E-03
11	DS_1	1.07E-02	3.98E-03	2.74E-03	4.02E-03	7.64E-04	3.94E-04	2.34E-05	1.25E-06	4.45E-07
	DS_2	\	2.66E-02	1.13E-02	\	1.38E-02	4.47E-03	\	2.66E-04	3.36E-05
	DS_3	\	\	3.71E-02	\	\	2.04E-02	\	\	5.87E-04
12	DS_1	9.11E-03	4.11E-03	2.77E-03	3.12E-03	8.69E-04	4.46E-04	1.40E-05	1.89E-06	6.94E-07
	DS_2	\	2.54E-02	1.07E-02	\	1.31E-02	4.26E-03	\	2.61E-04	4.23E-05
	DS_3	\	\	4.83E-02	\	\	2.60E-02	\	\	1.82E-03
13	DS_1	1.26E-02	5.03E-03	3.37E-03	5.26E-03	1.30E-03	7.34E-04	4.73E-05	4.55E-06	2.42E-06
	DS_2	\	2.98E-02	1.06E-02	\	1.56E-02	4.31E-03	\	6.15E-04	5.58E-05
	DS_3	\	\	3.74E-02	\	\	2.00E-02	\	\	1.08E-03
14	DS_1	1.09E-02	4.75E-03	3.12E-03	4.33E-03	1.31E-03	7.36E-04	4.00E-05	6.92E-06	3.67E-06
	DS_2	\	2.74E-02	1.02E-02	\	1.41E-02	4.24E-03	\	6.32E-04	8.14E-05
	DS_3	\	\	3.14E-02	\	\	1.63E-02	\	\	9.52E-04
15	DS_1	1.25E-02	5.13E-03	3.34E-03	5.36E-03	1.58E-03	8.96E-04	7.82E-05	1.32E-05	7.14E-06
	DS_2	\	2.75E-02	9.71E-03	\	1.41E-02	4.07E-03	\	7.53E-04	1.00E-04
	DS_3	\	\	4.11E-02	\	\	2.15E-02	\	\	1.97E-03

Table 4.10 Median η and logarithmic standard deviation β defining the state-dependent fragility curves of masonry structures (IM in g).

#	Materials	Available Ductility	H	DS	DS_2		DS_3		DS_4	
					η	β	η	β	η	β
1	STRUB	non-ductile	1	DS_1	0.099	0.257	0.143	0.199	0.170	0.183
				DS_2	\	\	0.042	0.436	0.083	0.392
				DS_3	\	\	\	\	0.030	0.443
2	STRUB	non-ductile	2	DS_1	0.052	0.381	0.105	0.305	0.137	0.302
				DS_2	\	\	0.036	0.440	0.070	0.424
				DS_3	\	\	\	\	0.031	0.545
3	STRUB	non-ductile	3	DS_1	0.068	0.414	0.122	0.371	0.162	0.406
				DS_2	\	\	0.044	0.482	0.086	0.470
				DS_3	\	\	\	\	0.038	0.586
4	STRUB	non-ductile	4	DS_1	0.063	0.455	0.124	0.442	0.168	0.456
				DS_2	\	\	0.048	0.575	0.089	0.529
				DS_3	\	\	\	\	0.047	0.665
5	STRUB	non-ductile	5	DS_1	0.073	0.489	0.137	0.475	0.186	0.476
				DS_2	\	\	0.054	0.581	0.106	0.542
				DS_3	\	\	\	\	0.053	0.765
6	CL99	non-ductile	3	DS_1	0.067	0.440	0.125	0.388	0.167	0.418
				DS_2	\	\	0.046	0.485	0.089	0.484
				DS_3	\	\	\	\	0.042	0.575
7	CL99	non-ductile	4	DS_1	0.067	0.483	0.134	0.462	0.181	0.464
				DS_2	\	\	0.053	0.596	0.100	0.543
				DS_3	\	\	\	\	0.050	0.712
8	CL99	non-ductile	5	DS_1	0.080	0.485	0.149	0.480	0.204	0.479
				DS_2	\	\	0.059	0.618	0.114	0.567
				DS_3	\	\	\	\	0.059	0.721
9	STDRE	non-ductile	4	DS_1	0.075	0.443	0.138	0.434	0.184	0.448
				DS_2	\	\	0.052	0.556	0.098	0.517
				DS_3	\	\	\	\	0.051	0.650
10	STDRE	non-ductile	5	DS_1	0.074	0.494	0.141	0.478	0.195	0.476
				DS_2	\	\	0.058	0.630	0.109	0.566
				DS_3	\	\	\	\	0.057	0.762
11	MCF	low	1	DS_1	0.119	0.328	0.220	0.208	0.272	0.189
				DS_2	\	\	0.065	0.364	0.120	0.340
				DS_3	\	\	\	\	0.050	0.418
12	MCF	low	2	DS_1	0.132	0.273	0.224	0.255	0.282	0.265
				DS_2	\	\	0.068	0.422	0.132	0.434
				DS_3	\	\	\	\	0.056	0.559
13	MCF	low	3	DS_1	0.112	0.389	0.205	0.348	0.271	0.382
				DS_2	\	\	0.072	0.504	0.141	0.472
				DS_3	\	\	\	\	0.063	0.587
14	MCF	low	4	DS_1	0.128	0.420	0.228	0.419	0.304	0.441
				DS_2	\	\	0.082	0.562	0.159	0.523
				DS_3	\	\	\	\	0.081	0.644
15	MCF	low	5	DS_1	0.125	0.476	0.233	0.465	0.315	0.472
				DS_2	\	\	0.090	0.601	0.177	0.572
				DS_3	\	\	\	\	0.093	0.743

4.5. Conclusions

This study shows the results of the assessment of state-dependent fragility functions for Italian reinforced concrete and masonry structures taken from the outcomes of the SERA project. Fragility assessment was conducted via back-to-back IDA of an ESDoF approximation of single structures, each representing a building class. In this context, two issues significantly affecting the assessment were addressed: the choice of the intensity measure and the identification of the number of ground motion records for the execution of nonlinear dynamic analyses. Based on a comparison of different intensity measures, it was confirmed that those entailing a geometric mean of spectral accelerations, that is, Sa_{avg} and I_{NP}, were to be preferred due to exhibiting greater efficiency than single-period spectral ordinates. In lack of a specific calibration of the I_{NP} intensity measure at this stage, Sa_{avg} was selected for the state-dependent fragilities. As far as the number of records is concerned, a set of 35 ground motions was used as a compromise between computational costs and the precision in fragility assessment, based on the statistical inference concept of estimation uncertainty.

The fragility curves for the intact structures and the state-dependent fragility curves were modeled assuming a lognormal distribution.

References

Baker, J.W., and C.A. Cornell (2006).Spectral shape, epsilon and record selection.*Earthquake Engineering and Structural Dynamics*.35(9).1077–1095.

Baltzopoulos, G., R. Baraschino, and I. Iervolino (2018a).On the number of records for structural risk estimation in PBEE.*Earthquake Engineering & Structural Dynamics*.

Baltzopoulos, G., R. Baraschino, I. Iervolino, and D. Vamvatsikos (2018b).Dynamic analysis of single-degree-of-freedom systems (DYANAS): a graphical user interface for OpenSees.*Engineering Structures*.177.395–408.

Baltzopoulos, G., I. Iervolino, and R. Baraschino (2019).“Ground motion sample size vs estimation uncertainty in seismic risk.”in: *13th International Conference on Applications of Statistics and Probability in Civil Engineering, ICASP 2019*.

Barani, S., D. Spallarossa, and P. Bazzurro (2009).Disaggregation of probabilistic ground-motion Hazard in Italy.*Bulletin of the Seismological Society of America*.99(5).2638–2661.

Bindi, D., F. Pacor, L. Luzi, R. Puglia, M. Massa, G. Ameri, and R. Paolucci

(2011).Ground motion prediction equations derived from the Italian strong motion database.*Bulletin of Earthquake Engineering*.9(6).1899–1920.

Bojórquez, E., and I. Iervolino (2011).Spectral shape proxies and nonlinear structural response.*Soil Dynamics and Earthquake Engineering*.31(7).996–1008.

Brzev, S., C. Scawthorn, A.W. Charleson, L. Allen, M. Greene, K. Jaiswal, and V. Silva (2013).GEM Building Taxonomy Version 2.0.*GEM Technical Report*.02.188.

CEN (2004).“EN 1998-1: Eurocode 8 - Design of structures for earthquake resistance. Part 1: General rules, seismic actions and rules for buildings, European Committee for Standardization.”

Chioccarelli, E., P. Cito, I. Iervolino, and M. Giorgio (2018).REASSESS V2.0: software for single- and multi-site probabilistic seismic hazard analysis.*Bulletin of Earthquake Engineering*.

Cornell, C.A. (1968).Engineering seismic risk analysis.*Bulletin of the Seismological Society of America*.58(5).1583–1606.

Eads, L., E. Miranda, and D.G. Lignos (2015).Average spectral acceleration as an intensity measure for collapse risk assessment.*Earthquake Engineering and Structural Dynamics*.44(12).2057–2073.

Goda, K. (2012).Nonlinear response potential of Mainshock-Aftershock sequences from Japanese earthquakes.*Bulletin of the Seismological Society of America*.102(5).2139–2156.

Iervolino, I. (2017).Assessing uncertainty in estimation of seismic response for PBEE.*Earthquake Engineering & Structural Dynamics*.46(10).1711–1723.

Iervolino, I., E. Chioccarelli, and A. Suzuki (2020).Seismic damage accumulation in multiple mainshock–aftershock sequences.*Earthquake Engineering and Structural Dynamics*.49(10).1007–1027.

Iervolino, I., M. Giorgio, and E. Chioccarelli (2016).Markovian modeling of seismic damage accumulation.*Earthquake Engineering & Structural Dynamics*.45(3).441–461.

Iervolino, I., G. Manfredi, M. Polese, G.M. Verderame, and G. Fabbrocino (2007).Seismic risk of R.C. building classes.*Engineering Structures*.29(5).813–820.

Kazantzi, A.K., and D. Vamvatsikos (2015).Intensity measure selection for vulnerability studies of building classes.*Earthquake Engineering and Structural Dynamics*.44(15).2677–2694.

Lagomarsino, S., and S. Giovinazzi (2006).Macroseismic and mechanical models for the vulnerability and damage assessment of current buildings.*Bulletin of Earthquake Engineering*.4(4).415–443.

Luco, N. (2002).Probabilistic seismic demand analysis, SMRF connection fractures, and near-source effects.

Luco, N., and C.A. Cornell (2007).Structure-specific scalar intensity measures for near-source and ordinary earthquake ground motions.*Earthquake Spectra*.23(2).357–392.

McKenna, F. (2011).OpenSees: A framework for earthquake engineering simulation.*Computing in Science and Engineering*.13(4).58–66.

Meletti, C., F. Galadini, G. Valensise, M. Stucchi, R. Basili, S. Barba, G. Vannucci, and E. Boschi (2008).A seismic source zone model for the seismic hazard assessment of the Italian territory.*Tectonophysics*.450(1–4).85–108.

Pacor, F., C. Felicetta, G. Lanzano, S. Sgobba, R. Puglia, M. D'Amico, E. Russo, G. Baltzopoulos, and I. Iervolino (2018).NESS v1.0: A worldwide collection of strong-motion data to investigate near source effects. *Seismological Research Letters*.

Padgett, J.E., B.G. Nielson, and R. Desroches (2007).Selection of optimal intensity measures in probabilistic seismic demand models of highway bridge portfolios.*Earthquake Engineering & Structural Dynamics*.37.711–725.

Petruzzelli, F., and I. Iervolino (2021).NODE: a large-scale seismic risk prioritization tool for Italy based on nominal structural performance.*Bulletin of Earthquake Engineering*.19(7).2763–2796.

Romao, X., J.M. Castro, N. Pereira, H. Crowley, V. Silva, L. Martins, and D. Rodrigues (2019).“Project SERA. Deliverable 26.5: European physical vulnerability models.”

Romao, X., N. Pereira, J.M. Castro, F. De Maio, H. Crowley, and V. Silva (2020).European Building Vulnerability Data Repository (Version v1.2) [Data set]. Zenodo.

Ryu, H., N. Luco, S.R. Uma, and A.B. Liel (2011).Developing fragilities for mainshock-damaged structures through incremental dynamic analysis. *Proceedings of the Ninth Pacific Conference on Earthquake Engineering*.(225).8.

Suzuki, A., and I. Iervolino (2019).Seismic Fragility of Code-conforming Italian Buildings Based on SDoF Approximation.*Journal of Earthquake Engineering*.

Vamvatsikos, D., and C.A. Cornell (2001).Incremental Dynamic Analysis.*Earthquake Engineering and Structural Dynamics*.31(3).491–514.

—— (2002).Incremental dynamic analysis.*Earthquake Engineering and Structural Dynamics*.31(3).491–514.

Villar-Vega, M., V. Silva, M. Eeri, H. Crowley, and Y. Catalina (2017).Assessment of earthquake damage considering the characteristics of past events in South America.*Soil Dynamics and Earthquake Engineering*.99(March).86–96.

5

Constant-ductility residual displacements ratio for SDOF structures exhibiting stiffness and strength degradation

Abstract

From this chapter was derived the paper:

- *Orlacchio M., Baltzopoulos G., Iervolino I. (2019), "Constant-ductility residual displacement ratios", Proceedings of COMPDYN 2019, 7th ECCOMAS Thematic Conference on Computational Methods in Structural Dynamics and Earthquake Engineering, 24-26 June 2019, Crete, Greece.*

Structures subjected to large inelastic deformations during earthquakes can experience residual displacements, i.e., permanent deviations from the original geometric configuration that may reflect damage due to hysteretic energy dissipation. In fact, observed residual displacements play a fundamental role in determining the feasibility of post-earthquake repair operations, against the alternative of demolition and replacement. Furthermore, seismic risk studies often use analytically derived estimates of the peak inelastic and residual displacements as proxies for structural damage and remaining post-shock capacity, respectively, the latter being an important ingredient for the evaluation of structural reliability in the face of seismic sequences. This chapter presents a predictive model for evaluating the central tendency and record-to-record variability of constant-ductility residual displacements of bilinear single-degree-of-freedom systems that exhibit strength and stiffness degradation under cyclic loading, such as typically observed in reinforced concrete structures with predominantly flexural behavior. In order to develop the model, systems with natural periods belonging to the 0.3 s to 2.0 s range with post-yield hardening ratios ranging from 0 to 10%, were analyzed. The most influential variables are post-yielding hardening slope, ductility demand and the level of stiffness and/or strength deterioration caused by the ground shaking. The resulting equations provide the joint distribution of residual displacement, elongated period and loss of lateral resistance. This model can be used for the probabilistic definition of the post-earthquake pushover of a damaged system.

Keywords: static pushover; cyclic degradation; sequence-based seismic reliability.

5.1. Introduction

The increased interest in the effects of earthquake sequences on structures (Iervolino et al., 2016, 2020) and the requirement to analytically evaluate retrofitting via seismic risk analysis, (Ramirez and Miranda, 2012; Ruiz-García and Aguilar, 2015) have stimulated a number of investigations into the issue of residual displacements. Thus, whereas the peak transient displacement of simple inelastic systems has been studied extensively for the last sixty years, (Veletsos and

Newmark, 1960; Ruiz-García and Miranda, 2003; Riddell, 2008) research in the residual displacement of such systems is gradually catching up.

The magnitude of residual displacements can determine the technical and economic feasibility of repair operations of seismic damage. In fact, large residual displacements may lead to a decision to demolish a structure, rather than repair it, and often represent a variable that dominates expected economic losses at intermediate levels of ground motion intensity (Ramirez and Miranda, 2012). Furthermore, the consideration of residual displacements as a supplement to the peak deformation demand, allows for a more complete quantification of building performance under sequential seismic excitation (Ruiz-García and Miranda, 2004; Christopoulos and Pampanin, 2004; Uma et al., 2010). Sequential seismic loading, that is, multiple instances of base acceleration arriving in succession without allowing for intermediate repairs to the structure, can be the result of earthquake shocks occurring clustered in time and space, that is, a seismic *sequence*. In fact, residual displacements were found to be a proxy for the remaining capacity of structures that have already experienced one damaging shock during a sequence, to withstand further aftershocks (Bazzurro et al., 2004; Luco et al., 2004).

According to the paradigm of *performance-based earthquake engineering* (PBEE, Cornell and Krawinkler, 2000) assessment of seismic structural reliability requires a probabilistic treatment of structural response. Past research has provided examples of such a probabilistic description of inelastic displacement demand for simple structural systems (Vamvatsikos and Cornell, 2006). However, in the case of residual displacements, there is scarcity of such models (Ruiz-García and Miranda, 2006; Liossatou, 2013). The objective of the present analytical study is to contribute to filling that gap by providing a predictive model aimed at probabilistically evaluating the residual displacement of simple yielding oscillators, while accounting for some of the parameters known to primarily affect its central tendency and variability.

Several studies have been focused on identifying the parameters that primarily affect the residual displacements of single-degree-of-freedom (SDoF) inelastic structures subjected to earthquake ground motion. From the early studies on residual displacement, the post-yield stiffness ratio emerged as one of the most important parameters for the evaluation of permanent deformations of bilinear SDoF systems (Riddell and Newmark, 1979a, 1979b) and this was also confirmed by subsequent investigations (G. A. Macrae and Kawashima, 1997; Borzi et al., 2001; Christopoulos et al., 2003; Ruiz-García and Miranda, 2006). Overall, it has been observed that bilinear oscillators with positive post-yield stiffness ratios generally exhibit smaller residual displacements than elastic–perfectly plastic systems. On the other hand, oscillators that exhibit negative stiffness after yield tend to undergo little reversal of inelastic deformation and thus exhibit larger residual displacements than corresponding elastoplastic or hardening systems (G. A. Macrae and Kawashima, 1997).

Other studies considered the importance of the hysteretic law, and investigated the impact of the shape of hysteresis loops on residual displacements among different models of cyclic behavior (Riddell and Newmark, 1979a, 1979b; Mahin and Bertero, 1981; Pampanin et al., 2003; Liossatou and Fardis, 2015; Christopoulos et al., 2003; Ruiz-García and Miranda, 2004, 2006). These studies pointed out that the unloading-reloading stiffness of the hysteretic model is one of the most influential parameters that determine residual displacements. In fact, it was observed that residual displacement demands for stiffness-degrading systems are, on average, smaller than their counterparts computed for elastoplastic systems with the same elastic dynamic properties and yield strength, especially if unloading from (and reloading to) the monotonic envelope passes through, or close-to, the origin (e.g., in the case of flag-shaped or pinched hysteresis loops).

Generally speaking, past studies indicate that for vibration periods of the structure below 1.0 s, the central tendency of residual displacements (e.g., mean or median) exhibits some dependence on period (G. A. Macrae and Kawashima, 1997; Ruiz-García and Miranda, 2004; Liossatou and Fardis, 2015), but this dependence does not persist for longer periods (Ruiz-García and Miranda, 2004; Liossatou and Fardis, 2015). However, residual displacements are also characterized by significant *record-to-record variability* (Mahin and Bertero, 1981; Ruiz-García and Miranda, 2004; Liossatou and Fardis, 2015; Christopoulos et al., 2003), which also depends on the system's period of natural vibration, being higher towards shorter periods (e.g., between 0.10 s and 0.5 s; Ruiz-García and Miranda, 2004; Liossatou and Fardis, 2015). For SDoF systems with bilinear backbones, this dispersion tends to increase as positive post-yield stiffness approaches zero and/or when the system exhibits stiffness degradation (Ruiz-García and Miranda, 2004; Liossatou and Fardis, 2015).

Although these observations were mostly made by investigating the residual displacements of SDoF systems under a *constant-strength* approach, that is, oscillators having the same ratio of elastic restoring force demand to yield strength (or strength ratio), a few studies also considered systems where ductility, is kept constant (G. A. Macrae and Kawashima, 1997; Borzi et al., 2001; Christopoulos et al., 2003; Madhu Girija and Gupta, 2020), the latter defined as the ratio of inelastic displacement demand to yield displacement, $\mu = \left|\delta_{max}\right| / \delta_y$. This is termed the *constant-ductility* approach and is also adopted in the present study. Thus, this investigation is focused on the *constant-ductility residual displacement ratio* $\left(C_\mu\right)$, defined as the ratio of residual to peak transient displacement, according to Eq.(5.1):

$$C_{\mu} = \delta_{res} / \delta_{max} \tag{5.1}$$

where both the residual displacement, δ_{res}, and peak transient displacement, δ_{max}, are considered preserving their sign. The choice of normalizing the residual displacement with the maximum inelastic displacement, which is also encountered in the literature (Ruiz-García and Miranda, 2004; Liossatou and Fardis, 2015; Madhu Girija and Gupta, 2020), as well as the constant-ductility approach, were motivated by the widespread use of inelastic displacement limits as thresholds for the definition of structural damage states in PBEE. In fact, it is common practice to define the transition of a structure from one damage state to another, during an earthquake shock, on the basis of crossing some transient displacement threshold (Georgios Baltzopoulos et al., 2017; Iervolino et al., 2018). In other words, the present study is oriented towards estimating residual displacements for a structure that can be considered to be in a certain damage state, after an earthquake.

Therefore, the objective of this chapter is to present an analytical predictive model for the central tendency and related record-to-record variability of the residual displacement ratio for SDoF systems with bilinear backbones that follow evolutionary hysteretic laws. This is a step forward from a preliminary version of the model (Orlacchio et al., 2019) C_{μ} which was limited to the consideration of stiffness degradation due to peak-oriented hysteretic behavior. Going forward, the present chapter provides a more general set of equations that also account for cyclic strength degradation, which can be representative of the behavior of *low-code* reinforced concrete structures with flexure-dominated inelastic response. The C_{μ} ratio is calculated for various combinations of input motion, natural vibration period and post-yielding hardening ratio, considering also different levels of strength degradation. The end result is a set of predictive equations for C_{μ} as a function of two other random variables (RVs): the elongated period (due to loss of stiffness), and the loss of lateral strength, both conditional on a given ductility demand. Thus, these equations effectively model the joint distribution of residual displacement, elongated period and strength degradation. As a consequence, this model allows for the probabilistic evaluation of enough parameters to define the *post-shock pushover curve* of the SDoF system, which reflects its state of seismic damage. In this sense, this constant-ductility approach could find application in the context of simplified estimation of seismic fragility characterizing the structure in its damaged state (Raghunandan et al., 2015; Bazzurro et al., 2004; Luco et al., 2004).

The remainder of this chapter follows this structure: first the analysis methodology is outlined describing the properties of the analyzed systems and the organization of the analyses used to collect the data set. The next two sections are dedicated to the detailed description of the predictive model's development and the numerical aspects of its practical implementation, such as the derivation of mean spectra for residual displacement ratios or the stochastic simulation of pushover curves characterizing the damaged system. Finally, an illustrative application is presented showing that the model can be used as a simplified tool to predict the residual displacements of a reinforced concrete multi-story frame. Some discussion and evaluation of the obtained results conclude the chapter.

5.2. Scope and methodology

5.2.1. Models considered for hysteretic behaviour

The purpose of the present study is the development of a predictive model for the constant-ductility residual displacement ratio, C_μ, of simple inelastic systems that can be deemed to be representative of high- and low-code reinforced concrete structures with flexure dominated inelastic response. These structures consisted of yielding SDoF systems characterized by piece-wise linear monotonic pushovers and peak-oriented hysteretic behavior, potentially exhibiting cyclic strength degradation. The analytical model adopted for the numerical implementation of the hysteretic rule was the modified *Ibarra-Medina-Krawinkler* (IMK, Ibarra et al., 2005; Lignos and Krawinkler, 2011) model. An example trilinear pushover, or *backbone* curve, is shown in Figure 5.1a using dimensionless $\{R, \mu\}$ coordinates, where $R = F/F_y$ is the strength ratio of the elastic force over the yield base shear of the system, and $\mu = \delta/\delta_y$ stands for the response-to-yield displacement ratio; i.e., the ductility.[2]

The analyzed systems have backbone curves consisting of an elastic branch followed by a post-yield hardening segment, the latter defined by a hardening slope α_h and ending at a capping point ductility μ_c.

---

[2] The notation μ is used herein to denote both maximum transient ductility demand due to base acceleration, $|\delta_{max}|/\delta_y$, and normalized displacement response under quasi-static loading δ/δ_y, as per the typical convention in earthquake engineering literature. In all cases presented herein, the normalizing yield displacement δ_y is that of the intact structural system.

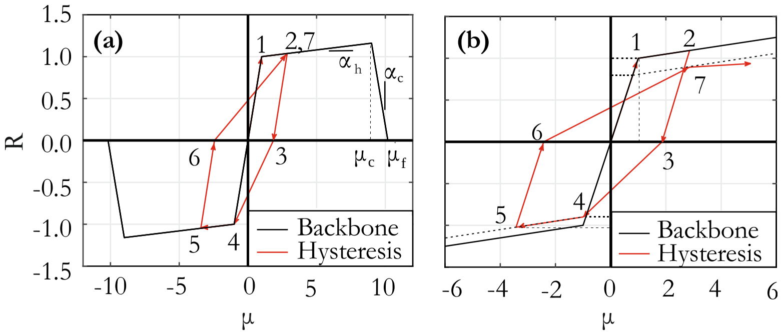

Figure 5.1 Peak-oriented modified IMK hysteretic model. Backbone curve and quasi-static cyclic response of an inelastic SDoF system without any cyclic strength degradation, shown in dimensionless $\{R, \mu\}$ coordinates (a); quasi-static cyclic response that includes cyclic strength degradation (b).

This hysteretic model allows for the investigation of two degradation modes, the first being the deterioration of reloading stiffness inherent in the peak-oriented model, where the direction of the loading path targets the maximum displacement on the opposite side, once the horizontal axis is intersected in each reloading cycle (Figure 5.1a). The second type of degradation considered is the cyclic deterioration of lateral strength, which involves the offset of the hardening branch towards the origin after each response half-cycle and the simultaneous deterioration of the hardening slope. The latter constitutes a case of *cyclic* strength degradation, so-termed to distinguish it from in-cycle degradation, which occurs when ductility demand exceeds the capping point μ_c and the response follows the softening branch (FEMA P440A, 2009). Figure 5.1 displays the quasi-static cyclic response of two simple inelastic systems that behave according to the modified IMK peak-oriented hysteretic model (Lignos, 2013) one of which corresponds to a case without cyclic strength degradation (Figure 5.1a) whereas the other does exhibit cyclic strength deterioration (Figure 5.1b). Although no ductility demands $\mu > \mu_c$ are considered in this investigation, and therefore no in-cycle strength degradation ever comes into play in the development of the predictive model, a descending softening branch, defined by a post-capping slope α_c and intercepting the zero-strength axis at a fracture ductility, μ_f, is still shown for the sake of completeness.

In order to investigate the effect of strength degradation on residual displacement, three hysteretic rules were established, characterized by increasing degradation levels that will be hereafter conventionally referred to as cases of low-, medium- and high-degradation. Although the labeling of these degradation levels is purely arbitrary, they were defined on a quantitative basis, according to the loss of lateral resistance following the numerical application of a specific loading protocol. In this context, a normalized lateral strength degradation measure is defined, hereafter referred to as the *strength loss*, ΔR and defined according to Eq. (5.2):

$$\Delta R = 1 - \frac{F'_{max^+} + F'_{max^-}}{2 \cdot F_{max}} \tag{5.2}$$

where $F_{max} = F_y \cdot \left[1 + \alpha_h \cdot (\mu - 1)\right]$ is the maximum restoring force reached along the hardening branch of the initial backbone at ductility $\mu \leq \mu_c$ under static loading (i.e., in the absence of cyclic strength degradation) and $F'_{max^\pm}$ represents the maximum force in the positive and negative loading directions, that can be reached at the same ductility on the deteriorated backbone after the system has been subjected to any cyclic loading; i.e., on the pushover of the damaged structure, as shown in Figure 5.2. On the same figure, it is worth noting that the evaluation of F'_{max^+} and F'_{max-} is performed upon the backbones of the damaged structure that have been shifted from the initial point of equilibrium by the residual displacement δ_{res}. The parameter F'_{max} is hereafter used to express the deteriorated lateral resistance at maximum ductility demand, evaluated as $F'_{max} = 1/2 \cdot \left(F'_{max^+} + F'_{max^-}\right)$, which simplifies Eq. (5.2) to $\Delta R = 1 - F'_{max} / F_{max}$.

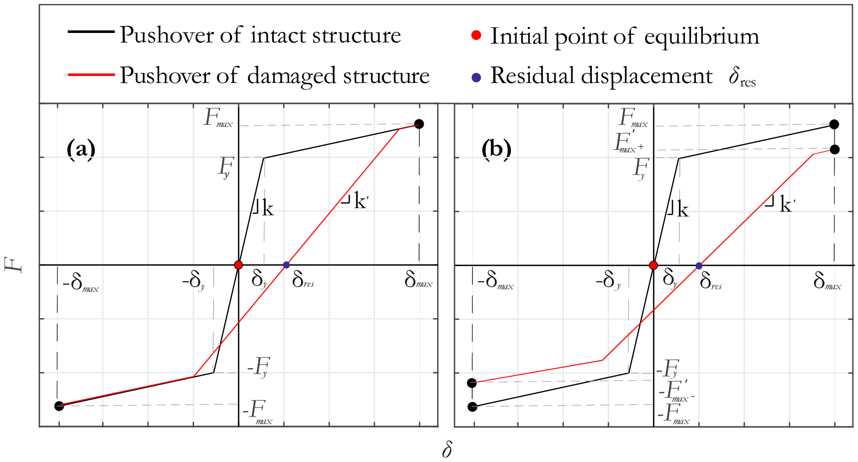

Figure 5.2 Examples of an SDoF structure's monotonic pushover (backbone) curve before and after the seismic damage. Intact-structure backbone (grey line) and post-shock backbone (dark line with pre-yield stiffness k', intersecting the zero-force horizontal axis at δ_{res}) for a generic stiffness-degrading system (a) and for a generic stiffness- and strength-degrading system (b).

Using this definition of strength loss, the conventional labeling of the three degradation levels was calibrated so that ΔR would result approximately equal to

0.20, 0.30 and 0.40 for the low-, medium- and high-degradation levels, respectively, at the end of a displacement-controlled quasi-static cyclic loading, as shown in Figure 5.2. These values were obtained as an average from the application of the loading protocol to SDoF systems with hardening slopes spanning the entire range considered for the model. The loading protocol arbitrarily used for this definition consisted of performing two symmetric full cycles at each increasing ductility level $\mu = \{2, 3, 4, 5, 6\}$. On the numerical side, this operation entails the calibration of the corresponding dimensionless cyclic degradation parameter λ (for more details, the interested reader can consult Lignos and Krawinkler, 2011) of the modified IMK model as implemented in the OpenSees platform (*Open System for Earthquake Engineering Simulation,* McKenna, 2011) via the DYANAS software (Baltzopoulos et al., 2018). The parameter λ, which normalizes a structure-dependent reference hysteretic dissipation energy E_t according to $\lambda = E_t \big/ \left(\delta_y \cdot F_y \right)$, was calibrated to take values equal to 163.6, 109.1 and 81.8 for the low-, medium- and high-degradation levels respectively. For the sake of brevity, the index *DL* is hereafter used assuming values of 0, 1, 2 and 3 in order to indicate: none, low, medium and high levels of degradation respectively, as reported in Figure 5.3.

Overall, the SDoF systems considered in this study had eight different periods of natural vibration ranging from 0.3 to 2.0 s, i.e., $T = \{0.3s, 0.6s, 0.9s, 1.0s, 1.2s, 1.5s, 1.8s, 2.0s\}$, eight distinct hardening stiffness ratios ranging from zero to ten percent of the elastic stiffness, $\alpha_h = \{0\%, 0.5\%, 1\%, 2\%, 3\%, 4\%, 5\%, 10\%\}$ and four levels of strength degradation (none, low, medium and high, as discussed above). The combination of all of these variants led to a total of two-hundred and fifty-six inelastic SDoF systems used in the analyses that will be described in the following. Furthermore, for each SDoF structure, nine levels of ductility demand were considered, with values $\mu = \{1.5, 2, 3, 4, 5, 6, 7, 8, 9\}$. All of these ductility values were set lower than the capping ductility μ_c, so that no structure is subjected to in-cycle degradation by experiencing inelastic displacements into the softening branch.

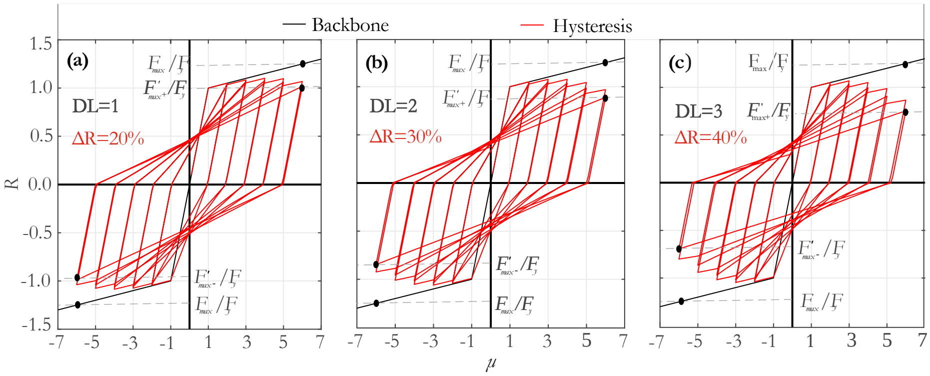

Figure 5.3 Three conventional levels of strength degradation used in this study, defined on the basis of strength loss after a quasi-static cyclic loading protocol: low-degradation peak-oriented hysteretic rule (a); medium-degradation (b); high-degradation (c).

5.2.2. Analysis methodology and input ground motions

The predictive model for C_μ must account for record-to-record variability in terms of residual displacement, and the amount of stiffness and strength degradation. This can be seen in Figure 5.4, which compares the initial static pushover of two SDoF structures in pristine conditions with their pushover after having been brought to an arbitrary damage state by being subjected to a single base acceleration time-history (three examples are provided in the figure, each corresponding to a different accelerogram). The two SDoF structures are characterized by $T = 1.0s$ and $\alpha_h = 2.0\%$ while all three base accelerations are designed to cause the same ductility demand of $\mu = 5.0$. The comparison of the initial and the final damaged state produced by each earthquake shock exhibits variability in all three aforementioned parameters of residual displacement, post-shock reloading stiffness and post-shock lateral resistance (where applicable - Figure 5.4b).

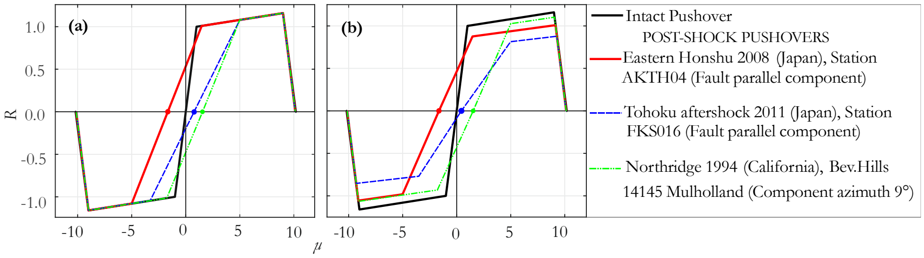

Figure 5.4 Examples of an SDoF structure's monotonic pushover (backbone) curve before and after the seismic damage in $\{R, \mu\}$ coordinates. Post-shock backbones and residual displacements of an SDoF system with $T = 1.0s$ and $\alpha_h = 2.0\%$, evaluated for three different records scaled to cause

ductility demand $\mu = 5.0$ without strength degradation (a) and with a high level of strength degradation (b).

In this light, a suite of one hundred single-horizontal-component earthquake ground motions was used in this study, selected from within the NESS dataset (Pacor et al., 2018). All one hundred records were recorded on firm soil at a closest-to-rupture-plane distance ranging from 0 km to 44.5 km and were produced by earthquakes with moment magnitude belonging to the 6.1-7.6 range. Furthermore, the selected records exhibit peak ground acceleration ranging from 0.05 g to 1.40 g and are devoid of apparent pulse-like directivity effects.

The analysis itself can be divided in two phases: the first phase consists of the execution of *incremental dynamic analysis* (IDA, Vamvatsikos and Cornell, 2001) using all one-hundred records in the aforementioned set. IDA involves performing multiple nonlinear dynamic analyses for each record, which is progressively scaled in amplitude to increasing levels of shaking intensity until a target ductility μ is reached. A mass-proportional viscous damping ratio $\xi = 5.0\%$ was used for all time-history analyses. This procedure allows calculating, for each accelerogram, the minimum amplitude scale factor (SF; defined as the non-negative scalar multiplier of all acceleration values in a record) required to bring the response of the structural model to a fixed ductility demand. The various target ductility levels analyzed can be considered to represent response thresholds whose attainment defines a generic damage level for the structure. In this sense, the IDAs allow determining the SFs that constrain all of the records to bring a given SDoF structure to the same damage state, assuming that the implied mainshock earthquake hits the intact structure.

The second phase consists of dynamic and static non-linear analyses for each record, SDoF structure, and ductility threshold, performed in sequence. During this procedure, dynamic analysis of the structure is performed for each ground motion, using a SF calculated in the previous IDA phase, leading to different numerical incarnations of the corresponding damage state. At the end of the acceleration history, the time needed for damping-out any remaining velocity of the mass is provided by zero-padding the end of the record; when the damaged system is at rest, the residual displacement δ_{res} is recorded and *static pushover analysis* is performed, in both positive and negative loading direction. Therefore, for each SDoF system and fixed ductility demand, one-hundred manifestations of the damaged structure's static pushover curve are obtained, representing the record-to-record variability of δ_{res}, degraded reloading stiffness k' and deteriorated lateral resistance at maximum ductility demand F'_{max}.

5.3. Predictive model for the residual displacement

5.3.1. Residual displacement ratio, period elongation and strength degradation

The analyses performed as part of this study, described in the preceding section, provided samples of residual displacement accompanied by the corresponding stiffness and strength degradation. The objective was to use this data for the development of a predictive model for $C_{\mu} = \delta_{res}/\delta_{max}$, which can potentially employ the stiffness and strength degradation information as predictor variables, along with ductility, vibration period and hardening slope.

In this model, the degradation of reloading stiffness is taken into account under the guise of *period elongation;* the reduction in reloading stiffness caused by the peak-oriented hysteresis, causes the post-seismic-shock SDoF structure to exhibit an initial branch with slope $k' < k$, which is apparent in Figure 5.2 and Figure 5.4, and consequently an elongated vibration period $T' = 2 \cdot \pi \cdot \sqrt{m/k'}$, where m is the mass of the SDoF system. In this context, the variable chosen to quantify period elongation is the natural logarithm of the relative increase in period $ln(\Delta T)$, which is defined according to Eq. (5.3):

$$\ln(\Delta T) = \ln\left(\frac{T' - T}{T}\right), \tag{5.3}$$

where it is worth recalling that T is the initial natural vibration period of the SDoF structure (i.e., prior to any earthquake-induced damage and loss of stiffness).

Strength degradation on the other hand, is quantified using the variable $\ln(\Delta R)$, with ΔR given by Eq. (5.2) and calculated for all three degradation levels defined previously; i.e., low, medium and high. It is important to note that the few cases exhibiting $\Delta R > 0.50$, that is, loss of lateral resistance exceeding fifty percent of the initial, were held to represent situations of incipient collapse and were not given further consideration.

The starting point for defining the model is the relation that was observed between the ratio of residual to peak transient displacement $\delta_{res}/\delta_{max}$ and $\ln(\Delta T)$, for the simplest case where strength degradation is absent. In fact, it was observed that the ratio $\delta_{res}/\delta_{max}$ exhibits persistently high negative linear correlation with $\ln(\Delta T)$, for varying T, μ and α_h (Orlacchio et al., 2019). More specifically, estimates of the correlation between $\ln(\Delta T)$ and $\delta_{res}/\delta_{max}$, indicated as $\hat{\rho}$ and calculated based on the available dynamic analysis responses according to the classical definition for linear correlation (Draper and Smith, 1998) range from -0.50 to -0.99 with $|\hat{\rho}| \geq 0.7$ for the majority of cases examined. The few cases for which the estimated correlation fell within the range $-0.5 < \hat{\rho} < -0.7$ were characterized by high ductility demands of $\mu \geq 7.0$, and some of the longer periods of natural vibration considered; i.e., $T \geq 1.8s$. This is illustrated in Figure 5.5a, where one should recall that both δ_{res} and δ_{max} preserve their sign in this formulation so that the ratio becomes negative when the two occur in opposite directions. In that panel, a scatter plot of the one hundred $\delta_{res}/\delta_{max}$ responses against the corresponding $\ln(\Delta T)$ values is given along with the regression line of the former against the latter.

Furthermore, it was observed that this level of (negative) correlation between $\delta_{res}/\delta_{max}$ and $\ln(\Delta T)$ also persists in the case of SDoF systems exhibiting cyclic strength deterioration, for all three degradation levels considered (see Figure 5.5b). In fact, values of the estimated correlation coefficient between $\ln(\Delta T)$ and $\delta_{res}/\delta_{max}$ of -0.93 and -0.88 characterize the cases reported in Figure 5.5a and Figure 5.5b, respectively. However, for the cases with strength degradation, a negative correlation was also observed between $\delta_{res}/\delta_{max}$ and $\ln(\Delta R)$, across all T, μ and α_h considered (see Figure 5.5c). The correlation coefficients between $\delta_{res}/\delta_{max}$ and $\ln(\Delta R)$ range from -0.3 to -0.8 with $|\hat{\rho}| \geq 0.5$ for the majority of analyzed cases. The cases for which the correlation coefficient fell within the range $-0.3 < \hat{\rho} < -0.5$ were characterized by ductility demands $\mu \geq 6.0$ and periods of natural vibration $T \geq 1.5s$. Therefore, an increase of the deterioration parameter $ln(\Delta R)$ is generally associated with a decrease in the ratio of residual to peak transient displacement.

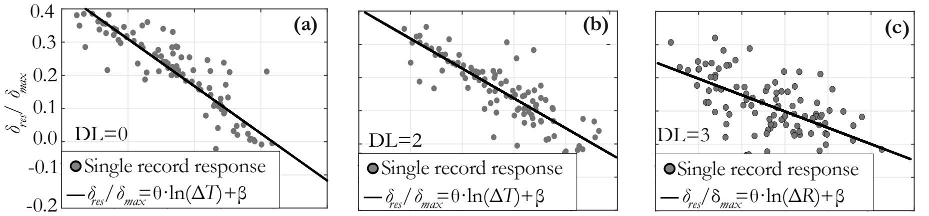

Figure 5.5 Examples of regression of $\delta_{res}/\delta_{max}$ against $\ln(\Delta T)$ and against $\ln(\Delta R)$ highlighting their (negative) linear correlation. Are shown the case of a SDoF system with $\alpha_h = 1.0\%$, $T = 1.0s$ and $\mu = 5.0$ without strength deterioration (a); the case of a SDoF system with $\alpha_h = 5.0\%$,

$T = 1.2s$ and $\mu = 4.0$ with a medium level of strength deterioration (b); and the case of a SDoF system with $\alpha_h = 10.0\%$, $T = 1.2s$ and $\mu = 4.0$ with a high level of strength deterioration (c).

Based on this observed linear trend, a linear model was adopted for the expected value of C_μ in case of absent strength degradation ($DL = 0$). The slope and intercept of the model are only functions of the ductility demand μ and of the post-yield hardening ratio α_h. Thus, the model for C_μ without strength degradation is given by Eq. (5.4):

$$\begin{cases} C_\mu = \delta_{res}/\delta_{max} = \theta_1 \cdot \ln(\Delta T) + \beta_1 + \varepsilon_0 \cdot \sigma_\delta \\ \theta_1 = b_{C1} + b_{C2} \cdot \sqrt{\mu - 1} + b_{C3} \cdot \alpha_h \\ \beta_1 = c_{C1} + c_{C2} \cdot \sqrt{\mu - 1} + c_{C3} \cdot \alpha_h \cdot \sqrt{\mu - 1} \\ \sigma_\delta = d_{C1} \cdot T + d_{C2} \cdot (\mu - 1) + d_{C3} \cdot \alpha_h + d_{C4} \cdot \alpha_h \cdot (\mu - 1) + d_{C5} \cdot (\mu - 1) \cdot T \cdot \alpha_h \end{cases} \quad (5.4)$$

where ε_0 is a standard Normal random variable, θ_1 and β_1 represent the slope and intercept of the model and σ_δ is the standard deviation of the regression residuals. As can be seen from the equation, θ_1 and β_1 are expressed as linear combinations of various simple functions of μ and α_h. The combination coefficients, b_{Cj} and c_{Cj} with $j = \{1, 2, 3\}$, are estimated by means of robust regression (Draper and Smith, 1998) of $\delta_{res}/\delta_{max}$ against $\{\ln(\Delta T), \mu, \alpha_h\}$ using iteratively re-weighted least squares with bisquare weighting. These coefficients are all reported in Table 5.1. The analytical form of the model for θ_1 and β_1 was determined by performing preliminary fits of the basic linear model on the analysis results, separately for the various SDoF systems and ductility levels considered, and observing the variation of these two parameters with respect to μ, α_h and T graphically.

Regarding the dispersion around the mean, σ_δ was found to be non-constant, varying with T, μ and α_h. Therefore, σ_δ was modelled by means of least-squares curve-fitting of an analytical expression to the regression residuals for the various T, μ and α_h values. This expression, which contains model coefficients d_{Cj} $j = \{1, 2, ..., 5\}$, is also included in Eq. (5.4). The coefficient estimates of the model for σ_δ are reported in Table 5.2.

Figure 5.6 shows a plot of the models for the central tendency of $\delta_{res}/\delta_{max}$ (Figure 5.6a) and standard deviation σ_δ (Figure 5.6d) in case of absent strength degradation. The model shown in Figure 5.6a refers to the case of $\alpha_h = 0.0\%$ and for the cases with $\mu = 5$ and $\mu = 8$ in Figure 5.6b and Figure 5.6c respectively, whereas the plot in Figure 5.6d shows the model of standard deviation σ_δ for $\alpha_h = 3.0\%$.

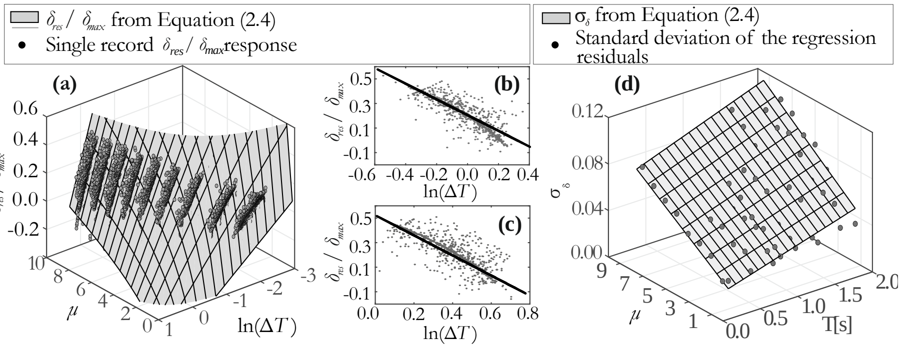

Figure 5.6 Central tendency and standard deviation of the model for the residual displacements in case of absent strength deterioration. Central tendency for $\alpha_h = 0.0\%$ (a); central tendency for $\alpha_h = 0.0\%$ and $\mu = 5$ (b); central tendency for $\alpha_h = 0.0\%$ and $\mu = 8$ (c); standard deviation σ_δ for $\alpha_h = 3.0\%$ (d).

On the base of the model shown in Eq. (5.4), the model for C_μ in case of $DL = 1, 2, 3$ was also defined including in the equation the variable $\ln(\Delta R)$ which accounts for strength degradation. The model for C_μ accounting for strength degradation is shown in Eq. (5.5) :

$$\begin{cases} C_\mu = \delta_{res} / \delta_{max} = \theta_1 \cdot \ln(\Delta R) + \beta_1 + \gamma_1 \cdot \ln(\Delta R)^{-2} + \varepsilon_0 \cdot \sigma_\delta \\ \theta_1 = b_{C1} + b_{C2} \cdot \sqrt{\mu - 1} + b_{C3} \cdot \alpha_h \\ \beta_1 = c_{C1} + c_{C2} \cdot \sqrt{\mu - 1} + c_{C3} \cdot \alpha_h \cdot \sqrt{\mu - 1} \\ \sigma_\delta = d_{C1} \cdot T + d_{C2} \cdot (\mu - 1) + d_{C3} \cdot \alpha_h + d_{C4} \cdot (\mu - 1)^2 \end{cases}, \tag{5.5}$$

where ε_0 is a standard Normal random variable and σ_δ is the standard deviation of the regression residuals. As can be seen from the equation, the model of the expected value of C_μ is composed of two parts, a linear part, that unlike the case of $DL = 0$ is function of the variable $\ln(\Delta R)$, and the second one which is function of $\ln(\Delta R)^{-2}$. Also in this case, θ_1 and β_1 are expressed as linear combinations of various simple functions of μ and α_h. The combination coefficients, b_{Cj} and c_{Cj} with $j = \{1, 2, 3\}$ and the coefficient γ_1 are estimated by means of robust regression (Draper and Smith, 1998) of $\delta_{res} / \delta_{max}$ against $\{\ln(\Delta R), \mu, \alpha_h\}$ using iteratively re-weighted least squares with bisquare weighting. The procedure was performed for each level of strength degradation separately, obtaining a set of coefficients for each *DL*. These coefficients are reported in Table 5.1.

Also in the cases where cyclic strength degradation is present in the hysteretic loops, σ_δ was found to be non-constant, varying with μ, T and α_h. σ_δ was modeled by means of least-squares curve-fitting of an analytical expression to the regression residuals for the various T, μ and α_h values and the estimates of the coefficients d_{Cj} $j=\{1,2,...,5\}$ shown in Eq. (5.5) are reported in Table 5.2. Figure 5.7 shows an example of the model for the expected value of $\delta_{res}/\delta_{max}$ and the model of standard deviation σ_δ for a system with $\alpha_h = 1.0\%$, $\mu = 6$ and , $T = 0.6\ s$ considering medium level of strength degradation.

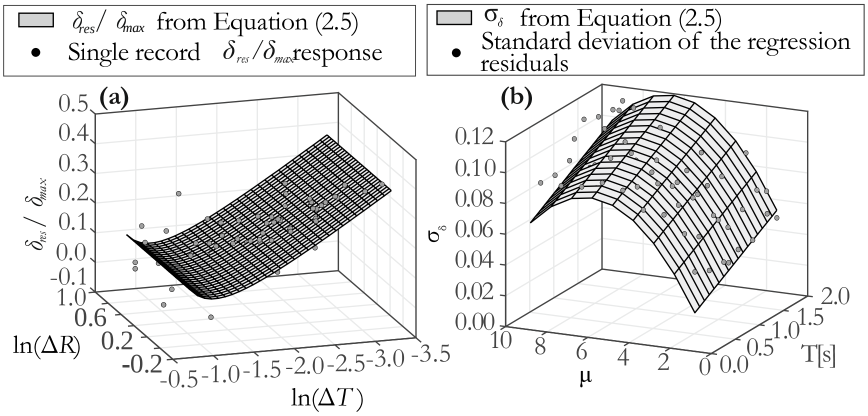

Figure 5.7 Central tendency and standard deviation of the model for the residual displacements in case of medium strength deterioration. Central tendency for $\alpha_h = 1.0\%$, $\mu = 6$ and $T = 0.6\ s$ (a); standard deviation σ_δ in the case of $\alpha_h = 1.0\%$, (b).

At this point, it should be highlighted that the predictor variables $\ln(\Delta T)$ and $\ln(\Delta R)$ used in the regression model for the constant-ductility residual displacement ratios of Eq. (5.4) and Eq.(5.5) are also RVs for a given ductility demand μ, due to record-to-record variability. However, it was observed that these two RVs, $\ln(\Delta T)$ and $\ln(\Delta R)$, are correlated for all DLs and T, μ, α_h ranges considered, as shown in Figure 5.8.

Therefore, completeness of the model requires the definition of the joint distributions of C_μ and $\ln(\Delta R)$ and $\ln(\Delta T)$ in case of strength degradation, or that of C_μ and $\ln(\Delta T)$ in the case where strength degradation is absent. To this end, the correlation between $\ln(\Delta T)$ and $\ln(\Delta R)$ was studied and Mardia's test of multivariate normality (Mardia, 2019) was performed. In that test, the null hypothesis is that the RVs $\ln(\Delta R)$ and $\ln(\Delta T)$ are jointly Normal distributed, for given initial characteristics of the structure T, α_h, DL and for a fixed ductility demand μ. The results showed that in almost all cases the null hypothesis could not be rejected at a 5% significance level.

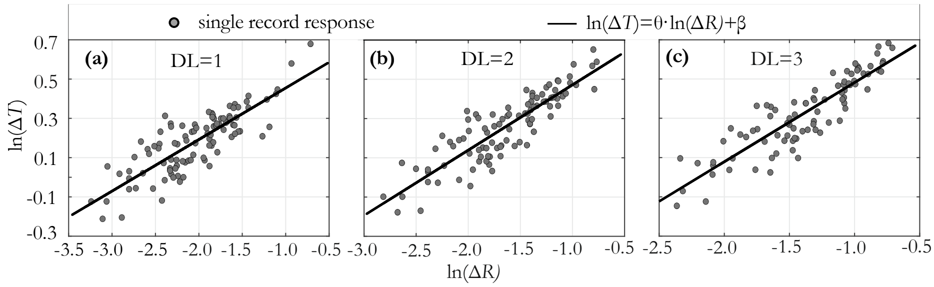

Figure 5.8 Examples of correlation between $\ln(\Delta T)$ and $\ln(\Delta R)$ for an SDoF system with $\alpha_h = 5.0\%$, $T = 0.3s$ and $\mu = 6.0$ in case of low level of strength deterioration (a); medium level of strength deterioration (b) and high level of strength deterioration (c).

Based on this result, it was assumed that $\{\ln(\Delta T), \ln(\Delta R)\}$ is a bivariate Gaussian variable, whose joint distribution can be completely defined knowing the marginal distributions of $\ln(\Delta T)$ and $\ln(\Delta R)$, and their correlation coefficient, $\rho_{\ln(\Delta T),\ln(\Delta R)}$. The plausibility of this bivariate normality assumption was verified by means of hypothesis testing, as mentioned above. Another assumption made was the conditional stochastic independence of $\{\ln(\Delta T), \ln(\Delta R)\}$ from C_μ, given a fixed ductility demand μ. The development of these additional segments of the model are presented in the following paragraphs.

5.3.2. Regression model for period elongation

The model for period elongation was defined starting from the case of absent strength degradation ($DL = 0$) and subsequently modelling the increments in terms of ΔT for the three levels $DL = 1, 2, 3$ to add to the model of the central tendency of ΔT for the case $DL = 0$.

The marginal distribution of period elongation in case of $DL = 0$ was defined assuming a Lognormal model for ΔT and consequently a Gaussian model for $\ln(\Delta T)$. The functional form adopted for the expected value of ΔT stems from the observation of data trend of ΔT with the inelastic portion of the ductility demand, $(\mu - 1)$, for each pair of T and α_h. Fitting of the model's parameters to the data was performed via weighted least squares regression because of the non-constant variance and the analytical form of the model in case of $DL = 0$ is reported in Eq. (5.6):

$$\begin{cases} \overline{\Delta T} = \overline{\left(\dfrac{T'-T}{T}\right)} = b_{T1} + b_{T2} \cdot \alpha_h \cdot \mu^{-1/2} + b_{T3} \cdot \alpha_h \cdot \mu + b_{T4} \cdot \mu^{1/2} \\ \sigma_{\Delta T} = d_{T1} + d_{T2} \cdot \overline{\Delta T} \end{cases} \tag{5.6}$$

where $\overline{\Delta T}$ is the mean of the Lognormal variable ΔT with standard deviation $\sigma_{\Delta T}$, which is estimated as the standard error of the regression residuals. The expected value of the model for period elongation in absence of strength degradation $\overline{\Delta T}$ depends on α_h and μ. The coefficients b_{Tj} with $j = \{1, \ldots, 4\}$ are provided in Table 5.3.

An analytical expression was also proposed for expressing $\sigma_{\Delta T}$ as a function only of $\overline{\Delta T}$. Table 5.3 provides the values of the parameters d_{Tj}, $j = \{1, 2\}$, appearing in Eq. (5.6) estimated from curve-fitting against the regression residuals for the level of strength degradation $DL = 0$.

Figure 5.9 shows a graph of the model for period elongation, highlighting the dependence of its central tendency on α_h and μ (Figure 5.9a). Figure 5.9b and Figure 5.9c represent the expected value of the model for period elongation in absence of strength degradation in the cases of $\alpha_h = 0.03$ and $\alpha_h = 0.05$, respectively.

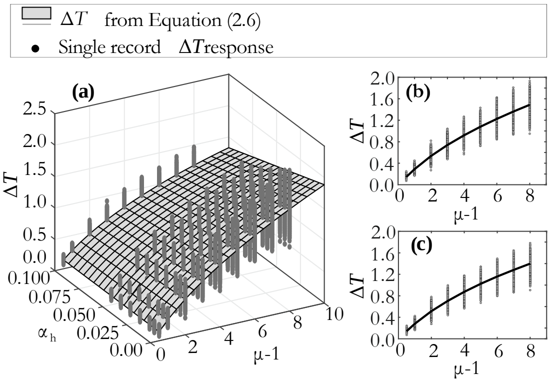

Figure 5.9 Model for period elongation in case of no strength degradation. Model for the central tendency of period elongation (a); central tendency of period elongation in case of $\alpha_h = 0.03$ (b); central tendency of period elongation in case of $\alpha_h = 0.05$ (c).

The marginal distribution of period elongation in the case of $DL = 1, 2, 3$ was defined by processing the data of each degradation level separately and modeling the differences obtained between the data sets of $DL = 1, 2, 3$ and the expected value of ΔT for $DL = 0$ shown in Eq. (5.6). Therefore in presence of strength degradation, the mean of the model for period elongation $\overline{\Delta T_{DL=1,2,3}}$ can be evaluated by adding to the expected value evaluated for $DL = 0$, $\overline{\Delta T}$, a quantity only function of μ as shown in Eq. (5.7):

$$\begin{cases} \overline{\Delta T_{DL=1,2,3}} = \overline{\Delta T} + b_{T5} + b_{T6} \cdot \mu^2 \\ \sigma_{\Delta T\, DL=1,2,3} = d_{T1} + d_{T2} \cdot \overline{\Delta T_{DL=1,2,3}} \end{cases}. \tag{5.7}$$

In the case of $DL = 1, 2, 3$ the standard deviation $\sigma_{\Delta T\, DL=1,2,3}$ is modeled as function only of the expected value of the model for period elongation $\overline{\Delta T_{DL=1,2,3}}$. Table 5.3 also provides the values of the parameters b_{T5}; b_{T6} and d_{Tj}, with $j = \{1, 2\}$. Figure 5.10 shows the increments in terms of ΔT for the three levels $DL = 1, 2, 3$ in case of $\alpha_h = 0.0\%$ (Figure 5.10a); $\alpha_h = 2.0\%$ (Figure 5.10b) and $\alpha_h = 5.0\%$ (Figure 5.10c).

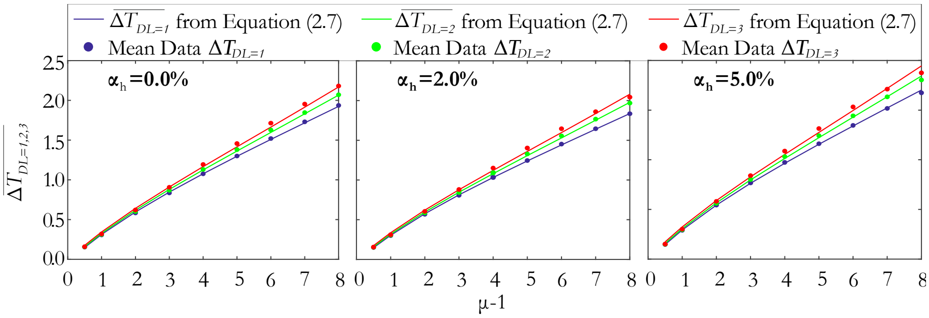

Figure 5.10 Increments in terms of ΔT for the three levels $DL = 1, 2, 3$ in case of $\alpha_h = 0.0\%$ (a); $\alpha_h = 2.0\%$ (b) and $\alpha_h = 5.0\%$ (c).

Finally, it should be noted that the mean $\overline{\ln(\Delta T)}$ and the standard deviation $\sigma_{\ln(\Delta T)}$ characterizing the Gaussian model of $\ln(\Delta T)$ can be evaluated by the relationships in Eq. (5.8):

$$\begin{cases} \ln(\Delta T) = \ln\left(\overline{\Delta T}\right) - 1/2 \cdot \sigma^2_{\ln(\Delta T)} + \varepsilon_1 \\ \sigma^2_{\ln(\Delta T)} = \ln\left(\sigma^2_{\Delta T} + \overline{\Delta T}^2\right) - 2 \cdot \ln\left(\overline{\Delta T}\right) \end{cases} \tag{5.8}$$

where ε_1 is a zero mean Normal random variable with standard deviation $\sigma_{\ln(\Delta T)}$. Although Eq. (5.8) is written for absence of strength degradation it is also applicable in the case of $DL = 1, 2, 3$.

5.3.3. Regression model for strength loss

The model for strength loss provides the ΔR parameter of the post-shock structure at a fixed ductility demand μ, given initial characteristics of the structure T, α_h and DL. The data showed a linear trend in log-space of ΔR with the ductility demand $(\mu - 1)$, for each pair of T and α_h and for each level of strength degradation. Therefore, the model for the central tendency of $\ln(\Delta R)$ is a linear equation as reported in Eq. (5.9):

$$\begin{cases} \ln(\Delta R) = \theta_3 \cdot \ln(\mu - 1) + \beta_3 + \varepsilon_2 \\ \theta_3 = b_{\mathrm{R}1} + b_{\mathrm{R}2} \cdot \alpha_h \\ \beta_3 = c_{\mathrm{R}1} + c_{\mathrm{R}2} \cdot \alpha_h + c_{\mathrm{R}3} \cdot T + c_{\mathrm{R}4} \cdot T^2 \end{cases} \tag{5.9}$$

The central tendency of $\ln(\Delta R)$ was found to exhibit some dependence on the initial period of natural vibration, T, and on the post-yield hardening ratio α_h. In Eq. (5.9) the coefficients $b_{\mathrm{R}j}$ with $j = \{1, 2\}$ and $c_{\mathrm{R}j}$ with $j = \{1, .., 4\}$, were evaluated by curve fitting of the results performed for each level of strength degradation using a weighted least squares regression because of the non-constant variance. Table 5.4 provides the values of the coefficients $b_{\mathrm{R}j}$ and $c_{\mathrm{R}j}$ that characterize the slope θ_3 and the intercept β_3 of the model. The term ε_2 in Eq. (5.9) is a zero mean Gaussian variable with standard deviation $\sigma_{\ln(\Delta R)}$, which is estimated as the standard error of the regression residual and was found to be dependent on the period of the intact structure and the ductility demand, as reported in Eq.(5.10):

$$\sigma_{\ln(\Delta R)} = d_{\mathrm{R}1} + d_{\mathrm{R}2} \cdot T + d_{\mathrm{R}3} \cdot T^2 + d_{\mathrm{R}4} \cdot (\mu - 1) + d_{\mathrm{R}5} \cdot (\mu - 1)^2 \tag{5.10}$$

Table 5.4 provides the values of the parameters $d_{\mathrm{R}j}$, $j = \{1, 2, ..., 5\}$ appearing in Eq. (5.10), estimated from curve-fitting against the regression residuals. Examples of the models for the mean and standard deviation of $\ln(\Delta R)$ are reported in Figure 5.11. Figure 5.11a shows the model for the mean of $\ln(\Delta R)$ for a system with hardening slope $\alpha_h = 0.01$ and low strength deterioration level, while Figure 5.1d shows the model of $\sigma_{\ln(\Delta R)}$ for the same level of degradation.

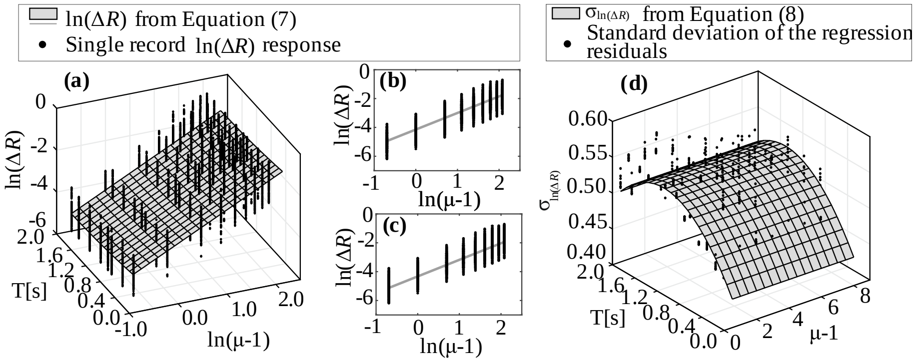

Figure 5.11 Model for strength reduction in case of low strength degradation level. Model for mean $\ln(\Delta R)$ in case of $\alpha_b = 0.01$ (a); central tendency of strength reduction in case of $\alpha_b = 0.01$ and $T = 0.6\,s$ (b); central tendency of strength reduction in case of $\alpha_b = 0.01$ and $T = 1.5\,s$ (c); model of standard deviation $\sigma_{\ln(\Delta R)}$ (d).

Table 5.1 Coefficient estimates for mean of $\delta_{res}/\delta_{max}$ in Eq. (5.4) and Eq.(5.5) .

	Mean of $\delta_{res}/\delta_{max}$										
	Coefficients $b_{C\,j}$				Coefficients $c_{C\,j}$				Coefficients γ_j		
	DL				*DL*				*DL*		
j	0	1	2	3	0	1	2	3	1	2	3
1	-0.009	-0.004	0.003	0.009	-0.078	-0.129	-0.108	-0.094	0.159	0.106	0.081
2	-0.277	-0.075	-0.083	-0.090	0.493	-0.049	-0.039	-0.033	-	-	-
3	-0.378	0.041	0.03	0.030	-1.412	-0.374	-0.387	-0.411	-	-	-

Table 5.2 Coefficient estimates for Standard deviation σ_δ in in Eq. (5.4) and Eq.(5.5) .

	Standard deviation σ_δ			
	Coefficients $d_{C\,j}$			
j	$DL = 0$	$DL = 1$	$DL = 2$	$DL = 3$
1	0.019	0.020	0.021	0.021
2	0.009	0.029	0.028	0.027
3	0.122	-0.149	-0.144	-0.149
4	0.0478	-0.003	-0.003	-0.002
5	0.018	-	-	-

Table 5.3 Coefficient estimates in Eq. (5.6) and Eq. (5.7).

	Mean of $\ln(\Delta T)$				Standard deviation $\sigma_{\ln(\Delta T)}$			
	Coefficients b_{Tj}				Coefficients d_{Tj}			
j	$DL=0$	$DL=1$	$DL=2$	$DL=3$	$DL=0$	$DL=1$	$DL=2$	$DL=3$
1	-0.876	-0.876	-0.876	-0.876	0.023	0.005	0.005	0.013
2	0.942	0.942	0.942	0.942	0.112	0.170	0.186	0.188
3	-0.530	-0.530	-0.530	-0.530	-	-	-	-
4	0.833	0.832	0.832	0.832	-	-	-	-
5	-	-0.004	0.003	0.0168	-	-	-	-
6	-	0.004	0.005	0.007	-	-	-	-

Table 5.4 Coefficient estimates in Eq. (5.9) and Eq.(5.10).

	Mean of $\ln(\Delta R)$						Standard deviation $\sigma_{\ln(\Delta R)}$		
	Coefficients b_{Rj}			Coefficients c_{Rj}			Coefficients d_{Rj}		
	DL			DL			DL		
j	1	2	3	1	2	3	1	2	3
1	1.128	1.118	1.095	-3.866	-3.460	-3.180	0.479	0.459	0.461
2	1.615	1.432	1.237	-0.706	-0.644	-0.499	0.081	0.090	0.094
3	-	-	-	-0.432	-0.425	-0.424	-0.041	-0.043	-0.042
4	-	-	-	0.095	0.096	0.102	0.004	0.0156	0.018
5	-	-	-	-	-	-	-0.001	-0.003	-0.004

5.3.4. Model for the correlation between stiffness and strength degradation

In order to completely define the joint distribution of $\ln(\Delta T)$ and $\ln(\Delta R)$, the definition of the covariance matrix Σ of the bivariate zero-mean Gaussian vector $\{\varepsilon_1, \varepsilon_2\}$ is needed as shown in Eq. (5.11):

$$\left\{ \Sigma = \begin{bmatrix} \sigma^2_{\ln(\Delta T)} & \sigma_{\ln(\Delta T)} \cdot \sigma_{\ln(\Delta R)} \cdot \rho_{\ln(\Delta T),\ln(\Delta R)} \\ \sigma_{\ln(\Delta T)} \cdot \sigma_{\ln(\Delta R)} \cdot \rho_{\ln(\Delta T),\ln(\Delta R)} & \sigma^2_{\ln(\Delta R)} \end{bmatrix} \right. \tag{5.11}$$

The covariance matrix is defined by the (estimated) standard deviations of the logarithms of period elongation $\sigma_{\ln(\Delta T)}$ and strength loss $\sigma_{\ln(\Delta R)}$ and their (estimated) correlation, $\rho_{\ln(\Delta T),\ln(\Delta R)}$, with the standard deviations being already available from Eq. (5.8) and Eq. (5.10). In this case, the correlation coefficients

$\rho_{\ln(\Delta T),\ln(\Delta R)}$ were modeled as a linear function of the ductility demand and hardening slope until a transition ductility μ_t is reached, as shown in Eq.(5.12).

$$\rho_{\ln(\Delta T),\ln(\Delta R)} = e_1 + e_2 \cdot (\mu - 1) + e_3 \cdot \alpha_h \qquad \text{with } 1.5 \le \mu \le \mu_t \tag{5.12}$$

In case of $\mu > \mu_t$, $\rho_{\ln(\Delta T),\ln(\Delta R)}$ varies only as function of α_h and can be evaluated from Eq. (5.12) assuming $\mu = \mu_t$. The value of μ_t differs by level of strength degradation, i.e., it is assumed equal to 7 for $DL = 1$; 6 for $DL = 2$ and 5 for $DL = 3$ on the basis of data observation.

The coefficients in Eq. (5.12) were defined by curve-fitting of the results performed separately for each level of strength degradation. Moreover, it was necessary to distinguish the fitting procedure of the model parameters into two separate cases $T < 1.5\text{s}$ and $T \ge 1.5\text{s}$. Figure 5.12 shows the model of $\rho_{\ln(\Delta T),\ln(\Delta R)}$ evaluated for the case of medium strength degradation in case of $T < 1.5\text{s}$ (Figure 5.12a) and $T \ge 1.5\text{s}$ (Figure 5.12b). Table 5.5 provides the values of the coefficients e_j $j = \{1, 2, 3\}$ in Eq. (5.12), evaluated for the three levels of strength degradation.

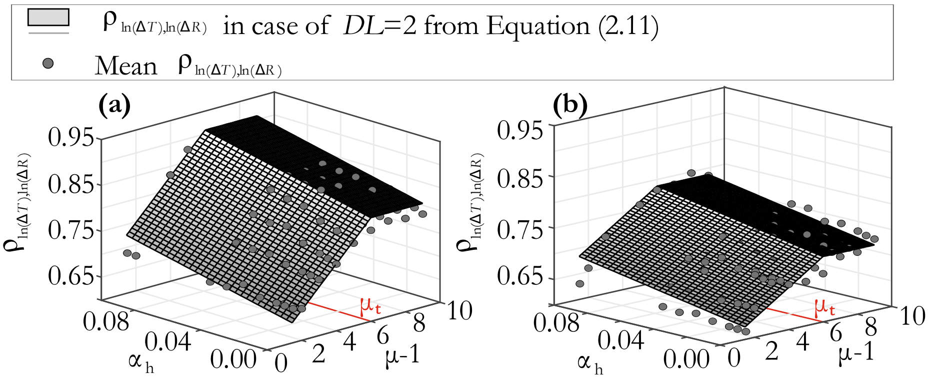

Figure 5.12 Model for $\rho_{\ln(\Delta T),\ln(\Delta R)}$ in case of medium strength degradation for $T < 1.5\text{s}$ (a) and $T \ge 1.5\text{s}$ (b).

Table 5.5 Coefficient estimates for the $\rho_{\ln(\Delta T),\ln(\Delta R)}$ model of Eq. (5.12).

	Coefficients e_j					
	$DL = 1$		$DL = 2$		$DL = 3$	
j	$T < 1.5$	$T \ge 1.5$	$T < 1.5$	$T \ge 1.5$	$T < 1.5$	$T \ge 1.5$
1	0.564	0.5723	0.5858	0.5915	0.6093	0.6172
2	0.03052	0.01749	0.04003	0.02266	0.04433	0.02578
3	1.151	0.5893	0.8276	0.5968	0.6419	0.4105
4	0.564	0.5723	0.5858	0.5915	0.6093	0.6172

5.4. Numerical implementation of the model

5.4.1. Distribution of C_μ and residual displacement ratio spectra

According to the previous sections, once the models for period elongation, strength deterioration and residual displacement have been completely defined, it is possible to estimate the joint distribution of $\left\{\ln(\Delta T), \ln(\Delta R), \delta_{res}/\delta_{max}\right\}$, given the ductility demand μ, period T, hardening slope α_h and the level of strength degradation *DL*. Although parametric models have been assumed for their marginal distributions, due to the complex functional dependence of $\delta_{res}/\delta_{max}$ on the other two it is convenient to obtain their joint distribution via a Monte-Carlo sampling scheme. The first step in such a procedure, entails selecting fixed values of μ, T, α_h, and *DL*, and then calculating the mean, $\overline{\ln(\Delta R)}$, and the standard deviation, $\sigma_{\ln(\Delta R)}$, conditional to these values from Eq. (5.9) and Eq. (5.10). Subsequently, at the *i*-th Monte Carlo replication, a random sample of $\ln(\Delta R) = x_i$ is extracted from a normal distribution having these parameters. At this point, given the marginal distribution of $\ln(\Delta T)$, which is another Gaussian function defined by the mean, $\overline{\ln(\Delta T)}$, and the standard deviation, $\sigma_{\ln(\Delta T)}$, evaluated from Eq. (5.8) it is possible to define the distribution of $\ln(\Delta T)$ conditional on $\ln(\Delta R) = x_i$ according to Eq.(5.13):

$$\begin{cases} \mathrm{E}\left[\ln(\Delta T) \middle| \ln(\Delta R) = x_i\right] = \overline{\ln(\Delta T)} + \rho_{\ln(\Delta T),\ln(\Delta R)} \cdot \left(\sigma_{\ln(\Delta T)}/\sigma_{\ln(\Delta R)}\right) \cdot \left[x_i - \overline{\ln(\Delta R)}\right] \\ \sigma_{\ln(\Delta T)|\ln(\Delta R)} = \sqrt{\left(1-\rho^2_{\ln(\Delta T),\ln(\Delta R)}\right) \cdot \sigma^2_{\ln(\Delta T)}} \end{cases} \tag{5.13}$$

where $\mathrm{E}\left[\ln(\Delta T) \middle| \ln(\Delta R) = x_i\right]$ represents the conditional mean of $\ln(\Delta T)$ and $\sigma_{\ln(\Delta T)|\ln(\Delta R)}$ the conditional standard deviation. Then, a value of $\ln(\Delta T) = y_i$ is randomly sampled from the corresponding (also Normal) conditional distribution. Finally, the conditional mean and standard deviation of the ratio $\delta_{res}/\delta_{max}$ is evaluated from Eq.(5.5) for the sampled vector of $\left\{\ln(\Delta R), \ln(\Delta T)\right\} = \left\{x_i, y_i\right\}$ and a random sample of $\delta_{res}/\delta_{max} = z_i$ is extracted from the corresponding Normal distribution, truncated between $-2 \cdot \sigma_\delta$ and $2 \cdot \sigma_\delta$. The C_μ value corresponding to the *i*-th sample is then simply $C_{\mu,i} = z_i$.

This procedure amounts to random sampling of a triplet of values $\left\{\ln\left(\Delta R\right),\ln\left(\Delta T\right),\delta_{res}/\delta_{max}\right\}=\left\{x_i,y_i,z_i\right\}$ from their joint conditional distribution. By repeating the sampling procedure a number of times N, one can obtain a representation of the joint densities of these RVs in the form of relative frequency diagrams of the sampled values. An example of such a representation is reported in Figure 5.13, that was constructed using one million samples. The results of this Monte-Carlo procedure can then be used to approximate the statistics of residual displacement ratio, such as its mean value, according to Eq. (5.14):

$$\overline{C_\mu}\approx 1/N\cdot\sum_{i=1}^{N} z_i \tag{5.14}$$

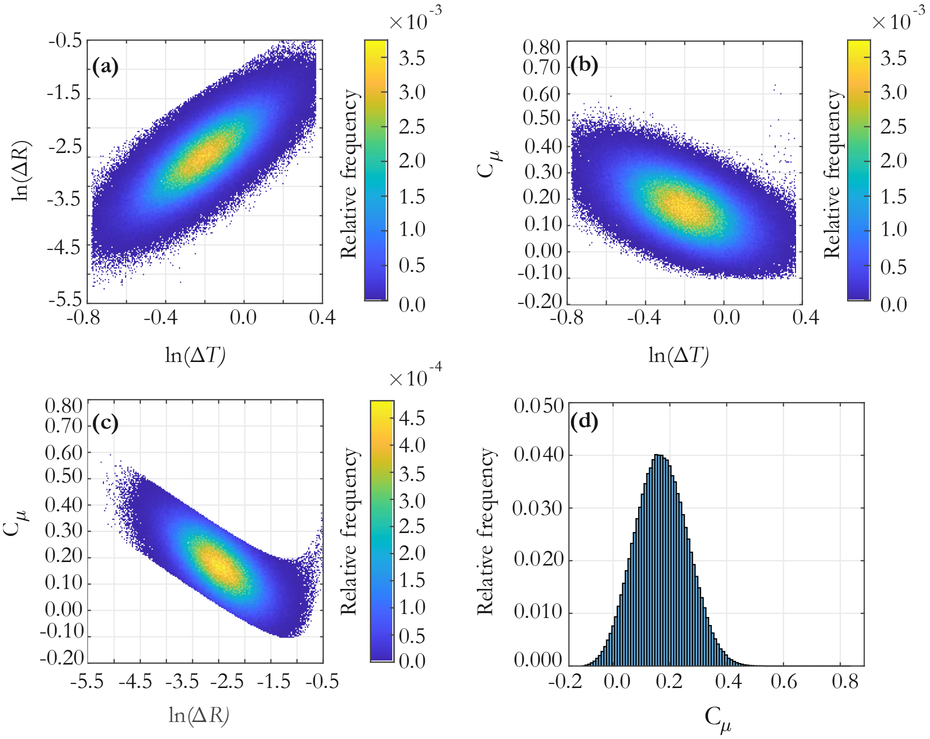

Figure 5.13 Monte-Carlo-based representation (relative frequency) of the joint distribution of period elongation and strength reduction (a), of period elongation and residual displacement (b), of strength reduction and residual displacement (c), for the case of ductility demand $\mu=4.0$, post-yield hardening ratio $\alpha_h=3.0\%$, period of the initial structure $T=0.8\,s$ and medium level of strength degradation; Monte-Carlo-based representation of the marginal distribution of C_μ (d).

In the case of no strength degradation, the Monte-Carlo scheme degenerates into sampling a value $\ln(\Delta T) = y_i$, from the marginal distribution of $\ln(\Delta T)$, and then directly sampling $\delta_{res}/\delta_{max} = z_i$ from its conditional distribution. Monte-Carlo is still useful in this case, for representing the marginal density of C_μ and calculating the mean $\overline{C_\mu}$, as shown in Figure 5.14.

It is worth highlighting that, as shown in Figure 5.13c and Figure 5.14a, the record-to-record variability of C_μ is such that residual displacement values near zero are still possible, with the left tail of the marginal distributions of C_μ being heavier. Another feature that is worth commenting is the slight distortion exhibited by the simulated joint distribution of period elongation and residual displacement ratio, shown in Figure 5.13b, towards the region of higher $\ln(\Delta T)$ values. This can be attributed to the contribution of the non-linear terms involving $\ln(\Delta R)$ in Eq. (5.9). For the same reason, there is a similar effect visible in the shape of the joint density of C_μ and $\ln(\Delta R)$ in Figure 5.13c.

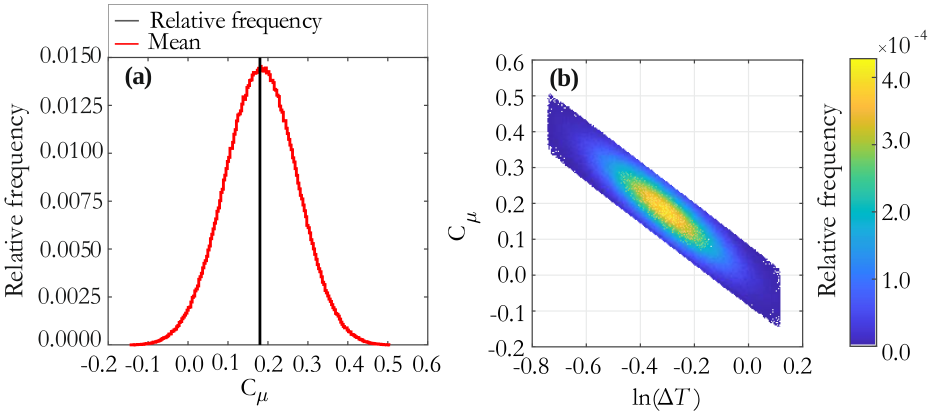

Figure 5.14 Monte-Carlo-based representation (relative frequency) of the marginal distribution of C_μ (a) and of the joint distribution of period elongation and residual displacement ratio (b), for the case of ductility demand $\mu = 4.0$, post-yield hardening ratio $\alpha_h = 3.0\%$ and period of the initial structure $T = 0.8\,s$.

The validation of the predictive model was undertaken by comparing the results of the Monte-Carlo resampling scheme with the data used for the development of the predictive model. The validation was made calculating the 25th, 50th and the 75th percentiles of residual displacement ratio for each combination of μ, α_h, T and DL and comparing the results from the resampling procedure with the corresponding percentiles estimated from the initial data set.

For sake of brevity, hereafter two examples of comparison are reported showing the good agreement of the model with the initial data set used. Figure 5.15 shows the results obtained for the case of absent strength degradation ($DL = 0$) and $\alpha_b = 0.01\%$ considering μ between 1.5 and 9.0 and four natural vibration periods T (i.e. 0.3, 0.9; 1.2; 1.8). Figure 5.16 shows the results obtained for the case of high strength degradation ($DL = 3$) and $\alpha_b = 0.02\%$ for all the values of μ from 1.5 to 9.0 and four natural vibration periods T (i.e. 0.3s, 0.9s; 1.2s; 1.8s). In both the figures the results obtained from the model are represented using black lines (dashed lines for 25th and 75th percentiles and solid line for the 50th percentile). On the other hand, the reference data are reported using a box plot representation in which the central mark indicates the median, and the top and the bottom edges of the box indicate the 25th and 75th percentiles, respectively.

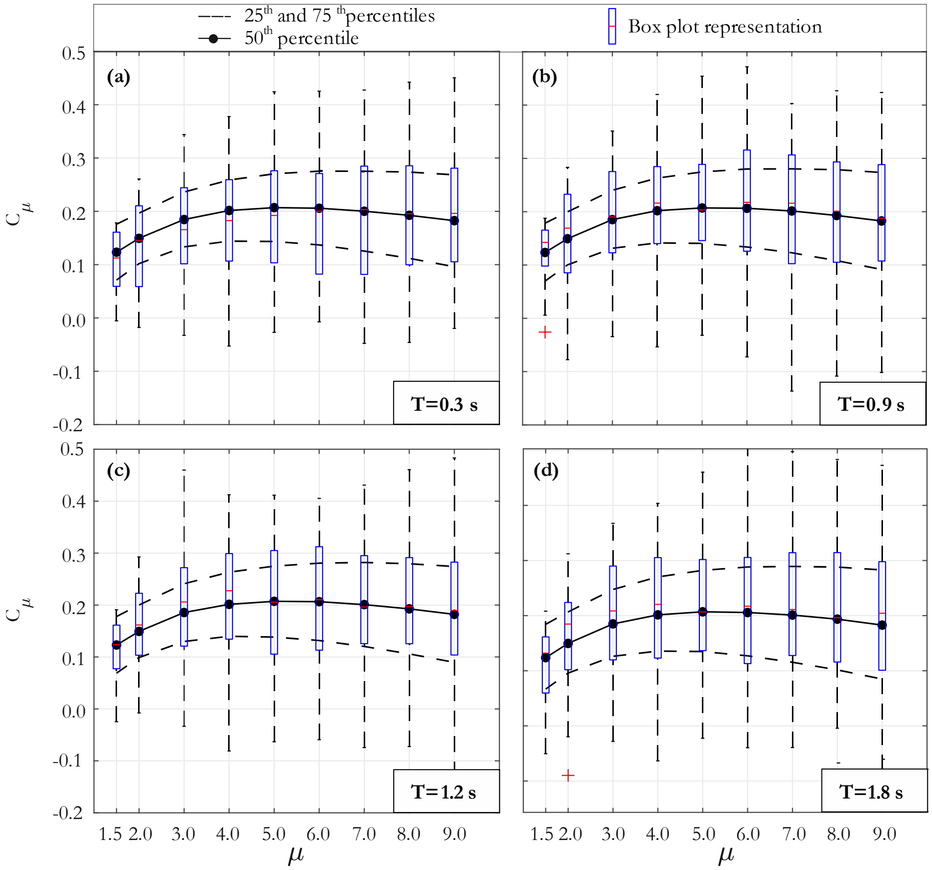

Figure 5.15 Comparison of the summary statistics in case of absent strength degradation and $\alpha_b = 0.01\%$ for period equal to 0.3s (a); 0.9s (b); 1.2s (d) and 1.8s (d).

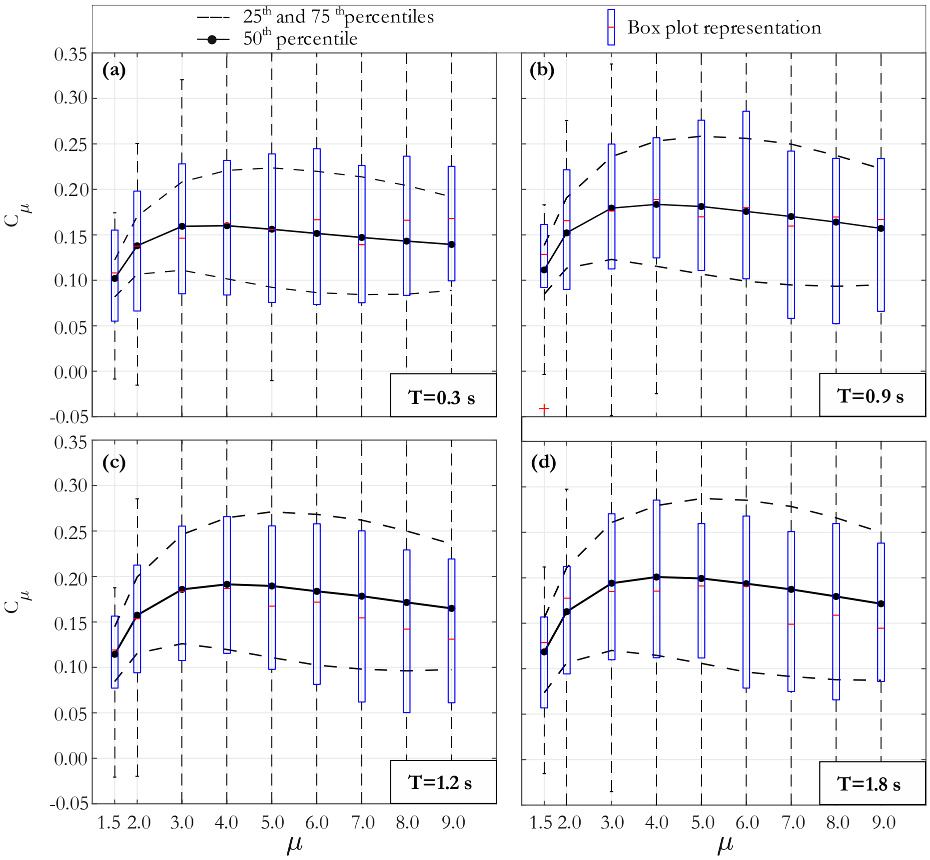

Figure 5.16 Comparison of the summary statistics in case of high level of strength degradation and $\alpha_h = 0.02\%$ for period equal to 0.3s (a); 0.9s (b); 1.2s (d) and 1.8s (d).

By repeating resampling procedure while varying μ and T, one can also obtain mean C_μ spectra from the model, such as the ones shown in Figure 5.17. Figure 5.17a highlights the fact that $\overline{C_\mu}$ is independent of period in the case of no cyclic strength degradation, which is in agreement with past studies (Ruiz-García and Miranda, 2004; Liossatou and Fardis, 2015; Madhu Girija and Gupta, 2020), despite some differences in the hysteretic laws considered then and now. Moreover, the obtained results have the same trend with μ. Past studies using the constant-strength approach (Ruiz-García and Miranda, 2004; Liossatou and Fardis, 2015) report that the mean residual displacement ratio tends to increase with increasing strength ratio (Ruiz-García and Miranda, 2004; Liossatou and Fardis, 2015) until a saturation point is reached. A similar trend with μ was found for the mean constant-ductility residual displacement ratio in the case of elastic-perfectly-plastic oscillators (Madhu Girija and Gupta, 2020). However, in the present case where peak-oriented and possibly strength-degrading hysteresis was examind, $\overline{C_\mu}$ does not increase monotonically with increasing μ in the range examined. This is attested to more clearly by Figure 5.17c,d which plots $\overline{C_\mu}$ as a function of μ, at various periods.

For systems without any strength deterioration (Figure 5.17c), it is possible to distinguish two regions in terms of ductility demand: for μ below a value of around four $\overline{C_\mu}$ increases with increasing ductility, while for higher values of μ the trend is reversed, with $\overline{C_\mu}$ decreasing as ductility demand increases from four to nine. On the other hand, the introduction of strength loss modifies this trend (Figure 5.17d); although $\overline{C_\mu}$ still peaks at $\mu \approx 4$, the subsequent downwards trend is not monotonic. These observations can be summed-up as a non-monotonic trend of $\overline{C_\mu}$ as a function of μ, for both cases of strength degrading and non-strength degrading systems.

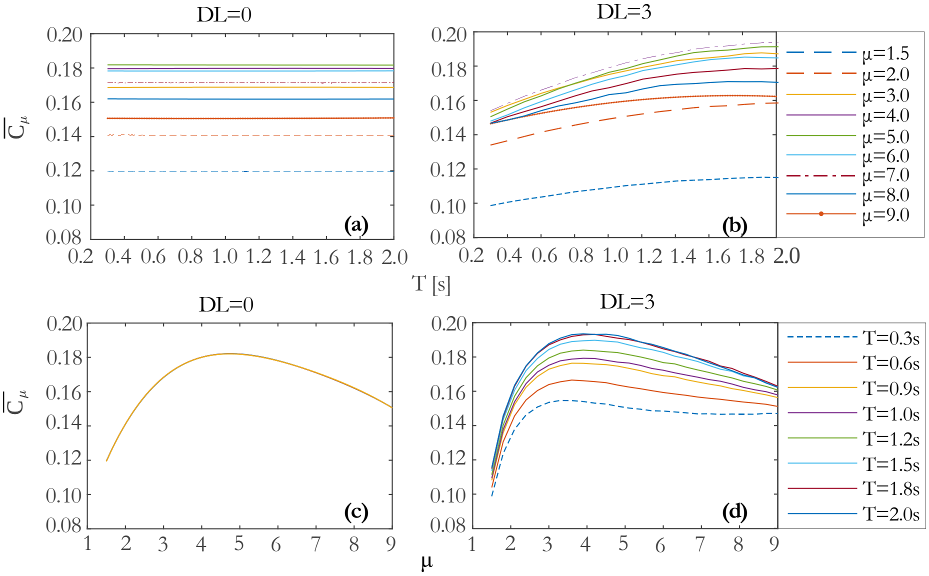

Figure 5.17 Mean C_μ spectra for various μ, evaluated for $\alpha_h = 3.0\%$ in case of no cyclic strength degradation ($DL = 0$) (a) and high strength degradation ($DL = 3$) (b); mean C_μ as a function of ductility demand in case of $DL = 0$ (c) and $DL = 3$ (d).

5.4.2. Simulation of the post-shock pushover curve

The fact that the above procedure requires multiple samples of the random vector $\left\{\ln(\Delta T), \ln(\Delta R), \delta_{res}/\delta_{max}\right\}$ to be extracted, allows for an additional surrogate result of the model, which may be of interest to earthquake engineers. For each triplet of period elongation, strength loss and residual displacement sampled from the model, it is possible to univocally define the corresponding bilinear backbone curve of the SDoF oscillator at the end of the seismic excitation. This means that, apart from the residual displacement ratio, the Monte-Carlo procedure can also provide stochastic realizations of the post-shock pushover curve of the SDoF system, which is a probabilistic representation of the damaged state to which the simple structure has transitioned.

In fact, after obtaining the corresponding residual displacement δ_{res}, elongated period T' and the deteriorated lateral resistance at maximum ductility demand F'_{max} for each random vector $\left\{\ln(\Delta T), \ln(\Delta R), \delta_{res}/\delta_{max}\right\}$, it is possible to evaluate all the parameters defining the post-shock pushover curve as illustrated in Figure 5.18. This figure shows the coordinates of the points defining the initial and post-shock curve in the displacement-force plane, using the notation with primes for the parameters of the damaged system.

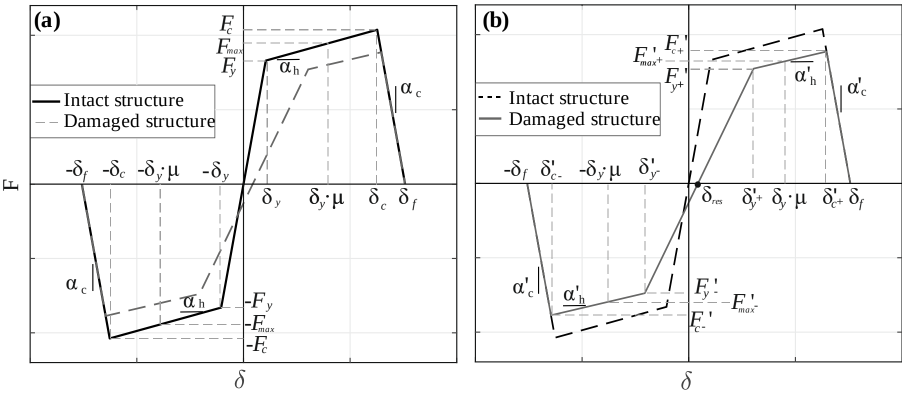

Figure 5.18 Parameters defining the pushover curves; parameters for the definition of the intact structure's pushover curve (a); and of the post-shock pushover curve (b).

The elastic branch of the damaged system's pushover can be determined by evaluating the yield force $F'_{y^{\pm}}$ and displacement $\delta'_{y^{\pm}}$ in the positive and negative direction, as reported in Eq. (5.15):

$$\begin{cases} F'_{y^{\pm}} = \left[F'_{max} - F'_{max} \cdot \dfrac{\alpha_h}{\delta_y} \cdot \dfrac{F_y}{F_{max}} \cdot \left(\mu \cdot \delta_y \mp \delta_{res} \right) \right] \Big/ \left[1 - \dfrac{F'_{max}}{F_{max}} \cdot \alpha_h \cdot \left(\dfrac{T'}{T} \right)^2 \right] \\ \delta'_{y^{\pm}} = \delta_y \cdot \dfrac{F'_{y^{\pm}}}{F_y} \cdot \left(\dfrac{T'}{T} \right)^2 \pm \delta_{res} \end{cases} \tag{5.15}$$

The post-yield branch is defined by the hardening slope α'_h, the capping point displacements in the two directions, $\delta'_{c^{\pm}}$ and corresponding forces $F'_{c^{\pm}}$. The hardening branch's slope can be defined once the degradation due to cyclic strength deterioration is known, which is implicit in the hysteretic model (Lignos and Krawinkler, 2011). The capping points can be calculated as the intersection points of the damaged structure's hardening branch and of the softening branch, the latter defined by the slope α_c, which is assumed to remain invariant, and the ultimate displacement δ_f. At this point, it is worth recalling that the predictive model was developed considering only ductility demands that maintain structural response displacement along the hardening branch, without crossing into the softening branch where in-cycle strength degradation could occur. Therefore, the softening branch was included exclusively for keeping track of the capping points in the damaged state. The hardening slope and the coordinates of the capping points for the post-shock pushover are calculated according to Eq. (5.16), where δ_c and F_c are the displacement and the corresponding force at the capping point for the intact structure:

$$\begin{cases} \alpha'_h = \alpha_h \cdot \dfrac{F'_{max}}{F_{max}} \cdot \left(\dfrac{F_y}{F'_{y^{\pm}}} \cdot \dfrac{\delta'_{y^{\pm}} \mp \delta_{res}}{\delta_y} \right) \\ \delta'_{c^{\pm}} = \left(F'_{y^{\pm}} - \dfrac{F'_{y^{\pm}} \cdot \alpha'_h \cdot \delta'_{y^{\pm}}}{\delta'_{y^{\pm}} \mp \delta_{res}} + \dfrac{F_c}{\delta_c - \delta_f} \delta_f \right) \Big/ \left(\dfrac{F_c}{\delta_c - \delta_f} - \dfrac{F'_{y^{\pm}}}{\delta'_{y^{\pm}} \mp \delta_{res}} \cdot \alpha'_h \right) \\ F'_{c^{\pm}} = \left[F_c \cdot \left(\delta'_{c^{\pm}} - \delta_f \right) \right] \Big/ \left(\delta_c - \delta_f \right) \end{cases} \tag{5.16}$$

An example of such definition of a set of pushovers, that represent different realizations of the damaged SDoF system, is given in Figure 5.19 for a case without strength deterioration and a case characterized by a medium level of strength degradation. This representation highlights the usefulness of the model, as the distribution of residual displacements is provided as a function of a set of RVs that have specific physical meaning for the SDoF structure that has been damaged by an earthquake shock.

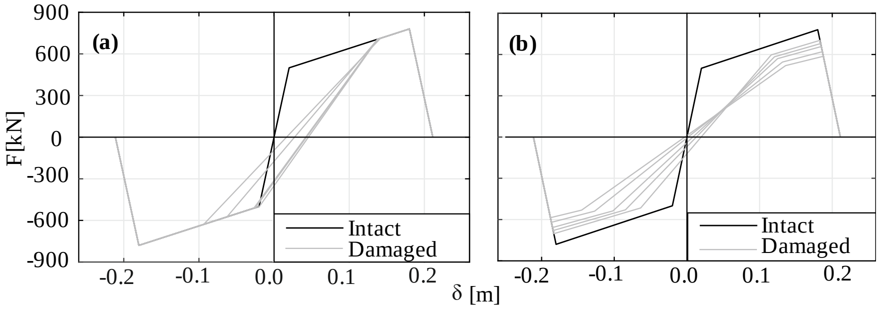

Figure 5.19 Pushover curves corresponding to different realizations of the damaged structural system: a case of $\alpha_h = 7.0\%$, $\mu = 6.0$, $T = 2.0\,s$ and no strength deterioration (a) and medium strength degradation (b).

5.5. Illustrative application on a RC frame structure

This section provides an example application of the predictive model for constant ductility residual displacement ratio in the context of the seismic assessment of a reinforced concrete multi-story moment-resisting frame. The case-study structural system, shown in Figure 5.20a, is a fixed-base plane reinforced concrete frame representing an internal frame of a symmetric four-story building without masonry in-fills. The system exhibits first-mode dominated dynamic elastic response with a first-mode period of natural vibration T_1 equal to 0.53 s and flexure-dominated inelastic response of the constituent beams and columns (see Baltzopoulos et al., 2015 for structural details). For the purposes of this application, an equivalent SDoF system was defined, based on a static nonlinear analysis that was carried out by applying a gradually increasing lateral force profile corresponding to the structure's first-mode excitation to base acceleration. The nonlinear structural model built for the execution of nonlinear static and dynamic analyses adopted a lumped plasticity approach, using a multi-linear moment-plastic rotation relation and the modified IMK model without cyclic strength degradation for the definition of the hysteretic behavior.

In this application, it is assumed that entry of the frame into a generic damage state occurs when the roof drift ratio (RDR) exceeds a threshold value of 0.01. The objective of the assessment is to determine, given that the structure has reached the damage state threshold in terms of RDR, the probability that the residual RDR will have exceeded a threshold value of 0.0033, which corresponds to rebar yielding having developed at all beam ends and the formation of a plastic mechanism for the structure. This assessment is first performed by employing the proposed predictive model via the pushover-based equivalent SDoF system and is the validated by means of dynamic analysis of the multiple-degree-of-freedom (MDoF) numerical model of the structure.

In order to obtain the data necessary for the application's validation, the MDoF system was subjected to incremental dynamic analysis using as input a set of fifty acceleration records, none of which were included in the suite of records employed for the development of the model. For the execution of the IDA, the pseudo-acceleration at the fundamental period of vibration $S_a(T_1)$ was assumed as intensity measure. Similar to the methodology used to develop the predictive model and presented in the previous paragraphs, the IDA results were used to determine the scale factor needed for each record to bring the structure at assumed damage state threshold, i.e. a RDR of 0.01 (Figure 5.20b). Subsequently, the records thus scaled were used for the execution of dynamic analyses that were immediately followed by static non-linear analyses, again mimicking the previously described analysis methodology, resulting in different realizations of the damaged structure's pushover to be obtained, as shown in Figure 5.20c.

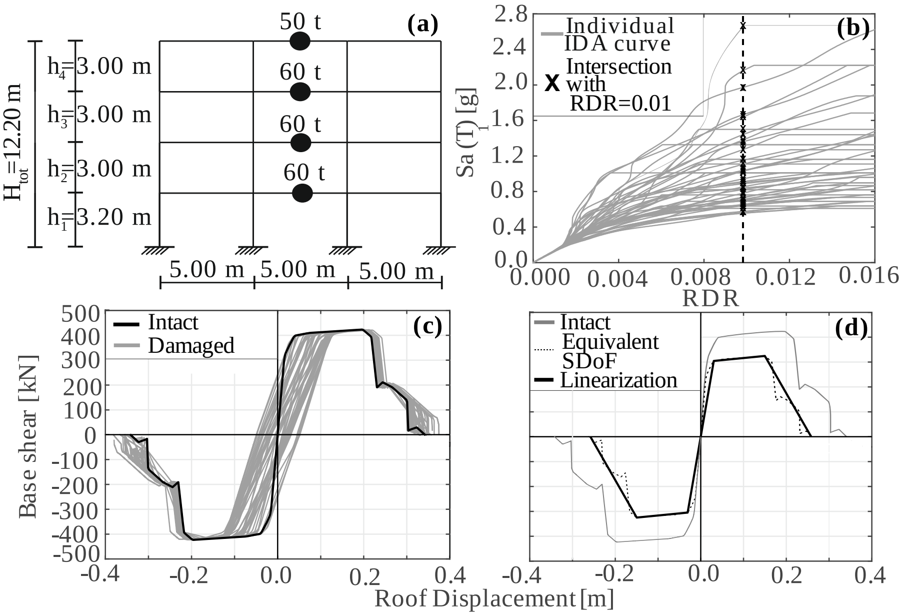

Figure 5.20 Basic information on the structure and analysis results. Case-study frame (a), IDA curves for the RC frame (b); pushover curves representing different realizations of the damaged system (c) and definition of the equivalent SDoF (d).

From these analyses, the residual displacements at each floor of the system were collected and the parameters defining the pushovers of the damaged system were evaluated, in order to make a comparison with the results deriving from the application of the predictive model in terms of the ratio of residual to peak displacement and elongated period. These are shown in Figure 5.21, where $\delta^{MDoF}_{res,i}/H_{tot}$ with $i=\{1,2,3,4\}$ is the ratio of residual displacement at the i-th floor to the total height of the structure whereas the residual inter-story drift $\Delta_{res,j}^{MDoF}/h_j$ at the j-th story is evaluated as $\Delta_{res,j}^{MDoF}/h_j = \left(\delta_{res,j}^{MDoF} - \delta_{res,(j-1)}^{MDoF}\right)/h_j$ where h_j is the inter-story height and $j = \{1,2,3,4\}$. It should be noted that the sign convention adopted for the figure is that $\delta_{res,i}^{MDoF}$ is assumed positive when it occurs in the same direction as the corresponding maximum transient roof displacement.

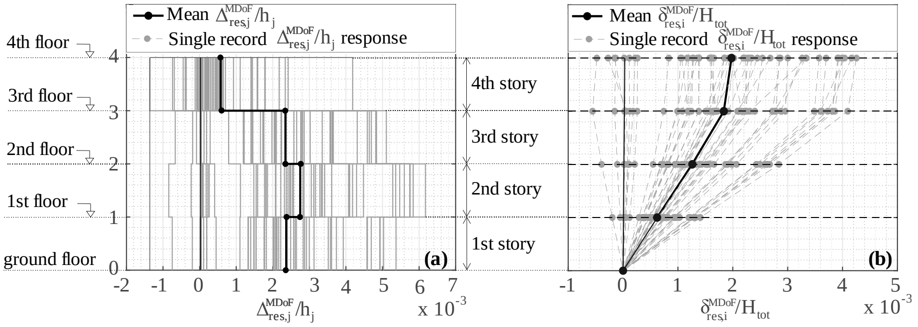

Figure 5.21 Cumulative values of residual inter-story drift ratios (a); residual roof drifts evaluated at each story(b).

For the purposes of the simplified pushover-based assessment, the predictive model was applied for the equivalent SDoF system representative of the intact structure. The backbone of this equivalent SDoF oscillator was obtained by dividing the frame's pushover force and roof displacement values by the first-mode modal participation factor (Fajfar, 2000) $\Gamma = 1.309$ and obtaining a multi-linear approximation of the resulting curve, as reported in Figure 5.20d. In this multi-linear approximation, the nominal yield point of the equivalent SDoF system is taken to correspond to a RDR of 0.0033, i.e., the point of formation of a global plastic mechanism for the structure. Therefore, the damage state threshold considered for this application corresponds to a ductility demand of three. The mass m^*, period T^* and hardening slope $\alpha_h{}^*$ of the equivalent SDoF are reported in Table 5.6.

Table 5.6 Characteristics of the equivalent SDOF system.

T^* [s]	m^* [ton]	$\alpha_h{}^*$
0.774	147.13	0.017

The mean and the standard deviation defining the distribution of the period elongation $\ln(\Delta T)$, from Eq.(5.6), the mean and standard deviation of the constant-ductility residual displacement ratio C_μ, obtained by means of Eq.(5.4) and the Monte-Carlo simulation procedure, were compared with the estimates obtained from the analysis results of the MDoF model and are reported in Table 5.7. In that table, the standard deviation of C_μ derived from the simulation is denoted as σ_{C_μ}.

Table 5.7 Mean and standard deviation defining the distributions of the period elongation and of the constant-ductility residual displacement ratio.

	$\overline{ln(\Delta T)}$	$\sigma_{ln(\Delta T)}$	$\overline{C_\mu}$	σ_{C_μ}
Predictive Model	-0.615	0.154	0.190	0.102
MDoF	-0.761	0.153	0.209	0.127

The cumulative distribution functions of percentile loss of stiffness, ΔK, and residual RDR, $\delta^{MDoF}_{res,4}/H_{tot}$, obtained by means of the predictive model and empirically using the analyses results are compared in Figure 5.22. In the same figure, x represents a generic realization of the random variables ΔK and $\delta^{MDoF}_{res,4}/H_{tot}$, while the percentile loss of stiffness is computed as $\Delta K = \left|(k'-k)/k\right| = \left|(T/T')^2 - 1\right|$.

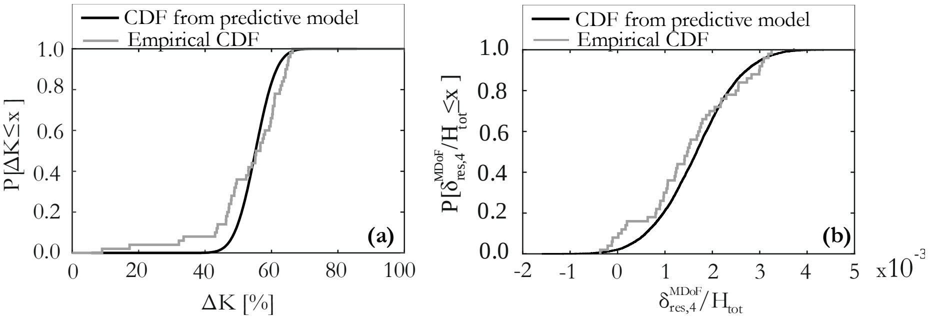

Figure 5.22 Comparison of the cumulative distribution function of period elongation (a) and constant ductility residual displacement ratio (b).

Apart from these comparisons, the stated objective of the assessment was to evaluate the probability that the residual RDR exceeds the threshold of 0.0033 given that the structure has arrived at a generic damage state. This estimation can be of engineering interest because eventual high values of residual roof drift can determine the feasibility of repair operations. In this case, the simplified pushover-based procedure that made use of the proposed predictive model, leads to an estimated probability of 15.5%, while the dynamic analysis of the MDoF model provided a probability of 16%. This shows good agreement of the approximate procedure with the more rigorous analysis, which is also apparent from the comparison of the obtained response statistics.

5.6. Discussion and conclusions

The main purpose of this study was to present a predictive model for the central tendency and the related record-to-record variability of residual displacements for bilinear single-degree-of-freedom systems exhibiting stiffness and strength degradation. This model ultimately provides the probability distribution of the constant-ductility residual displacement ratio, C_μ, which is defined as the ratio of residual to peak transient displacement. In order to develop the model, a multitude of SDoF systems with different values of natural vibration period and post-yielding hardening ratio and governed by the peak-oriented modified Ibarra-Medina-Krawinkler hysteretic model, were subjected to nonlinear dynamic analyses. These dynamic runs were designed to hold the ductility demand μ constant at various predefined levels, by appropriately scaling the input motion.

From the data obtained from these dynamic analyses, it was observed that the residual displacement never exceeded about a half of the corresponding peak inelastic displacement demand for all the cases considered and that this overall maximum residual displacement ratio tends to decrease with increasing levels of strength degradation. The results also confirmed that the main parameter affecting mean residual displacement is the post-yield hardening ratio, in agreement with previous studies (G. A. Macrae and Kawashima, 1997; Borzi et al., 2001; Christopoulos et al., 2003; Ruiz-García and Miranda, 2006). Other parameters whose influence was examined were the (initial) period of each SDoF oscillator and the level of ductility demand. Generally speaking, the period of the structure showed a limited influence on residual displacements within the 0.3s to 2.0s interval considered in this study. On the other hand, ductility demand was observed to have a more significant effect in each level of strength degradation.

The proposed model suggests that the mean residual displacement ratio can be considered as a function of two random variables, elongated period and strength loss, that represent the effects of stiffness and strength degradation, and which were found to be correlated with each other. Therefore, a complete definition of the model also required the development of subsidiary models providing the marginal distributions of elongated period and strength loss, as well as their correlation. The functional form proposed for the mean constant-ductility residual displacement ratio also contains the ductility demand and post-yield hardening ratio as independent variables. The variance of the residual displacement ratios was found to be non-constant. For any level of strength degradation, the standard deviation of the ratio was modeled as a function of post-yield hardening slope, period of the natural vibration and ductility demand. It was also observed that central tendency of period elongation mainly depends on the post-yield hardening ratio and ductility demand, whereas the corresponding variance was modeled only as function of the expected value of the model. On the other hand, the central tendency of strength loss mainly depends on ductility demand, hardening slope and structural period whereas its variance only appears to depend on period and ductility demand. The correlation coefficient between period elongation and strength loss was found to be mainly affected by the initial period of the oscillator and the ductility demand.

On a closing note, it should be highlighted that the complete proposed model, allowed to represent the joint distribution of the three random variables: residual displacement, period elongation and strength degradation, given ductility demand, initial period and hardening slope of the structure and the level of cyclic strength degradation. As shown in the paragraph concerning the numerical implementation of the model, this representation of their joint distribution can be achieved via a Monte-Carlo sampling scheme. This procedure can be used to derive pushover curves, considering uncertainties, characterizing a damaged structural system where the damage level is reflected by the ductility demand provoked by an earthquake shock.

References

Baltzopoulos, G., R. Baraschino, I. Iervolino, and D. Vamvatsikos (2017), SPO2FRAG: software for seismic fragility assessment based on static pushover, *Bull. Earthq. Eng.*, 15(10), 4399–4425.

—— (2018), Dynamic analysis of single-degree-of-freedom systems (DYANAS): a graphical user interface for OpenSees, *Eng. Struct.*, 177, 395–408.

Baltzopoulos, G., E. Chioccarelli, and I. Iervolino (2015), The displacement coefficient method in near-source conditions, *Earthq. Eng. Struct. Dyn.*, 44(7), 1015–1033.

Bazzurro, P., C.A. Cornell, C. Menun, and M. Motahari (2004), Guidelines for seismic assessment of damaged buildings, *Proc. 13th World Conf. Earthq. Eng.*, (1708), Paper No. 1708.

Borzi, B., G.M. Calvi, A.S. Elnashai, E. Faccioli, and J.J. Bommer (2001), Inelastic spectra for displacement-based seismic design, *Soil Dyn. Earthq. Eng.*, 21(1), 47–61.

Christopoulos, C., and S. Pampanin (2004), Towards performance-based design of MDOF structures with explicit consideration of residual deformations, *ISET J. Earthq. Technol.*, 41(440), 53–73.

Christopoulos, C., S. Pampanin, and M.J. Nigel Priestley (2003), Performance-based seismic response of frame structures including residual deformations. Part I: Single-degree of freedom systems, *J. Earthq. Eng.*, 7(1), 97–118.

Cornell, C.A., and H. Krawinkler (2000), Progress and challenges in seismic performance assessment, *PEER Cent. News*, 3(2), 1–4.

Draper, N.R., and H. Smith (1998), *Applied Regression Analysis*, 3rd ed., John Wiley & Sons, New York.

Fajfar, P. (2000), A nonlinear analysis method for performance based seismic design., *Earthq. Spectra*, 16(3), 573–592.

FEMA P440A (2009), *Effects of Strength and Stiffness Degradation on Seismic Response.*

Ibarra, L.F., R.A. Medina, and H. Krawinkler (2005), Hysteretic models that incorporate strength and stiffness deterioration, *Earthq. Eng. Struct. Dyn.*, 34(12), 1489–1511.

Iervolino, I., E. Chioccarelli, and A. Suzuki (2020), Seismic damage accumulation in multiple mainshock-aftershock sequences, *Earthq. Eng. Struct. Dyn.*

Iervolino, I., M. Giorgio, and E. Chioccarelli (2016), Markovian modeling of seismic damage accumulation, *Earthq. Eng. Struct. Dyn.*, 45(3), 441–461.

Iervolino, I., A. Spillatura, and P. Bazzurro (2018), Seismic reliability of code-conforming Italian buildings, *J. Earthq. Eng.*

Lignos, D. (2013), Sidesway collapse of deteriorating structural systems under seismic excitations, *PhD thesis*, 53(9), 1689–1699.

Lignos, D., and H. Krawinkler (2011), Deterioration modeling of steel components in support of collapse prediction of steel moment frames under earthquake loading, *J. Struct. Eng.*, 137(11), 1291–1302.

Liossatou, E. (2013), Residual seismic displacements of RC structures., Thesis submitted to the Civil Engineering Department in partial fulfilment of the requirements for a Doctorate, University of Patras,.

Liossatou, E., and M.N. Fardis (2015), Residual displacements of RC structures as SDOF systems, *Earthq. Eng. Struct. Dyn.*, 44, 713–734.

Luco, N., P. Bazzurro, and C.A. Cornell (2004), "Dynamic versus static computation of the residual capacity of a mainshock-damaged building to withstand an aftershock," in: *13th World Conference on Earthquake Engineering, Vancouver, B.C., Canada August 1-6*.

Macrae, G A, and K. Kawashima (1997), Post-earthquake residual displacements of bilinear oscillators, *Earthq. Eng. Struct. Dyn.*, 26(7), 701–716.

Macrae, G. A., and K. Kawashima (1997), Post-earthquake residual displacements of bilinear oscillators, *Earthq. Eng. Struct. Dyn.*, 26(7), 701–716.

Madhu Girija, H., and V.K. Gupta (2020), Scaling of constant-ductility residual displacement spectrum, *Earthq. Eng. Struct. Dyn.*, 49(3), 215–233.

Mahin, S., and V. V Bertero (1981), An evaluation of inelatic seismic design spectra, *J. Struct. Eng.*, 107(9), 1777–1795.

Mardia, V.K. (2019), Measures of multivariate skewness and kurtosis with applications, *Biometrika*, 57(3), 519–530.

McKenna, F. (2011), OpenSees: A framework for earthquake engineering simulation, *Comput. Sci. Eng.*, 13(4), 58–66.

Orlacchio, M., G. Baltzopoulos, and I. Iervolino (2019), Constant-ductility residual displacement ratios, *Proc. COMPDYN 2019, 7th ECCOMAS Themat. Conf. Comput. Methods Struct. Dyn. Earthq. Eng. Crete, Greece June, 24-26*.

—— (2020), "State-dependent seismic fragility via pushover analysis," in: *Proceedings of the 17th World Conference on Earthquake Engineering, 17WCEE Sendai,Japan*.

Pacor, F., C. Felicetta, G. Lanzano, S. Sgobba, R. Puglia, M. D'Amico, E. Russo, G. Baltzopoulos, and I. Iervolino (2018), NESS v1.0: A worldwide collection of strong-motion data to investigate near source effects., *Seismol. Res. Lett.*, 89(6), 2299–2313.

Pampanin, S., C. Christopoulos, and M.J.N. Priestley (2003), Performance-based seismic response of frame structures including residual deformations. PartII : Multi-degree of freedom systems, *J. Earthq. Eng.*, 7(1), 119–147.

Raghunandan, M., A.B. Liel, and N. Luco (2015), Aftershock collapse vulnerability assessment of reinforced concrete frame structures, *Earthq. Eng. Struct. Dyn.*, 44(3), 419–439.

Ramirez, C.M., and E. Miranda (2012), Significance of residual drifts in building earthquake loss estimation, *Earthq. Eng. Struct. Dyn.*, 41, 1477–1493.

Riddell, R. (2008), Inelastic response spectrum: early history, *Earthq. Eng. Struct.*

Dyn.

Riddell, R., and N.M. Newmark (1979a), Statistical analysis of the response of nonlinear systems subjected to earthquakes, *Res. Rep. 468*, (August), 291 pp.

—— (1979b), Force-deformation models for nonlinear analysis, *ASCE J. Struct. Div.*, 105(12), 2773–2778.

Ruiz-García, J., and J.D. Aguilar (2015), Aftershock seismic assessment taking into account postmainshock residual drifts, *Earthq. Eng. Struct. Dyn.*, 44, 1391–1407.

Ruiz-García, J., and E. Miranda (2003), Inelastic displacement ratios for evaluation of existing structures, *Earthq. Eng. Struct. Dyn.*, 32(8), 1237–1258.

—— (2004), Performance-based assessment of existing structures accounting for residual displacement, vol. 153, Technical Report No.153 John A. Blume Earthquake Engineering Center, Stanford University, Standford, CA.

—— (2006), Residual displacement ratios for assessment of existing structures, *Earthq. Eng. Struct. Dyn.*, 35(3), 315–336.

Uma, S.R., S. Pampanin, and C. Christopoulos (2010), Development of probabilistic framework for performance-based seismic assessment of structures considering residual deformations, *J. Earthq. Eng.*, 14(7), 1092–1111.

Vamvatsikos, D., and C.A. Cornell (2001), Incremental Dynamic Analysis, *Earthq. Eng. Struct. Dyn.*, 31(3), 491–514.

Vamvatsikos, D., and C.A. Cornell (2006), Direct estimation of the seismic demand and capacity of oscillators with multi-linear static pushovers through IDA, *Earthq. Eng. Struct. Dyn.*, 35(9), 1097–1117.

Veletsos, A., and N.M. Newmark (1960), *Effect of inelastic behavior on the response of simple systems to earthquake motions.*

6

State-dependent seismic fragility via pushover analysis.

Abstract

From this chapter was derived the paper:

- *Orlacchio M., Baltzopoulos G., Iervolino I. (2020), "State-dependent seismic fragility via pushover analysis." Proceedings of the 17th World Conference on Earthquake Engineering, 17WCEE Sendai, Japan.*

Earthquakes are clustered in space and time. This means that structures in seismically active regions can be subjected to multiple consecutive instances of base acceleration, with insufficient in-between time for repair operations to take place. In such situations, buildings may experience degradation of their lateral-force-resisting capacity due to damage accumulation. Consequently, the use of seismic fragility functions developed for the intact structure may not be enough, in the context of seismic risk assessment studies that consider the effect of seismic clusters. In these cases, one may employ state-dependent fragility curves, which are separate fragility functions assigned to the same structure, depending on distinct damage states that it may be brought to by prior shocks.

State-of-the-art analytical estimation of structure-specific fragility entails the use of dynamic analysis of a numerical model of the structure, for example, incremental dynamic analysis (IDA), which can be computationally laborious, thus motivating the development of simplified, less time-consuming methods, often based on substituting the structural model by equivalent single-degree-of-freedom (SDOF) systems that can be defined via pushover analysis. In fact, existing procedures in the literature, such as back-to-back IDA, that can be used to estimate state-dependent fragility curves, tend to increase computational costs, rendering the development of simplified methodologies for this case a topical issue.

In this context, this chapter presents a method for estimating state-dependent seismic fragility functions, based on pushover analysis and a predictive model for constant-ductility residual displacement ratio. The latter is defined as the residual-to-peak-transient seismic displacement ratio of an equivalent SDOF structure. The residual displacement model, which considers yielding SDOF systems that exhibit stiffness and strength degradation, with natural periods between 0.3 s and 2.0 s and post-yield hardening ratios from 0 % to 10%, is outlined first. The model also estimates the joint probability distribution of normalized elongated period and strength degradation, for a given ductility demand. This information allows for a probabilistic evaluation of the pushover curve characterizing a damaged structural system, which is then used to obtain state-dependent fragility when damage states are defined via ductility demand thresholds. The state-dependent fragility curves are estimated via IDA of SDOF oscillators with pushovers that were previously determined from the model. An illustrative application showcases the ability of the proposed methodology to provide state-dependent fragility estimates in an expedient manner.

Keywords: sequence-based seismic reliability; damage accumulation; residual displacements.

6.1. Introduction

Seismic risk analysis, in its classical form, does not consider structural failure that is reached progressively due to damage accumulation in multiple events. This can be justified by considering that, for example, after some seismic event damages the structure of interest, enough time will elapse until the next earthquake for the stakeholders to repair it back to its initial state. However, earthquakes are known to be clustered in both space and time and this means that the necessary repair time between seismic shocks may not be available. One such typical case is that of short-term emergency management, during the aftershock sequence that follows an earthquake characterized as the mainshock. In that case, the possibility of aftershock-induced ground shaking exacerbating any damage caused by the main event must be taken into account in risk assessment (Iervolino et al., 2016, 2020).

Fragility functions are well-established tools, used in seismic risk analyses to probabilistically quantify structural vulnerability (discussion to follow). Traditionally, one fragility per structure is assigned, assuming that earthquake-induced shaking will find the structure in the absence of seismic damage. In order to extend the use of this tool to sequence-based risk assessment, the concept of a set of state-dependent seismic fragility functions must be introduced. State-dependent fragilities provide a full picture of the seismic vulnerability of a structure in which damage can accumulate due to transitions across *damage states* (DSs). State-of-the-art analytical estimation of structure-specific fragility involves the use of dynamic analysis of a numerical model of the structure; e.g., incremental dynamic analysis (IDA, Vamvatsikos and Cornell, 2001, 2004). For the evaluation of state-dependent fragility curves, an extended version of IDA has been suggested in several studies (Luco et al., 2004; Ryu et al., 2011; Goda, 2012; Ruiz-García, 2012; Raghunandan et al., 2015; Goda, 2015; Baltzopoulos et al., 2018), referred to as *back-to-back* IDA. The main disadvantage of deriving fragility functions based on nonlinear dynamic analysis is the high computational cost involved, which includes both the time investment required for effectively modelling nonlinear structural behavior and computer time needed to run multitudes of analyses and post-process the results. This has motivated the development of simplified procedures for analytical fragility estimation, based on static nonlinear analysis, which is often termed *pushover analysis*. These methods make recourse to a surrogate structure in the form of an equivalent inelastic single-degree-of-freedom (SDOF) system, whose definition is based on the original structure's pushover curve. One such example, used in the case of traditional fragility estimation, is the method proposed in Vamvatsikos and Cornell (2005), which has been recently streamlined into a dedicated software tool (G. Baltzopoulos et al., 2017).

Herein a simplified pushover-based methodology is discussed, adapted specifically for the estimation of state-dependent fragility functions. While traditional fragility estimation requires a large number of non-linear runs, governed by the need for obtaining accurate estimates in the face of record-to-record variability of structural response (Iervolino, 2017; Baltzopoulos et al., 2019), this is even more so for state-dependent fragility, when the analysis should ostensibly represent all the possible effects, in terms of damage, of two consecutive earthquakes. Therefore, there is reason for exploring possible simplification in the latter case. In fact, in the case of sequential loading of the structure by consecutive instances of base-acceleration, without the possibility of intermediate remedial measures, the first shaking determines an intermediate damaged state of the structure, which will be called upon to sustain the second shock. This intermediate incarnation of the damaged structure is itself subject to some variability in terms of the fundamental dynamic structural properties, such as loss of stiffness and strength against lateral loads, and also residual displacements due to plastic deformation. In this context, a possible shortcut could be to account for the variability in structural properties of the damaged system via an analytical stochastic model, eschewing the need for dynamic runs representing the first shock, which brings the system to the damage state of interest.

The present chapter discusses exactly such a simplification, by considering this variability in structural properties, at the given damage state, directly on the static pushover; i.e., on the backbone curve of the equivalent SDOF. This can be achieved by using a semi-empirical predictive model for constant-ductility residual displacement ratios presented in the previous chapter; this model provides the joint probability distribution of residual displacement and other parameters necessary for the definition of the post-(first-)shock static pushover of an inelastic SDOF system, conditional on the attainment of a specific displacement demand during that shock. Thus, in lieu of executing sequential dynamic runs in order to represent a succession of damaging events within a sequence, the damaged structural configuration is obtained via Monte-Carlo simulation and analyses are executed only to account for the second shock, further reducing the computational cost.

The remainder of this chapter is organized as follows: first comes a discussion on the analytical derivation of fragility functions, both for the case of an intact structure and for an already-damaged structure. Subsequently, the procedure for simulating the damaged structures' pushovers is outlined, starting from a brief presentation of the residual displacement model and going on to describe the stochastic generation of backbone curves, given that the structure is in a specific damage state. Finally, the simplified methodology for state-dependent fragility derivation is illustrated via an application, whose results are then compared to those of a more rigorous procedure that involves sequential dynamic analysis. The chapter closes with some concluding remarks.

6.2. State-dependent structure-specific seismic fragility

A structure-specific seismic fragility function defines the conditional probability that, given a ground-shaking intensity measure (IM) is at a specific level (im), the structure fails to meet some performance objective. This failure is often termed exceedance of a *limit-* or *damage-*state and traditionally considers an intact structure that experiences a single seismic event. In the simplest of cases, fragility can be defined considering an appropriate measure of structural response, often termed an engineering demand parameter (EDP), and a threshold value thereof, edp_{DS}, whose exceedance is taken to signify transition of the structure from its initial state to the generic damage state DS, as expressed by Eq. (6.1):

$$P\left[DS|IM=im\right]=P\left[EDP>edp_{DS}|IM=im\right] \tag{6.1}$$

One of the possible strategies for fragility assessment, via dynamic analysis of a structure's non-linear numerical model, is the so-called *IM-based* approach (Jalayer, 2003), which employs the results of IDA (Vamvatsikos and Cornell, 2001, 2004). IDA scales a set of acceleration records to progressively higher im values, for which the numerical model provides the corresponding EDP responses. For every record used, the obtained EDPs can be plotted against the corresponding im level that the record had been scaled to – a graph that is usually designated as an IDA curve (Figure 6.1).

The IM-based method entails finding the intersections of the IDA curves, im_{DS}, with the vertical line passing through the threshold edp_{DS} value (Figure 6.1). These im_{DS} values can be regarded as realizations of a random variable (RV), IM_{DS}, which is the seismic intensity to which one needs to scale the ground motion in order for the structure to reach damage state DS. It is common practice to assume that IM_{DS} follows a lognormal distribution (Jalayer and Cornell, 2003; G. Baltzopoulos et al., 2017), in which case the fragility function can be estimated according to Eq.(6.2):

$$\begin{cases} P\left[DS \mid IM = im\right] = P\left[IM_{DS} \leq im\right] = \Phi\left[\left(\ln(im) - \eta\right)/\beta\right] \\ \eta = \dfrac{1}{n} \cdot \sum_{i=1}^{n} \ln\left(im_{DS,i}\right) \\ \beta = \sqrt{\dfrac{1}{n-1} \cdot \sum_{i=1}^{n} \left[\ln\left(im_{DS,i}\right) - \eta\right]^2} \end{cases}, \tag{6.2}$$

where η and β are the parameter estimates (median and logarithmic standard deviation) of the assumed lognormal distribution of IM_{DS}, $im_{DS,i}$ is the realization of the RV coming from to the *i*-th record and $\Phi(\cdot)$ is the standard Gaussian (cumulative) function.

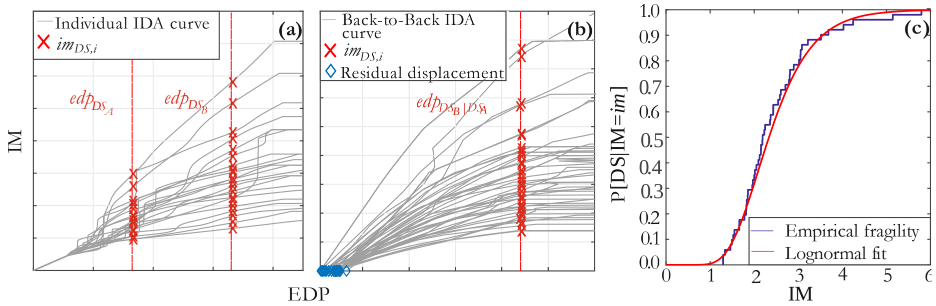

Figure 6.1 Example of IDA curves used for the evaluation of fragility curves for an intact structure (a); example of back-to-back IDA curves for the evaluation of state-dependent fragility curves (b); fragility curve estimation obtained by means of the IM-based approach (c).

When seismic reliability calculations are expected to account for earthquake clusters, the need arises to evaluate the probability that an already-damaged structure transitions from one damage state, say DS_A, to another more severe one, DS_B, in one seismic event. A state-dependent fragility function will provide that probability, conditional on occurrence of a shaking intensity *im* during one of the shocks in the cluster, which can be expressed as $P\left[EDP > edp_{DS_B|DS_A} \middle| DS_A \cap IM = im\right]$. In this case, the notation $edp_{DS_B|DS_A}$ denotes the EDP threshold for DS_B when the structure is already found in DS_A and the state-dependent fragility can simply denoted as $P\left[DS_B \middle| DS_A \cap IM = im\right]$. As already mentioned, one way of analytically estimating a state-dependent version of a fragility function, is my means of a variant of IDA, which is termed by some authors back-to-back IDA. In this type of dynamic analysis, the structural model is first subjected to a set of records hitting the structure at its intact (or initial) state, each scaled in amplitude to the lowest im value that results in $EDP = edp_{DS_A}$. At the end of each run, a different realization of the structure is produced, which can be considered to have made the transition to DS_A. Subsequently, each damaged incarnation of the structure is subjected to a second set of accelerograms representing a subsequent event of the same cluster. These records of the second set are scaled to progressively increasing im levels, similar to the traditional IDA procedure, until $EDP = edp_{DS_B|DS_A}$ is verified for the damaged structure, at an intensity of the shock which can be noted as $im_{DS_B,i}$ for the *i*-th succession of base accelerations. These intensity values can be used for the estimation of the parameters of a lognormal model for the state-dependent fragility, according to Eq.(6.2), in the same manner as in the case of traditional fragility. In Figure 6.1 an example of back-to-back IDA curves is provided, where it can be seen that at zero intensity, the curves start from a residual EDP value that the damaged structure has inherited from the first event.

6.3. Simulating the static pushover of an earthquake-damaged structure

6.3.1. Predictive model for constant-ductility residual displacement ratio

As mentioned previously, this study introduces a further simplification in pushover-based state-dependent fragility assessment; i.e., apart from use on an equivalent SDOF substitute structure, in the form of analytical probabilistic definition of the possible pushover curves that characterize the structure that has been damaged by a previous shock. This can be achieved by random sampling of the parameters that define a set of pushover curves, which represent different realizations of the damaged system. In this case, the chosen parameters are the residual displacement δ_{res}, the relative period elongation ΔT, and the loss of lateral strength ΔR (to follow). The analytical arsenal for performing this simulation is provided by a predictive model for the constant-ductility residual displacement ratio, C_μ, developed by the same authors; a preliminary version of this model, limited to non-degrading systems, was presented in Orlacchio et al. (2019), while the complete model that includes cyclic strength degradation in the hysteresis is given in the previous chapter and it is also briefly recalled to follow.

The constant-ductility residual displacement ratio is defined as $C_\mu = \delta_{res} / \delta_{max}$, that is the ratio of residual displacement δ_{res} to peak transient displacement δ_{max}, corresponding to a certain ductility μ. Relative period elongation is a measure of the loss of lateral stiffness of the structure during ground shaking and is defined as $\Delta T = \left(T' - T\right)/T$, where T' is the elongated post-shock period and T is the initial period of the SDOF structure. The elongated period is calculated as $T' = 2 \cdot \pi \cdot \sqrt{m/k'}$, where k' is the post-shock reloading stiffness (Figure 6.2a). Finally, loss of lateral strength is defined as $\Delta R = \left(F_{max} - F'_{max}\right)/F_{max}$, where $F_{max} = F_y \cdot \left[1 + \alpha_h \cdot (\mu - 1)\right]$ is the restoring force reached along the hardening branch of the initial backbone when pushed at ductility μ under static regime (i.e., in the absence of cyclic strength deterioration), F_y and α_h are, respectively, the yield force and hardening slope of the intact structure and F'_{max} represents the restoring force that can be reached at the same ductility on the backbone of the damaged SDOF system, when it exhibits cyclic strength degradation. As shown in Figure 6.2b, cyclic strength degradation entails a gradual offset of the force-displacement envelope towards the horizontal axis, due to progressive deterioration of structural elements. This is often modeled analytically by updating the backbone each time a hysteretic half-cycle is completed, with a reduction in resistance that is proportional to the dissipated energy (FEMA, 2009), by a factor that can be calibrated to represent a certain range of structural behavior, in terms of susceptibility deterioration phenomena. In this case, four deterioration levels are considered, termed as no degradation and low-, medium-, high-degradation cases, with the first being representative of modern code-conforming structural elements and the last of structural elements with poor dissipative characteristics. In analytical terms, these lateral strength degradation levels are represented by the dummy variable $DL = \{0, 1, 2, 3\}$, with $DL = 0$ corresponding to no degradation, $DL = 3$ to high-degradation level etc.

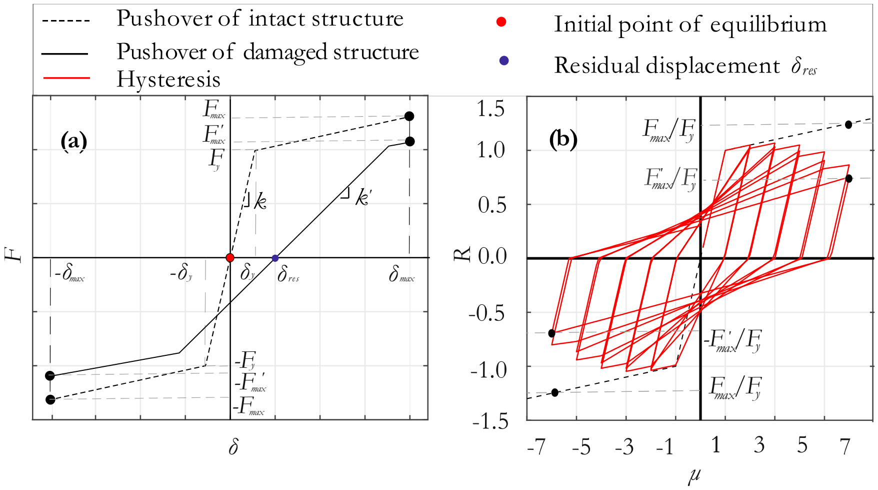

Figure 6.2 Examples of an SDOF structure's monotonic pushover (backbone) curve before and after incurring seismic damage (a); example of peak-oriented hysteresis at medium strength degradation level (b).

For a given ductility demand, that can represent the threshold edp_{DS} of some DS, the parameters C_μ, ΔT and ΔR are RVs whose joint distribution is provided by the predictive model given in the previous chapter. For sake of brevity, hereafter the equations and figures given in the previous chapter will be used to briefly recall the model.

In case of absent strength degradation $DL = 0$, only the joint distribution of C_μ and ΔT has to be evaluated by means the definition of the Lognormal marginal distribution of ΔT, completely defined by Eq.(5.6), and the Gaussian distribution of C_μ conditional to $\ln(\Delta T)$ expressed by Eq.(5.4). On the other hand, in presence of strength degradation $(DL = 1,2,3)$, the joint distribution of the three random variables C_μ, ΔT and ΔR has to be evaluated. This distribution can be defined from the joint distribution of $\{\ln(\Delta T), \ln(\Delta R)\}$ and the Gaussian distribution of C_μ conditional to $\ln(\Delta R)$ expressed by Eq.(5.5). $\{\ln(\Delta T), \ln(\Delta R)\}$ is a bivariate Gaussian variable and its joint distribution is defined using the marginal distribution of $\Delta T_{DL=1,2,3}$ shown in Eq.(5.7); the marginal distribution of $\ln(\Delta R)$ provided by Eq.(5.9) and Eq.(5.10) and the covariance matrix with the correlation coefficient $\rho_{\ln(\Delta T),\ln(\Delta R)}$ in Eq. (5.12).

The predictive model was developed considering the modified Ibarra-Medina-Krawinkler (mIMK) hysteretic model (Lignos and Krawinkler, 2011) with peak-oriented response. The model's range of applicability is for vibration periods

T between 0.3 s and 2.0 s, post-yield hardening ratios α_h ranging from 0 to 10% and ductility demands μ along the hardening branch between 1.5 and 9.

Examples of the model are given in Figure 5.7, Figure 5. 9 and Figure 5.11 of previous chapter where Figure 5.7, shows the model for the expected value of $\delta_{res}/\delta_{max}$ and the model of standard deviation σ_{δ} in presence of strength deterioration, while Figure 5. 9 and Figure 5.11 show a graph of the mean of period elongation, $\overline{(\Delta T)}$ in case of absent strength degradation $(DL=0)$ and the models for central tendency and standard deviation of $\ln(\Delta R)$ in the case of $DL=1$ (low stregth degradation level).

6.3.2. Simulation of the damaged structure's backbone curve

A single realization of the pushover curve characterizing a damaged structural system, can be obtained by random sampling triplets of values for elongated period, strength degradation and residual displacement from their joint distribution, given ductility demand. In this context, the conditioning ductility demand μ represents the threshold edp_{DS} that defines transition to the damage state under consideration. At this point, it should be noted that Eq.(5.4) and Eq.(5.5) implies that, given a certain ductility demand, the random vector $\{\ln(\Delta T),\ln(\Delta R)\}$ is conditionally independent of the residual displacement and follows a bivariate normal distribution. This means that a sample $\{x,y,z\}$, of the random vector $\{\ln(\Delta T),\ln(\Delta R),\delta_{res}/\delta_{max}\}$, can be obtained by the following procedure: first, given μ defining the DS, the level of strength deterioration and the characteristics of the initial structure T and α_h, a random value of $\ln(\Delta T)=x$ is extracted from a Gaussian distribution with mean $\overline{\ln(\Delta T)}$ and standard deviation $\sigma_{\ln(\Delta T)}$ given by Eq.(5.8). Subsequently, a value of $\ln(\Delta R)=y$ is randomly sampled from the conditional distribution of $\ln(\Delta R)$ given $\ln(\Delta T)=x$, which is also a Gaussian with mean and standard deviation given by Eq. *equation reference goes here*:

$$\begin{cases} \mathrm{E}\left[\ln(\Delta R)\middle|\ln(\Delta T)=x\right]=\overline{\ln(\Delta R)}+\rho_{\ln(\Delta T),\ln(\Delta R)}\cdot\left(\sigma_{\ln(\Delta R)}/\sigma_{\ln(\Delta T)}\right)\cdot\left[x-\overline{\ln(\Delta T)}\right] \\ \sigma_{\ln(\Delta R)|\ln(\Delta T)}=\sqrt{\left(1-\rho^{2}_{\ln(\Delta T),\ln(\Delta R)}\right)\cdot\sigma^{2}_{\ln(\Delta R)}} \end{cases} \tag{6.3}$$

where $\mathrm{E}\left[\ln(\Delta R)\middle|\ln(\Delta T)=x\right]$ represents the conditional mean of $\ln(\Delta R)$, $\sigma_{\ln(\Delta R)|\ln(\Delta T)}$ its conditional standard deviation, $\overline{\ln(\Delta R)}$ the marginal mean and $\sigma_{\ln(\Delta R)}$ the standard deviation from Eq.(5.9) and Eq.(5.10); and $\rho_{\ln(\Delta T),\ln(\Delta R)}$ is from Eq.(5.11). Finally, by substituting $\{\ln(\Delta T),\ln(\Delta R)\}=\{x,y\}$ into Eq.(5.4) and Eq.(5.5) thus evaluating the conditional mean and standard deviation of the ratio $\delta_{res}/\delta_{max}$, a value of $\delta_{res}/\delta_{max}=z$ is randomly sampled from the corresponding normal distribution, which is, however, truncated between $-2\cdot\sigma_{\delta}$ and $2\cdot\sigma_{\delta}$.

From this random sample of $\{\ln(\Delta T)=x,\ln(\Delta R)=y,\delta_{res}/\delta_{max}=z\}$, it is straightforward to obtain the corresponding residual displacement δ_{res}, elongated period T' and F'_{max}, all of which were defined previously. From this triplet of parameters, it is then possible to univocally define the realization of the damaged system's pushover curve by means of mechanical and geometric considerations. This is illustrated in Figure 6.3, where the coordinates of the points defining the initial and post-shock curve are given in the displacement-force plane. In the figure, the notation with primes represents the value of the corresponding parameter in the damaged system and the signed subscripts indicate the direction; e.g., δ'_{y+} and δ'_{y-} denote yield displacements of the post-shock backbone in the positive and negative direction, respectively. In fact, the elastic branch of the damaged system's pushover can be determined by evaluating the yield force and displacement in both directions as reported in Eq.(6.4):

$$\begin{cases} F'_{y^{\pm}}=\left[F'_{max}-F'_{max}\cdot\dfrac{\alpha_h}{\delta_y}\cdot\dfrac{F_y}{F_{max}}\cdot\left(\mu\cdot\delta_y\mp\delta_{res}\right)\right]\Big/\left[1-\dfrac{F'_{max}}{F_{max}}\cdot\alpha_h\cdot\left(\dfrac{T'}{T}\right)^2\right] \\ \delta'_{y^{\pm}}=\delta_y\cdot\dfrac{F'_{y^{\pm}}}{F_y}\cdot\left(\dfrac{T'}{T}\right)^2\pm\delta_{res} \end{cases} \quad .(6.4)$$

On the other hand, the degradation of the hardening branch's slope due to cyclic strength deterioration mode, which is implicit in the hysteretic model of Lignos and Krawinkler (2011), is given by Eq.(6.5) :

$$\alpha'_h=\alpha_h\cdot\frac{F'_{max}}{F_{max}}\cdot\left(\frac{F_y}{F'_{y^{\pm}}}\cdot\frac{\delta'_{y^{\pm}}\mp\delta_{res}}{\delta_y}\right) \quad (6.5)$$

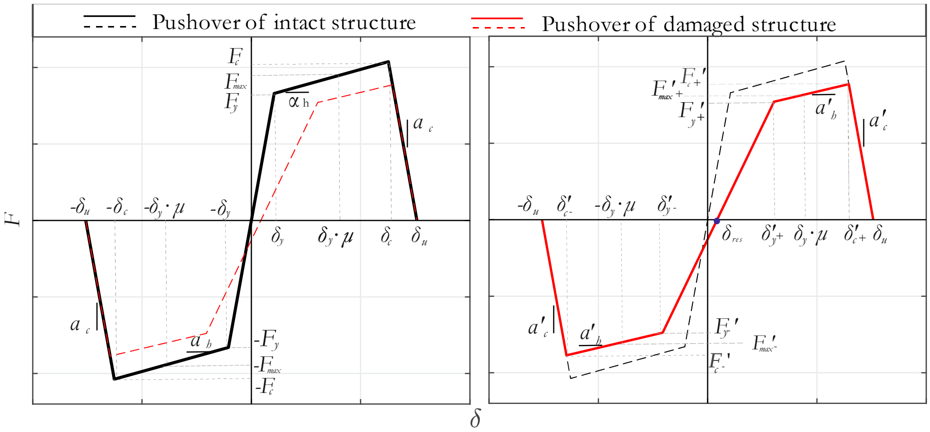

Figure 6.3 Parameters defining the pushover curves; parameters for the definition of the intact structure's pushover curve (a); and the damaged structure's pushover curve (b).

Apart from α'_b , the other parameters, which are needed to define the post-yield branch, are the capping point displacements in the two directions, $\delta'_{c^\pm}$ and corresponding forces $F'_{c^\pm}$. These can be calculated as the intersection points of the damaged structure's hardening branch of the and softening branch, whose slope is assumed to remain invariant, according to Eq.(6.6):

$$\begin{cases} \delta'_{c^\pm} = \left(F'_{y^\pm} - \dfrac{F'_{y^\pm}\cdot\alpha'_b\cdot\delta'_{y^\pm}}{\delta'_{y^\pm}\mp\delta_{res}} + \dfrac{F_c}{\delta_c-\delta_u}\delta_u \right) \Big/ \left(\dfrac{F_c}{\delta_c-\delta_u} - \dfrac{F'_{y^\pm}}{\delta'_{y^\pm}\mp\delta_{res}}\cdot\alpha'_b \right) \\ F'_{c^\pm} = \left[F_c\cdot\left(\delta'_{c^\pm}-\delta_u\right) \right] \big/ \left(\delta_c-\delta_u\right) \end{cases} . \quad (6.6)$$

6.4. Simplified evaluation of state-dependent fragility curves

The SDOF structure's backbone curves, sampled using the predictive model for C_μ , can be assumed to represent the pushover curves that correspond to different realizations of the structure, when that structure has transitioned to a certain damage state DS_A due to one shock within an earthquake cluster. Each realization has an asymmetric backbone due to the residual displacement δ_{res} , exhibiting elongated period T' and lateral resistance at yield and capping points in the two directions, $F'_{y^\pm}$ and $F'_{c^\pm}$.

In order to estimate the state-dependent fragility of the damaged structure, which is already at DS_A, each SDOF realization from Monte-Carlo simulation is subjected to incremental dynamic analysis, performed using a single record, randomly selected from a pool of available ground motions meant to simulate ground shaking due to a subsequent shock of the same cluster. The use of a single record per realization of the structure has been used before in the past, in the context of accounting for model uncertainty in seismic risk analysis Franchin et al., (2018). The records used in this phase are scaled to increasing im levels until the structural response of each realization reaches the threshold $edp_{DS_B|DS_A}$ defining the transition from damage state DS_A to DS_B. The final result of this procedure is a set of IDA curves, which constitute a more expedient substitute of the back-to-back IDA curves, and that can be used to evaluate the state-dependent fragility via the IM-based approach. In other words, the intensity values $im_{DS_B,i}$, causing the *i*-th simulated realization of the damaged system to reach $edp_{DS_B|DS_A}$, can be used for the estimation of the parameters defining a lognormal model for the state-dependent fragility, according to Eq.(6.2). This simplified procedure for state-dependent seismic fragility estimation is showcased by means of an illustrative application, which follows.

6.5. Illustrative application

This paragraph presents an application of the simplified procedure for the estimation of state-dependent seismic fragility curves. The objective of this application is to evaluate the accuracy of the introduced simplified method by comparing the calculated state-dependent fragility curves with the corresponding curves obtained using a more rigorous method, such as back-to-back IDA.

The application considers as case-study the structural system already presented in the previous chapter and hereafter briefly described. The system is a fixed-base four-storey plane reinforced concrete frame without masonry in-fills (Figure 6.4a). The structure geometry was defined so that the frame would exhibits a first-mode dominated dynamic elastic response with a first-mode period of natural vibration T_1 equal to 0.53 s and a flexural-dominated inelastic response (see Baltzopoulos et al., 2015 for structural details). The nonlinear structural model built for running nonlinear (static and dynamic) analyses adopted a lumped plasticity approach, using a piece-wise linear moment-rotation relation and the modified IMK model for the definition of the hysteretic behavior.

For the purposes of this application, an equivalent SDoF system was defined, based on a static nonlinear analysis that was carried out by applying a gradually increasing lateral force profile corresponding to the structure's first-mode excitation to base acceleration. The backbone of this equivalent SDoF oscillator was obtained by dividing the frame's pushover force and roof displacement values by a first-mode modal participation factor (Fajfar, 2000) of $\Gamma = 1.309$ and obtaining a multi-linear approximation of the resulting curve, as reported in Figure 6.4b.

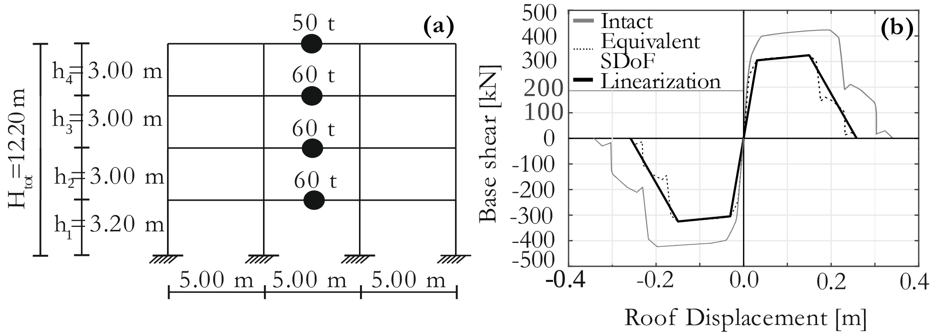

Figure 6.4 Basic information on the structure (a) and definition of the equivalent SDoF system (b).

In this multi-linear approximation, the nominal yield point of the equivalent SDoF system is taken to correspond to a RDR of 0.0033, i.e., the point of formation of a global plastic mechanism for the structure with yielding limited to beam ends. The mass m^*, period T^*, hardening slope α_h^* and all the other parameters defining the equivalent SDoF backbone curve are reported in Table 6.1.

Table 6.1 Characteristics of the equivalent SDoF system.

$T^*\ [s]$	$m^*\ [ton]$	$F_y\ [kN]$	δ_y [m]	$\alpha_h^*\ [-]$	δ_c [m]	δ_u [m]	$\alpha_c\ [-]$
0.774	147.13	304.81	0.031	0.017	0.147	0.244	-0.3

Although in pushover-based based methods the inelastic SDoF system is used as a proxy for the actual structure, introducing an additional approximation, this illustrative example directly considers the SDoF system, to isolate the consequences of the proposed procedure from effects stemming from the multi- to single-DoF substitution. Therefore, both the simplified method and the back-to-back IDA are conducted considering the equivalent SDoF system whose backbone is shown in Figure 6.4b. For the nonlinear dynamic analysis required by the procedure, the reference system is characterized by the modified IMK hysteretic model considered at first without strength degradation and then with a medium level of strength degradation, to test the effectiveness of the procedure in both cases. In order to showcase the simplified procedure, four damage states are arbitrarily defined, denoted from DS_1 to DS_4. The transition of the intact structure to damage state DS_1 is considered to occur when the structural response of the system exceeds the threshold edp_{DS_1} defined by a seismic ductility demand

μ, equal to 2, which corresponds to $\delta_{max} = 0.061$ m in this case. Along the same line, it is considered that the direct transition of the intact structure into DS_2, DS_3 and DS_4 occurs when μ exceeds the value of 3, 4 and 8.3, respectively. The last damage state corresponds to the collapse of the structure, i.e., a maximum inelastic displacement equal to 0.244 m. The four damage states are reported in Table 6.2 with the correspondent thresholds edp_{DS}.

Table 6.2 Damage states considered for the assessment of the state-dependent fragility curves.

Damage state	DS_1	DS_2	DS_3	DS_4
μ	2	3	4	8.3
edp_{DS} [m]	0.061	0.092	0.122	0.244

The threshold EDP values edp_{DS} used for the *direct* transition of the intact system into one of the four generic damage states (i.e., when the transition from intact to each DS is due to a single earthquake shock) are also considered as threshold EDP defining the transition of the already-damaged system. Although the exact value of the threshold displacement should take into account the nature of the DS and structural typology, the practice of using displacement demand alone to mark the exceedance of limit states on the pushover of the intact structure, is common in earthquake engineering (e.g., Ricci et al., 2018).

For this application, the conditioning values of $\mu = 2$ and $\mu = 3$, i.e., $edp_{DS1} = 0.061\text{m}$ and $edp_{DS2} = 0.092\text{m}$, are used to simulate the sets of one-hundred backbone curves, according to the sampling procedure previously described. In each set, the backbones represent one hundred possible realizations of the pushover of the structure having reached damage state DS_1 or DS_2. The backbone curves obtained from the predictive model for the cases of absent or medium level of strength degradation and for the two values of conditioning ductility are given in Figure 6.5. It is worth noting that in absence of strength degradation (Figure 6.5a-b) the backbone curves of the damaged structure differ among themselves only in residual displacement and elastic stiffness.

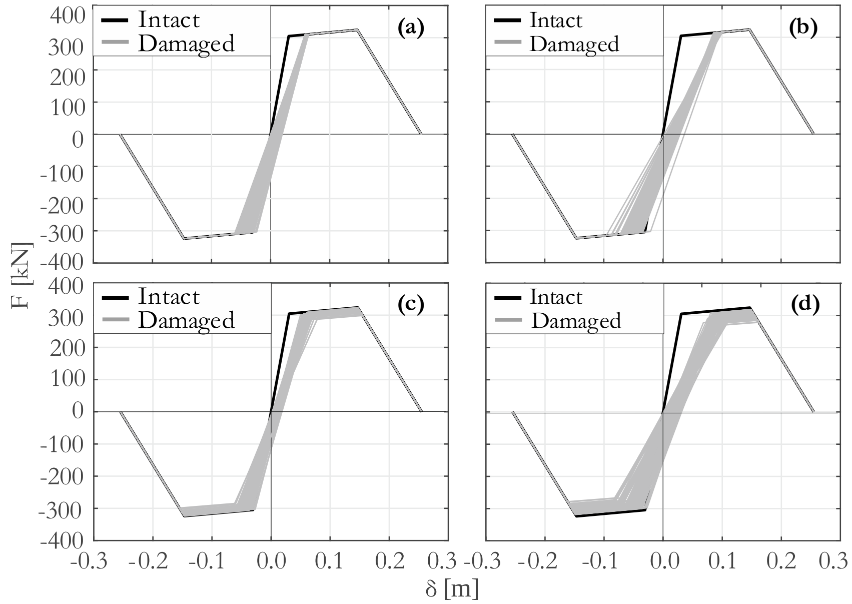

Figure 6.5 Backbone curves representing different realizations of the damaged structure in case of DL=0 and conditioning ductility equal to 2 (a); DL=0 and conditioning ductility equal to 3 (b); DL=2 and conditioning ductility equal to 2 (c); DL=2 and conditioning ductility equal to 3 (d).

Subsequently, for each set of one-hundred backbone each realization of the damaged system is subjected to IDA, using one record per extracted pushover, which is scaled upwards until the transition from the initial damage state (DS_1 or DS_2) to a more severe one occurs. The IM considered during IDA is the spectral acceleration at the period of the intact structure, $Sa(T)$. These analyses were run using the OPENSees finite-element platform McKenna (2011), where a custom-made version of the mIMK hysteretic model was implemented, which also allows for user-defined unloading stiffness. The IDA curves obtained in this manner are shown in Figure 6.6 where the im_{DS_i} points, obtained from their intersection with the edp_{DSi} lines, are shown as red crosses. At this point, these im_{DS_i} values of each edp_{DSi} can be used to estimate the parameters of a lognormal model for the state-dependent fragility curves according to Eq. (6.2).

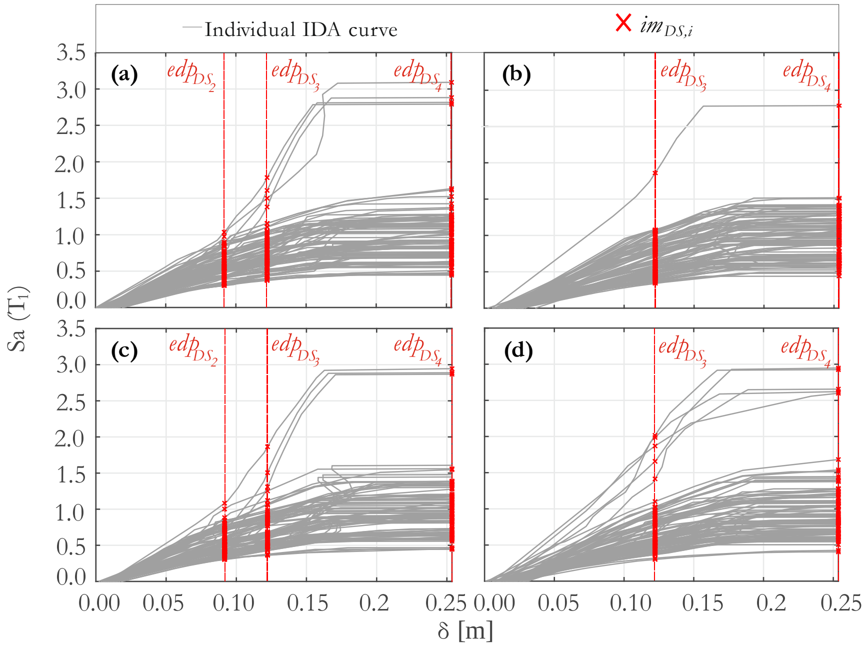

Figure 6.6 IDA curves obtained from the application of the simplified methodology in case of DL=0 and conditioning ductility equal to 2(a); DL=0 and conditioning ductility equal to 3 (b); DL=2 and conditioning ductility equal to 2 (c); DL=2 and conditioning ductility equal to 3 (d).

In order to obtain some points of reference for comparing the results of this procedure, the same state-dependent fragilities were estimated by means of back-to-back IDA, using a set of twenty records to represent the first damaging shock of the cluster, scaled so as to cause a ductility demand of two or three, and another 20 subsequent-shock accelerograms per initial shock, for a total of four-hundred curves. Additionally, a twenty-record IDA was used to estimate the intact structure's traditional fragility curves for the four damage states reported in Table 6.2, $P\left[DS_i \mid IM = im\right]$. These runs were performed using an OPENSees user interface developed to streamline the back-to-back IDA Baltzopoulos et al., (2018).

The resulting median and standard deviations defining the fragility curves for the intact structure in case of $DL = 0$ and of $DL = 2$ are reported in Table 6. 3. The corresponding cumulative probability functions are shown in Figure 6.7 in which the blue, green, orange and red solid lines refer to DS_1, DS_2, DS_3 and DS_4 respectively.

Table 6. 3 Median η and logarithmic standard deviation β defining the fragility curves for the two intact structures (IM in g).

	MEDIAN η				SIGMA β			
DL	DS_1	DS_2	DS_3	DS_4	DS_1	DS_2	DS_3	DS_4
0	0.426	0.610	0.774	1.072	0.237	0.297	0.353	0.408
2	0.430	0.610	0.767	1.082	0.240	0.295	0.3646	0.416

Table 6.4 and Table 6.5 collect the values of the median, η, and logarithmic standard deviation, β, defining the parametric state-dependent fragility curves for the two systems evaluated by means of the simplified method and of back-to-back IDA procedure, respectively. In the tables, the second column gives the initial damage state whereas the damage states reported in the rest of the row represent the arrival damage states.

Table 6.4 Median η and logarithmic standard deviation β defining the state-dependent fragility curves of the two intact structures evaluated using the simplified methodology (IM in g).

DL	DS	DS_2		DS_3		DS_4	
		η	β	η	β	η	β
0	DS_1	0.546	0.312	0.703	0.337	0.948	0.378
	DS_2	\	\	0.651	0.340	0.936	0.336
2	DS_1	0.518	0.293	0.662	0.323	0.941	0.364
	DS_2	\	\	0.629	0.377	0.934	0.393

Table 6.5 Median η and logarithmic standard deviation β defining the state-dependent fragility curves of the two intact structures evaluated using the back-to-back IDA (IM in g).

DL	DS	DS_2		DS_3		DS_4	
		η	β	η	β	η	β
0	DS_1	0.555	0.314	0.734	0.343	1.058	0.425
	DS_2	\	\	0.654	0.378	1.057	0.410
2	DS_1	0.554	0.314	0.732	0.344	1.071	0.430
	DS_2	\	\	0.654	0.379	1.065	0.426

The corresponding cumulative probability functions evaluated with the simplified procedure and the rigorous method of back-to-back IDA are shown in Figure 6.8 and Figure 6.9 for the case $DL = 0$ and in Figure 6.10 and Figure 6.11 for the case $DL = 2$. Figure 6.8 and Figure 6.10 refer to the transitions having DS_1 as initial damage state and DS_2 (panel (a)), DS_3 (panel (b)) and DS_4 (panel (a)) as final damage state. Figure 6.9 and Figure 6.11 refer to the transitions having DS_2 as initial damage state and DS_3 (panel (a)) and DS_4 (panel (c)) as final damage state.

The comparison shows that the simplified procedure provided state-dependent fragilities estimates which are similar to those coming from the more rigorous back-to-back IDA. For the transitions that does not have DS_4 as final damage state, the results of the simplified method are very close to those derived from the rigorous method, any slight difference can be explained by taking into account the concept of estimation uncertainty of the parameters defining the fragility due to the use of a reduced number of records in the assessment (Iervolino, 2017; Baltzopoulos et al. 2019). A larger difference is observable for the transitions having DS_4 as final damage state, this is in accordance with other studies concerning the damage state of collapse (Zareian, 2006; Eads et al., 2013).

On a side-note, the fragility functions of the intact structure serve as a reference, showcasing the characteristic shift-to-the-left of the state-dependent curves, due to the drop in median capacity caused by the transition to the first damage state (DS_1 or DS_2) due to the damage induced by the first shock.

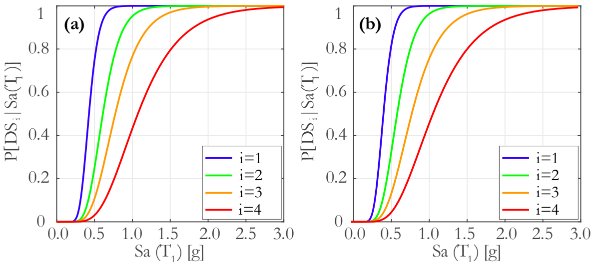

Figure 6.7 Fragility curves of intact structure evaluated at the four damage states by means of IDA evaluated in case of $DL = 0$ (a) and $DL = 2$ (b).

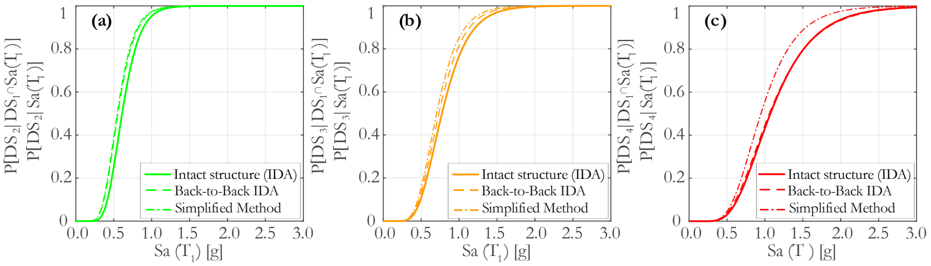

Figure 6.8 State-dependent fragility curves evaluated with the simplified methodology and the back-to-back IDA approach conditioned to the damage state DS_1 and fragility curves of intact structure evaluated for the case with $DL = 0$.

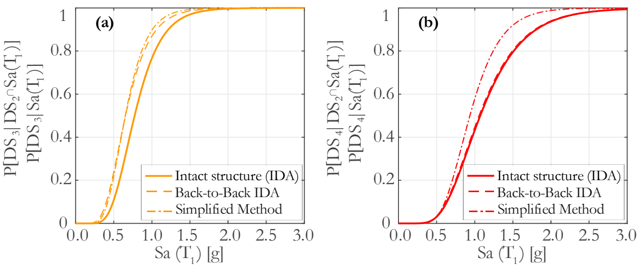

Figure 6.9 State dependent fragility curves evaluated with the simplified methodology and the back-to-back IDA approach conditioned to the damage state DS_2 and fragility curves of intact structure evaluated in case of $DL = 0$.

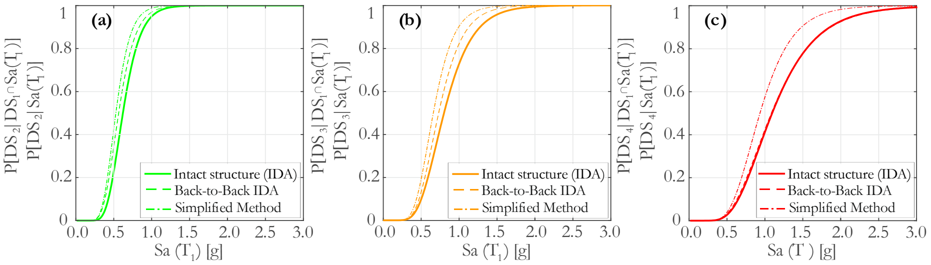

Figure 6.10 State dependent fragility curves evaluated with the simplified methodology and the back-to-back IDA approach conditioned to the damage state DS_1 and fragility curves of intact structure in case of $DL = 2$.

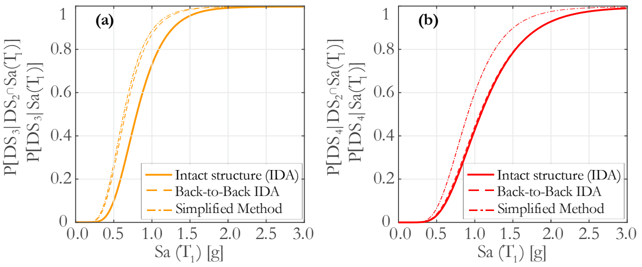

Figure 6.11 State-dependent fragility curves evaluated with the simplified methodology and the back-to-back IDA approach conditioned to the damage state DS_2 and fragility curves of intact structure evaluated in case of $DL = 2$.

Concerning the computational cost, the simplified procedure allowed to assess the state-dependent fragility curve for each transition probability defining only 100 IDA curve rather than the 400 curves required by the back-to-back IDA. In terms of time, for each SDoF analyzed in this application the simplified procedure required 1.0 hour and 5.0 minutes rather than the about 2 hours (1.0 hour and 55 minutes) required by the back-to-back IDA.

6.6. Conclusions

The main objective of this chapter was to present a simplified pushover-based procedure aimed at the estimation of state-dependent seismic fragility curves. The proposed methodology uses a semi-empirical predictive model for constant-ductility displacement ratios to obtain, through Monte-Carlo simulation, a set of realizations of the damaged structure's pushover curve. The usefulness of this shortcut lies in the fact that, due to the record-to-record variability of structural response to strong earthquakes, a structure subjected to a single instance of base-acceleration may fall under a generic damage state while exhibiting different permutations of basic dynamic properties, such as resistance to inertial load, stiffness and residual displacement. Such variability is typically accounted for via sequential runs to accelerogram couples that represent the alternation of two damaging shocks within an earthquake cluster, as in the case of back-to-back incremental dynamic analysis. In the simplified proposal, the first part of the sequential analysis is avoided, replaced by simulation of the principal characteristics of the equivalent SDOF system at a given damage state. The illustrative application presented as part of this chapter shows that the proposed methodology can represent a viable alternative to the more computationally intensive procedures, at least for regular structures for whom pushover-based procedures are a viable approximation.

References

Baltzopoulos, G., R. Baraschino, and I. Iervolino (2019), On the number of records for structural risk estimation in PBEE, *Earthq. Eng. Struct. Dyn.*, 48(5), 489–506.

Baltzopoulos, G., R. Baraschino, I. Iervolino, and D. Vamvatsikos (2017), SPO2FRAG: software for seismic fragility assessment based on static pushover, *Bull. Earthq. Eng.*, 15(10).

Baltzopoulos, G., R. Baraschino, I. Iervolino, and D. Vamvatsikos (2018), Dynamic analysis of single-degree-of-freedom systems (DYANAS): a graphical user interface for OpenSees, *Eng. Struct.*, 177, 395–408.

Baltzopoulos, G., E. Chioccarelli, and I. Iervolino (2015), The displacement coefficient method in near-source conditions, *Earthq. Eng. Struct. Dyn.*, 44(7), 1015–1033.

Eads, L., E. Miranda, H. Krawinkler, and D.G. Lignos (2013), An efficient method for estimating the collapse risk of structures in seismic regions, *Earthq. Eng. Struct. Dyn*, 42(1), 25–41.

Fajfar, P. (2000), A nonlinear analysis method for performance based seismic design., *Earthq. Spectra*, 16(3), 573–592.

FEMA (2009), FEMA P440 - Effects of Strength and Stiffness Degradation on Seismic Response, *Fema P440a*, (June), 312.

Franchin, P., L. Ragni, M. Rota, and A. Zona (2018), Modelling Uncertainties of Italian Code- Conforming Structures for the Purpose of Seismic Response Analysis, *J. Earthq. Eng.*, 22(2), 28–53.

Goda, K. (2012), Nonlinear response potential of Mainshock-Aftershock sequences from Japanese earthquakes, *Bull. Seismol. Soc. Am.*, 102(5), 2139–2156.

—— (2015), Record selection for aftershock incremental dynamic analysis, *Earthq. Eng. Struct. Dyn.*, 44, 1157–1162.

Iervolino, I. (2017), Assessing uncertainty in estimation of seismic response for PBEE, *Earthq. Eng. Struct. Dyn.*, 46(10), 1711–1723.

Iervolino, I., E. Chioccarelli, and A. Suzuki (2020), Seismic damage accumulation in multiple mainshock-aftershock sequences, *Earthq. Eng. Struct. Dyn.*

Iervolino, I., M. Giorgio, and E. Chioccarelli (2016), Markovian modeling of seismic damage accumulation, *Earthq. Eng. Struct. Dyn.*, 45(3), 441–461.

Jalayer, F. (2003), Direct Probabilistic Seismic Analysis : Implementing Non-Linear Dynamic Assessments, Stanford University.

Jalayer, F., and C.A. Cornell (2003), A Technical Framework for Probability-Based Demand and Capacity Factor Design (DCFD) Seismic Formats, *PEER Rep. 2003/8*, 122.

Lignos, D., and H. Krawinkler (2011), Deterioration modeling of steel components in support of collapse prediction of steel moment frames under earthquake loading, *J. Struct. Eng.*, 137(11), 1291–1302.

Luco, N., P. Bazzurro, and C.A. Cornell (2004), "Dynamic versus static computation of the residual capacity of a mainshock-damaged building to withstand an aftershock," in: *13th World Conference on Earthquake Engineering, Vancouver, B.C., Canada August 1-6*.

McKenna, F. (2011), OpenSees: A framework for earthquake engineering simulation, *Comput. Sci. Eng.*, 13(4), 58–66.

Orlacchio, M., G. Baltzopoulos, and I. Iervolino (2019), Constant-ductility residual displacement ratios, *Proc. COMPDYN 2019, 7th ECCOMAS Themat. Conf. Comput. Methods Struct. Dyn. Earthq. Eng. Crete, Greece June, 24-26*.

Raghunandan, M., A.B. Liel, and N. Luco (2015), Aftershock collapse vulnerability assessment of reinforced concrete frame structures, *Earthq. Eng. Struct. Dyn.*, 44(3), 419–439.

Ricci, P., V. Manfredi, F. Noto, M. Terrenzi, C. Petrone, F. Celano, M.T. De Risi, G. Camata, P. Franchin, G. Magliulo, A. Masi, F. Mollaioli, E. Spacone, and G.M. Verderame (2018), Modeling and Seismic Response Analysis of Italian Code-Conforming Reinforced Concrete Buildings, *J. Earthq. Eng.*

Ruiz-García, J. (2012), Mainshock-aftershock ground motion features and their influence in building's seismic response, *J. Earthq. Eng.*, 16(5), 719–737.

Ryu, H., N. Luco, S.R. Uma, and A.B. Liel (2011), Developing fragilities for mainshock-damaged structures through incremental dynamic analysis, *Proc. Ninth Pacific Conf. Earthq. Eng.*, (225), 8.

Vamvatsikos, D., and C.A. Cornell (2001), Incremental Dynamic Analysis, *Earthq. Eng. Struct. Dyn.*, 31(3), 491–514.

—— (2004), Applied incremental dynamic analysis, *Earthq. Spectra*, 20(2), 523–553.

—— (2005), Direct estimation of the seismic demand and capacity of MDOF systems through Incremental Dynamic Analysis of an SDOF approximation, *J. Struct. Eng.*, 131(4), 589–599.

Zareian, F. (2006), Simplified performance-based earthquake engineering, Stanford University.

Summary and conclusions

The current best practice for seismic risk assessment is the Performance-Based Earthquake Engineering (PBEE) framework developed by the Pacific Earthquake Engineering Research Center (PEER). This approach does, however, have a limitation, as it generally only examines single events, neglecting the possibility of a succession of earthquakes, for example, in the form of seismic sequences. Large earthquakes (i.e., mainshocks) typically trigger a sequence of lower magnitude events clustered in both time and space. Some modifications to the seismic risk-assessment framework are therefore required to account for these multiple events from the viewpoints of the seismic hazard and seismic vulnerability. In relation to the first of these perspectives, the occurrence of further earthquakes after the main event has to be considered, for example, this is possible via the Sequence-Based Probabilistic Seismic Hazard Analysis (SPSHA) which enables account to be taken of hazard increments due to aftershocks. Meanwhile, from the point of view of structural vulnerability, it has also to be assumed that each seismic event does not always affect a structure in an intact condition, with the prospect of damage accumulation requiring investigation. This can be achieved by exploiting state-dependent fragilities, i.e., fragilities that describe the probability of failure of a structure that has already sustained damage, referred to as its initial damage state.

This thesis focused on these two components - seismic hazard - (Chapter 2) and -structural vulnerability - (from Chapter 3 to Chapter 6). In detail, the study addressed the elements that enable the classical seismic-risk assessment framework to be extended to also cover the issue of seismic sequences. The conclusions reached and relevant remarks from each chapter are summarized in what follows.

Chapter 2 investigated the implications on the definition of design seismic actions in the United Kingdom, stemming from including seismic sequences in hazard analysis. To this end, the recent source model from the British Geological Survey (BGS) was used to conduct SPSHA to investigate the hazard increments caused by aftershocks. The parameters of the modified Omori law, which was employed to model aftershocks occurrences, were calibrated based on four seismic sequences that had occurred in the UK and were assumed to be complete in the magnitude range of interest. To ensure that a consistent comparison was possible, a classical Probabilistic Seismic Hazard Analysis (PSHA) was also performed and validated based on the official BGS results. Hazard maps for four exceedance return periods (within 95 yr and 2475 yr) and in terms of peak ground acceleration PGA, and pseudo-accelerations at two vibration periods, i.e., 0.2 s and 1.0 s, $Sa(T = 0.2\mathrm{s})$ and $Sa(T = 1.0\mathrm{s})$, were obtained from SPSHA and compared to their PSHA counterparts. The comparison was conducted in terms of maximum and average increments expressed in absolute and percentage terms. The maps revealed that the hazard increases for each spectral and return period tends to be more relevant in the areas covering most of Wales, the center of northern England and western Scotland (the areas exposed to the greatest hazard according to the classical PSHA and in accordance with the findings of the previous literature). The largest percentage increase due to aftershocks across the country for a given spectral ordinate, has a non-monotonic trend in relation to the return period; the highest value was equal to 10%, which was found at $T_r = 1100\ \text{yr}$ for $Sa(T = 1.0\,\text{s})$; meanwhile, for PGA and $Sa(T = 0.2\,\text{s})$, it was 14% at $T_r = 2475\ \text{yr}$. Taking into account the range of return periods between 95 yr and 2475 yr, the largest average percentage differences were equal to 11% for PGA, 3% for $Sa(T = 0.2\,\text{s})$, and 10% for $Sa(T = 1.0\,\text{s})$; they were found at $T_r = 2475\ \text{yr}$, $T_r = 95\,\text{yr}$ and $T_r = 475\,\text{yr}$, respectively. The maximum absolute differences between the results of SPSHA and PSHA for a given spectral ordinate across the country increased monotonically with the return period (in the range considered). Nationwide, the largest differences between SPSHA and PSHA for $T_r = 2475\,\text{yr}$ were equal to 0.033 g, 0.069 g and 0.006 g for PGA, $Sa(T = 0.2\,\text{s})$ and $Sa(T = 1.0\,\text{s})$, respectively. On average the absolute differences across the country for $T_r = 2475\ \text{yr}$ were 0.0051 g, 0.0041 g and 0.0013 g again for PGA, $Sa(T = 0.2\,\text{s})$ and $Sa(T = 1.0\,\text{s})$, respectively.

To gain further insight into the aftershock implications, the results of the PSHA and SPSHA for exceedance return-periods up to 10000 yr, and taking into account 24 spectral ordinates, were compared and exanimated in greater detail. This comparison concerned three sites, Edinburgh, Cardiff and Llangefni which were selected because their exposures to comparatively low, medium and high seismic hazard, respectively, according to PSHA results. The analysis for specific sites revealed that the aftershock effects were more significant at vibration periods shorter than 0.3s, tending to improve with longer periods and becoming almost constant from 1.0 s onwards. The largest relative difference between the results of SPSHA and PSHA was identified at 0.1s for all the sites. In Llangefni, which is the site characterized by the highest seismic hazard countrywide, the return period for which the largest hazard increase was found to vary significantly between the different spectral ordinates, equaling 4060 yr, 1720 yr and 1830 yr for PGA, $Sa(T = 0.2\,\text{s})$ and $Sa(T = 1.0\,\text{s})$, respectively. Finally, the aftershock effects estimated for the UK were briefly compared to the findings of a previous SPSHA study conducted for Italy, where the seismic hazard is relatively higher. The comparison showed that at the most hazardous sites of the UK, the hazard percentage increments obtained with the SPSHA compared to the results of the

PSHA were about a half of those found of the most hazardous areas in Italy, although in Italy the largest spectral acceleration associated to a given return period can be even three times larger than the analogous one in the UK.

Chapter 3 and **Chapter 4** dealt with the assessment of state-dependent fragility curves using the rigorous method of back-to-back incremental dynamic analysis (IDA) applying it to single structures and buildings classes. In detail, **Chapter 3** sets out the assessment of the intact-structures fragilities and the state-dependent fragilities for a case-study system representative of the unreinforced masonry terraced houses commonly found in the Groningen region of the Netherlands. These have been the subject of extensive research, because of the seismicity induced in the area by the commercial extraction of gas. The first part of the chapter dealt with the assessment of the fragility curves of the intact structure obtained via Cloud Analysis of 3D model developed in collaboration with the firm Arup Italy using the finite element software LS-DYNA. This allowed us to touch some critical points concerning the fragility assessment of masonry buildings such as: 1) the definition of an engineering demand parameter (EDP) representative of the structural response and 2) the definition of the limit states. The main issue of the masonry structures in the context of the fragility assessment is the possibility that the structural failure may occur locally without affecting the whole structure and requiring therefore to monitor the damage at different levels; i.e., at the levels of the structural elements, at the macro-elements level and at the level of the whole structure. Moreover, both the failure modes (flexural and shear) of piers and spandrels have to be considered. The assessment in this chapter was conducted assuming the definition of the limit states based on the multiscale approach described in the Italian Guidelines and Technical Instructions of the National Research Council (CNR-DT 212/2013) which allows taking into account the damage spread at different levels of the structure. It should be recalled that this assessment was conducted assuming the shear failure mode for the single structural elements in order to obtain a conservative assessment of the structural fragility. A more precise evaluation of the fragilities would require the identification for each element of the failure mode developed during each nonlinear dynamic analysis.

The high computational cost for the assessment of fragility curves of the intact structure conducted using the 3D model have demonstrated the impossibility assessing the state-dependent fragility curves in a reduced period of time for this type of structure. Therefore, this assessment was conducted resorting to two equivalent single degree-of-freedom (ESDoF) systems defined and calibrated to be representative of the behavior of the structure in its two main directions. The calibration was based on the monotonic and cyclic pushover curves of the initial structure, which were obtained using two type of force distributions (the uniform mass-proportional and the inverse triangular). The SDoF systems were analyzed via back-to-back IDA and the state-dependent fragility curves were obtained via the IM-based approach, assuming a lognormal distribution model. The fragility curves and the state-dependent fragility curves were estimated in terms of the average spectral acceleration, which was evaluated by taking into account 20 equally spaced periods between 0.01 s and 0.2 s.

Chapter 4 described the assessment of the intact-structures and state-dependent fragility functions for Italian reinforced concrete (RC) and masonry structures classes. These evaluations constitute one of the outcomes of the European research project RISE and were conducted using IDA and back-to-back IDA, respectively. The assessments employed the ESDoF approximation of single structures, with each of them representing a building class. The analyses were performed using the OpenSees platform via a recent version of the DYANAS software. Also in this chapter, two issues that significantly affect the assessment of fragilities in case of structure classes are addressed: 1) the choice of the intensity measure (IM) and 2) the reduction of the computational cost for nonlinear dynamic analyses. They were addressed by considering four benchmark systems (two representative of reinforced concrete structures and two representative of masonry structures). Concerning the first issue, the comparison of the different IMs confirmed that, due to their greater efficiency, those involving a geometric mean of spectral accelerations, i.e., Sa_{avg} and I_{NP}, performed better than single-period spectral ordinates. In view of the absence of a specific calibration of the I_{NP} intensity measure, Sa_{avg} was selected for fragilities and state-dependent fragilities in both structures' typologies. The use of this type of intensity measure seems to represent a better solution when a unique IM has to be selected for different structures; i.e., in the case of building classes for which the spectral acceleration at a single vibration period may not be representative of the whole class, since the structural properties of the buildings within each class may vary substantially. As far as the limitation of the computational cost, in this chapter the issue was addressed identifying a limited number of records required for the fragility assessment. In this case, 35 ground motions was used, being a compromise between the computational cost and precision in fragility assessment, based on the statistical-inference concept of estimation uncertainty. Finally, some considerations were made for the definition of the distribution model to be assumed to define the parametric fragilities. The lognormal distribution was assumed to define the parametric fragility curves of the intact structure. In relation to the state-dependent fragility curves, the choice was made between the lognormal and the gamma distribution models on the basis of the seismic-hazard failure rates assessed at three Italian sites: L'Aquila, Naples and Milan. The lognormal distribution model was ultimately selected because it enabled us to obtain failure-rate values that were closer than the reference values obtained with the empirical fragility curves (without any approximation due to the distribution assumption). Therefore, the chapter provides lognormal fragility parameters defining the fragility curves for the intact structures and the state-dependent fragility curves for Italian RC and masonry structures classes.

Since the SERA project provided a set of capacity curves for each class of the RC structures, future evaluations will address the evaluation of fragilities and state-dependent fragilities using for each class different capacity curves and not only the average capacity curves.

Finally, the main purpose of **Chapter 5** and **Chapter 6** was to present a simplified pushover-based procedure aimed at estimating state-dependent seismic fragility curves for first-mode dominated RC structures. The proposed methodology employs a semi-empirical predictive model for the central tendency and the related record-to-record variability of residual displacements of bilinear SDoF systems exhibiting stiffness and strength degradations. This model was introduced in **Chapter 5** from its definition to all its possible applications. The predictive model, and consequently the simplified method, is applicable to SDoF systems with values of natural vibration period between 0.2 s and 2.0 s and post-yielding hardening ratio between 0% and 10%. Moreover, the model was developed for systems whose hysteretic behavior can be described by the peak-oriented modified Ibarra-Medina-Krawinkler hysteretic model and analyses for which the achievement of the damage state can be globally defined in terms of ductility demand considered ranged from 1.5 to 9.0 but always lower than the capping ductility of the capacity curve (i.e., in-cycle degradation is not considered). In the model, the mean residual-displacement ratio is defined as a function of two correlated random variables, the elongated period and the strength loss representing the effects of degradations in stiffness and strength, respectively. Consequently, the complete definition of the model also required the development of subsidiary models providing the marginal distributions of the elongated period and loss of strength, as well as their correlation. Given the characteristics of the capacity curves of the intact structure and the reached damage state expressed in terms of ductility demand, the predictive model allows to define via a Monte-Carlo sampling scheme: 1) the joint distribution of the three random variables (residual displacement, period elongation and strength degradation), 2) the residual displacement ratio spectra and 3) the pushover curve of the damaged structure. Indeed, the final goal of the model is the derivation of pushover curves considering the uncertainties characterizing a damaged structural system. The generation of the post-damaged pushover curves constitutes the basis of the simplified methodology for assessing of state-dependent fragility curves, as described and applied in **Chapter 6**. Due to the record-to-record variability of structural response to strong earthquakes, a structure subjected to a single instance of base-acceleration may fall under a generic damage state while exhibiting different permutations of basic dynamic properties, such as resistance to inertial load, stiffness and residual displacement. Such variability is typically accounted for via sequential runs to accelerogram couples representing the alternation of two damaging shocks within an earthquake cluster, with an example being the back-to-back Incremental dynamic analysis. The value of this method comes from the fact that the first part of the sequential analysis is avoided, replaced by a simulation of the principal characteristics of the equivalent SDoF system at a given damage state. After the production of the set of pushover curves, the method requires the execution on an IDA conducted with one record for each damaged system. The illustrative applications shown in Chapter 6 demonstrated the capacity of this simplified methodology to facilitate the calculation of state-dependent fragilities with good approximation and using fewer NLDAs than the rigorous and more time-consuming back-to-back IDA method.

Future developments of the simplified method may concern the overcoming of the limits of applicability of the predictive model, extending the field of application of the parameters and considering other types of capacity curves and hysteretic behavior, thus allowing the extension of the simplified methodology to other structural typologies.

Author's Publications

1. Orlacchio M., Baltzopoulos G., Iervolino I. (2019), "Constant-ductility residual displacement ratios", Proceedings of COMPDYN 2019, 7th ECCOMAS Thematic Conference on Computational Methods in Structural Dynamics and Earthquake Engineering, 24-26 June 2019, Crete, Greece.

2. Orlacchio M., Baltzopoulos G., Iervolino I. (2020), "State-dependent seismic fragility via pushover analysis." Proceedings of the 17th World Conference on Earthquake Engineering, 17WCEE Sendai, Japan.

3. Orlacchio M., Chioccarelli E., Baltzopoulos G., Iervolino I. (2021), "State-dependent seismic fragility functions for Italian reinforced concrete structures: preliminary results." Proceedings of the 31st European Safety and Reliability Conference (ESREL), 19-23 September 2021, Angers, France.

4. Orlacchio M., Cito P., Polidoro B., Villani M., Iervolino I. (2021), "Sequence based hazard maps for the United Kingdom" (Under review).